Formation and paleoclimatic interpretation of a continuously laminated sapropel S_5: a window to the climate variability during the Eemian interglacial in the Eastern Mediterranean

Dissertation

der Mathematisch-Naturwissenschaftlichen Fakultät

der Eberhard Karls Universität Tübingen

zur Erlangung des Grades eines

Doktors der Naturwissenschaften

(Dr. rer. nat.)

vorgelegt von

Tobias Franz Moller

aus Stuttgart

Tübingen

2012

Tag der mündlichen Qualifikation: 15.06.2012

Dekan:	Prof. Dr. Wolfgang Rosenstiel
1. Berichterstatter:	Dr. Hartmut Schulz
2. Berichterstatter:	Prof. Dr. Michal Kučera

Abstract

The deep sea sediment record of the Eastern Mediterranean is characterised by the periodic deposition of organic-rich layers (sapropels), coinciding with freshwater flooding episodes, which reflect insolation-controlled changes in monsoonal precipitation over Africa. The sapropels are thought to correspond to several thousand years of deposition, resulting in a thickness of a few decimetres. A remarkable exception occurred during the deposition of the last interglacial sapropel S_5 in parts of the Levantine Basin. Here, the S_5 sapropel reaches a thickness of almost one meter, allowing the study of environmental processes during the peak warmth of the last interglacial with decadal resolution. This work aims to take advantage of this unique paleoenvironmental archive and investigates the oceanographic conditions as well as the land-sea interactions in the Levant during the last interglacial, including an assessment of the effect of solar forcing on the depositional system and the plankton community and to provide an explanation for the unusual thickness of the studied sapropel. To this end, the expanded S_5 horizon has been studied in three cores from the northern Levantin Basin in the Eastern Mediterranean. The S_5 sapropel in these cores features a fine, sub-mm thin lamination, seeming to reflect the annual blooming of mat-forming diatoms. Beside the lamination, a pattern of cm-scale layering can be correlated throughout the three sediment cores. This allows the subdivision of the sapropel into eleven zones, also mirroring in the record of elemental abundances. Data on sediment properties, as well as an event-stratigraphic age model indicate a major shift in the depositional regime, with mass occurrence of diatoms, firstly seen ~9 cm above the onset of the sapropel. A floating age model, based on laminae counts, results in an estimated duration of ~2.9 thousand years (ka) for the diatomitic upper interval and, by inference from the event-based regional correlation, ~1.9 ka for the basal, non-diatomitic interval. The total age of about ~4.8 ka corresponds with radiometrically dated speleothem records of a regional wet phase. The onset of the mass occurrence of diatoms coincides with a distinct change in the hydrographic conditions, indicating that it represents a primary signal of enhanced diatom production. Here, a shoaling of the nutricline might favour the diatom proliferation, due to the enhanced availability of nutrients. The thickness of the sapropel made it possible to determine that both the onset of the sapropel and the subsequent re-oxygenation at the termination of the sapropel occurred within a few decades. Finally, wavelet analysis of multiple proxies unveils a cyclic component with a duration of ~80 years, which coincides in its length with the Gleissberg solar cycle, but is also within the range of the Atlantic Multidecadal Oscillation (AMO). Likewise, also a 180 – 240 year periodicity was revealed, which is persistent throughout the sapropel, but difficult to attribute to any known climatic process. The results confirm the great potential of the expanded sapropel as a high-resolution window into the thermal optimum of the last interglacial in the Levantine region.

Zusammenfassung

Das östliche Mittelmeer ist durch die periodische Ablagerung organisch reicher Sedimente (Sapropele) gekennzeichnet. Ihre Entstehung ist an Episoden erhöhten Süßwassereintrags gekoppelt, welche ihrerseits von insolationsgesteuerten Monsun-Niederschlägen abhängig sind. Gemeinhin geht man bei Sapropelen von einer Entstehungsdauer von einigen tausend Jahren und einer Mächtigkeit von wenigen Dezimetern aus. Eine Ausnahme stellt hier das letzte Interglazial dar, wo in Teilen des Levantinischen Beckens Sapropele mit Mächtigkeiten von ~1 m abgelagert wurden, sodass Umweltprozesse mit höchster zeitlicher Auflösung untersucht werden können. Die vorliegende Studie nimmt diesen Umstand zum Anlass, die ozeanographischen Bedingungen sowie die Land-Meer Interaktion im östlichen Mittelmeer während des letzten Interglazials anhand dieses einzigartigen Klimaarchivs zu untersuchen. Die Auswirkungen des Solar-Forcings auf das Ablagerungssystem und das Plankton sowie die Ursachen für die hohe Mächtigkeit dieses Sapropels stellen dabei weitere Aspekte dar. Zu diesem Zweck wurde ein außergewöhnlich mächtiger S_5-Horizont in drei Sedimentkernen des nördlichen Levantinischen Beckens im östlichen Mittelmeer untersucht, welcher außerdem eine sub-mm feine Lamination aufweist, hervorgerufen durch die jährliche Blüte von mattenbildenden Diatomeen. Daneben kann auch eine cm-mächtige Schichtung zwischen allen Kernen korreliert und eine Unterteilung des Sapropels in elf Zonen vorgenommen werden, die sich auch in der Verteilung chemischer Elemente widerspiegelt. Sowohl die Sediment-eigenschaften als auch ein eventstratigraphisches Altersmodell weisen auf einen rapiden Anstieg der Sedimentationsrate ~9 cm über der Basis des Sapropels hin, welcher durch das massenhafte Auftreten von mattenbildenden Diatomeen ausgelöst wird. Basierend auf Zählungen der Laminae gelangen wir zu einem Alter von ~2.9 ka für den diatomitischen oberen Teil und ~1.9 ka für den nicht diatomitischen unteren Teil des Sapropels. Das resultierende Gesamtalter von ~4.8 ka deckt sich auch mit dem von radiometrisch datierten Höhlensedimenten, die eine humide Phase in dieser Region anzeigen. Da ihr verstärktes Auftreten mit Veränderungen in der Hydrographie einhergeht, betrachten wir das Erscheinen der Diatomeen als ein primäres Signal erhöhter Produktivität. Besonders ein Shoaling der Nutrikline könnte die Nährstoffversorgung verbessern und so die Vermehrung der Diatomeen fördern. Durch die hohe zeitliche Auflösung beziffern wir die Dauer des Übergangs zu Beginn und am Ende des Sapropels auf wenige Jahrzehnte. Waveletanalysen an verschiedenen Proxies deuten außerdem auf einen Zyklus mit einer Dauer von ~80 Jahren hin, was sowohl dem solaren Gleissberg-Zyklus als auch der Atlantischen Multidekadischen Oszillation (AMO) nahe kommt. Daneben existiert ein 180 – 240 Jahre dauernder Zyklus, der zwar durchgehend innerhalb des Sapropels auftritt, jedoch schwer einem klimatischen Prozess zuzuordnen ist. Die Ergebnisse bestätigen insgesamt das hohe Potential dieses außergewöhnlich mächtigen Sapropels als hochauflösendes Klimaarchiv für das thermale Optimum des letzten Interglazials im östlichen Mittelmeer.

Table of Contents

Parts of the methods, the results and the discussion presented in this dissertation have been published in Moller et al. (2011a).

1 Introduction

The climate of the Earth has ever been changing and evolving at different timescales and with various amplitudes. Although it might seem stable from the perspective of the relatively short duration of a human life, the Earth's climate in reality remains rather seldom in a steady state. On the time scales of millions of years and more, climate change can be driven by shifting the intensity of the sun (Gough, 1981), tectonic processes, such as the global rate of erosion or the configuration of the land masses, and by the biosphere, which affects global biogeochemical cycles of elements like carbon or nitrogen (Walker et al., 1981; Berner and Berner, 1997). However, as numerous evidences from the geological record show, the climate of the Earth can also change on the time scale of thousands of years or less. Such changes can be driven by periodic variations in the Earth's orbit, by short cycles of solar activity, internal oscillations and unique events. At present, the Earth is experiencing one of such unique events: a manipulation of the greenhouse gas content of the atmosphere by human activities with unprecedented rate. In this case, mankind constitutes for the first time in Earth history an active participant in the climatic system and actively, though unintentionally, influences the balance of the natural fluxes and reservoirs of climate-active agents by agriculture and industrialization. As a result, the climate is changing and our society is increasingly concerned about the potential warming of Earth's climate in the near future. In this respect, significant uncertainties emerge from the research of Earth's climate, especially in estimating the natural pace and magnitude of change in climatic parameters and the separation of the fraction of the current trends that could be ascribed to anthropogenic processes. The need to better predict future climate change has thus recently inspired much research on the interactions of the different aspects of the climatic system.

One possibility to understand how the Earth reacts to changing climatic forcing and what are the magnitudes of climate change under natural conditions, is to study past interglacial periods, which forego the actual interglacial period of the Holocene. These provide an opportunity to study warm climates on the Earth, with global temperature and sea levels similar to today, but lack the interference of mankind. There are of course no direct records of the climate during such past warm periods, but it is possible to reconstruct interglacial climatic conditions by analyzing geological climate archives. Highly interesting are hereby the last four interglacials after the Mid-Pleistocene Transition, after which glacial and interglacial periods followed the 100 ka-cycle of eccentricity (Shackleton and Opdyke, 1973). Of these, the last interglacial maximum during Marine Isotopic Stage 5e, which lasted from about 132 – 115 ka, featured temperatures and sea levels slightly above the present day (Rohling et al., 2007). Although the insolation played a more important role, compared to today, and also the influence of actual

ambient temperatures seem to be smaller (van de Berg et al., 2011), the Eemian period yet might provide valuable insights in the pace and functionality in climate systems.

For the research of the climatic optimum of the last interglacial period, the Mediterranean Sea provides an extraordinarily well-suited test bed. This is owed to its geological structure as well as its geographical position. The Mediterranean Sea is an evaporative basin, as the evaporation in this nearly landlocked basin exceeds the input of freshwater, which results in a two-layer exchange of water through the Strait of Gibraltar and a complex thermohaline circulation pattern with specific locations of intermediate and deep water formation (Gilman and Garrett, 1994; Milder et al., 1999; Tsimplis et al., 2006; Robinson et al., 2009). After circulating through the Mediterranean, the water re-enters the Atlantic Ocean through the Strait of Gibraltar at intermediate depths and is traceable throughout the North Atlantic Ocean, where it may play an important role for deep water formation and the stability of the global thermohaline equilibrium state (Bethoux et al., 1999; Robinson et al., 2009). Due to its position at the interface of the subtropical monsoonal climate system and the temperate climate of the mid latitudes, the Mediterranean Sea is especially sensitive to changes of atmospheric environmental parameters (Rohling et al., 2009). The short reaction time and potentially amplified response to external forcing make the Mediterranean Sea an interesting target area for climate scientists interested in short scale climatic variations.

A manifestation of this sensitivity is found in the sedimentary record in the Mediterranean basin in the form of organic rich, dark sediment layers, called sapropels, which disrupt the normally deposited bright marls. The formation of Mediterranean sapropels has been linked to insolation maxima in the Northern Hemisphere (Rossignol-Strick, 1985) and prominent sapropel layers have been deposited at the onset of all recent interglacials. The process responsible for the formation of the sapropels is likely linked to a stronger monsoon over Northern Africa, which causes an elevated input of freshwater into the Mediterranean, hindering the overturning circulation. Consequently, the progression of anoxic conditions in deep and intermediate waters follows and favours the accumulation of organic material on the sea floor. Initially recovered in 1947 and first described by Kullenberg (1952) and Olausson (1961), Mediterranean sapropels have been the subject of a multitude of studies with various focal points (Kullenberg, 1952; Olausson, 1961; Cita et al., 1977; Thunell et al., 1977; Vergnaud-Grazzini et al., 1977; Kidd et al., 1978; Rossignol-Strick et al., 1982; Rossignol-Strick, 1985; Rohling et al., 1997; de Rijk et al., 1999). Although the broad mechanism of their genesis is understood, many details concerning their formation remain elusive. The thickness of single sapropel layers, for example, varies strongly throughout the Eastern Mediterranean basin and can also be under the influence of the seasonal export flux of mat forming diatoms (Pearce et al., 1998; Kemp et al., 1999; Kemp et al.,

2000). In such diatomaceous sapropel horizons, a sub-millimetre thin lamination can be observed, allowing the reconstruction of climatic processes in the region on the time scale of years and decades.

This study presents the analysis of such a strongly expanded diatomitic S_5 sapropel from the peak warmth of the last interglacial maximum from the Eastern Mediterranean basin with an extraordinary temporal resolution. During this period, the lack of anthropogenic bias enables us to observe and analyse the forcing and response of different environmental components in a stagnating oceanic basin within a climate with higher temperatures and higher sea-levels than the present day (Kukla and Briskin, 1983).

1.1 The Mediterranean

1.1.1. Geological setting

The geological history of the Mediterranean Sea begins about 30 million years (ma) (Frisch and Meschede, 2007; Mather, 2009) ago in the upper Palaeogene, when the tectonic plates of Africa and Europe started to collide and the precursor of the Mediterranean Sea, the Tethys Ocean got destroyed. The several seaways that existed between the Tethys and the Indian Ocean in the east and the Atlantic Ocean in the west became gradually closed. Intermittently, during the uppermost stage of the Miocene, the Mediterranean Sea even became completely isolated, by the closure of the Rifian Corridor (Morocco) and the Betic Corridor (Iberian Peninsula), which connected the Mediterranean Sea with the Atlantic Ocean. This event, during which the Mediterranean dried-out, is known as the Messinian Salinity Crisis (MSC) (Krijgsman et al., 1999) and comprises the period between 5.8 and 5.32 ma (Krijgsman et al., 1999). Here, the evaporation, accompanied with the lack of inflowing water consequently led to the precipitation of massive amounts of evaporates of 2000 – 3000 m thickness (Hsü et al., 1973). The dropping sea level also caused strongly enhanced erosion at the adjacent land masses and led to the deposition of the so-called Lago Mare facies, which is characterized by terrigenous sediment and brackish shallow living fauna even in deepest basins of the Mediterranean (Ruggieri, 1967; Mather, 2009). A reconnection of the Mediterranean Sea to the open Atlantic Ocean was realized by opening a narrow corridor, known as the Strait of Gibraltar, by ongoing tectonic movement, which established normal marine conditions at around 5.33 ma, also marking the boundary between Miocene and Pliocene.

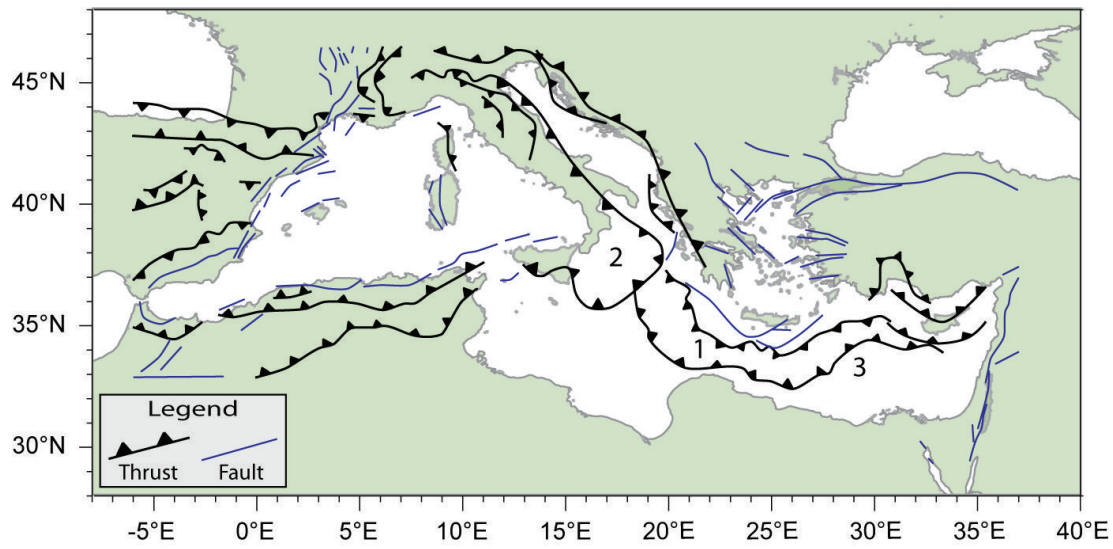

Figure 1: Tectonic sketch of the Mediterranean basin, illustrating the complex tectonic compressive stress field with its major thrusts and faults and major features of the Eastern Mediterranean: 1) The Mediterranean Ridge, 2) Calabrian arc, 3) Herodotus Deep abyssal plain (modified after Barrier et al., 2004).

In terms of tectonics, the Mediterranean Sea is characterized by an overall, yet very complex converging movement of the African and the European plate (Figure 1) and is accompanied by seismic and volcanic activity, which are mostly bound to the subduction zones (Vannucci, 2004; Mather, 2009). Active volcanism today is mostly limited to the Calabrian and Aegean arc (e.g. Stromboli, Etna, Vesuv, Santorini) but used to cover a much larger field throughout the Oligocene and Miocene (Mather, 2009). Another sign of the compressional tectonic movement becomes apparent in the Mediterranean Ridge, a 1500 km long pile of accretioned sediment (Limonov et al., 1996), as well as undersea mud diapirism, where overpressured mud rises in faults of the accretionary prism and which is especially pronounced around the Mediterranean Ridge (Robertson, 1996; Robertson and Kopf, 1998) (Figure 1). Despite the overall converging movement, smaller sub-basins, such as the Aegean Sea and the Tyrrhenian Sea are of extentional character and, in the latter case also experience deepening, which is due to a rollback of the subduction zone and the accompanying back-arc stretching (Goes et al., 2004).

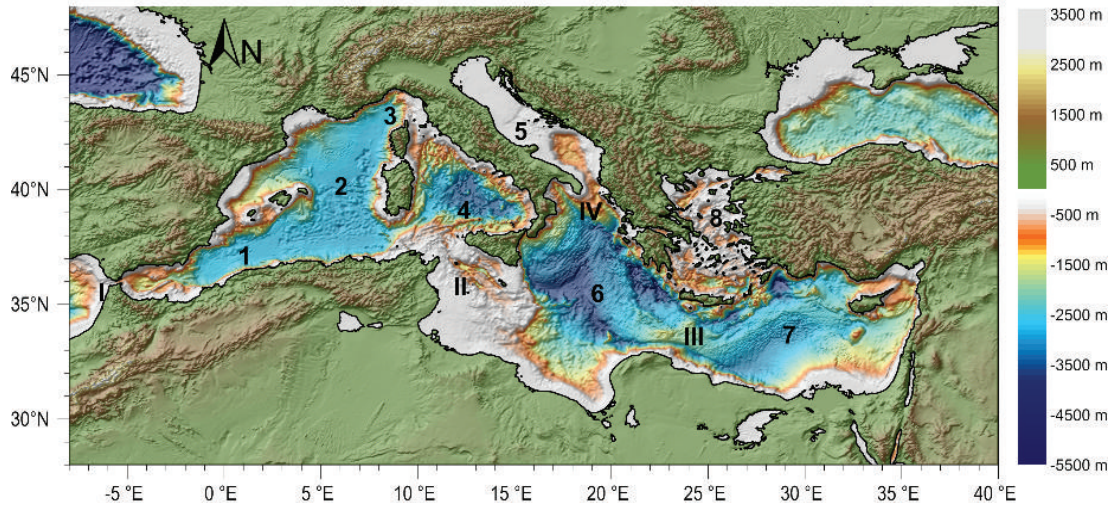

Figure 2: Bathymetric map of the Mediterranean Sea (topography from ETOPO 1 minute grid, (Amante et al., 2009)). The major sub basins of the Western Mediterranean sea are the Alboran Sea (1), the Balearic Sea (2), the Ligurian Sea (3) and the Thyrrenian Sea (4). The major sub basins of the Eastern Mediterranean sea are the Adriatic Sea (5), the Ionian Sea (6), the Levantin Sea (7) and Aegean Sea (8). Important sills and passages are the Strait of Gibraltar (I), the Strait of Sicily (II), the Cretan Passage (III) and the Strait of Otranto (IV).

Generally, the Mediterranean Sea today poses a semi-enclosed marginal sea, with only one narrow connection to the open Atlantic Ocean (Strait of Gibraltar) and comprises an area of 2.5 million km^2 with a coastline of 46000 km length (Hsü et al., 1973; Rohling et al., 2009). The average depth is 1500 m but can be as deep as ~5200 m in the Calypso Deep (Rohling et al., 2009). The Strait of Sicily poses a further important sill structure with a depth of about 330 m (Wüst, 1961; Bryden and Kinder, 1991; Rohling et al., 2009) and separates the Mediterranean Sea into a western and an eastern basin, these being further classified into several sub-basins (Figure 2).

1.1.2. Climatology

Due to its geographical position between 45°N and 30°N, the Mediterranean Sea and its adjacent landmasses are influenced both by the mid-latitude westerlies of central and northern Europe and the monsoonal climate of Northern Africa (Boucher, 1975; Harding et al., 2009) and is also eponymic for the so-called Mediterranean Climate.

Here, during winter, the planetary insolation and air pressure-belt is shifted equator wards and the Mediterranean is mostly influenced by the cyclonic weather conditions of the mid latitudes (Schultz, 2008). In particular, a general low pressure field over the Mediterranean provokes a defined inflow of cool and dry continental air, especially at the Gulf of Lyon (Mistral), in the Western Mediterranean and the Adriatic and the Aegean (Bora and Vardar) in the Eastern Mediterranean. This causes a pronounced cooling of the water and intense evaporation, which are important for the deep water formation as well as for the formation of cyclones (Rohling et al., 2009). During summer, the Mediterranean region is strongly influenced by the northward shifted sub-tropic high pressure zone, which results in dry and insolation dominated weather conditions (Schultz, 2008).

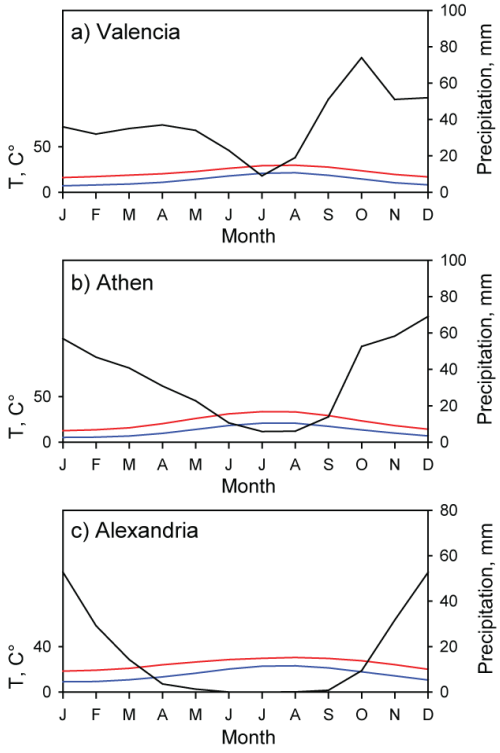

Figure 3: Climate diagrams from (a) Valencia (1971 – 2000) and (b) Athen (1955 – 1997) and (c) Alexandria (1971 – 2000) with averaged temperature (red: day, blue: night) and rainfall curves (black) as representatives of the Mediterranean Climate with arid and hot summers and humid and mild winters (World-Meteorological-Organization, 2010).

The majority of the annual precipitation in the Mediterranean region (~75%) is concentrated to a period between October and March (Harding et al., 2009). Despite this common characteristic, large local variations in the annual average temperature and amount of precipitation exist. The Western Mediterranean region for example is characterized by a milder, more maritime climate, which is due to the influence of the Atlantic Ocean (Figure 3a). The Eastern Mediterranean is thus more coined by a continental climate with higher seasonal contrasts in temperature and rainfall (Figure 3b). This contrast can also be seen in differences between the north and the south of the Mediterranean region. Consequently, the south eastern part of the Mediterranean,

which is under the steady influence of the subtropical high pressure field, features a very low precipitation with several months of drought (Figure 3c) (Harding et al., 2009).

1.1.3. Oceanography

Given by the climatic conditions, the Mediterranean Sea has a negative water balance, where evaporation exceeds the inflow of freshwater by rivers as well as meteoric waters (Gilman and Garrett, 1994; Robinson et al., 2009). As a consequence, the Mediterranean Sea is characterized by a thermohaline circulation, driven by buoyancy loss due to intense evaporation and wind stress (Lascaratos et al., 1999; Rohling et al., 2009), with a general eastward transport of warmer and lower saline waters from the Atlantic Ocean near the surface and a westward directed flow of cooler, saltier waters in intermediate depths (Rohling, 1994). This dense water, which re-enters the Atlantic Ocean, is traceable to the North Atlantic Ocean and due to its elevated salinity, poses an important factor for the deep water formation in the Northern Atlantic Ocean (Bethoux et al., 1999; Cramp and O'Sullivan, 1999; Rohling et al., 2009). In terms of nutrients the Mediterranean Sea is oligotrophic and is regarded as a nutrient desert (Emeis et al., 1996) (Figure 4). The reason for the lack of nutrients is due to the anti-estuarine pattern of a two layer exchange system at the Strait of Gibraltar, where relative nutrient poor Atlantic waters flow into the Mediterranean near the surface and, in exchange, relative nutrient rich waters exit the Mediterranean at intermediate depths.

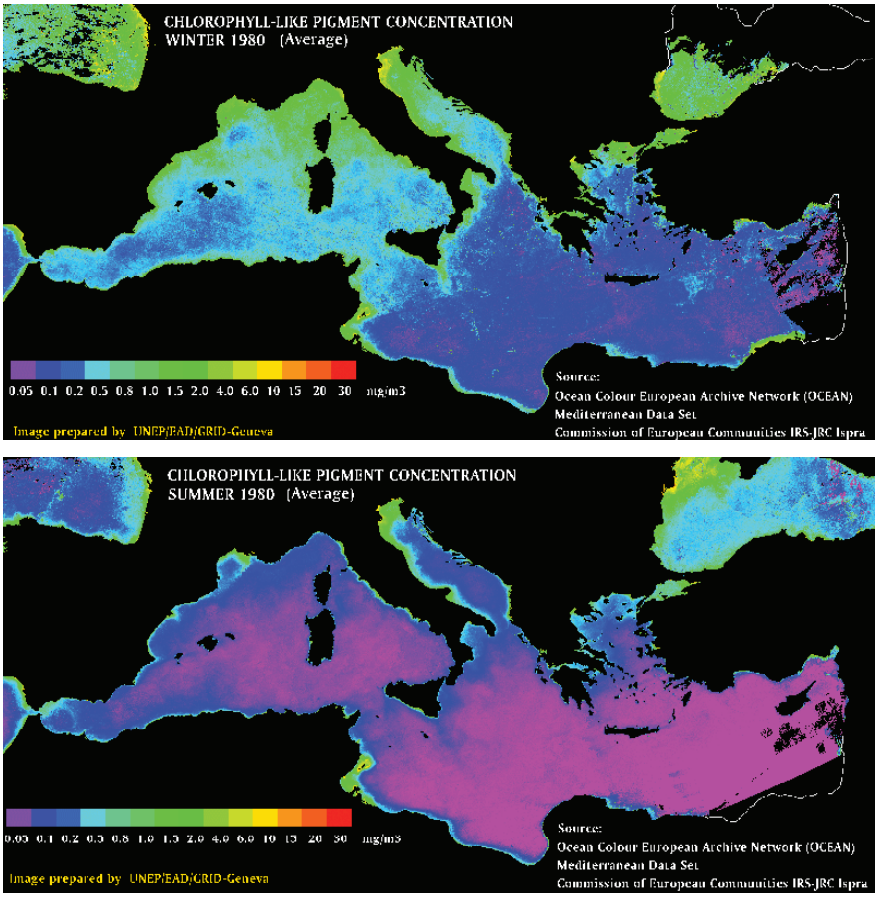

Figure 4: Chlorophyll like pigment concentration in the Mediterranean Sea, highlighting the pattern of primary productivity. The upper graph shows the more productive winter season. The lower graph illustrates the low primary productivity during the summer season, due to enhanced stratification (Ocean Project (Comission of the European Communities European Space Agency), 1980).

Surface water circulation

The net-loss of water through the excess of evaporation is out-balanced by the water-mass exchanges at the Strait of Gibraltar (Figure 5). Here, surface near waters from the Atlantic Ocean (AW) enter the Mediterranean Sea with average temperatures of ~15°C and a salinity of ~36.2 psu (Coste et al., 1988; Rohling et al., 2009). By entering the Mediterranean, AW mixes with underlying Mediterranean Intermediate Water (MIW) and surface waters of the Alboran Sea, which results in higher temperatures and salinities and is now described as Modified Atlantic Waters (MAW) (Gascard and Richez, 1985; Malanotte-Rizzoli et al., 1997). Generally the MAW propagates eastward in the Algerian Current and creates several cyclonic and anti-cyclonic gyres and also diverts into branches into the Tyrrhenian Sea. The Algerian Current and the MAW respectively, enter the eastern basin of the Mediterranean through the Strait of Sicily, merge into the Atlantic Ionian Stream and then further propagate eastward into the Levantine Sea to form the Mid Mediterranean Jet. Within the Levantine Sea, the Mid Mediterranean Jet provokes a number of gyres; the Mersa-Matruh Gyre System north of the Egyptian coast, the Shikamona

Gyre west of Israel and the Rhodes Gyre and the Iera-Petra Gyre between Cyprus and Crete (Pinardi and Masetti, 2000) (Figure 5).

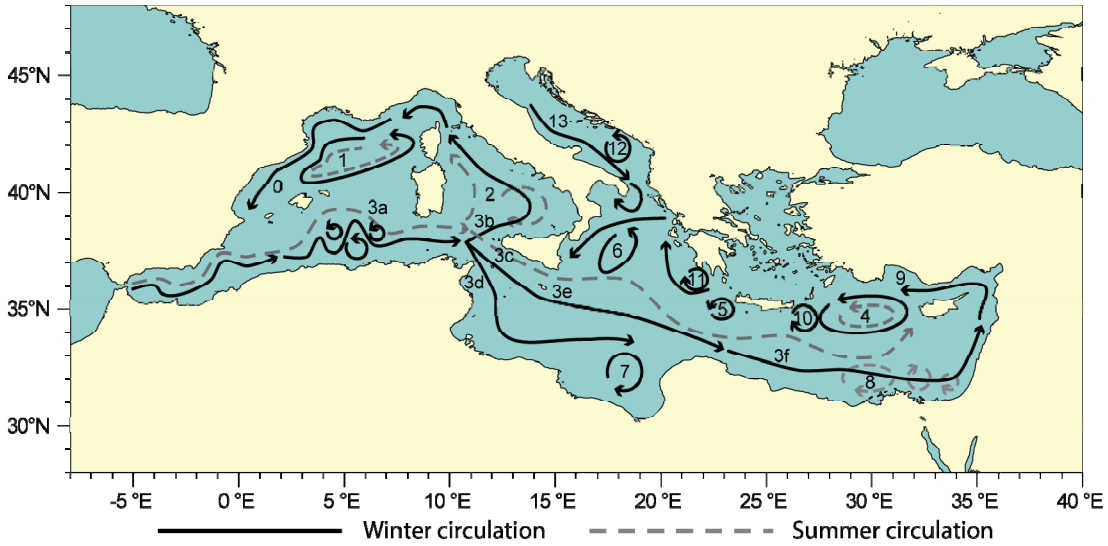

Figure 5: Major Currents and Gyres in the Mediterranean Sea. (0) Ligurian-Provencal current. (1) Lyon Gyre. (2) Tyrrhenian cyclonic circulation with summer weakening and eastern anticyclone.(3a) Algerian current and eddies, (3b, c, d) Branching of Atlantic-Ionian Stream. (3e) Atlantic Ionian Stream. (3f) Mid-Mediterranean Jet. (4) Rhodes Gyre.(5) Western Cretan Gyre.(6) Western Ionian Gyre.(7) Anticyclone in the Gulf of Syrte. (8) Shikmona and Mersa- and Matruh Gyre System. (9) Cilician and Asia Minor Current. (10) Iera-Petra Gyre. (11) Pelops Gyre. (12) Southern Adriatic Gyre. (13) Western Adriatic Coastal Current (Pinardi and Masetti, 2000).

Intermediate water formation

Throughout the general eastward drift of the MAW from the Strait of Gibraltar into the Levantine Basin, intense evaporation increases the salinity of the surface water and thus also its density (Wüst, 1961). While the MAW enters the Mediterranean with a salinity of ~36.2psu (Coste et al., 1988) the values increase to ~37.0 – 38.5psu (Rohling et al., 2009), when the MAW enters the Eastern Mediterranean basin and reaches its highest values in a zone delimited by Crete to the west and Cyprus to the east (Pinardi and Masetti, 2000) with values up to 38.9psu (Wüst, 1960; Tsimplis et al., 2006; Rohling et al., 2009). Especially during the winter season, cooler air temperatures and continuing evaporation further increase the density of the MAW at the Cyprus-Rhodes area to an amount, where sinking becomes possible and Levantine Intermediate Water (LIW) is formed, which settles to a depth of about ~150 - 600 m (Tsimplis et al., 2006; Rohling et al., 2009) (Figure 6). Upwardly, a discontinuity layer with a steep salinity gradient separates both, the LIW and the MAW. From its locus of formation, the LIW spreads westwards where it contributes the majority of outflow into the Atlantic Ocean (Lascaratos et al., 1999) but also northwards into the Adriatic Sea, which poses a location of deep water formation in the Mediterranean Sea (Pinardi and Masetti, 2000).

Deep Water formation

In opposite to the LIW, deep waters, which settle below 600 m, are formed in the Western Mediterranean as well as in the Eastern Mediterranean, namely the Gulf of Lyon and the Adriatic Sea (Figure 6). Both sources of deep water formation are a consistent oceanic feature, thus characterizing the Mediterranean deep water as well oxygenated (Rohling et al., 2009). Eastern Mediterranean Deep Water (EMDW) is formed in the southern part of the Adriatic Sea, by the mixing of intermediate water and so-called Adriatic Deep Water, which itself is formed in the northern Adriatic Sea during the winter season by evaporation and cooling (North East Bora winds). After mixing, EMDW enters the Ionian Sea through the Strait of Otranto with average temperatures of 13°C and 38.65psu (Gacic et al., 1996; Lascaratos et al., 1999).

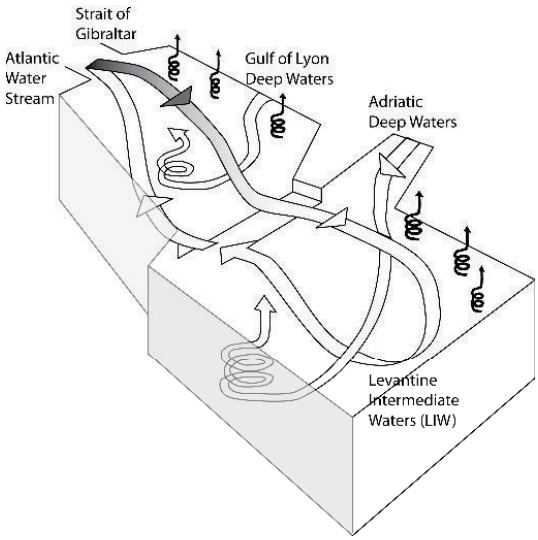

Figure 6: Schematic overview of the overturning circulation in the Mediterranean Sea with the Levantine Intermediate Waters to be formed in the eastern basin and the deep water formations in the Adriatic Sea and the Gulf of Lyon (after Lascaratos et al., 1999).

Western Mediterranean Deep Water (WMDW) is formed in the Gulf of Lyon during the winter season and preferentially during longer lasting Mistral winds from the north, which provide intensive heat loss of the surface waters (Lascaratos et al., 1999). After this phase of preconditioning, a phase of violent mixing and rapid sinking follows, during which the water settles below intermediate waters (Rohling et al., 2009).

Hypersaline brines

Another noteworthy, yet small-scale feature of the Mediterranean Sea are anoxic brines, which fill depression structures or smaller basins, that are hydrographically largely decoupled from the regular bottom water circulation (de Lange et al., 1990). Instead, these deeps are filled with extremely high saline waters, where salinities can exceed the values of regular deep waters by the eight fold (de Lange et al., 1990). The high salt content derives from evaporites of the Messinian facies, which can become directly exposed to the sea water by tectonic activities, such as faults and thrusts (Rohling et al., 2009). Examples of hypersaline brines in the Mediterranean Sea are found in the Tyro and Bannoc area, which are both located in the Eastern Mediterranean Sea in proximity to the Mediterranean Ridge (de Lange and ten Haven, 1983) (Figure 1, Figure 2). Here, the high saline waters form a halocline, which is associated with a pycnocline and effectively isolates these depressions from the overlaying bottom waters. The permanent anoxic

environment in these brines allows the undisturbed accumulation of sediment and organic material, and thus, the formation of sapropels and sapropelic layers *sensu stricto*, yet with limited lateral extension (de Lange et al., 1990).

1.2 Mediterranean sapropels

As illustrated in chapter 1.1, the waters of the Mediterranean Sea are well oxygenated, due to a defined circulation system with an intense vertical mixing and a relative short residence time of the water. Yet, looking at the geological record testifies, that the Mediterranean Sea has undergone numerous minor and major variations in the thermohaline circulation pattern as a result of climatic changes, which are manifested in discrete layers of dark, organic rich sediment. Over eighty (80) (Emeis et al., 2000) of these low-oxygen events are found in Mediterranean sediments after the Messinian Salinity Crisis (5.3 ma), mostly during interglacial complexes as a consequence of a northern hemisphere insolation maxima (Rossignol-Strick, 1983; Rossignol-Strick, 1985). Compared to the Palaeozoic, the Jurassic and the Cretaceous, where massive development of black shales occurred, and constitute an important source rock for hydrocarbons, the organic rich layers in the Mediterranean depict one of the few Neogene examples of enhanced accumulation and preservation of organic matter (Thunell et al., 1984).

These dark layers of sediment are called sapropels and the terminus was first introduced on behest of Prof. Schulze by Potonié (1904) (Cramp and O'Sullivan, 1999) and is used to describe dark mud of greyish-brownish and greenish colour, which forms within stagnating waterbodies as a result of decaying organic matter. The word sapropel itself is a transliteration of the German word “Faulschlamm” into the Greek words “sapros” and “pelos”, meaning “putrefied” and “soil”. Stagnating hydrographic conditions, which include the formation of (varved) anoxic sediments in the Mediterranean Sea, were postulated already in 1938 by Bradley, as the result of lower sea levels during glacial periods, accompanied by enhanced precipitation and lower evaporation rates. In fact, Mediterranean Sapropel horizons were firstly recovered in 1947 by the Swedish deep sea expedition and initially mentioned by Kullenberg (1952) and Olausson (1960; 1961). A more quantitative definition for Mediterranean sapropels was carried out by Kidd et al. (1978), where a minimum of 2% organic carbon, a minimum thickness of 1 cm and a minimum water depth of 500 m was appointed. Intervals with C_{org} values between 0.5 – 2 % and water depths less than 500 m are instead addressed with the term “sapropelic layer”. The definition was later modified by Hilgen (1991), who states a sapropel to be an often laminated, brownish interbed. The thickness of sapropels varies strongly and approximately lies between 2 – 30 cm (Cramp and O'Sullivan, 1999). Anyhow, the thickness in individual cores can be well above 50 cm as examples from the last interglacial show. Here, the thickness of the sapropel in M50-4 SL67 (Hieke et al., 1999), M51-3 SL103, M51-3 SL103 (Hemleben et al., 2003) from the Levantine Basin and 971 B (Cane et al., 2002) near the Napoli Dome are beyond 80 cm and core LC21 from the Aegean Sea with a sapropel thickness of 120 cm (Morigi, 2009) is the thickest sapropel found so far.

Since their first discovery, a total number of about 1500 sapropel layers were reported from the Mediterranean, either by gravity cores or from a shipboard drilling projects such as the Deep Sea Drilling Project (DSDP), the Ocean Drilling Program (ODP) or the Integrated Ocean Drilling Program (IODP) (Cramp and O'Sullivan, 1999). Based on this broad set of data, sapropels are dated back to the Miocene (Kidd et al., 1978), although the majority of published sapropels derives from the late Pleistocene. Further a spatial pattern of sapropels is visible, whereby the geological record of sapropels is better in the Eastern Mediterranean basin (Rohling, 1994) and might result from the differential export productivity in both basins (Martinez-Ruiz et al., 2000). Principally, the deposition of Organic Rich Layers, as the equivalents of sapropels are called in the Western Mediterranean Sea (Comas et al., 1996) is possible, as shown for example in the Tyrrhenian Sea (Anderson et al., 1989).

For the nomenclature of Mediterranean sapropels, a number of methods have been established. The original nomenclature goes back to the unpublished PhD-Thesis of McCoy (1974), where individual layers of sapropels got numbered and have the prefix 'S'. The youngest sapropel from the Holocene thus is S_1 followed by S_2, S_3…. This system is widely used, although it is little flexible, for example when a new and yet unknown sapropel layer is discovered. Advances in the astronomical calibration by Hilgen (1991) established the i-cycle (i = insolation) nomenclature based on the peaks of the precession cycle, which was further refined by Lourens et al. (1996). For the sake of completeness, also the nomenclature of Hieke et al. (1973) for Sapropels in the Ionian Sea is mentioned, which labels the individual horizons alphabetical with A, B, C….

1.2.1. Timing of sapropel formation

In contradiction to the original idea of Bradley (1938), it was assumed quite early, that the reason for stagnating character of the hydrography of the Mediterranean was not a low level stand of the sea level during glacial periods, but instead an massive inflow of low saline water into the Mediterranean basin, which effectively hinders the water from sinking (Olausson, 1960). The formation of sapropels could be further linked to warming periods as for example the stratigraphic studies of Van Straaten (Van Straaten, 1966; van Straaten, 1970) showed. Here, on the base of an annual lamination and the occurrence of pelagic molluscs, the organic rich

Table 1: Late Pleistocene to Holocene sapropel sequences with their according i-cycle and Marine Isotopic Stage. (Combined data from Cramp and O'Sullivan (1999) and Lourens (2004)).

Sapropel	i-cycle	Marine Isotopic Stage	Age, ka
S_1	2	1	8.5
S_2	6	3	#
S_3	8	5a	81
S_4	10	5c	101
S_5	12	5e	124
S_6	16	7	172
S_7	18	7a	195
S_8	20	7d	216
S_9	22	7e	239
S_{10}	30	9	331
S_{11}	38	11	407
S_{12}	48	11	461

sediment (Sapropel S_1) in the central parts of the Aegean Sea was related to the Atlanic stage (Van Straaten, 1966), which poses the thermal optimum of the Holocene or the warming period of Marine Isotopic Stage 1, respectively. Since then, this issue has been further corroborated by a multitude of studies, which could link the formation of the 11 youngest sapropels from the upper Pleistocene, which belong to the mostly studied sapropels, to warming phases according to the oxygen isotopic stages (Table 1). Here, for example, the faunal assemblages of planktonic foraminifera (Thunell et al., 1977; Rossignol-Strick, 1985) as well as the oxygen isotopy of their shells (Cita et al., 1977; Kidd et al., 1978) point at a warm climate during sapropel formation. Further proxies comprise geochemical data, such as Ti/Al, which is indicative for windblown dust and affirm the formation of sapropels to occur within warm periods, where a moister climate and lower wind intensities prevail (Larrasoaña et al., 2003; Revel et al., 2010).

1.2.2. Astronomical forcing of sapropel formation

Despite the broad acceptance of the general boundary conditions during sapropel formation, such as a stratified water column with suppressed deep water ventilation due to enhanced fresh water input, a controversial issue was the provenance of the additional water masses. A feasible source was supposed to lay in the melt water, being provided by retreating glaciers (Ryan, 1972; Thunell et al., 1977; Kidd et al., 1978). Here, the melt water was supposed to derive from the Fennoscandian Ice Shield, which was rooted into the Black Sea, from where it entered the Mediterranean at the Aegean Sea (Olausson, 1960; Olausson, 1961; Williams and Thunell, 1979; Muerdter, 1984). Yet, this hypothesis was rejected, when C^{14}-dating revealed a lag of a few thousand years between the onset of sapropel formation and the melt water peak (Rossignol-Strick et al., 1982).

In return, synchronism between the onset of sapropel formation and particular maxima of the North African summer monsoon was affirmed (Rossignol-Strick et al., 1982). Here, the river Nile plays a crucial role, by draining the continental precipitation of the monsoon during the summer season into the eastern basin of the Mediterranean Sea. The water from this seasonal flood is supposed to form a cursory layer of fresh water with low salinities, which diminishes the buoyancy-loss and hinders convective mixing with the intermediate and deep waters. As a consequence, a highly stratified water column becomes established, where the deep waters (>500 m) suffer from ventilation, thus favouring the accumulation of organic matter under low oxygen or even anoxic bottom water conditions (Rossignol-Strick et al., 1982; Rossignol-Strick, 1983; Rossignol-Strick, 1985).

The controlling agent for the enhanced freshwater input into the basin is believed to be related to monsoonal activity, triggered by the 21 ka cycle of Earths precession, which strongly affects

the incoming solar radiation, and in this way modulates the intensity of the North African Monsoon as a part of the African-Asian Monsoon System (Rossignol-Strick, 1983; Rossignol-Strick, 1985). In detail, the precession describes the orientation of Earth's tilted axis in space and determines the moment of summer and winter solstice during Earth's revolution around the sun. A minimum in Earth's precession means, that summer solstice coincides with the perihelion position of earth and sun. This provokes a higher insolation during northern hemispheres summer and therefore intensifies the symptoms of the summer monsoon. These variations of insolation in dependence of the orbital parameters culminate in the so-called monsoon index M, following $M = I_T + (I_T - I_E)$, where I_T is the insolation at the Tropic of Cancer and I_E the insolation at the equator during summer. Further, the monsoon index is given as $\Delta M = M^t - M^{1950}$, which describes the deviation of Monsoon index at a certain time (M^t) from the Monsoon index at 1950 AD (M^{1950}). A ΔM value of 42 is here supposed to mark the threshold, where the formation of sapropel horizons are mostly induced (Figure 7) (Rossignol-Strick, 1983; Rossignol-Strick, 1985).

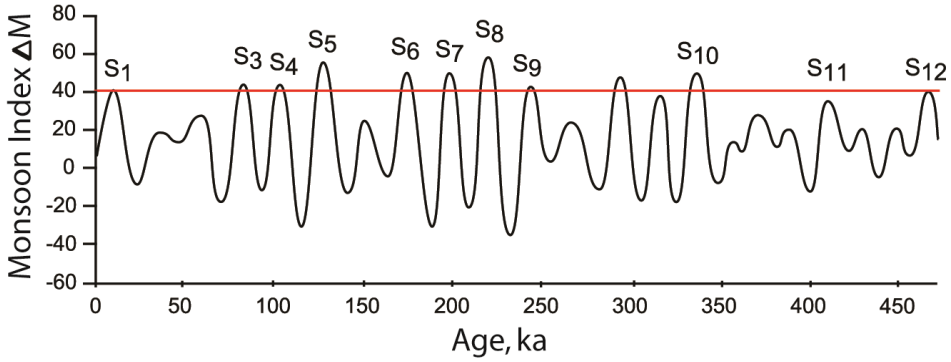

Figure 7: Monsoon index variation throughout the last 450 ka and the according sapropel occurrence above a Monsoon Index of 42 (red line) following the solution of Berger (1978). (Modified after Rossignol-Strick and Paterne (1999)).

However, not during every precession minimum a sapropel gets formed. Instead, their occurrence in the geological record follows a grouping into smaller and larger clusters. It seems that the 100 ka (smaller clusters) and the 400 ka cycle (larger clusters) of Earth's eccentricity further modulate the incoming solar radiation and thus monsoonal precipitation (Hilgen, 1991). The 41 ka signal of Earth's obliquity, to mention the last of the three orbital parameters, constitutes a high latitude signal and is not visible in the stratigraphic record of the Mediterranean sapropels, indicating a lowered influence of the northern catchment of the Mediterranean on sapropel formation (de Vernal et al., 2006). According to this delicate balance of orbital configuration, the duration of sapropel formation is restricted to a time frame of a few thousand years within interglacial periods, although the exact onset and duration are still debated. Whereas older studies propose a duration of ~10 ka for a sapropel (Keller et al., 1978; Muerdter et al., 1984; Vergnaud-Grazzini et al., 1986), which would comprise a complete interglacial period, actual studies tend to a shorter duration of about 3 – 6 ka (Nijenhuis et al.,

1998; Bar-Matthews et al., 2000), which is also supported by direct radiocarbon dating of the youngest sapropel S_1 (Mercone et al., 2000), whereby the midpoint of the sapropel lags 3 ka behind the insolation maxima (Lourens et al., 1996; Langereis et al., 1997; Cramp and O'Sullivan, 1999; Ziegler et al., 2010).

1.2.3. Mechanisms of sapropel formation

Although the stagnating character of the Mediterranean Sea during sapropel formation due to enhanced freshwater input during summer insolation maxima is widely accepted in the scientific community, there exist slightly different views on the exact mechanism and the unfolding effects, such as the circulation pattern in the upper water column and the dominance of either the stagnating deep waters or enhanced productivity as a controlling factor for the accumulation of organic matter during sapropel formation.

While some studies concede the possibility, that export productivity on the present day level is high enough to produce a sapropel and restricted deep water ventilation is dominant factor in sapropel formation (Mangini and Schlosser, 1986; Nolet and Corliss, 1990), most scientists assume an elevated primary productivity in the Eastern Mediterranean due to the broad evidence from proxy data such as nitrogen and carbon isotopes, enrichments in sedimentary barium and various biomarkers and also diatoms (Schrader and Matherne, 1981; Calvert et al., 1992; Martinez-Ruiz et al., 2000; Struck et al., 2001; Menzel et al., 2003). Howell and Thunell (1992) for example could also show, that the C_{org} values in three sediment cores from the Bannock basin increase during the period of the formation of Sapropel S_1. In this hyper saline basin, the permanent anoxic conditions prevailed for more than 100 ka, which indicates that preferential preservation under anoxic conditions alone, cannot explain sapropel formation. A further hint against the dominance of bottom water anoxia is the Black Sea. Neither winter cooling nor evaporation is high enough to promote a sufficient ventilation below 200 m water depth, for at least the last 7 ka (Ryan and Cita, 1977). Despite the permanent anoxic conditions, the Black Sea does not show signs of accumulating organic matter (Cramp and O'Sullivan, 1999).

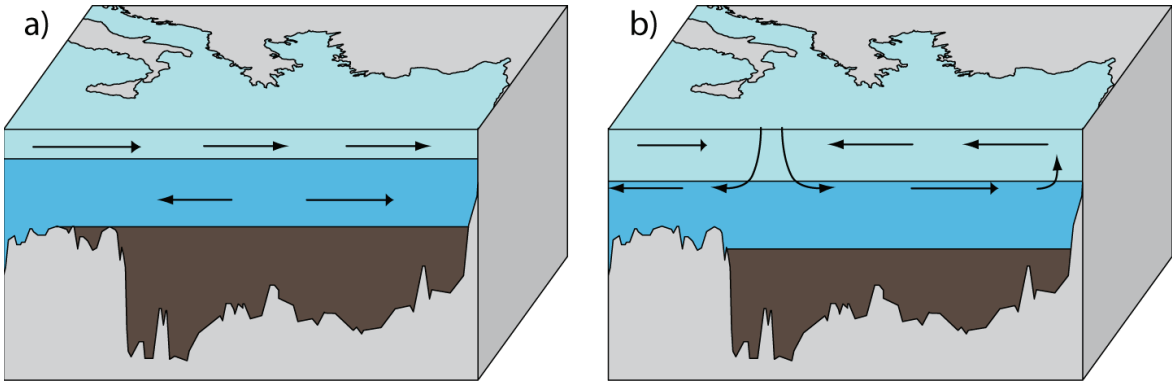

Figure 8: Schematic paths of circulation during the formation of Pleistocene and Holocene sapropels. a) Weakened anti-estuarine circulation, with stagnating anoxic deep waters and shoaling of pycnocline (after Rohling and Gieskes (1989) and Rohling (1994)). b) Estuarine circulation and intermediate water formation in the Adriatic Sea traps nutrients in the eastern basin (after Struck et al., (2001)).

Slightly different theories have also emerged about the mode of surface water circulation during sapropel formation and the way, how larger amounts of nutrients become available to euphotic primary producers. The enhanced discharge of fresh water by rivers as well as increased precipitation (Rohling and Hilgen, 1991) shifts the generally negative water balance of the Eastern Mediterranean towards a more positive state, which diminishes the demand for an intensive exchange between the two Mediterranean basins and the open ocean becomes weakened. A potential scenario for the surface water circulation is proposed by Rohling and Gieskes (1989) and Rohling (1994), which suggests a shoaling of the nutricline. While the general but weakened anti-estuarine character of the surface water circulation remains, the lack of buoyancy loss of surface waters is the supposed main mechanism, which lifts the boundary layer of surface and intermediate waters into the euphotic zone (Figure 8a). Hence, nutrients, which usually reside below the photic zone, become available for deep dwelling euphotic organisms in a layer, defined by the pycnocline to the top and the depth of light penetration to the base. Another feasible scenario proposes a shift from the overall anti-estuarine circulation of surface and intermediate waters (Cramp and O'Sullivan, 1999) towards an estuarine circulation in the Eastern Mediterranean, due to the elevated discharge of rivers (Calvert, 1983; Myers et al., 1998; Struck et al., 2001) (Figure 8b). Since the anti-estuarine circulation extends until the Strait of Sicily, due to intermediate water formation in the Adriatic Sea, nutrients might become trapped and experience recycling by intense winter mixing or a shallower redox boundary, which would allow the fixation of nitrogen by a deep chlorophyll maxima (Myers et al., 1998; Struck et al., 2001). The simulation, conducted by Stratford et al. (2000) tests both scenarios as well as the present day scenario for calibration and concludes that both models allow the formation of sapropel horizons, whereby the weak estuarine scenario is characterized by a higher export flux of organic matter compared to the weak anti-estuarine scenario.

In opposite to the sapropels from the Pleistocene and the Holocene, as described above, sapropels from the Pliocene take an exceptional position. During the early Pliocene, the formation of sapropels seems to be restricted to deeper basins, and in the upper Pliocene they seem to be restricted only to the Eastern Mediterranean. Notably, Pliocene sapropels also feature relative minor depletion in their $\delta^{18}O$ values compared to the post-Pliocene sapropels (Thunell et al., 1984). Therefore, it is assumed, that the formation of Pliocene sapropels is not triggered by enhanced fresh water input but is merely a product of a generally "sluggish" circulation and relative stable, warmer and humid climatic conditions in the Eastern Mediterranean region (Thunell et al., 1984).

1.2.4. Laminated sapropels

As suggested by the definition of Hilgen (1991), sapropels can show a fine, sub-mm thick lamination. Techniques of soft sediment preparation, and the subsequent investigation of the microfabric with scanning electron microscopy (SEM) and backscatter electron imagery (BSEI) revealed steep chemical gradients between single laminae, whereby darker layers consist of predominantly terrigenous silt, clay and a mixed assemblage of mostly solitary diatoms (Pearce et al., 1998). Here, the occurrence of *Thalassionema frauenfeldii*, a typical winter and spring species suggests that these dark laminae are formed during the wet season (Pearce et al., 1998; Kemp et al., 1999). The bright-coloured laminae instead are built up nearly exclusively of diatoms (Pearce et al., 1998), such as species of rhizosolenid diatoms (Pearce et al., 1998) or *Thalassiotrix* (Kemp and Baldauf, 1993), which grow throughout the late spring until the late summer. The onset of the winter provokes the breakdown of the strongly stratified water column of the summer, due to a more intense mixing and induces the decease of the diatom bloom, being sensitive to hydrographic changes (Williams and Thunell, 1979; Kemp et al., 1999) (Figure 9).

Hallmarking for this strongly elongated species in the bright laminae is their capability to form macroscopic chains and meshes, which can extend to several square kilometres (Yoder et al., 1994). Observations in the Pacific Ocean further point at several adaptations towards a deeper dwelling of certain diatom species. For example, patches of Rhizosolenia are capable of active vertical migration in the water column, for either the uptake of nutrients at the nutricline or to perform photosynthesis near the surface (Villareal et al., 1993). Yoder et al. (1994) could show on samples of *Rhizosolenia*, which he collected in different states of sinking and rising, that the nitrogen content shows large differences, and values were highest in rising patches of Rhizosolenia and lowest in sinking patches. Living in symbiosis with nitrogen fixating symbionts, the capability of active buoyancy control of *Rhizosolenia* is thus largely used to incorporate nitrogen, as a crucial component in amino acids and DNA molecules at depth, and to

gain energy by photosynthesis in a second step in the sun penetrated surface waters (Villareal et al., 1993). Due to this mode of living, *Rhizosolenia* is especially adapted to water bodies with a defined discontinuity layer with steep physical and chemical gradients, where nutrients are concentrated (Villareal et al., 1993). Today, the Mediterranean Sea during the summer season and most likely also during sapropel formation may provide these boundary conditions.

Contrary to the definition of Hilgen (1991), most sapropels recovered so far, are not characterized by the presence of diatoms and subsequently do not feature a lamination (Cramp and O'Sullivan, 1999). A lamination in a sapropel is, if existent, restricted to only some sites and not a common feature of a certain sapropel from a certain period. The rather patchy distribution of laminated sapropels suggests that their occurrence is either a matter of extraordinary preservation (Pearce et al., 1998; Rutten et al., 1999), or instead, a local limited primary signal of suitable environmental conditions, which allows the growth of mat forming diatoms (Yoder et al., 1994; Gingele and Schmieder, 2001).

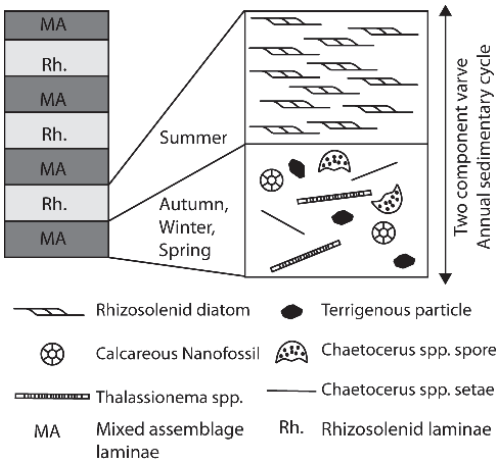

Figure 9: Model of two component layer fabrics in a Pleistocene sapropel from ODP leg 160, Hole 971C (modified after Pearce et al., 1998). Here the annual flux is built up by a bright almost monospecific summer layer of rhizosolenid diatoms and a darker winter layer with a more mixed assemblage.

An annual or even seasonal lamination of a sapropel from the Eastern Mediterranean is documented for example in the youngest sapropel S_1 in the Aegean Sea (van Straaten, 1970) and also in Sapropel S_4 in M51-3 SL103, south of Crete (Hemleben et al., 2003). Anyhow, it seems, that sapropel horizons with a faint or even distinct annual lamination and pronounced thickness (Struck et al., 2001; Rohling et al., 2002; Weldeab et al., 2003b), are mainly concentrated to the last interglacial optimum during MIS 5e, which corresponds to the so-called Eemian period in the terrestrial realm (Cramp and O'Sullivan, 1999).

1.3 The Eemian interglacial/ MIS 5e

As shown in chapter 1.2.1 and 1.2.2, the formation of sapropels is mostly limited to interglacial periods. As the negative values in the oxygen isotopic curve show, Stage 5, which comprises the last interglacial complex prior to the present Holocene, is a period with relatively small ice volume, stored at the poles (Sánchez-Goñi et al., 1999) (Figure 10). Moreover, substage 5e is especially prominent and a sea level of 5 - 7 m above the present is assumed for this period (Szabo et al., 1994; Bard et al., 1996; Linsley, 1996) as well as warmer temperatures (Guiot et al., 1989; Sánchez-Goñi, 2007). Compared to MIS 5e, the following substages are less extreme and MIS 5d and b constitute cool interstadials. MIS 5c and MIS 5a pose warmer periods, during which the sapropels S_4 and S_3 were formed, albeit not as thick as S_5 (Cramp and O'Sullivan, 1999). Although the sub stages 5a-d belong to the overall interglacial complex of MIS 5, they may coincide with the early phase of the terrestrial Weichsel/ Würm glacial (Woillard, 1978 and references therein; Müller et al., 2003). The sapropels S_3 and S_4, being formed therein, may thus not constitute a practical analogue to the actual interglacial of the Holocene, because sea level was lower and the terrestrial boundary conditions might have been quite different from today.

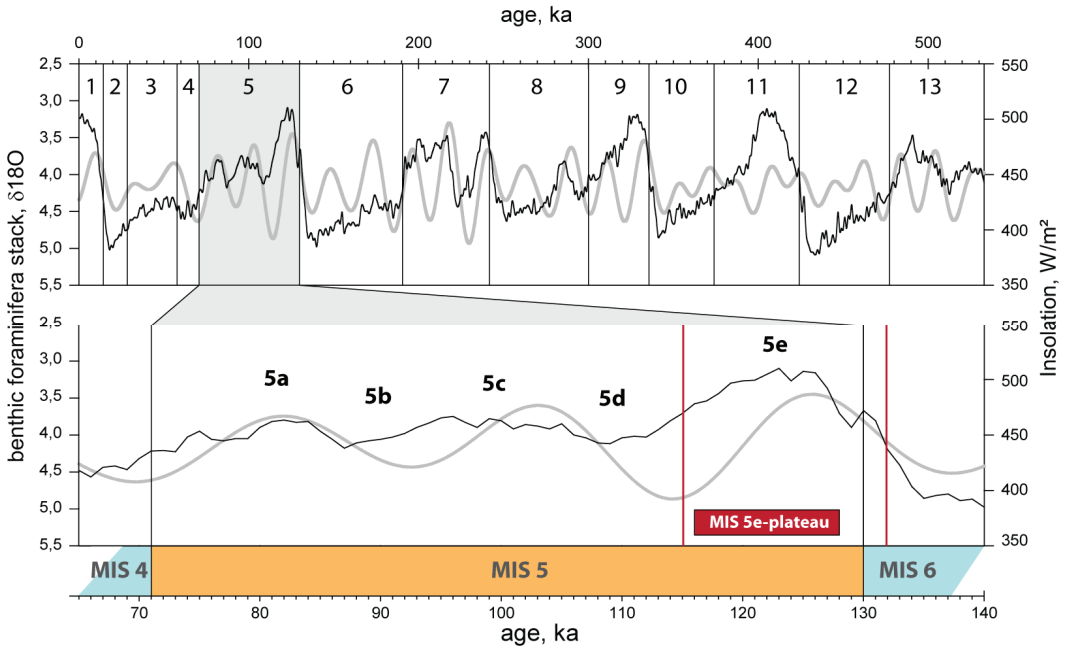

Figure 10: Oxygen Isotopic Stages based on benthic foraminifera (black curve) (Lisiecki and Raymo, 2005) and summer insolation at 65°N (grey) (Berger and Loutre, 1991) during the late Pleistocene and Holocene. Black vertical bars indicate borders between MIS Stages following Lisiecki and Raymo (2005). Red vertical lines indicate onset and termination of MIS 5e and the red bar indicates the plateau of MIS 5e following Shackleton et al. (2002).

1.3.1. Timing of MIS 5e, the Eemian and sapropel S_5

Due to the large number of studies at various sites and conducted with various methods, a certain variability exists for the absolute ages of MIS 5e, the Eemian as a terrestrial counterpart and also sapropel S_5. Mostly, the last interglacial period is given with an age of about 130 – 116 ka (Kukla et al., 2002; Lisiecki and Raymo, 2005). Deviating from this result, the Thorium-230 dating of corals from Oahu, Hawaii, here indicates ages of 131 ka and 114 ka for onset and termination of the last interglacial and a total duration of 17 ka (Szabo et al., 1994), whereas the extended glacial timescale at the Vostok ice core suggests an earlier onset of the last interglacial in Antarctica (Jouzel et al., 1993), where warming started around 134 ka. In proximity to the here presented material, the benthic isotopic data from core MD95-2042 off Portugal (Latitude: 37°48'N, Longitude: 10°10'W, Bathymetry: 3146 m), which were correlated to the radiometric dated timescale of corals, Shackleton et al. (2002) locate the Termination II (End of the penultimate glacial) at 132 ka and the end of MIS 5e at 115 ka and further define a "plateau" from 128 – 116 ka (Figure 10).

This plateau correlates more closely with the terrestrial corresponding unit, the Eemian, which is biostratigraphically defined by pollen assemblages of thermophile and temperated trees and located between the more open tundra vegetation of the preceding Riss/Saale glacial and the following Weichsel/Würm glacial (Bosch et al., 2000). Anyhow, discrepancies emerge from the fact that the Eemian is a biostratigraphic unit, which depends on the locally varying climatic conditions and the pace of plant migration and thus should be regarded as a time transgressive unit (Kukla et al., 2002; Gornitz, 2009).

1.3.2. Climate variability of MIS 5e

Generally, the climatic conditions during the last interglacial period are regarded to be warmer than the actual climate of the Holocene, which for example is corroborated by the widespread occurrence of thermophile trees (Woillard, 1978; Cheddadi et al., 1998; Müller et al., 2003). Studies from lower, monsoonal influenced latitudes point at a more humid climate (Sarnthein, 1978; Rohling et al., 2002), caused by a higher insolation and a subsequently stronger northward penetration of the Inter Tropical Convergence Zone, potentially even beyond the Saharan watershed (~21°N). This issue is further followed-up by Osborne et al. (2008), proclaiming a humid corridor throughout the Libyan Sahara and Tunisia as a potential migration path for Homo sapiens out of Africa around 130 ka. Consequently the freshwater forcing, as a basic condition for sapropel formation was much stronger during the formation of S_5 than for example during the beginning of the Holocene and the formation of sapropel S_1, which was deposited about ~10 – 6 ka B.P. (Struck et al., 2001; Rohling et al., 2002; Weldeab et al., 2003b; Marino et al., 2007; Morigi, 2009).

Concerning the variability of the climatic conditions during the Eemian interglacial, the various studies come to different results. While some studies suggest relatively stable conditions throughout the Eemian (Tzedakis, 1993; Litt et al., 1996; Caspers et al., 2002), other studies point at a more variable climate. Here, for example the modern analogue technique, performed on pollen records from France (Grand Pile) and Germany (Bispingen, Gröbingen), suggest numerous cold events with a duration of 70 – 700 years (Field et al., 1994). A distinct cooling at the mid of the Eemian is also evident at various sites. Here, pollen data and isotopic measurements (*G. bulloides*) at the north Iberian coast point at a terrestrial winter cooling accompanied with enhanced precipitation as well as lower SST at around 121 ka (Sánchez Goñi et al., 2005). This mid Eemian cooling is also evident in Northern Germany (Kühl and Litt, 2003). Noteworthy is also a pulse of more arid climate with cooler temperatures during the end of the Eemian, which Sirocko et al. (2005) could identify in a pollen record in a dried Eifel Maar. This interval lasted only for about 400 years and is characterized by a decline of temperate trees such as *Quercus*, *Ulmu*s and *Corylus* and an erratic increase of grass pollen, whereby the onset and the termination of this Late Eemian Aridity Pulse (LEAP) occurred each within less than three decades. The trigger of this LEAP is supposed to be the declining insolation, which passed a threshold of about 416 W/m^2 (Berger and Loutre, 1991; Sirocko et al., 2005). Generally the LEAP is a good example for short, yet quite significant effects of astronomical forcing on the climatic conditions and also is supposed to illustrate how the actual interglacial period might be terminated.

Also the time immediate before the last interglacial features a climatic oscillation. In an Atlantic sediment core off the Iberian coast, pollen data indicate relative mild conditions at the end of MIS 6, which switched back to glacial conditions in the uppermost stage of MIS 6 (Sánchez-Goñi et al., 1999). This two step changeover is known as Zeifen-Kattegat Oscillation (Seidenkrantz et al., 1996) and is not dissimilar to the two-tiered changeover of the Bølling-Allerød interstadial and the subsequent Younger Dryas stadial at the end of Termination I.

1.4 Study aims

Aware of this unique combination of oceanographic setting, geographic position and climatic conditions, as being demonstrated in the previous chapters, this work focuses on the investigation of an expanded and laminated S_5 sapropel, being present in three parallel sediment cores from one location in the northern Levantine Basin. To make the most of this unique high-resolution window into a warm interglacial climate, a series of investigations have been carried out, whereas the following aims are declared.

1. The identification of the major lithological components of the sapropel and a stratigraphic subdivision of the sapropel. This shall be achieved by combining lithological descriptions with analyses of abundances of environmentally sensitive elements from continuous XRF scans, which were strengthened by discrete ICP-OES measurements. Multivariate statistical methods will be applied in order to objectively detect major changes throughout the peak warmth of the last interglacial period. The identified subunits and patterns of variability in sediment physical and chemical properties will then be interpreted in terms of their paleoenvironmental significance.

2. Precise estimate of the age and duration of sapropel deposition. Given the lack of absolute dating possibilities, this remains a hotly debated point. Here, we first will determine the positions of major changes in sedimentation rate, using an established event-stratigraphic framework, based on planktonic foraminifera and stable isotopes. This knowledge will then be combined with counts of individual yearly laminae to generate a total chronology.

3. Development of a genetic model of the laminated S_5 sapropel. Combining data on sediment properties with micropalaeontological and isotopic paleoenvironmental indicators, we will attempt to explain the environmental events leading to the deposition of the sapropel, the cessation of the anoxia and the appearance of the mat forming diatoms in the study area of the northern Levantine basin, which today constitutes an important locus of intermediate and deep water formation.

4. Assessment of the response of the planktonic foraminiferal community composition and test size to environmental changes during the S_5 sapropel deposition. The high temporal resolution, being provided by the studied section allowed us to investigate how the planktonic community responded to environmental stress associated with oceanographic changes preceding the sapropel deposition, occurring within the sapropel and also with the cessation of sapropel deposition.

5. Detection of cyclicities of potential astronomical origin during the formation of the sapropel interval as a potential driver in the climate system. Finally, benefitting from the high-precision laminae-count based age model, we will be able to submit data on sediment properties and paleoenvironmental proxies to a wavelet analysis method, which is capable of detecting cyclicities with high spatial precession. This analysis thus allows determining whether or not the climate of the last interglacial in the Eastern Mediterranean was stable or instead modulated by short cycles of possibly solar origin. An understanding of the forcing of interglacial climate under natural conditions is important for assessment of scenarios of future climate change.

2 Material

This work is based on the sapropel S_5 (i-cycle 12 of the correlative peak in the precession index) from the last interglacial maximum (MIS 5e), found in the three sediment cores M40-4 SL67, M51-3 SL103 and M51-3 SL104 from the Meteor cruises M40-4 from 1998 (Hieke et al., 1999) and M51-3 from 2001 (Hemleben et al., 2003). All cores are located in the northernmost part of the Levantin Basin, about 90 km east of Crete and 70 km south of Karpathos. The core locations reside on a relatively flat ground in about 2150 m water depth on a ridge, bordered by the Pliny Trench to the north-west, the Cretan-Rhodes Ridge to the north and north-east and the Strabo Trench to the south (Figure 11) (Maldonado et al., 1981). The three cores are between 0.5 km and 2.5 km apart from each other.

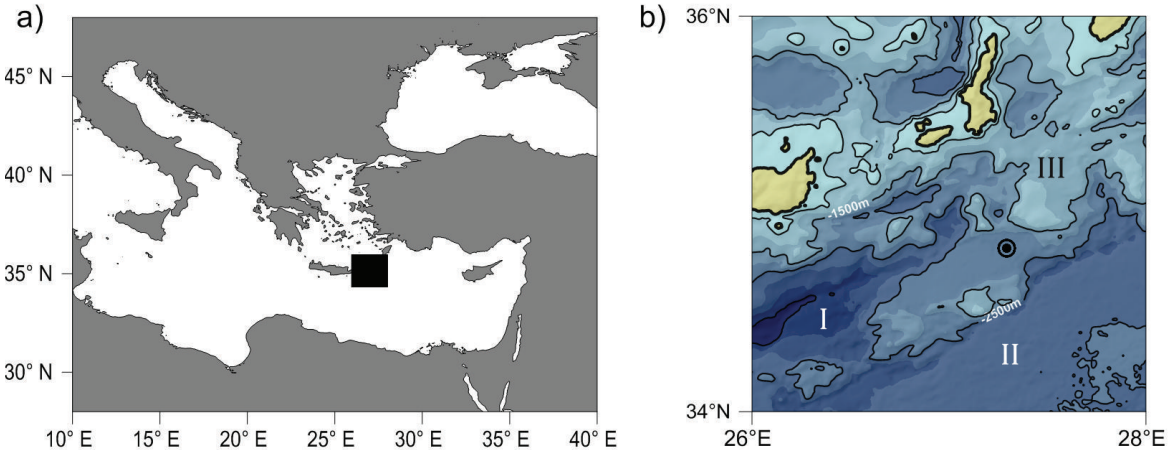

Figure 11: Overview of the Eastern Mediterranean (a) and detailed outcrop of the area south-east of Crete (b), showing the position of M40-4 SL67, M51-3 SL103 and M51-3 SL104 and also the Pliny Trench (I), the Strabo Trench (II) and the Cretan-Rhodes Ridge (III) as the major geological entities in very proximity of the gravity cores (bathymetric map is based on ETOPO 1 minute grid (Amante et al., 2009)).

Sapropel S_5 is located in all cores at a depth of about 3.6 m below sediment surface and resides in sections one and two of the gravity cores (Figure 12, Table 2). Various characteristics were used to identify the S_5 sapropel, separating it from other sapropels within the cores. One point is the unusual thickness of S_5, which mostly exceeds those of other sapropels. S_5 can also be identified by sapropel counting, since there are four younger sapropels above, although this method provides uncertainties since sapropels might experience post depositional oxidation and S_2 is rarely found in the Mediterranean (Muerdter et al., 1984; Cramp and O'Sullivan, 1999) (Figure 12). In the studied cores, sapropels S_1, S_3, S_4, S_5 and S_6 could be clearly identified in all cases, allowing unambiguous attribution of the studied horizon to S_5. Typical for S_5 sapropels from this region, is the massive abundance of diatoms (Schrader and Matherne, 1981; Thunell and Williams, 1982; tenHaven et al., 1987), which was confirmed for our studied sapropel by Frydas and Hemleben (2007). Finally, the permanent presence of the planktonic foraminifera *G. ruber*, a warm water species, helps to define the interglacial S_5 sapropel against the underlying S_6

sapropel, which was formed during a glacial maximum and is dominated by *G. bulloides* and *T. quinqueloba*, two species, which are more known to dwell in temperate waters (tenHaven et al., 1987). The presence of *G. ruber* in the studied sapropel section was confirmed by smear-slide analyses.

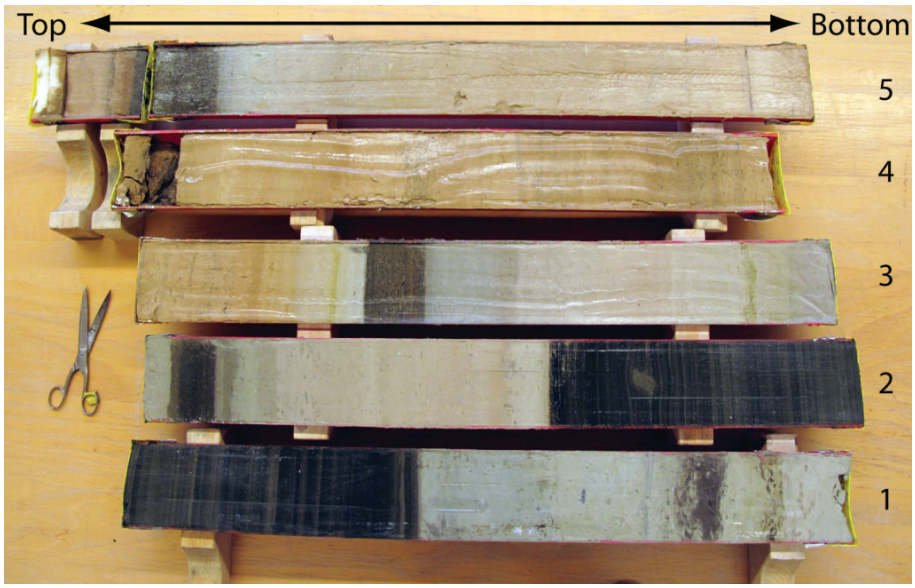

Figure 12: Gravity core SL103 from Meteor Cruise M51 Leg 3. The core is separated into five sections with lengths of one meter and a shorter top section. Clearly visible is sapropel S_1 in the top section and section five, sapropel S_3 in section three, sapropel S_4 in section two, sapropel S_5 in sections two and one and sapropel S_6 in section one.

Table 2: Basic information on the S_5 sapropel in the six core sections from gravity cores from the Tübingen core repository (Hieke et al., 1999, Hemleben et al., 2003). Depths and thicknesses experienced minor corrections. Data in brackets indicate the original data from the preliminary data.

Core	M40-4 SL67	M51-3 SL103	M51-3 SL104
Latitude	34°48.85'N	34°48.74'N	34°48.89'N
Longitude	27°17.76'E	27°17.10'E	27°16.93'E
Water depth	2158 m	2151 m	2154 m
Core depth	Section 2	Section 2	Section 2
S_5-Top	364 cm	375.5 cm	359.5 cm
Core Depth	Section 1	Section 1	Section 1
S_5-Base	455.4 cm (454 cm)	460.6 cm (460.5 cm)	446.3 cm (444 cm)
S_5-Thickness	91.4 cm (90 cm)	85.1 cm (85 cm)	86.8 cm (84.5 cm)

3 Methods

3.1 Sediment physical properties

3.1.1. Sediment colour

Photographic images from the archive halves of sections one and two, which contained the S_5 sapropel, of all three sediment cores were obtained with the 'CoreScan Colour' from the 'Deutsche Montan Technologie GmbH' and the 'DigiCore' software. The images capture the complete length and width of the sections and provide discrete measurements of colour (red, green, blue) and lightness ((red + green + blue)/3) at a spatial resolution of twenty measurements per millimetre (50 µm), integrated over a width of 8.5 cm. To ascertain the reproducibility of these high-resolution colour scans, the measurements were repeated five times for each core (Figure 13). Between each run, the surface was newly smoothened to an optimal flat shape by a glass slide, guided perpendicular to the length of the core. Data from the five measurements were compared and the dataset with the least amount of disturbances (scratches on the core surface causing shadows) has been selected for further analysis. The comparison has shown excellent reproducibility of the scans and revealed that the largest source of differences was the preparation of the sediment surface. The further description and evaluation of the sediment colour is based on the soil-colour chart after Munsell (1995).

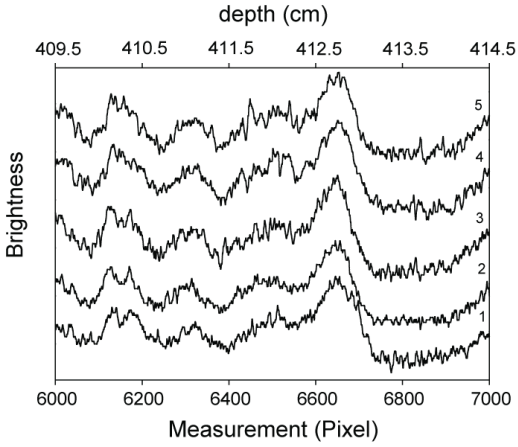

Figure 13: A five-centimetre section (409.5 – 414.5 cm, 1000 pixels) from M51-3 SL104 with repeated measurements of sediment lightness. The effect of sediment surface preparation on the quality of the recorded sediment colour variation is shown in five scans. The five scans have been aligned to achieve a maximum fit and are shown with an arbitrary vertical offset (From Moller et al., 2011a).

3.1.2. Water content and magnetic susceptibility

The natural water content (Richards, 1967) and the magnetic susceptibility (St-Onge et al., 2007; Stoner and St-Onge, 2007) were determined from discrete samples of 2 x 2 x 0.3 cm volume from U-channels, which were continuously sub-sampled with a spacing of 3 mm. So far, this is the highest spatial resolution to be applied to a sapropel horizon, yet justified by the unusual thickness and the lamination of the sapropel. Although an even more dense sampling is possible in theory, here, a potential bias might be introduced, since a level of inter- or even intra annual signal variability might be introduced (Koch, 2010). Two parallel U-channels were extracted from the working half of core M51-3 SL104 and one from the working half M51-3 SL103. The

discrete samples (about 340 samples per U-channel) were stored in standard 30 ml containers of known weight, and the weight of the wet and freeze-dried sample was noted. The natural water-content was determined in the three U-channel series from different cores, relating the weight of the sediment water to the weight of the dry sample. Bulk magnetic susceptibility was analysed for one U-channel series per sediment core by a Multi-function Kappabridge (Agico) instrument, which is designed to determine the content of magnetic minerals in samples of a constant volume. Each sample plus the container was introduced manually into the pickup-unit. All measurements were corrected by subtracting the averaged magnetic susceptibility of five empty containers. Since it was not always possible to precisely estimate the sediment volume, we related the corrected susceptibility to the weight of the dry (U-channel 2 from M51-3 SL104) or the wet (U-channel from M51-3 SL103) sample.

The water content provides information about the porosity of the sediment and, in this case, potentially indicates the varying occurrence of diatoms, which feature a highly porous silica shell. The magnetic susceptibility is a viable tool to detect a potential post depositional oxidation (vanSantvoort et al., 1997), and also allows the detection of ash layers, where volcanic activity has introduced magnetic minerals into the sediment.

3.2 Sediment chemical properties

3.2.1. XRF scanning

The non-destructive X-Ray fluorescence (XRF) scanning of marine sediment cores allows the tracking of relative changes of elemental abundances and their subsequent interpretation in terms of environmental impact. The high spatial resolution of the XRF scanning thus constitutes an ideal tool for the analysis of here presented laminated sapropel horizon and allows the correlation between the cores, the detection of potential causative coherences between different elements as well as leads and lags. Principally, a mobile radioactive source is automatically moved stepwise along the surface of the sediment core (along depth axis), where atoms in a defined area are excited by the penetrating radiation and release electrons from their inner shells. The vacant positions in the inner shells are refilled with electrons falling back from the outer shells by the subsequent emission of energy, which is absorbed by a detector and whose amount is characteristic for each element (Jenkins et al., 1967; Rothwell, 2006). Depending on the abundance of the element, the detector collects an according amount of energy per time unit for that position. The results, produced by the XRF scanner is thus a matrix where the columns represent different elements and the lines the number of the measurement (here core depth), which themselves are given as counts per area or counts per second (counts per area/measurement period).

For this study, the AVAATECH XRF-Scanner at the ETH Zurich was used to analyse the contents of ten selected elements (Al, Si, S, Cl, Ca, Ti, Fe, Br, Mo, Ba) in the archive sections of all three sediment cores with special regard to their environmental meaning (see below for further explanation). The measurements were conducted in three passages, each with a different voltage and filter (without filter at 10 kV, Palladium filter at 30 kV, Copper filter at 50 kV) with a count time of 20 seconds. Before the measurement, the sediment surfaces of the cores were covered by a 4 µm thick *Ultralene SPEX CertiPrep*-foil. The spatial resolution of individual measurements is given by a down-core slit-size of 0.2 mm, integrated over a cross-core slit size of 12 mm. Due to the extensive duration of the analyses (one measurement required 20 seconds), the complete S_5 sapropel, but only 5 cm of enclosing marl below and above the sapropel have been scanned from each core. The XRF scanning was completely conducted at the ETH Zürich, under the supervision of Dr. Yvonne Hamann from the Climate Geology Group.

Normalization of elemental data:

In order to accommodate for changes in the accumulation rate and potential contrasts in sediment porosity within the sapropel and in comparison to the enclosing marls, the normalization of elemental data from XRF-scanning data has become a common step prior to

interpretation (Rothwell, 2006; Calvert and Pedersen, 2007; Weltje and Tjallingii, 2008). To asses actual enrichments or depletions of Ti, Ba, Si, Ca, Fe and Mo, normalization with Aluminium is common and out-balances the terrestrial background due to its wide spread occurrence and the conservative behaviour as a lithogenic element (Calvert and Pedersen, 2007). S and Br are presented as a ratio of Cl, which counterbalances the water content (Mercone et al., 2001; Ziegler et al., 2008).

Elemental ratios, indicating terrestrial Input:

Titanium (Ti/Al)

Ti is enriched in soils during intense weathering and is carried in the silt and fine-sand fraction in form of the heavy minerals rutile (TiO_2), sphene ($CaTiSiO_5$) and ilmenite ($FeTiO_3$) and can be used to track primarily aeolian sediment transport (Brumsack and Wehausen, 1999; Calvert and Pedersen, 2007; Larrasoaña et al., 2008). The primary source for dust, which is enriched in Ti in Mediterranean sediments is the Sahara and Ti has therefore been used to reconstruct variations in aridity over North Africa and variations in monsoonal wind strength (Calvert and Fontugne, 2001; Mercone et al., 2001).

Elemental ratios, indicating productivity:

Barium (Ba/Al)

As demonstrated by Dymond et al. (1992), Ba is concentrated as barite in organic material during its production and deposition. Although the exact mechanism of Ba uptake is not completely understood yet, Ba is widely used as an indicator for paleoproductivity (Langereis et al., 1997; Mercone et al., 2001; Thomson et al., 2006). Even after postdepositional oxidation of a sapropel, Ba remains in the sediments at elevated levels, which allows to detect even completely oxidized 'ghost-sapropels', as well as to assess the amount of postdepositional oxygenation in preserved sapropels (Thomson et al., 1995; vanSantvoort et al., 1997; Thomson et al., 2006).

Bromine (Br/Cl)

Complementary to barium, we also use the element bromine as indicator of productivity. As Ziegler et al. (2008) could show, XRF scanning data of bromine in sediment cores of the Red Sea and the anoxic Urania Basin in the Mediterranean are strongly correlated to TOC measurements in discrete samples. Here, bromine seems to mainly reflect the marine organic matter (Mayer et al., 2007). Yet, bromine can be influenced by terrestrial organic matter, which is relatively low in bromine. Especially interglacial warm periods, which feature an enhanced river discharge, are prone to this source of error, as the deviation in the Arabian Sea core NIOP 463 near the monsoonal influenced Indus river shows (Ziegler et al., 2008). Varying salinities of the water are

another agent, capable of altering the linear relationship between organic carbon and bromine, and is thus, similar to Mercone et al. (2001), corrected against chlorine.

Silicon (Si/Al)

Silicon can be both, an index for terrestrial input, since it is a widespread element in minerals, but also the main part of diatom frustules, which are very abundant in the here presented S_5 sapropel (Frydas and Hemleben, 2007) and thus qualifies silicon as an index for primary productivity. Since the amount of wind-blown dust is lower during warm periods (Larrasoaña et al., 2008) and productivity is supposed to be increased during sapropel formation, a interpretation of silicon in terms of productivity is reasonable, and strengthened by the normalisation of silicon against Aluminium. Furthermore, comparing silicon with other representative elements for productivity, allows a more differentiated analysis and also to relate peaks in productivity with diatoms or potential other primary producers.

Calcium (Ca/Al)

Calcium is present in minerals like plagioclase, clinopyroxene and amphibole, where it is prone to weathering by the presence of water. Generally, surface waters are saturated in Ca (Albarède, 2009), and form a source for skeletal elements in various microfossils. Thus, complementary to silicon, calcium is here used to track the abundance of calcareous microfossils such as planktonic foraminifera and coccolithophores or detrital calcite crystals, which can be a matter of calcareous shell productivity as well as calcium carbonate preservation.

Elemental ratios, indicating redox conditions:

Due to the low oxygen content, redox-sensitive minerals become enriched in the sediment during sapropel formation, either by diffusion and precipitation from the bottom water, by the release of pore waters, which are supersaturated by remineralisation of organic matter, or by the dissolution of a solid phase and the subsequent fixation of dissolved elements in a different phase within the sediments (Calvert and Pedersen, 2007).

Sulphur (S/Cl)

Sulphides, such as FeS_2, are commonly associated with reducing conditions and are known to be enriched in sapropels by the dominant SO_4^{2-} reduction by micro organisms (Passier et al., 1999a; Calvert and Pedersen, 2007) and can be indirectly estimated by the abundance of S. As a major ion, S is highly concentrated in the sea water, which makes it necessary to normalize S against Cl to counterbalance the salt in the pore water (Mercone et al., 2001).

Iron (Fe/Al)

Complementary to sulphur, iron becomes enriched under reducing conditions where it forms pyrite (FeS_2) (Wehausen and Brumsack, 1999). Passier et al. (1999b) here describes a more detailed model of pyrite formation in context with the amount of microbial production of reduced S and points at the possibility of pronounced peaks of pyrite below the base of the sapropel under high SO_4^{2-} production and a subsequent downward migration.

Molybdenum (Mo/Al)

Beside S and Fe, also molybdenum constitutes another redox sensitive trace metal and becomes enriched during sapropel formation and anoxic basins (Mercone et al., 2001; Thomson et al., 2006). In contrary to these results, Thomson et al. (1995) showed peaks of Mo below the sapropel horizon, which suggests either a remobilization or a preferred redox potential before the onset of the sapropel. Compared to Fe, Mo experiences strongest enrichments under anoxic conditions, while Fe peaks in slightly less extreme milieus with reducing conditions (Calvert and Pedersen, 2007).

3.2.2. ICP-OES measurements (Inductively coupled plasma optical emission spectroscopy)

Despite normalizing, the use of XRF-scanning data remains problematic, since the elemental contents (given in counts per second) represent uncalibrated data and could be affected by varying sediment physical properties in the scanned core (Tjallingii et al., 2007). The measurements are expressed as counts per second, and only provide evidence about relative changes (St-Onge et al., 2007). To address this issue, the concentration of several elements in twenty six 3 mm thick discrete samples from a U-channel from the working half of M51-3 SL104 were determined quantitatively (Table 3). For this multi-element analysis about 20 mg of sample was homogenized and was treated over night with 0.5 ml HNO_3 to oxidise organic matter. The remaining material was digested in closed PTFE vessels at 180°C after adding 2 ml concentrated HF and 1 ml $HClO_4$ (Heinrichs et al., 1986). After digestion, the acids were evaporated at 180°C; residues were re-dissolved and fumed off three times with 2 ml semi-concentrated HCl and diluted with 2 vol.% HNO_3 to a final dilution factor of 250. All acids used were of supra pure quality. Major (Ti, Al, Fe, Ca, S) and trace elements (Ba, Mo, Zr) were analysed by ICP-OES (iCAP 6300Duo, Thermo Scientific) equipped with a MicroMist nebulizer (Institut für Ostseeforschung, Warnemünde, Dr. Olaf Dellwig). Precision (1σ) and accuracy of all measurements were checked by parallel analysis of international (SDO-1, SGR-1) and in-house reference materials (TW-TUC, OBSS) and were <3.3%/<3.1% for major elements and <5.3%/<7.1% for trace elements. Results of the multi-element analysis were then compared with the average values of the corresponding 3 mm wide sections of XRF-scan measurements, centred over the very position of the absolute measurements (Moller et al., 2011a).

Table 3: Depths of the midpoints of the 3 mm intervals, being used for ICP-OES measurements and characterization of the sediment fabric.

Depth, cm	Sediment fabric
358.00	Enclosing Marl
361.00	Bioturbated Zone
363.50	Bioturbated Zone
365.50	Bright Layer
366.50	Dark Layer
367.50	Bright Layer
371.50	Dark Layer
377.00	Dark Layer
384.00	Bright Layer
393.00	Bright Layer
397.00	Dark Layer
404.70	Bright Layer
405.50	Dark Layer
413.50	Bright Layer
417.20	Bright Layer
418.80	Dark Layer
426.00	Bright Layer
427.20	Dark Layer
432.50	Bright Layer
433.50	Dark Layer
437.40	Dark Layer
440.30	Bright Layer
444.00	Bright Layer
445.00	Dark Layer
446.90	Bright Layer
450.00	Enclosing Marl

3.3 Paleoenvironmental proxies

For the analysis of the microfossils, we use the same 3 mm sub samples from the U-channel of M51-3 SL104, which have previously been used to estimate contents of water and to measure the magnetic susceptibility. The freeze-dried samples were washed over a 63 µm mesh and the coarse fraction (>63 µm) was further separated by dry sieving into fractions of 63 – 150 µm, 150 – 250 µm and >250 µm.

For this study, we mainly rely on planktonic foraminifera, which unify several advantages. Planktonic foraminifera are widespread in the world's oceans and follow a distribution scheme that is largely controlled by the waters sea surface temperature (SST), whereby the optimum temperature window is positively correlated with relative and absolute abundances as well as largest shell size. Other advantages are the enhanced preservation in marine sediments and furthermore the multitude of applicable proxies (Kucera, 2007). Specifically, planktonic foraminifera are analyzed in terms of their faunal assemblage in each sample (Chapter 3.3.1), $\delta^{18}O$ and $\delta^{13}C$ stable isotopes (Chapter 3.3.3) and transfer function, namely artificial neural networks (Chapter 3.3.4). Since the shell morphology of juvenile stages of planktonic foraminifera often strongly differs from that of the adult stages, only the combined data from the fractions 150 –250 µm and >250 µm were used to determine the faunal abundances in each sample.

Along with the planktonic foraminifera, also benthic foraminifera and radiolaria were counted but without further determining the species level. Living either epi- or infaunal, certain species of benthic foraminifera are adapted to low oxygen content in the surrounding water, where they provide a solid indicator for bottom water oxygenation (Armstrong and Brasier, 2005) and have also recovered in sapropel S_5 and S_6 (Schmiedl et al., 2003a).

Radiolaria are single celled, silicon shelled planktonic organisms, which tend to bloom seasonally in response to the availabilities in silicon and food (Armstrong and Brasier, 2005). Although the Mediterranean is generally undersaturated in silica (Cramp and O'Sullivan, 1999) and preservation potential of such species is poor, it has been shown that anoxic conditions in general and the S_5 sapropel interval in particular, can provide the ideal conditions for excellent preservation of fragile silicon shelled organisms (Björklund and De Ruiter, 1987; Pearce et al., 1998; Frydas and Hemleben, 2007) and the abundances of radiolaria is here used to complement other indices (Ba/Al, Br/Cl) of paleoproductivity.

Census counts of planktonic foraminifera for each size fraction were obtained from equal aliquots with at least 300 specimens. Analysis and counting was conducted with a binocular with an overhead lamp, a standard gridded tray and a wet brush to perform manipulations of individual specimens. Beside the present study, the census counts of the lowermost 13.8 cm and the uppermost 11.7 cm were accomplished by Koch (2010) in line of a diploma thesis and depict the samples of the enclosing marls as well as the visible onset and the termination of the sapropel.

3.3.1. Planktonic foraminiferal assemblages

The faunal assemblage gives detailed information about occurrence and disappearance of each species of planktonic foraminifera at any point in the observed interval. The so gained census data were then investigated with regard to an already established high resolution biostratigraphic framework (Cane et al., 2002), which uses an event based scheme of planktonic foraminiferal relative abundances. Comparing the results with other S_5 sapropels from the Eastern Mediterranean allows the monitoring of changes in sedimentation rate, as well as getting evidence of the integrity of the S_5 sapropel as a whole. Being counted in two different size fractions individually (chapter 3.3), the proportion of larger individuals of one species (>250 µm) toward the whole sample (>150 µm) can be calculated for each sample and evaluated in terms of SST, which represents the most important factor to control the test size (Kucera, 2007).

3.3.2. Taxonomy of planktonic foraminifera

Based on the taxonomy of Saito et al. (1981), Hemleben et al. (1989) and Postuma (1971), 24 species of planktonic foraminifera were identified in the discrete samples of the S_5 sapropel and the enclosing marls in M51-3 SL104, and are further complemented by data from specific literature. The species names follow the taxonomy of Hemleben et al. (1989). All species are documented as examples by Secondary Electronic Microscope (SEM Leo-1450VP).

Globigerinella siphonifera (d'Orbigny, 1839a)……..……..(Plate 1a-b)
Spinose, symbiont bearing species of medium to large size. Low trochospiral test during juvenile stages and almost plansprial, evolute test during the adult stage with five to six globular chambers per whorl. Inhabits tropical to subtropical water and is also common in the Mediterranean Sea. It features a rather large depth range up to 300 m and feeds on zooplankton (Spindler et al., 1984).

Globorotalia inflata (d'Orbigny, 1839b)……(Plate 1c-d)
Non-spinose species with four, subglobular chambers in the last whorl. Thick, smooth and finely perforated test. *G. inflata* inhabits cool to temperate waters. It has a large range of depths of up

to 400 m and is therefore interpreted as an indicator of well ventilated waters (Rohling et al., 2004).

Globigerinoides sacculifer (Brady, 1877)……..(Plate 1f)
Symbiont bearing species of medium to large size. Trochospiral, with three chambers in the last whorl. Chambers are spherical with exception of the last chamber, which is elongated and sack like. *G. sacculifer* occurs from the tropics to subtropics, where it inhabits the upper water column.

Globigerinoides trilobus (Reuss, 1850)……..(Plate 1e)
Often lumped together with *G. sacculifer*, and regarded as one of two morphotypes. Morphology is identical to *G. sacculifer* with exception of the sac-like last chamber. Also the habitat is identical to *G. sacculifer*.

Globigerinoides ruber (d'Orbigny, 1839a)……..(Plate 1g-k)
Small to large spinose, symbiont-bearing species, which feeds on phytoplankton as well as significantly larger copepods. Trochospiral growth of the three subspherical chambers in the outer whorl, increasing moderately in size. Interiomarginal, umbilical primary aperture and secondary sutural apertures situated opposite sutures of earlier chamber. Pigmentation can result in a pink to red variety of the otherwise far more common white variety; the first is counted separately as *G. ruber* (pink). *G. ruber* shows a wide range of variation in size, the height of the spire and tightness of the test coiling. Here we further separate *G. ruber* (elongate) for species with a tightly coiled trochospire and, following Numberger et al. (2009), we further separately identify, *G. ruber* (platys) for forms with a slightly flattened final chamber and *G. ruber* (kummerform), with a kummerform developed last chamber. Generally, *G. ruber* is a typical warm water species and is distributed throughout the worlds oceans and also the most common species in the Mediterranean, where it inhabits the uppermost water column up to 50 m. *G. ruber* is also known to tolerate extremely high, but also low salinities.

Globigerinoides conglobatus (Brady, 1879)……..(Plate 1l)
Large trochospiral species with three chambers in the final whorl. Generally subglobular to subquadrate chambers and coarsely perforated thick wall. Interiomarginal primary aperture, which is comparatively long and low. Small, irregular secondary apertures occur on the spiral side. Distribution in equatorial to temperate waters as well as the Mediterranean Sea. As a symbiont bearing species, *G. conglobatus* inhabits shallow waters.

Orbulina universa (d'Orbigny, 1839a)……(Plate 1p)
Large, spinose species, which is widely distributed from the tropics to subpolar regions. Its size is correlated with temperature as well as nutrients. *O. universa* is carnivorous, particularly during its spherical adult phase and difficult to recognize during its juvenile stages. During reproduction *O. universa* can sink to depths of about 300 m. Similarly to *G. ruber*, *O. universa* is also tolerant against enhanced levels of lower saline fresh water (Rohling et al., 2004).

Globorotalia truncatulinoides (d'Orbigny, 1839b)……(Plate 1m-o)
Non spinose, medium to large species with very low trochospiral test. Chambers are rhomboid shaped, whereas the spiral side is almost flat and the umbilical side is convex, which gives the specimen a strongly conical appearance. *G. truncatulinoides* inhabits tropical to temperate waters and is known to live as deep as 1000 m. It is thus indicative for a well ventilated water column. Also strongly stratified waters are supposed to hinder the reproduction of *G. truncatulinoides* (Lohmann and Schweitzer, 1990).

Globigerina bulloides (d'Orbigny, 1826)……(Plate 2a-b)
Variable test size with three to five lobulated chambers in the final whorl. Interiomarginal large primary aperture on the umbilical side with high symmetrical arc. Densely perforated wall structure. *G. bulloides* is most common in cooler waters (Schiebel et al., 1997), yet it is also found in the tropics and often related to upwelling areas where it inhabits shallower waters above the thermocline (Hemleben et al., 1989).

Beella digitata (Brady, 1879)……(Plate 2c-d)
Highly variable test size. Trochospiral species with 4 – 5 chambers in the outer whorl. Chambers initially subspherical but becoming ovate and in later whorls highly elongated and also increase rapidly in size as added. Interiomarginal primary aperture with usually high arc. *B. digitata* prefers subtropical water and occurs quite often in the Mediterranean Sea, where it seems to be restricted to deeper waters.

Globoturborotalita tenella (Parker, 1958)……(Plate 2e-f)
Small species with trochospiral winding and four chambers in the outer whorl. Almost similar morphology to *G. rubescens*, except for the pigmentation and the secondary aperture on the spiral site of the last chamber. Tropical to temperate species.

Globorotalia scitula (Brady, 1882)……(Plate 2g)
Medium to low trochospiral, biconvex species. Four to five strongly compressed chambers in the outer whorl with curved sutures, which moderately increase in size and no peripheral keel. Thin and smooth shell, which is finely and densely perforated. *G. scitula* occurs in tropical to temperate waters but is absent in the contemporary Mediterranean Sea (Rohling et al., 2004).

Dentogloborotalia anfracta (Parker, 1967)……(Plate 2h)
Small, low trochospiral species with an almost flat spiral site and 4 – 5 chambers in the last whorl. Thin, translucent test with slightly curved sutures. *D. anfracta* is a tropical species.

Globoturborotalita rubescens (Hofker, 1956)……(Plate 2i)
Small, trochospiral test with four chambers in the last whorl, which rapidly increase in size. Small, rounded aperture with high arc. Coarsely perforated wall. Distinctive pink to red pigmentation. Occurs in warm to temperate waters.

Neogloboquadrina incompta (Cifelli, 1961)……(Plate 2j)
Small size. Throchospiral winding with 4 – 4 1/2 chambers in the outer whorl. Interiomarginal aperture with low arc, extending to the periphery. Next to the dominant dextral winding a small percentage can also wind up in an opposite (sinistal) direction (Darling et al., 2006). *N. incompta* is a temperate species, which prefers a range of depths between 70 – 200 m and today is more common in the Western Mediterranean (Rohling et al., 2004). According the coiling paradoxon of *N. pachyderma* and *N. incompta* (Darling et al., 2006), we use the species name *N. incompta*, whereas cited references (Cane et al., 2002; Marino et al., 2007) refer to *N. pachyderma*, yet meaning the same species.

Neogloboquadrina dutertrei (d'Orbigny, 1839a)……(Plate 2k)
Trochospiral species, with 5 – 6 chambers in the last whorl, which increase slowly in size. *N. dutertrei* is found in tropical to transitional waters, whereas the number of chambers in the last whorl seems to be positively correlated to the temperature of the surrounding water. Bé and Tolderlund (1971) further suggest a correlation to low saline waters. *N. dutertrei* feeds almost exclusively on phytoplankton at the thermocline (Watkins et al., 1996), and has a potential lunar periodic reproduction cylce.

Globigerina falconensis (Blow, 1959)……..(Plate 2l)
Trochospiral, small to medium in sized species with three to five chambers in the final whorl. Last chamber slightly elongated or ovoid with an apertual flap. The umbilical aperture is often completely obscured by the base of the last chamber. *G. falconensis* carries symbionts and lives in the photic zone of temperate to subpolar waters.

Turborotalita quinqueloba (Natland, 1938)……..(Plate 2o)
Small, low trochospiral species with five chambers in the outer whorl. Final chamber is often extended and can cover the umbilicus like a bulla. *T. quinqueloba* inhabits subpolar waters and its abundances decrease from high to low latitudes but can also be found in the Mediterranean, especially near the strait of Gibraltar, where Atlantic waters enter the Mediterranean (Thunell, 1978). Reproduction is eventually lunar cyclic.

Globigerinita glutinata (Egger, 1893)……..(Plate 2m-n)
Trochospiral, small to medium sized species with four globular chambers in the last whorl. Primary aperture features a thin lip, which is often completely obscured by a bulla. *G. glutinata* presumably dwells in shallow waters up to a depth of about 50 m. *G. glutinata* inhabits waters from the poles as well into the tropics and thus features a wide tolerance against water temperature and salinity.

Globigerinella calida (Parker, 1962)……..(Plate 2p)
Small to medium species, with low trochospiral winding. four to six slightly elongated and strong lobulate chambers in the outer whorl. *G. calida* inhabits subtropical waters.

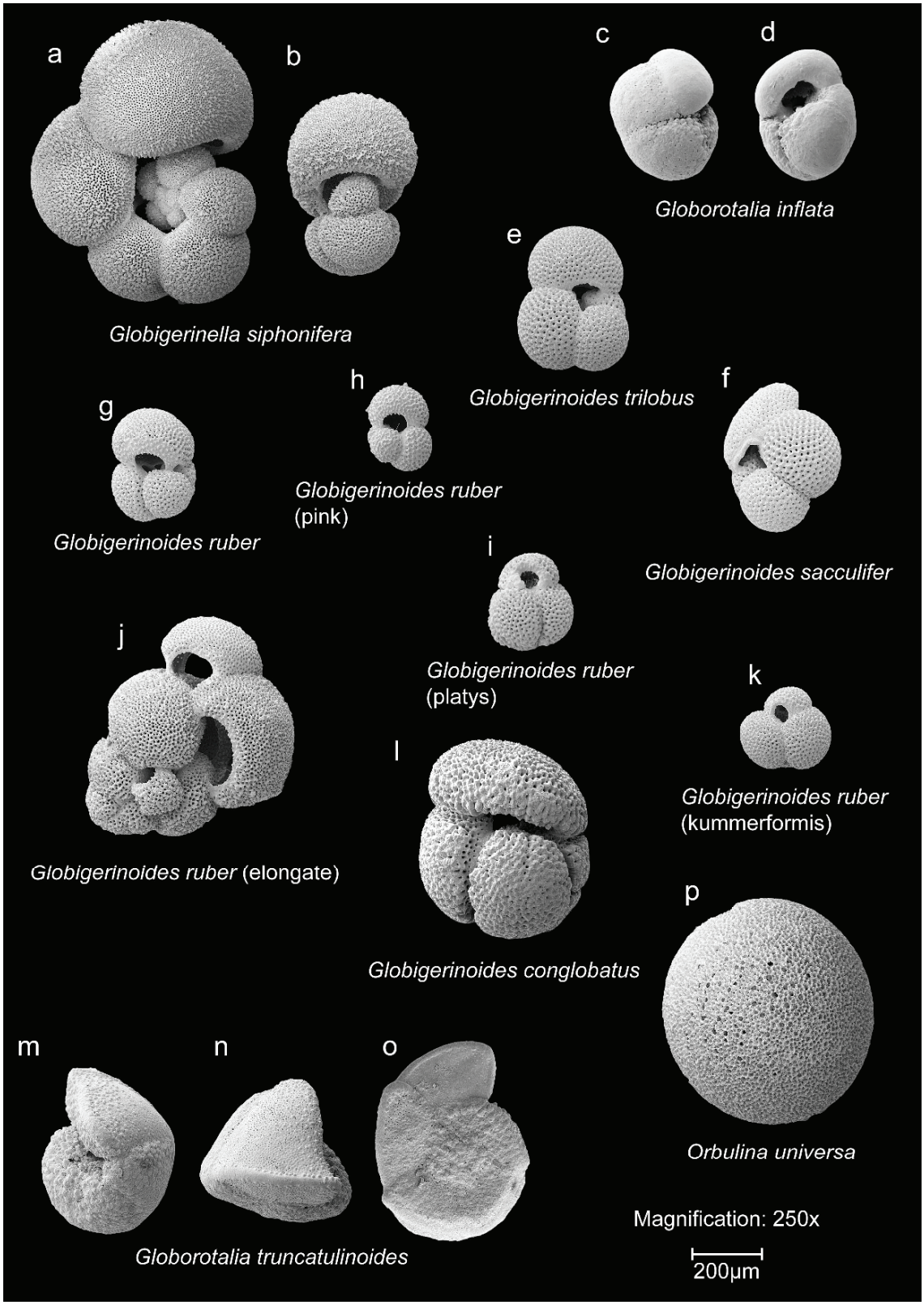

Plate 1: Planktonic foraminifera from M51-3 SL104 with respective sample depth in the sediment core. **a-b**: *Globigerinella siphonifera*, 365.2 cm, **c-d**: *Globorotalia inflata*, 453.1 cm*, **e**: *Globigerinoides trilobus*, 397.9 cm, **f**: *Globigerinoides sacculifer*, 397.9 cm, **g**: *Globigerinoides ruber* (white), 365.2 cm, **h**: *Globigerinoides ruber* (pink), 446.5 cm, **i**: *Globigerinoides ruber* (platys), 398.8 cm, **j**: *Globigerinoides ruber* (elongate), 423.1 cm, **k**: *Globigerinoides ruber* (kummerform), 388.3 cm, **l**: *Globigerinoides conglobatus*, 454.3 cm*, **m-o**: *Globorotalia truncatulinoides*, 453.1 cm*, **p**: *Orbulina universa*, 410.5 cm. (Figures with * where taken from (Koch, 2010)).

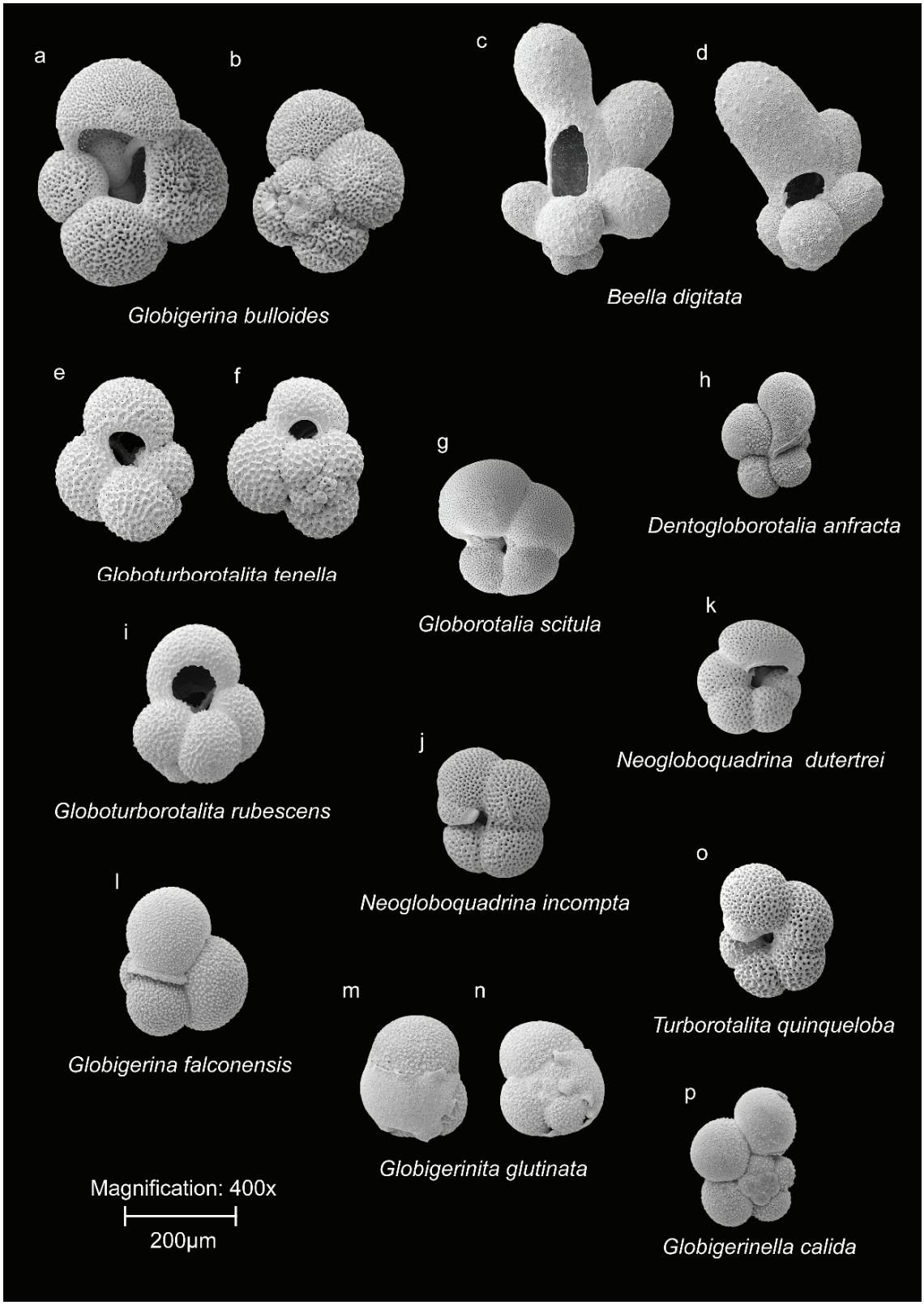

Plate 2: Planktonic foraminifera from M51-3 SL104 with respective sample depth in the sediment core. **a-b**: *Globigerina bulloides*, 403.9 cm, **c-d**: *Beella digitata* ,413.8 cm, **e-f**: *Globoturborotalita tenella*, 393.4 cm, **g**: *Globorotalia scitula*, 441,7 cm*, **h**: *Dentogloborotalia anfracta*, 441,7 cm*, **i**: *Globoturborotalita rubescens*, 365.2 cm, **j**: *Neogloboquadrina incompta*, 403.9 cm, **k**: *Neogloboquadrina dutertrei*, 365.2 cm, **l**: *Globigerina falconensis*,424.3 cm, **m-n**: *Globigerinita glutinata*, 365.2 cm, **o**: *Turborotalita quinqueloba*, 388.9 cm, **p**: *Globigerinella calida*, 369.1 cm. (Figures with * where taken from (Koch, 2010)).

3.3.3. Planktonic foraminiferal stable isotopes

With the two oxygen stable isotopes, ^{18}O and ^{16}O, a kinetic fractionation takes place during the repeated evaporation and precipitation of water and its successive transport from the lower to the higher latitudes. Hereby, the ^{18}O isotope condenses preferentially, compared to the slightly lighter ^{16}O isotope, which ultimately benefits an enrichment of light ^{16}O in polar ice masses and a successive depletion of the remaining, isotopic heavier ocean water (Ravelo and Hillaire-Marcel, 2007). Since foraminiferal tests incorporate the oxygen isotopes in equilibrium to the surrounding water, oxygen isotopy has become an important tool for climate scientists to track changes in the global ice volume (Ravelo and Hillaire-Marcel, 2007). Anyhow, also local effects play a role, especially in the isolated basin of the Mediterranean Sea; Oxygen isotopic values at depth are generally enriched by ~1.5‰ in comparison with the North Atlantic Deep Water (NADW) due to the more saline waterbody of the Mediterranean. Also cyclicities super-imposed on the 100 ka cycles have been detected, with pronounced light isotopic values to occur during sapropel formation (Vergnaud-Grazzini et al., 1977). The dominating local effects are here the evaporation and precipitation, which elevate and diminish $\delta^{18}O$. Since evaporation and precipitation result in changes in the surface salinity, the oxygen isotopy of the foraminiferal species analysis can be used as proxy for the past oceanic and atmospheric changes in the Mediterranean Sea (Ravelo and Hillaire-Marcel, 2007).

In opposite to the oxygen isotopy, the carbon isotopes ^{12}C and ^{13}C are more difficult to interpret. One point here is that the incorporation of carbon into the foraminiferal test does not take place in equilibrium to the $\delta^{13}C$ ratio of the dissolved inorganic carbon (DIC) in the surrounding water (Ravelo and Hillaire-Marcel, 2007). Further factors, influencing the $\delta^{13}C$ ratio of the dissolved inorganic carbon are for example the exchange rate of carbon between sea air and soil, internal heterogeneities in the local water body, vital effects and global as well as local variations in the sea surface productivity, whereby the individual portions are hard to distinguish (Hemleben et al., 1989). Anyhow, contrasts between sapropels and enclosing marls have been investigated in the Mediterranean and the variations were hereby explained by the ^{13}C deficiency in freshwater and by enhanced photosynthetic activity (Fontugne and Calvert, 1992).

For this study, we use *G. ruber* (white), as a surface dwelling species and *G. bulloides*, which usually inhabits slightly deeper waters (Hemleben et al., 1989), in order to track changes in $\delta^{18}O$ and $\delta^{13}C$, which can be interpreted as proxies in the hydrological regime during sapropel formation. Samples derive from the narrow fraction between 250 – 315 µm (Friedrich et al., 2006) to avoid ontogenetic effects (Ravelo and Hillaire-Marcel, 2007) and were extracted from

every 3 mm sample of a U-channel of M51-3 SL104, covering the complete sapropel and also the enclosing marls.

3.3.4. Transfer functions

Artificial neural networks (ANNs) are a branch of artificial intelligence, which are capable of learning and are here used to reconstruct past SSTs from the census data of planktonic foraminifera, providing the annual mean, as well as summer and winter seasonal temperature averages. Learning in this case means, to minimize the error between a known calibration dataset and an also known training dataset by self adjusting error minimization in multiple iterations (Malmgren and Nordlund, 1997). An ANN consists of so-called neurons, arranged in several layers, whereby the number of neurons depends on the complexity of the problem. The incoming signal is transformed by the neuron by some kind of non-linear function and handed over to the next neuron, whereby the weight between neurons is the result of the error minimization (Gardner and Dorling, 1998).

Table 4: Species list of planktonic foraminifera, being introduced into the artificial neural network. Species were either applied as they are, or as functional group (*), e. g. *G. siphonifera* and *G. calida*.

ANN Species List
O. universa
G. conglobatus
G. ruber total
G. tenella
G. sacc total
S. dehiscens
G. siphonifera + G. calida
G. bulloides
G. falconensis
B. digitata
G. rubescens
T. quinqueloba
N. pachyderma L
N. dutertrei
P/D integrade + N. pachyderma R
P. obliquiloculata
G. inflata
G. truncatulinoides total
G. crassaformis
G. hirsuta
G. scitula
G. menardii + tumida
G. glutinata

Compared to other transfer functions, which rely on k-nearest neighbour techniques (MAT, SIMMAX, RAM), the ANNs are not as dependent of the size and balance of the calibration data set (Hayes et al., 2005) and have successfully developed and applied in the Mediterranean sea to reconstruct temperature gradients throughout the complete Mediterranean during the last LGM (Hayes et al., 2005). Yet, as well as other transfer functions, potential issues emerge, since the water body in the Mediterranean during the formation of sapropels could represent a non-analogue situation compared to the present day. Hence, Rohling et al. (2004) have shown that most species of planktonic foraminifera seem to have a stable habitat, which allows for a successful application of ANN transfer function during sapropel formation. Here, percentages of planktonic foraminifera were either used alone or grouped to functional types (Table 4) and used as input vectors. Notably, not all species of planktonic foraminifera being detected in the here presented material were introduced to the ANN. Other species, necessary for the input vectors, which have not been found in our material, were instead surrogated by zeros.

The so created dataset is then applied ten times to the ANN, resulting in ten slightly different temperature curves, for the annual average, the summer and the winter season. We here use the average of the ten results and add or subtract the standard deviation, which itself comprises 0.6°C by average, to result in an upper and lower temperature limit. The size of the standard deviation in one sample depends on the comparability of the census data and the training data set, where the temperature is known. We here use the ANN to visualize strong contrasts or trends in the SSTs, which then can be further related to other environmental parameters and blend into a conclusive environmental model during sapropel formation.

3.4 Data analysis

As described in the subsections of the previous chapter, a large amount of data is generated by numerous methods, whose resolutions range from the millimetre to the sub-millimetre scale, and also slightly vary in their vertical coverage of the gravity cores (e.g., depending on the extent of horizontal integration and on the varying vertical resolution of each sensor). In order to maximize the explanatory power of the gained data, it thus became necessary to pre-process the data, prior to the very analysis and interpretation. First, the measured series were aligned within each core to achieve maximum fit, which is especially important where the sapropel extended over two core sections, which had to be merged together. The alignment was guided by changes in sediment properties at the onset and the end of the sapropel deposition, as well as pronounced layers and rare, unique events of bioturbation, which could be easily recognized in the scanned picture, the XRF-measurements or the natural water content. Second, the spatial resolution of measurements of lightness (50 µm) were reduced by linear interpolation by a factor of four, when processed together with XRF-scanning data (spatial resolution 200 µm), to meet the requirements of the multivariate analyses, which depend on datasets of the same size. The same accounts for analyses, where measurements of lightness and XRF scan data meet the data from discrete samples, such as water content, magnetic susceptibility, census data of planktonic foraminifera and varve counts. Third, due to a model curve, being fitted and subtracted from the XRF measurement during scanning, the element Ti occasionally features negative values, which is problematic, when forming a ratio with Al. In this case each value of Al and Ti was increased by absolute value plus one of the minimum of Ti.

After carrying out the necessary pre-processing of the data, we rely on a number of uni- and multivariate methods of data analysis as implemented in the free software PAST. These methods allow for efficient analyses and structuring of large amounts of data by extracting and visualizing inherent patterns and are described in detail in the following sub section of this chapter. In order to underline the general high optical and chemical correlation of the S_5 interval between the three gravity cores, a common depth scale, which orients on the thickest of the three sapropels (M40-4 SL67) was established. In this way, the study profits from more uniform descriptions and diagrams, which better underline the mutuality between the different gravity cores.

The S_5 sapropel interval as well as the enclosing marls in the archive half of M40-4 SL67 had already been sampled prior to this study, which left conspicuous holes in the centre of the cores surface. Unfortunately, this issue strongly affects the measurements of sediment colour and the XRF scans. While the extraction of colour and lightness values in the software of the DMT core

scanner is based on an automatic integration over a certain width, here, after the scanning, it is possible to manually extract narrower bands from the digital image. Specifically, we averaged five selected traces (each 1px width), which have been placed next to the sampling holes and provide an uninterrupted track of sediment lightness. A similar procedure is not possible for the elemental abundances of the XRF scans, which lets us to exclude M40-4 SL67 from the analysis where elemental XRF abundances are involved.

3.4.1. Principal component analysis

The principal component analysis (PCA) is used to reduce the dimensionality of large datasets (matrixes), where each sample features more than one attribute. Hereby, the original, measured variables become converted by linear combination into a set of derived variables, the so-called principal components (PC) (Wold et al., 1987; Jolliffe, 2005). The useful reduction of variables is possible when some of the variables are redundant and show a certain amount of correlation to each other, and thus can be replaced by one new, artificial variable (the PC). After the calculation of the PCs for each sample, PC1 and PC2, which join the majority of variance of the whole dataset, can be plotted against each other (Figure 14). This allows the interpretation of each sample in relation to the other samples of the dataset, and the identification of distinct groups or trends (Q-Mode analysis). Next to the individual samples, also the relationship of variables to each other can be analysed, either on a more qualitative base by looking at the direction and length of each variables vector (R-mode analysis) or more quantitatively by looking at the weight of the original variables with which they contribute to the PCs. This allows the interpretation of the dataset in terms of the original variables instead of the abstract and artificial PCs. PCA can be performed either on base of the co-variance matrix or the correlation matrix. The co-variance matrix is used when the variables that are applied to the PCA are measured on the same scale. The use of the correlation matrix contains a second step, where the variables are referred to the variance and is mostly used when the variables were measured on different scales (such as length, weight, area, ratios etc.) (Leyer and Wesche, 2007).

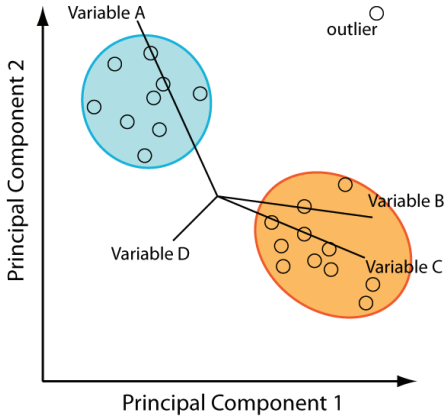

Figure 14: Schematic illustration of a PCA with two defined groups of samples and one outlier. Variable B and C are correlated to each other and anti correlated to variable A. Variable D does not show a defined correlation to the variables A, B and C. (Modified after Leyer and Wesche, 2007).

In this work, we apply the PCA on XRF scan data of the sapropel, whereby we use the correlation matrix, since the XRF scan data of individual elements differ in scale in the order of magnitudes.

In this way, we use the Q-Mode PCA to visualize changes in the basic chemical regime throughout the complete length of the sapropel, whereby the optical defined subunits are highlighted in terms of colour. R-Mode PCA is instead used to investigate and compare individual zones and to identify correlating and anti-correlating elements in these zones.

3.4.2. Cluster analysis

Cluster analysis is a method of agglomerative classification, which seeks to find similarities in samples of high-dimensional data sets. In opposite to divisive clustering, the agglomerative approach starts with the formation of a cluster of the two most similar objects. During the following steps, samples or clusters are added in the order of decreasing similarity (Hammer and Harper, 2006). The result is a hierarchical tree diagram, in which the end-members of the branches represent the samples and the length of the branches represents the distance of the samples to each other (Leyer and Wesche, 2007). The cluster analysis can be conducted with a multitude of combinations of algorithms and measurements of distance and is suited for presence and absence data as well as nominal measured data (Leyer and Wesche, 2007).

Similar to the PCA, we apply the cluster analysis to investigate chemical abundances from high resolution XRF-scanning data along the sapropel and the enclosing marls, whereby the cluster analysis is used in a constrained way, which respects the stratigraphic position of measurements. While the PCA visualizes trends and provides information about the degree of correlation of elements, the cluster analysis is more adopted to give proof of a previously performed division of the cores into a set of optically defined subgroups.

For this study, we use the paired group algorithm, which joins the clusters on the based on the average distance of all members in the two groups and is suggested for ecological data (Hammer and Harper, 2006). As a measure of distance the Euclidean distance is used, which is the geometric distance in the multidimensional space (Hammer and Harper, 2006).

3.4.3. Detrended correspondence analysis

The detrended correspondence analysis (DCA) poses an advancement over the normal correspondence analysis (CA) and today poses the most popular method of indirect gradient analysis. Generally the CA and the DCA themselves are not dissimilar to the PCA but were especially designed for ecological problems and assume an unimodal arrangement of species, with an optimum around a certain environmental parameter (Leyer and Wesche, 2007). The normal CA has its issues with compression effects at the end of the ordination axis and also arch effects, where the primary ordination axis of the analyzed dataset is present on the first and the second axis. These issues are faced by the DCA by rescaling and detrending of the dataset.

Specifically, rescaling in this case means, that the variance of the sample and taxon scores are standardized so that their variance is equal to one and ultimately diminishes the edge effect. For the detrending, the first axis is subdivided into a number of segments of equal length. The ordination scores of the second axis in each segment are then normalized by subtracting the average score within this segment (Hammer and Harper, 2006; Leyer and Wesche, 2007).

For this study we apply the DCA to the census data of planktonic foraminifera for two purposes. First, we wish to identify species, which behave similar in their pattern of increasing and decreasing abundances throughout the formation of the sapropel. Second, on base of the individual species we visualize the differences of the community of planktonic foraminifera throughout the formation of the sapropel, potentially as a reaction to environmental parameters.

3.4.4. Pearson's correlation coefficient

The correlation coefficient after Pearson, given with r (between -1 and 1), is a measure of the strength of a relation between two variables, although a causal link between both variables is not necessary and not established by Pearson correlation. Described graphically, both variables are plotted against each other in a coordinate plane and a regression line is laid into the point cloud. The proximity of the data points to the regression line stands for the strength of linkage between both variables and is calculated as follows:

$$r = \sum_{i=1}^{n} (x_i - \bar{x})(y_i - \bar{y}) / \sqrt{\sum_{i=1}^{n} (x_i - \bar{x})^2 \sum_{i=1}^{n} (y_i - \bar{y})^2}$$

Pearson's correlation coefficient is always between -1 (perfect anticorrelation) and 1 (perfect correlation). Values close to 0 instead indicate, that there is no linear relationship between both observed variables (Hammer and Harper, 2006; Leyer and Wesche, 2007).

We use Pearson's correlation coefficient to investigate the linkage between the visible sediment fabric, the layering of the sapropel, which is expressed by measurements of sediment lightness and the XRF-scan data of the different elements (see chapter 3.2.1). Specifically, r is calculated individually for each element in each previously defined sub unit of the sapropel, which allows to track changes in the quality of correlation throughout the sapropel and in opposite to the more advanced multivariate methods provides a clear and easy accessible overview of the behaviour of each element in each zone.

3.5 Time series analysis/ Wavelet analysis

Wavelet analysis is a branch of the time series analysis and transforms measured data into the frequency space in order to extract information from a dataset, that otherwise would not have been apparent in a time-amplitude plot. The classical approach of time series analysis is the Fourier-Transformation, which decomposes a signal into a set of sinus and cosine-waves of infinite length. This brings several disadvantages during the analysis of geological data, such as the fact that local characteristics of a time series are not taken into account (Wengert, 2002). Here, the wavelet analysis uses so-called wavelets, which are characterized by a finite lengths and smooth ends, which approach to zero (Trauth, 2007). Due to the flexible adaptation of the wavelets in terms of frequency and time, this method allows to bypass effectively the disadvantages of the classical spectral analysis and allows a detailed investigation of changes in the time-frequency domain (Wengert, 2002; Trauth, 2007) (Figure 15). Adjusting the Morlet Factor ω_0 (Standard value 6, Figure 15b), allows to customize the resolution of time and frequency. Here, increasing ω_0 increases the accuracy of the frequency but lowers the temporal resolution. Lower values of ω_0 instead increase the temporal resolution by lacking of the frequencies accuracy (Wengert, 2002). Wavelet analysis is based on a Fourier Transformation, which assumes an infinite and cyclic character of the time series. Due to the actual finite length of the time series, edge effects at the beginning and the end of the time series occur and here lead to a weakening of the signals amplitude and are indicated in the wavelet plot by the cone of influence (Torrence and Compo, 1998). First order trends are a common feature in time series derived from geological measurements and are identified by the algorithm as low frequency signals with high amplitudes, which often overhaul the higher frequency signals of interest (Hasselmann, 1976). To overcome this issue, a high pass filter with a defined cut-off frequency (~360 years), which is below the longest expected signal to be found in the investigated dataset, is applied to the time series prior to analysis. To accommodate for the fact that signals with higher frequencies bear lower amplitudes in geological derived time series, a red noise spectrum, which gradually

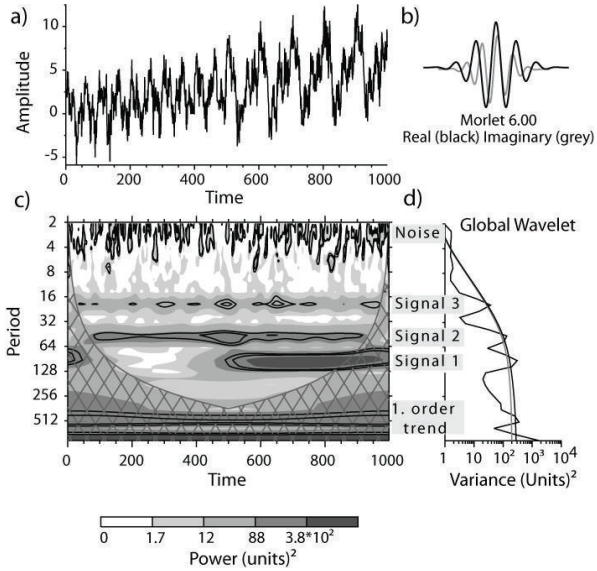

Figure 15: **a)** Time-Amplitude plot with three superimposed signals, a first order trend and noise. **b)** Morlet-wavelet with a parameter of 6. **c)** Corresponding wavelet transformation of the time amplitude-plot with red-noise spectrum of 80% and 90% of significance. Apparently, the signal with the lowest frequency first occurs at a time of 500. **d)** Global wavelet showing the three signals, the first-order trend and high frequency noise, which peak above the 80% and 90% of significance, given by the red noise-spectrum.

decreases in amplitude with increasing frequency, acts as a null hypothesis for the significance of identified signals (Hasselmann, 1976).

In this study we use wavelet analysis as implemented in the free online ION-Wavelet script (Torrence and Compo, 1998, http://ion.researchsystems.com/IONScript/wavelet/) to detect cyclicities in XRF elemental abundances, as well as $\delta^{18}O$ isotopic measurements from *G. ruber* and the juvenile indices of *G. ruber* and *G. siphonifera*. Although it is possible to analyze raw, unevenly spaced data, a proper time-series analysis requires boundary conditions. Here, the total age of the investigated interval should be known in order to allocate potential, significant signals to a certain frequency. Secondly, changes in the sedimentation rate should be known, since otherwise, the algorithm allocates different frequencies to the same signal at different positions in the time-series, which can lead to wrong interpretations. Here, event based stratigraphy (Cane et al., 2002) helped to identify a strong change in the sedimentation rate. Minor changes in the sedimentation rate, as well as a direct assessment of the age of the sapropel were provided by the census of the sub-millimetre thin lamination of the sapropel. These information about the total age and major and minor shifts in the sedimentation rate were used to transform series of measurements with equally spatial resolution into data series with an even temporal spacing of 2 years (XRF-Data) and 20 years (discrete samples).

3.6 Sediment micro fabric analysis

For an effective assessment of the number of laminae within the here presented sapropel interval, as well as the analysis of the substructure of single laminae, it is necessary to rely on more sophisticated methods than photographic images of the archive section alone. Instead, we here use fluid displacive resin impregnation as established by Pike and Kemp (1996) to preserve the sapropel in M51-3 SL104 and parts of the enclosing marls in thin sections, allowing for a more accurate and detailed analysis.

3.6.1. Preparation

Extraction of sediment from the working half of M51-3 SL104 is performed with a double L-channel (Figure 16a), which bears several advantages compared to a more common U-channel. For example, after extraction of sediment, the outer L-Frame can be detached and allows for an easier access to the extracted sediment. In this way, the sediment experiences less shearing stress during cutting and the further extraction of bits of sediment (Figure 16b).

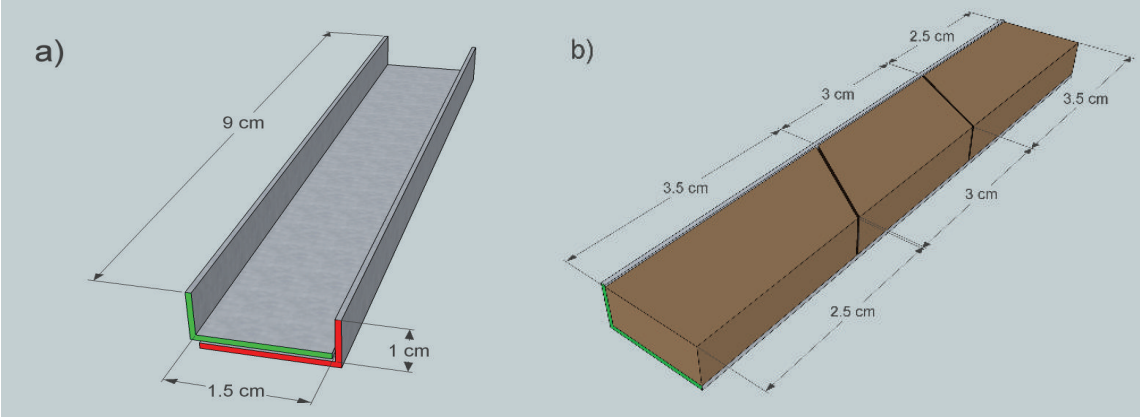

Figure 16: **a)** Illustration of the two L-shaped metal frames (outer frame highlighted red, inner frame highlighted green), put together to form a U-channel. **b)** Illustration of a single L-shaped frame filled with sediment after extraction from the archive half of the sediment core. The diagonal manner of the further subdivision is illustrated.

The two L-shaped metal frames are put together and the construct is then pressed into the sediment with the sidewalls facing down towards the sediment. A wire sling, pulled beneath the double L-channel, cuts the sediment out of the working half of the core. Following this approach, the complete sapropel and several centimetres of enclosing marl are sampled, whereby 1 cm of overlap (Figure 17) is included between each interval to provide a backup against loss of sediment during the following steps of preparation.

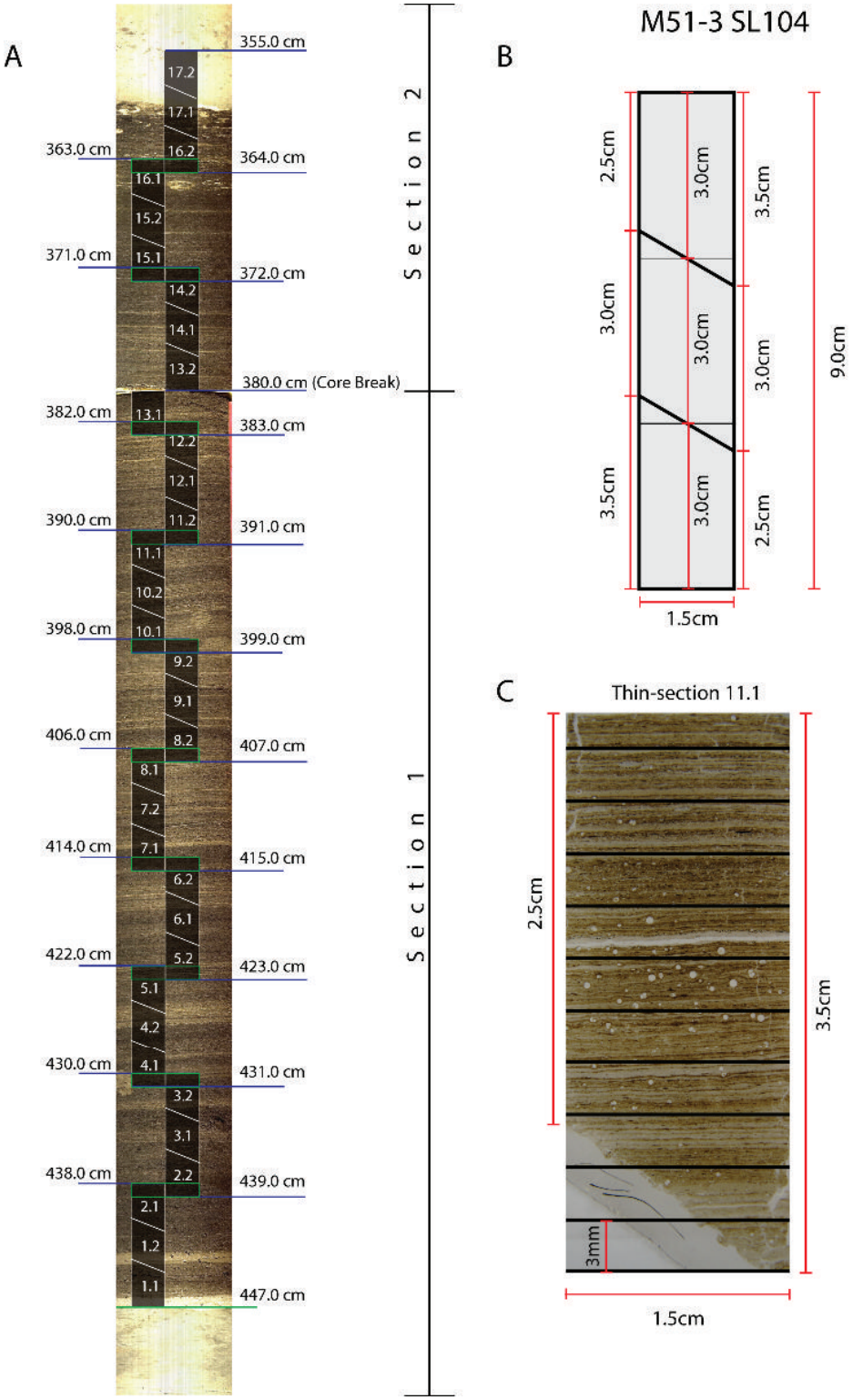

Figure 17: **A:** Sampling scheme from M51-3 SL104 for the resin impregnated thin sections. Double L-Frames with a length of 9 cm were used to extract stripes of sediment. Sampling was performed with 1 cm overlap to the next stripe. The numbering of the individual bits follows the plastic boxes, in which the actual resin-impregnation was performed, whereas each box contained two bits of sediment. **B:** Each 9 cm section was further cut in three smaller bits in a diagonal manner for providing a sufficient overlap. **C:** Illustration of the subdivision of a ready prepared thin-section into intervals of 3 mm width, being conform to the samples from the U-channels.

After extraction from the sediment core, each 9 cm interval is further subdivided into three smaller bits in a diagonal manner (Figure 16B, Figure 17B), which again is to provide redundancy against loss during the following steps of preparation. The single bits are placed onto perforated tinfoil, which is wrapped up on the sides to maintain the integrity of the wet and unconsolidated sediment. The so prepared sediment bits are then placed into acetone resistant plastic boxes. Summarized, we resulted in a set of 34 bits of sediment, and 17 boxes, since each box bears enough space for two bits, which lowers the amount of chemicals significantly as well as the time, that is needed to perform the exchange of each batch of chemicals. Each of the boxes is numbered and labelled with an arrow, helping to correctly orientate the sediment bits.

Table 5: Proportions of resin and acetone as well as the number of repetitions during each step of the fluid displacive resin impregnation method.

Step	Ratio: resin to acetone	n iterations
1	Pure Acetone	12
2	3 Resin: 2 Acteone	3
3	11 Resin: 4 Acetone	2
4	13 Resin: 2 Acetone	2
5	Pure Resin	3

The chemical treatment is performed with acetone (Analytical grade 99.9%) in a first step, followed by a mixture of resin and acetone, whereby the amount of resin is increased stepwise (Steps 2 – 4) and finally results in pure resin (Step 5)(Table 5). Acetone is an effective agent to remove water out of the pore space of the samples and is exchanged three times a day for the length of four days (overall 12 times) (See Table 5, Step 1). The addition of acetone is carried with a wash bottle, whereby the acetone is added gently on the side of each box, until the samples are completely covered. Single use dropping glasses are used to draw away the acetone in the same gentle manner. The resin, produced by TAAB (http://www.taab.co.uk/), is a low viscosity resin and poses the less poisonous successor of the Spurr resin and itself consists of three components (TAAB low viscosity (TLV) resin, TLV hardener VH2 and TLV accelerator) in a defined mixture (100g of ready mixed resin contain 48g of TLV resin, 52g of VH2 hardener and 2.5 ml of accelerator). The necessary amount of resin is prepared newly prior to each batch and mixed with the correct amount of acetone (Table 5). The addition of the mixture is carried out with single use dropping glasses until the sample is completely covered. Similar to the acetone, also the mixture is added on the side of each box, so the chemicals can enter the sediment from below through the perforated tin foil, which prevents air from being trapped in the pore volume of the sediment and allows the air to exit the sediment bits upwardly. This procedure is repeated twice a day for the length of five days, whereby the portion of resin is increased stepwise (See

Table 5, Steps 2 – 4) and results in pure resin in the last three batches (See Table 5, Step 5). The resin needs to harden for four weeks, after which the solid blocks of resin can be sawed into appropriate size, fixed on a sample slides (48 mm * 28 mm) and further grinded down to a thickness of about 30 – 40 µm.

3.6.2. Counting of varves

The ready prepared thin-sections were photographed with transmitted light and stitched together at the computer to provide a continuous record of the entire S_5 sapropel. Alignment of the individual images was provided by the overlap of each bit of sediment to the predecessor as well as the successor (Figure 17). Where observable, we followed the concept of Pearce et al. (1998) and counted lamina couplets, which represent one year and consist of one bright, almost mono specific summer lamina and one dark winter lamina with a more mixed species assemblage (Figure 9, Figure 39).

The continuous photographic record of the sapropel by the thin-sections was subdivided into 3 mm intervals, which correspond to the intervals of the discrete samples from the U-channels of M51-3 SL104 (Figure 17C), on which the analysis of the water content, the magnetic susceptibility and census counts of planktonic foraminifera is based, and in this way enhances the comparability and uniformity between the different sets of data. Consequently the number of laminae couplets (years) was determined individually in each 3 mm interval, which allows for a detailed and small scaled investigation of changes in the sedimentation rate throughout the entire sapropel interval. Assuming a duration of one year per lamina couplet, the calculation of the sedimentation rate for each 3 mm interval follows the equation: $sedimentation\ rate\ in\ cm/yr = 1/((n/3)\times 10)$, where *n* is the number of counted varves in one 3 mm interval.

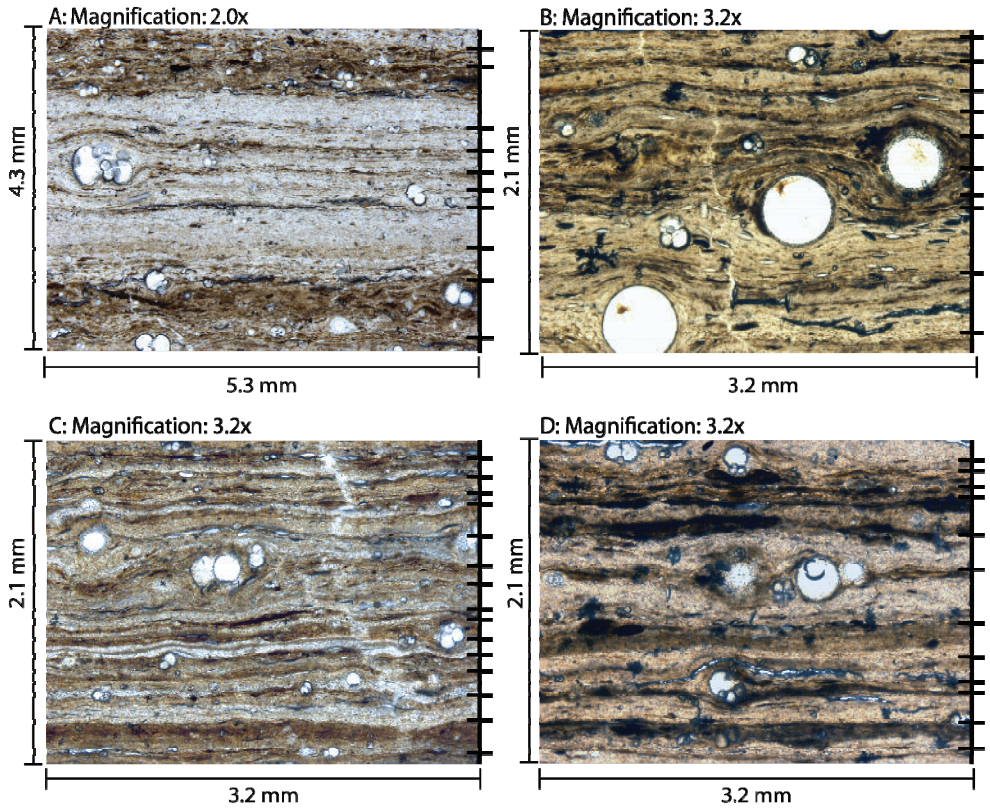

Figure 18: Different outcrops of thin sections from different positions in M51-3 SL104, which illustrate the optical variations in the laminae couplets, concerning their colour intensity, thickness and contrast to the adjacent laminae. Next to each image, bars are placed at the top of each dark (winter) laminae.

As Figure 18 shows, the lamination in the here investigated S_5 sapropel interval features a significant amount of visual variability. The main differences here affect the thickness of individual bright and dark laminae, their colour saturation and the contrast to the adjacent laminae above and below. Variations in the sediment colour also vary between the thin sections, which here is mostly due to variations in the thickness of the thin-sections themselves, which were grinded by hand to an appropriate thickness (Figure 18B for example must be thicker by several µms, since it appears more yellowish, compared to Figure 18A, C and D, which appear more neutral). The described optical variations make it more difficult to count the laminae-couplets, since very faint or thin laminae might get ignored unintended. To overcome this issue, redundancy was assured by a six-fold census of the laminae-couplets. Here the first four counts represent a training curve, during which the numbers of recognized laminae increases until a stable plateau is reached in the following iterations five and six.

4 Results

4.1 Thickness of S_5 sapropels in the Eastern Mediterranean

In the past decades, the sapropel S_5 has been the subject of numerous studies. However, the basic characteristics of individual S_5 horizons (e.g. thickness, water depth and average sedimentation rate) have not yet been compiled. Here, we complemented literature data with own observations in unpublished sediment cores from Meteor cruises M40-4 and M51-3 (Hieke et al., 1999; Hemleben et al., 2003) to generate a database with 39 records of S_5 horizons (Figure 19, Table 6).

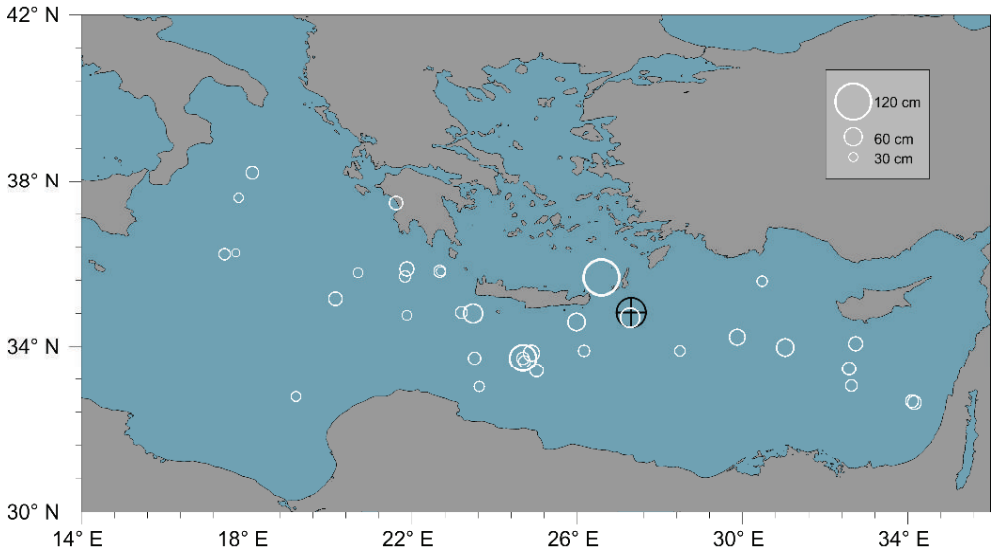

Figure 19: Geographic position of the here investigated gravity cores and distribution of the thickness of sapropel S_5 in Eastern Mediterranean sediments (For further detail, see Table 6). Crossed black circle indicates the position of S_5 sapropels, being investigated in this study (Figure 10, Table 2). Modified after Moller et al. (2011a).

The data reveal that the thicknesses of the majority of the sapropel S_5 horizons varies very little (23.5 cm ± 12 cm), irrespective of water depths (ranging from 930 – 4270 m), sedimentary environment (tectonically active regions and trenches, mud diapirism and deep basins) and proximity to the continental margin (Figure 20). Five sapropel horizons stand out of this pattern by showing a thickness greater than 50 cm. The thickest S_5 horizon (120 cm) was observed in core LC21 (Marino et al., 2007). This core derives from the Aegean Sea and the sapropel shows intermittent lamination. The position of the S_5 sapropel in this core indicates the highest sedimentation rate at this location, which could have contributed to the anomalous thickness of the sapropel. The 82 cm S_5 sapropel in ODP Hole 971C is also conspicuously thick and similarly to our material was formed under a diatomitic regime, but is interrupted by turbidite layers (0.5 – 12 cm) and thin beds, interpreted as re-deposited exudates of the nearby Napoli mud volcano (Cane et al., 2002); the thickness of the same sapropel in the nearby Hole 971A is only 22.8 cm (Table 6).

Table 6: Thickness and position of known S_5 sapropel layers: [1] Weldeab et al. (2003b), [2] Cane et al. (2002), [3] Marino et al. (2007), [4] Calvert et al. (1992); Struck et al. (2001), [5] Parker (1958), [6] Cita et al. (1977), [7] Giunta et al. (2006); Morigi (2009), [8] Gourgiotis (2004); Triantaphyllou et al. (2009), [9] (This study).

Core No.	Author Code	Latitude (dec)	Longitude (dec)	Thickness of S5 (cm)	Depth in sediment (cm)	Water depth (m)
KL83	1	32.6242	34.1581	27.5	390	1431
ODP 969E		33.8461	24.8939	37.5	318.75	2212
SL71		34.8186	23.2008	20	260	2827
KS205	2	38.2072	18.1344	23.5	482.5	2384
ODP 971A		33.7167	24.6833	22.8	40.2	2026
ODP 967C		34.0742	32.7314	28.5	74.5	2554
ODP 971C		33.7167	24.6833	82	80	2141
LC21	3	35.6667	26.5833	120	885	1522
KC01B	4	36.2569	17.7428	4	876	3643
Site 969		34.2333	29.8667	36	366	2400
Site 967		34.0742	32.7314	28	74	2550
MD 84641		33.0333	32.6333	18.5	371.5	1375
ALB 198	5	36.2167	17.4667	17.5	670	3555
ALB 197		35.7833	20.7000	10.7	443	2940
ALB 196		35.6833	21.8333	17.5	536	4270
ALB 195		35.8667	21.8833	28.6	393	3665
ALB 194		34.8000	23.4833	50	485	3000
ALB 192		34.6000	25.9833	42.9	557	2680
ALB 190		33.9000	26.1667	17.5	329	2900
ALB 189		33.9000	28.4833	14.3	336	2664
ALB 187		33.9833	31.0333	42.9	600	2500
RC9-181	6	33.4167	25.0167	26.6	226	2286
RC9-185		37.4500	21.6167	26.6	234	2858
KS09		35.1500	20.1500	26.6	213	2900
SIN97-GC01	7	35.8169	22.7011	7	285	933
BAN89-GC09		33.6439	24.7247	19.8	234.25	2011
BD02-GC01		37.5750	17.8089	9	329	2470
ADE3-23 8	8	34.7500	21.8800	10.5	225.5	2459
M40-4 SL67	9	34.8236	27.3044	91.4	364	2157
M40/4 68SL		34.6931	27.2739	52	398	2121
M40/4 75SL		35.8175	22.6728	20	350	1012
M51/3 SL96		32.7794	19.1961	11.5	225.5	1390
M51/3 SL98		33.7186	23.5097	22	251	1879
M51/3 SL99		33.0103	23.6336	13	252	1496
M51-3 SL103		34.8206	27.2861	85.1	375.5	2154
M51-3 SL104		34.8247	27.2925	86.8	359.5	2155
M51/3 SL110		32.6575	34.1050	24	601	1437
M51/3 SLF107		33.4536	32.5822	27	335.5	1296
M51/3 SL120		35.5781	30.4683	14	445	1275

The most extensive fully laminated S_5 sapropel horizons deposited under a normal sedimentary regime all derive from the same region of the Pliny Trench. These S_5 sections are not expanded because of higher sedimentation rates. This is clearly visible in Figure 20, which demonstrates that there is no relationship between sedimentation rate (here approximated by the depth of the S_5 horizon in each core) and the water depth on the one hand and the thickness of the expanded Pliny Trench S_5 sapropels on the other hand. Depth below sediment surface for the majority of the 39 S_5 sapropels varies between 2 and 9 metres (cores with S_5 depth below 1 m are here interpreted as disturbed), indicating mean sedimentation rates varying by a factor of four. The

exceptionally thick Pliny Trench S_5 sapropels all derive from the mid-range of the presumed sedimentation rates (Figure 20).

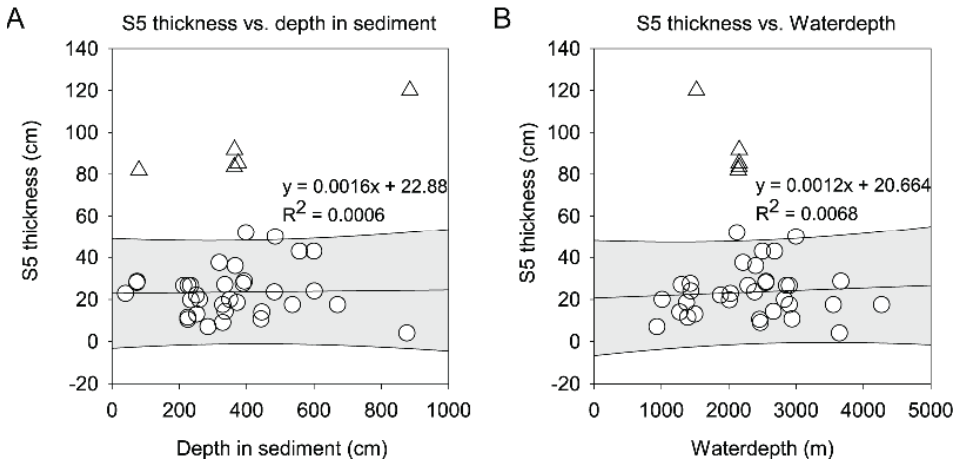

Figure 20: Relationship between S_5 sapropel thickness (Figure 19, Table 6) and **A)** depth below sediment surface and **B)** water depth. Triangles indicate S_5 sapropels thicker than 60 cm. The low correlation and flat regression lines for the rest of the sapropels indicate that their thickness is not related neither to water depth, nor to the average sedimentation rate (approximated by depth below sediment surface). Grey shaded area shows 95% prediction intervals. (Figure from Moller et al. (2011a)).

4.2 Lithostratigraphy of the studied S_5 horizons

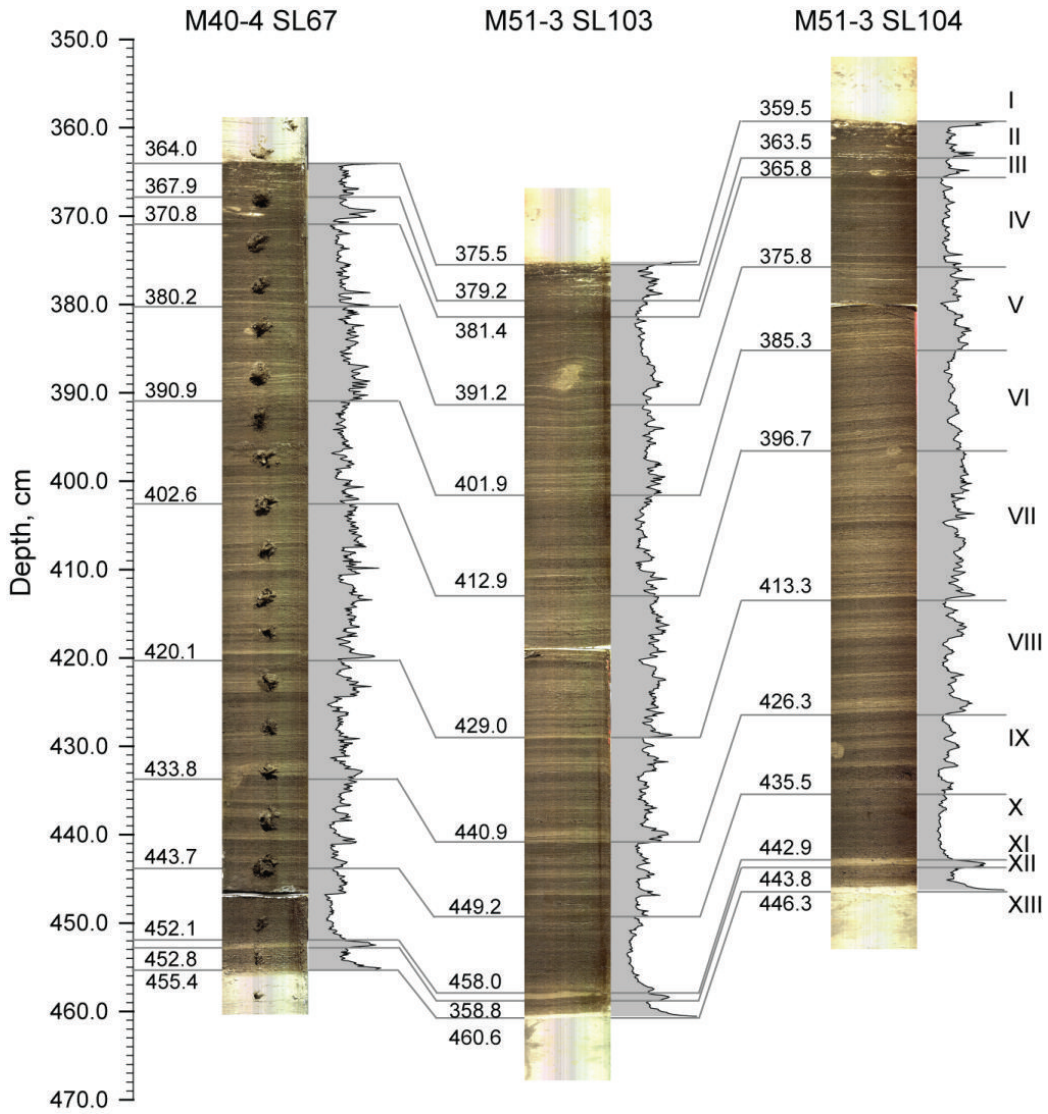

Figure 21: Photographic images of sections one and two of the three sediment cores M40-4 SL67, M51-3 SL103 and M51-3 SL104 containing the S_5 sapropel. Additionally, the curve with measurements of sediment-lightness is added on the right side of each core to highlight their similarities and to pronounce the layering within the sapropel. The position of each subunit is highlighted with grey lines and correlated between the cores and further complemented by their very depths in each core. (The photographic images experienced enhancement by adjusting the histogram to enrich the images contrasts). (Modified after Moller et al. (2011a)).

Overall, the here investigated sapropel is characterized by a complex lithostratigraphic structure with two levels of hierarchy. On the one hand, a macroscopic layering of alternating darker and brighter beds is visible (Figure 21), whereby the thickness of single layers ranges from several millimetres to more than one centimetre. On the other hand, especially within the brighter layers a subordinated level of hierarchy becomes apparent. There, a finer lamination, with alternating brighter and darker millimetre to sub-millimetre thin laminae, can be spotted with the bare eye. This impression is affirmed by the microscopic investigation of the resin

impregnated thin sections (Figure 22, Figure 18), which were prepared for the complete sapropel section and the enclosing marls in M51-3 SL104. Following the model of Pearce et al. (1998), the here visible couplets of bright and dark laminae reflect the seasonal flux of either diatom mats (bright) or a mixed assemblage of clastic material and microfossils (dark). The balance of thickness, contrast and colour intensity between dark and bright laminae can strongly vary (Figure 18). Furthermore, it seems that it is this differential character of the lamination, which creates the macroscopic impression of darker and brighter cm-scale layers. Subsequently, bright layers are more dominated by well developed bright laminae (Figure 22), whereas in the darker layers, dark laminae dominate over bright laminae, periodically up to a degree where bright laminae are not noticeable any more.

Due to the irregular pattern in the macroscopic layering (Figure 21), it seemed reasonable to classify the sapropel and the enclosing marls into a number of subunits on an optical base and we resulted in a total of thirteen zones (Figure 21). The following description is nearly identical in all three cores and refers to Figure 21, which shows sapropel S_5 in all three cores together with the depths of the defined subunits as well as curves of measurements of brightness.

Figure 22: Photographic image of thin section 4.2 (428 – 424.6 cm). The highlight here lies on the brighter intervals at the top and the base of the thin section and, the darker interval in the centre as a result of the differential character of the annual lamination.

Due to its dark colour, the S_5 sapropel horizon in the investigated cores shows a strong contrast to the surrounding bright marls (Lithostratigraphic Zones I and XIII). The onset (Zone XII) of the sapropel is marked by a stepwise change of colour, from a Greyish Yellow (Munsell Colour Chart, 1995) 5Y 8/4)) over Dark Greenish Gray (5G 4/1) to Olive Gray (5Y 3/2) within 3 cm. The sapropel is then abruptly interrupted by a clayey, homogenous layer (Zone XI), which is 0.6 – 0.9 cm thick and Pale Olive (10Y 6/2) and suggests a unique depositional origin. The following 17 cm (Zone X and IX) are built up by alternation of darker (Olive Gray (5Y 3/2) to Greenish Black (5YG/ 2/1)) and brighter layers (Light Olive Gray, 5Y 5/2), ranging between 5 to 15 mm. Within zone X, the alternation is faint, but becomes more pronounced in zone IX, which is mainly caused by more pronounced bright layers and the laminae therein (Yellowish Gray; 5Y 7/2 and 5Y 8/1).

Subunit VIII features a contrast rich, cm-thick layering, whereas the dark layers appear more homogenous (Olive Gray; 5Y 3/2) and the brighter layers again feature a finer lamination that can be spotted macroscopically (Yellowish Gray 5Y 7/2 and 5Y 8/1). Zone VII is generally bright (Light Olive Gray (5Y 6/1) to Olive Gray (5Y 4/1)) and features a subordinated lamination in the sub-mm scale. Furthermore, the base of zone VII features a prominent bright layer, the middle of zone VII a prominent dark episode. The overall impression of subunit VI is darker than VII and V. A layering (Light Olive Gray; (5Y 5/2) to Olive Gray (5Y 3/2) and Greenish Black (5GY 4/1)) is especially visible at the base of zone VI but looses its contrast upwards and fades into a more homogenous dark. In favour of a fine lamination, the overall impression of subunit V is bright and a cm-thick layering is visible. The uppermost section without bioturbation (Zone IV) spans about 12 cm. Defined bright (Light Olive Gray; (5Y 5/2) and dark beds (Olive Gray (5y 3/2)) are visible, whereby the dark layers are constantly thicker than the bright layers.

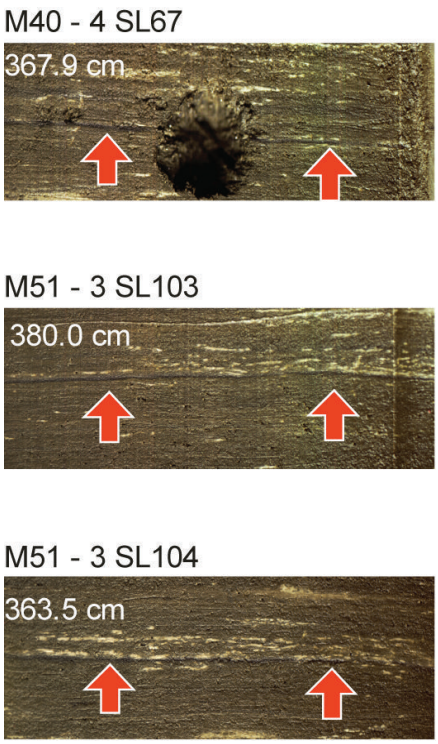

Figure 23: The corresponding section of the S_5 sapropel layer in the three investigated cores showing the position of the tephra layer (arrows) with their exact depths. A sampling hole in the archive half is visible in the M40-4 SL67 sapropel. (From Moller et al., 2011a)

The top 6 cm (Zone III and II) of the here presented sapropel are characterized by bioturbation. The degree of the bioturbation gradually increases towards the overlying marl and is also preferentially oriented parallel to the original lamination of the sediment, which is still visible in this section. Within this bioturbated episode a distinct ~ 1 mm thin layer is clearly visible in all the three cores (Figure 23) and separates zones III and II. This pronounced, dark-grey to black layer provides an additional tie point in the correlation scheme. The transition from the sapropel to the overlying marl (Zone I) is formed by a wavy, indistinct fringe of Pale Greenish Yellow colour (10Y 82).

This broad congruence of the lamination pattern at different scales in the Pliny Trench S_5 sapropels is therefore assumed to reflect a response of the sedimentary system to the same basin-wide environmental changes.

4.3 Sediment physical properties

Variations in water content and magnetic susceptibility in the two best-preserved cores are shown in Figure 24. In both cores, the sapropel horizon is marked by elevated water content and is remarkably similar in both cores, even in the bioturbated top centimetres. The water content increases from about 40% in the enclosing marls to an average of about 75% in the sapropel, peaking at 80%. This means, that the weight of the water exceeds the weight of the dry sediment by a factor of up to four and implies porosities in excess of 80%. In core M51-3 SL104, sapropel S_5 exhibits two intervals with substantially lower water content, which cannot be correlated to core M51-3 SL103 and of which each only occurs in one of the two parallel U-channel series. These intervals represent bioturbation, possibly caused by a larger sediment feeder (e.g., Figure 21). Therefore, the water content curve for M51-3 SL104 has been averaged between the parallel U-channels and the decreased water-content values at the very position of the bioturbation structures were excluded.

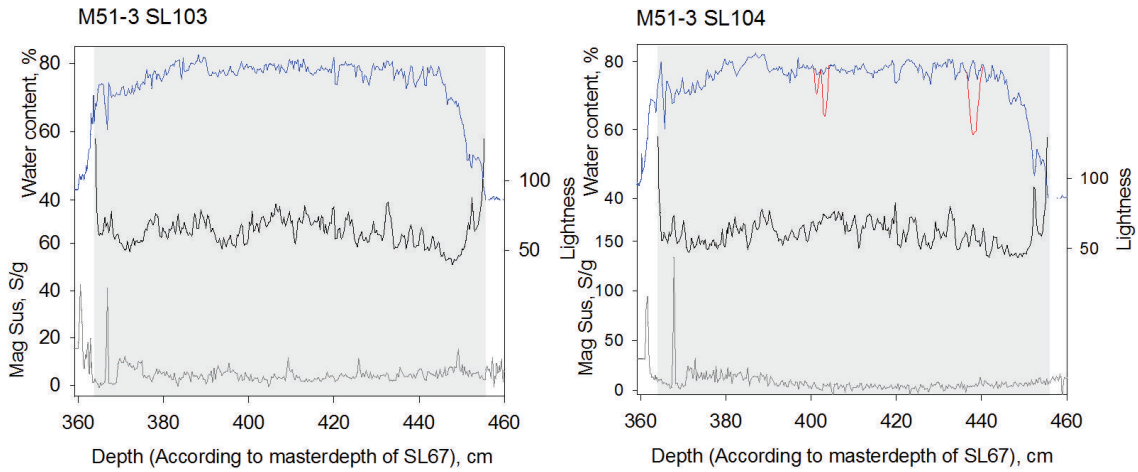

Figure 24: Water content (blue) and magnetic susceptibility (grey) in sapropel S_5 and several cm of the enclosing marls in M51-3 SL103 and M51-3 SL104. Values of measurements of sediment lightness (black curve in the middle) are complemented. Since the water content in M51-3 SL104 has been measured in two U-channels, the blue curve here represents the average between both curves. The red curve represents bioturbations, where the porosity and the water content collapsed. In this case no average was formed and both curves represent the original measurements. (From Moller et al., 2011a).

The good agreement in the water content curves and sediment fabrics point to the conclusion, that light sediment colour, intact lamination and high water content of the sediment are highly correlated. In this model, the lower porosity of the bioturbated sediment could be explained by a collapse of the porous primary structure through ingesting and excreting the sediment by the bioturbating organism, leading to a loss of the ability to store the same amounts of water as undisturbed sapropelic sediments. Similarly, the observation that lighter sediments tend to be able to store more water than darker layers could be explained by a higher amount of porous

particles (diatom valves, (Frydas and Hemleben, 2007)) in these layers, building up a more porous fabric than in the darker layers.

The overall variability of magnetic susceptibility is generally low throughout the sapropel in both cores (Figure 24). A very small decrease in magnetic susceptibility can be observed between the sapropel and the enclosing marls. This is possibly owed to the diamagnetic behaviour of organic material, which is enriched in the sapropel, but also to the decreased supply of Saharan dust (Larrasoaña et al., 2008), resulting in a lower flux of paramagnetic materials like Ti during moist warm periods. Also the lack of iron oxides in the more reducing environment during the formation of the sapropel has to be taken into account. Highly increased values of magnetic susceptibility can be observed in both cores at a depth of 367.9 cm, following the common depth scale (Figure 24) (Original depth SL103: 380 cm, Original depth SL104: 363.5 cm), which coincides with the assumed tephra layer (Figure 23). The high susceptibility values for this interval thus validate this layer as a tephra of a yet-unknown origin.

4.4 Sediment chemistry

4.4.1. XRF data quality

Since the water content of the investigated sediment section ranges from 40 – 80% (Figure 24), it is essential to ground truth the XRF scanning data (Figure 25, Figure 26, Figure 27) prior to interpretation. Since the XRF method assumes that the same volume of sediment is irradiated during each measurement, large changes in porosity could potentially cause changes in observed elemental abundances (Phedorin and Goldberg, 2005). Therefore, we first compared the XRF scan data with the discrete geochemical measurements from 22 levels within the sapropel (Table 3, Table 7). This comparison reveals a good correspondence in the abundance measurements of most elements. With the exception of Ba and Mo, the elements show a statistically significant positive linear relationship (Figure 28). The reason, why the abundances of Ba and Mo do not show a systematic relationship could be explained by the fact that their concentrations are near a detection limit of the XRF-scanner, which increases the signal to noise ratio. Beside these outliers, the systematic link between "in situ" XRF-measurements and absolute measurements conducted on freeze-dried samples underlines the reliability of the scanner data. Thus, we conclude that the continuous, high-resolution XRF-measurements of elemental abundances can be interpreted in terms of a primary signal of the sedimentary system to environmental parameters like productivity, clastic sediment input and degree of anoxia.

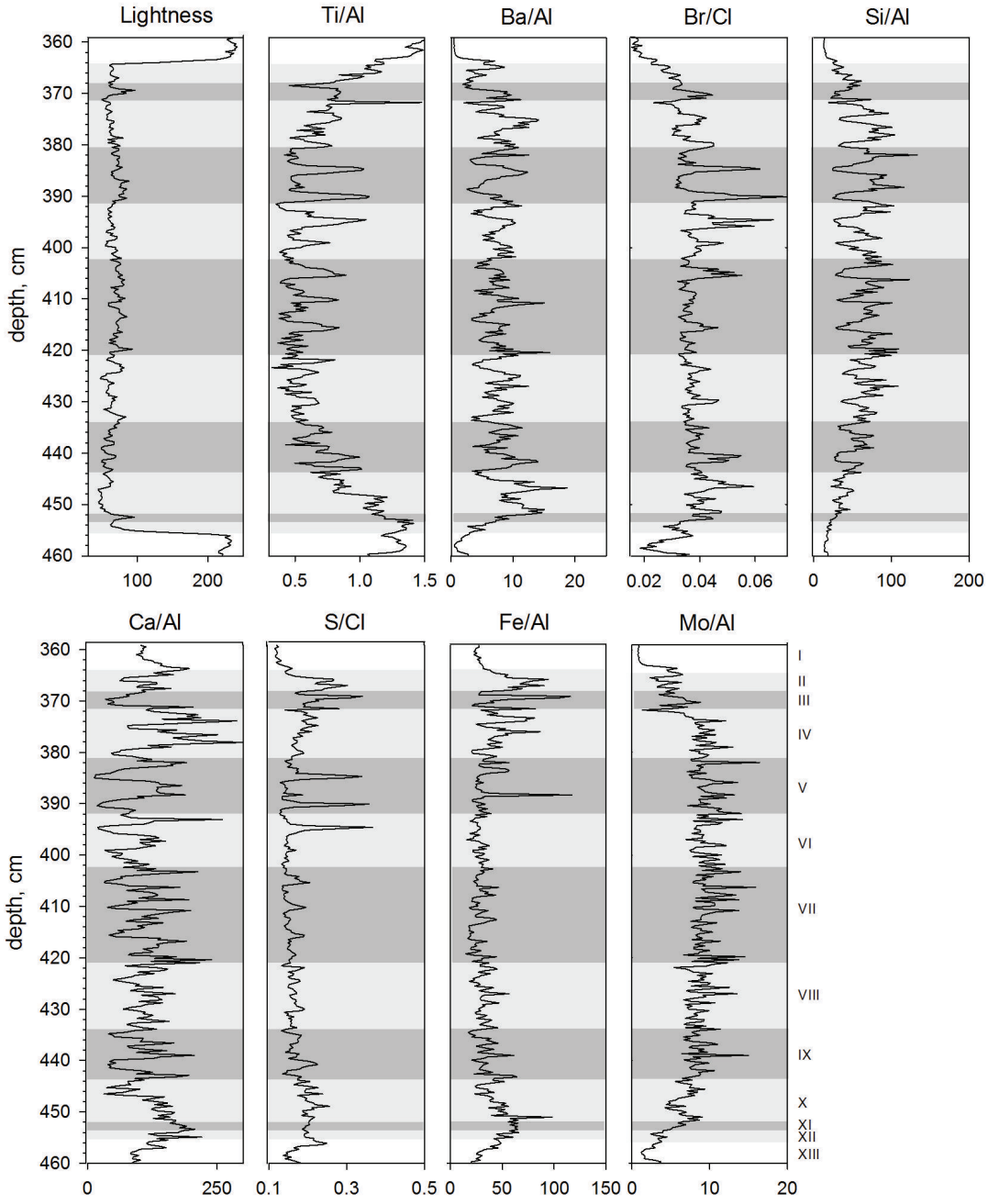

Figure 25: Sediment lightness and elemental ratios from XRF-measurements of M40-4 SL67. The positions of the lithostratigraphic zones (Figure 21) are highlighted in grey and dark grey. The conspicuous high amplitude shifts in the elemental ratios in the centre of the archive half is due to a previous sampling campaign, which can be also seen for example in Figure 21. Here, the XRF scanning method, which is also conducted in the centre of the core, can only resolve the broad scheme of enrichments and depletion of the elemental ratios.

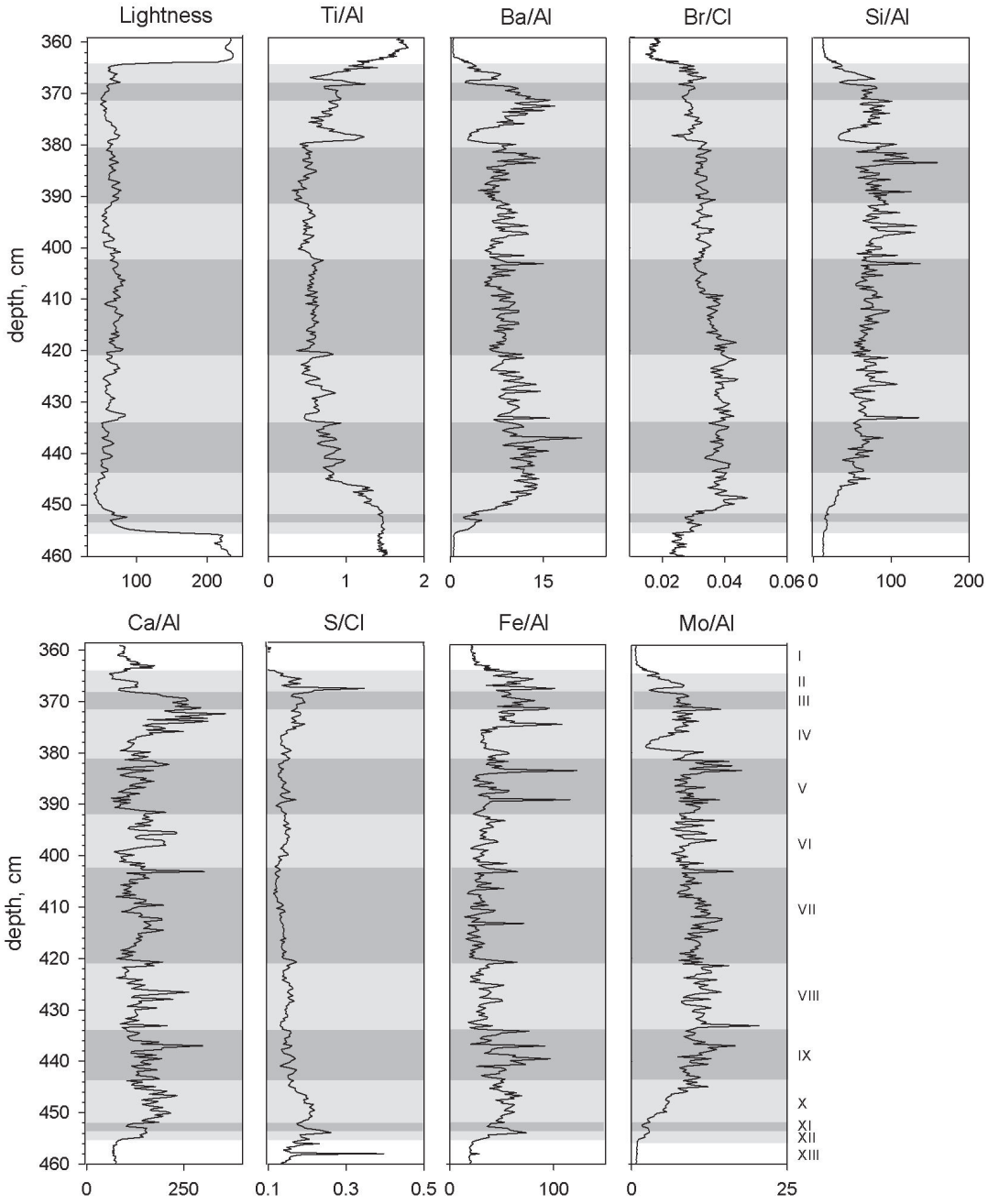

Figure 26: Sediment lightness and elemental ratios from XRF-measurements of M51-3 SL103 plotted against the master depth scale of M40-4 SL67. The positions of the lithostratigraphic zones (Figure 21) highlighted in grey and dark grey. (Modified after Moller et al., 2011).

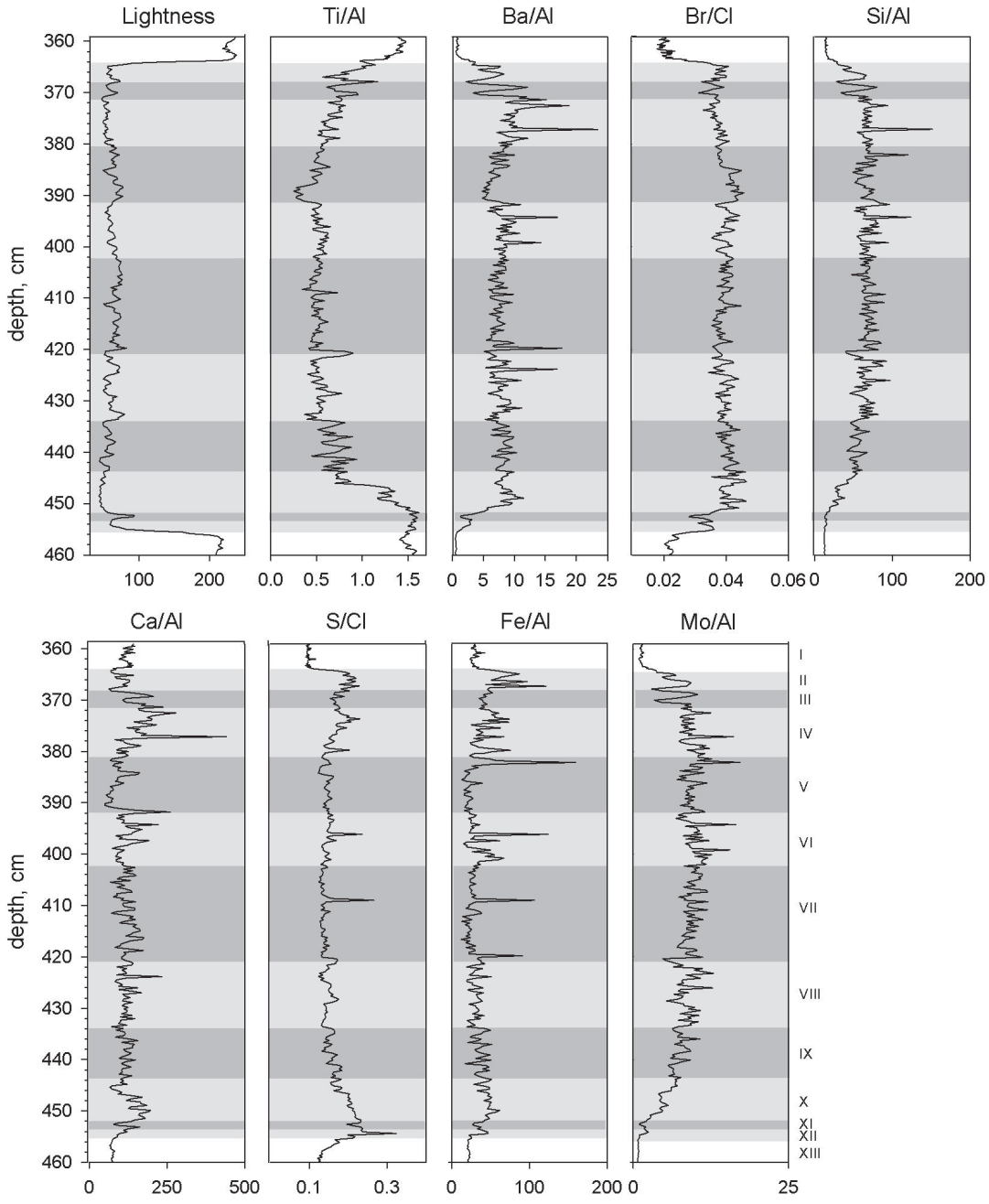

Figure 27: Sediment lightness and element ratios from XRF-measurements of M51-3 SL104 plotted against the master depth of M40-4 SL67. The positions of the lithostratigraphic zones (Figure 21) are highlighted grey and dark grey.

Table 7: ICP-OES element concentrations from discrete samples at various depths. According to table 3, each sample envelopes either a bright or dark layer or was taken from the enclosing marls or the bioturbated samples within zone II and III.

Depth (cm)	Ti [%]	Al [%]	Fe [%]	Ca [%]	K [%]	P [%]	S [%]	Ba [mg/kg]	Cr [mg/kg]	Mn [mg/kg]	Mo [mg/kg]	Pb [mg/kg]	Sr [mg/kg]	V [mg/kg]	Zn [mg/kg]	Zr [mg/kg]
358	0.24	3.81	2.61	16.40	1.17	0.053	0.3	232	113	1140	6	9	723	85	58	90
361	0.12	1.77	3.50	4.89	0.70	0.034	2.8	471	82	267	82	5	227	448	51	53
363.5	0.16	2.20	4.51	6.06	0.81	0.038	3.8	317	56	325	74	4	280	701	42	59
365.5	0.16	2.38	3.63	8.63	0.84	0.040	2.6	689	85	425	60	4	375	450	42	65
366.5	0.06	0.91	2.62	8.07	0.49	0.030	2.7	418	51	330	80	4	361	454	31	33
367.5	0.05	0.92	2.03	6.47	0.45	0.024	2.1	838	43	273	83	2	306	438	27	28
371.5	0.05	0.85	2.09	7.59	0.45	0.023	2.1	982	48	337	102	3	351	393	30	30
377	0.04	0.62	2.40	3.33	0.46	0.019	3.1	691	28	217	64	2	189	213	21	21
384	0.02	0.37	0.52	3.13	0.39	0.009	1.4	460	16	145	52	2	183	101	12	15
393	0.04	0.67	0.79	6.36	0.39	0.024	1.2	734	38	253	56	2	314	200	21	22
397	0.06	1.06	1.21	6.88	0.49	0.024	1.4	813	52	304	62	3	314	150	29	28
404.7	0.05	0.83	0.86	7.22	0.44	0.016	1.2	984	40	287	56	4	335	176	26	24
405.5	0.06	0.96	1.01	3.90	0.51	0.020	1.3	1000	52	247	72	3	250	221	28	27
413.5	0.05	0.88	0.81	3.80	0.50	0.015	1.3	798	35	201	66	2	229	129	23	20
417.2	0.04	0.74	0.77	5.57	0.46	0.015	1.2	896	44	225	61	3	289	166	21	23
418.8	0.05	0.85	0.96	5.56	0.49	0.021	1.4	438	52	266	71	2	285	212	28	29
426	0.05	0.88	0.80	5.50	0.48	0.130	1.2	747	40	260	49	2	298	107	22	21
427.2	0.11	1.90	1.77	6.08	0.74	0.030	1.5	377	67	416	79	5	312	178	43	57
432.5	0.07	1.14	1.08	6.92	0.56	0.019	1.2	932	47	252	75	4	337	129	26	32
433.5	0.09	1.53	1.54	7.26	0.61	0.023	2.4	626	68	280	107	3	326	141	40	39
437.4	0.11	1.94	1.87	8.61	0.71	0.043	1.7	1265	80	392	89	6	393	196	48	44
440.3	0.15	2.66	2.68	12.70	0.88	0.038	1.8	452	126	542	108	7	595	240	60	64
444	0.26	4.42	3.36	13.40	1.35	0.042	1.4	822	166	668	43	10	739	193	81	86
445	0.20	3.59	4.00	14.80	1.13	0.046	3.2	1320	136	563	92	8	801	211	70	75
446.9	0.53	8.96	6.29	29.90	2.67	0.073	2.0	841	313	1777	42	18	1500	286	133	188
450	0.29	4.69	3.46	13.90	1.40	0.039	1.4	267	155	784	29	9	608	99	64	105

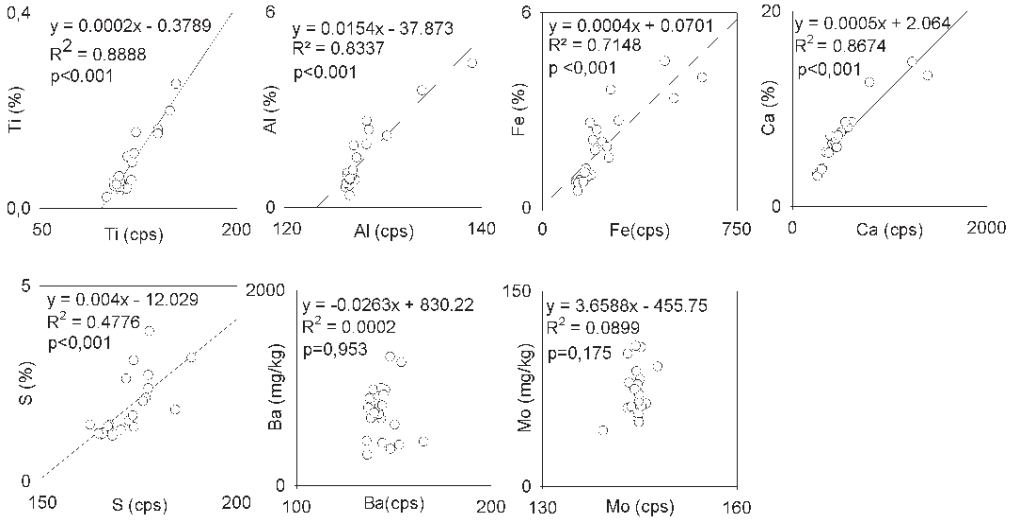

Figure 28: Cross plots of abundances of raw XRF-Measurements in counts per second (cps) against concentrations in % or mg/kg. Where significant, the linear regression lines and equations are indicated.

4.4.2. XRF elemental abundances

The data show that the sapropel is not completely chemically homogenous and that the transitions between the sapropel and the enclosing marls appear with varying degrees of sharpness for different elements (Figure 25, Figure 26, Figure 27). The variability in sediment chemistry corresponds with the lithostratigraphic subdivisions of the sapropel (Figure 21), as seen in the depth-constrained cluster analysis of elemental ratios (Figure 29A). This analysis reveals that most of the lithological units correspond to major shifts in sediment chemistry, although these shifts are often leading or lagging the lithological boundaries by several mm. This correspondence is particularly well developed during the transition between sapropel and the enclosing marl, whereas within the sapropel, some lithological units do not appear to be correlated with geochemical change (Figure 29A, e.g., Zone IX-X in M51-3 SL103, Zone VIII-IX in M51-3 SL104). To highlight the hierarchy of the chemical shifts across the sapropel, we calculated the mean chemical composition of each zone (by averaging among the samples from each zone) and subjected these artificial data to a separate depth-constrained cluster analysis (Figure 29B). This analysis reveals a symmetric nested hierarchical structure across the sapropel in both cores, with differences between lithostratigraphic zones becoming progressively less distinct towards the centre of the sapropel. Both analyses show that the lithostratigraphic Zones XII and XI and a part of Zone X at the base of the sapropel are chemically more similar to the underlying marl than to the rest of the sapropel, although the sediment itself is clearly sapropelic. This is in contrast to the top of the sapropel, which, despite the onset of bioturbation, still shows geochemical affinity to the main body of the sapropel rather than the overlying marl.

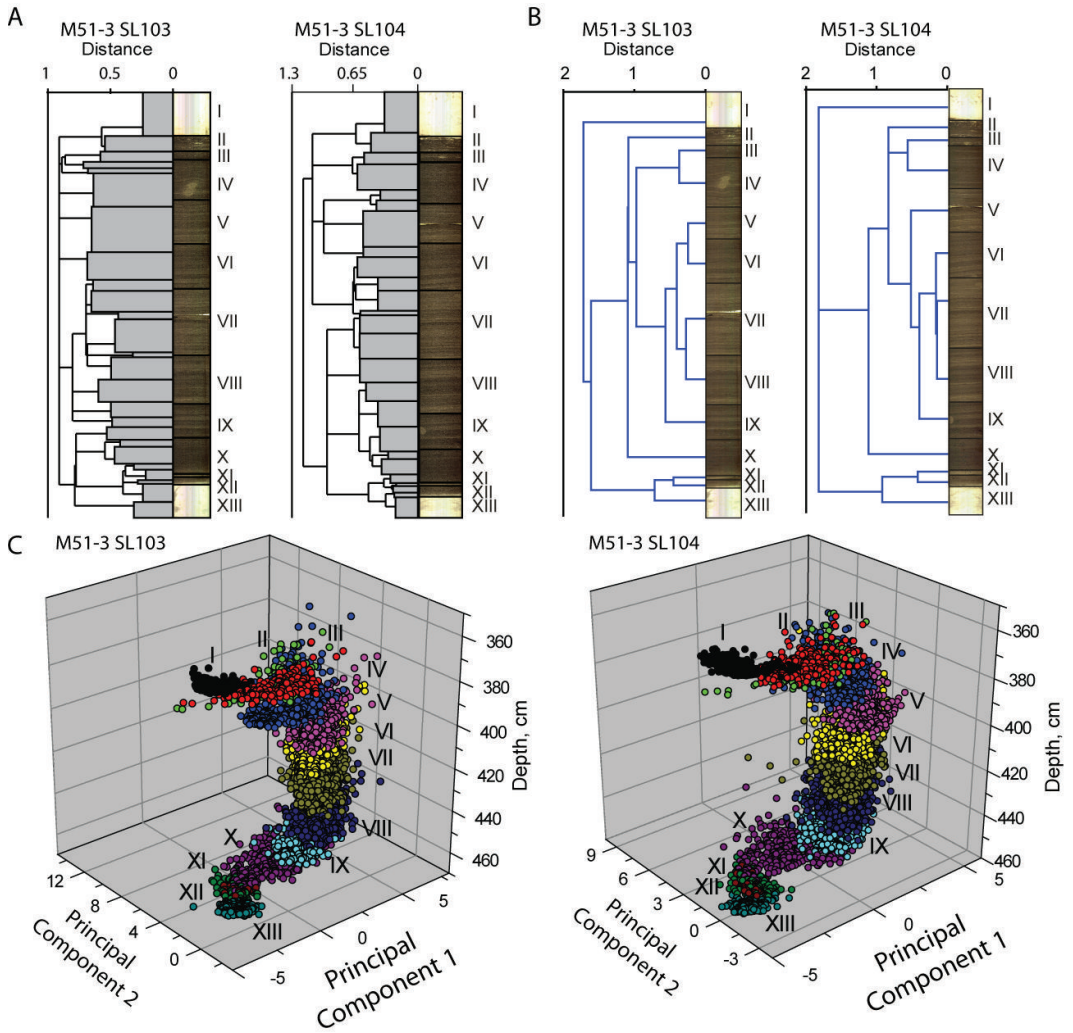

Figure 29: (A) Simplified hierarchical tree-diagram from a constrained cluster analysis of M51-3 SL103 and M51-3 SL104, ran by the exclusive use of raw XRF-measurements with the full resolution of 0.2 mm. It shows the fit between multivariate computed geochemical and lithostratigraphic zonation. (B) Hierarchical tree-diagram from a constrained cluster analysis of and M51-3 SL103 and M51-3 SL104, ran by the exclusive use of raw XRF-measurements. In contrast to Figure 29A, here, elemental abundances of raw XRF-measurements were averaged across the dimensions of the lithological boundaries from Fig. 3 and clarify the relationship of each zone to each other. (C) Result of case wise conducted principal component analysis of M51-3 SL103 and M51-3 SL104 by the exclusive use of raw XRF-measurements. X- and Y- axis represent principal components1 and 2. Z-axis represents depth of the sapropel below sediment. The subunits I-XIII, defined in Figure 21, are pronounced by colour-coded data points. (Graph taken from Moller et al. (2011a)).

In order to visualize the most significant chemical gradient in the sediment, a PCA was carried out on normalized elemental ratios (Figure 29C). The first two axes explained ~76 % (~56% and ~20%) of the total variance in the 8-variable space. The analysis reveals a circular trend in the data with the base of the sapropel (Zones XIII, XII, XI and the base of Zone X) being chemically similar to the top of the sapropel (Zone I). In both cores, Zones IX to III appear chemically more homogenous, confirming the result of the cluster analysis. Whereas the chemical gradients at the base and the top of the sapropel can be expected to reflect redox processes during and after the deposition, the chemical homogeneity of the core sapropel

indicates that it may be possible to search for a link between the physical properties and structure of the sediment, including the origin of the lamination, and sediment chemical composition. To confirm this hypothesis, we examined the relationship between sediment colour, water content and elemental abundances across the lower part (Zones XII-VIII) and the termination (Zone V-II) of the sapropel deposition in core M51-3 SL103 (Figure 30).

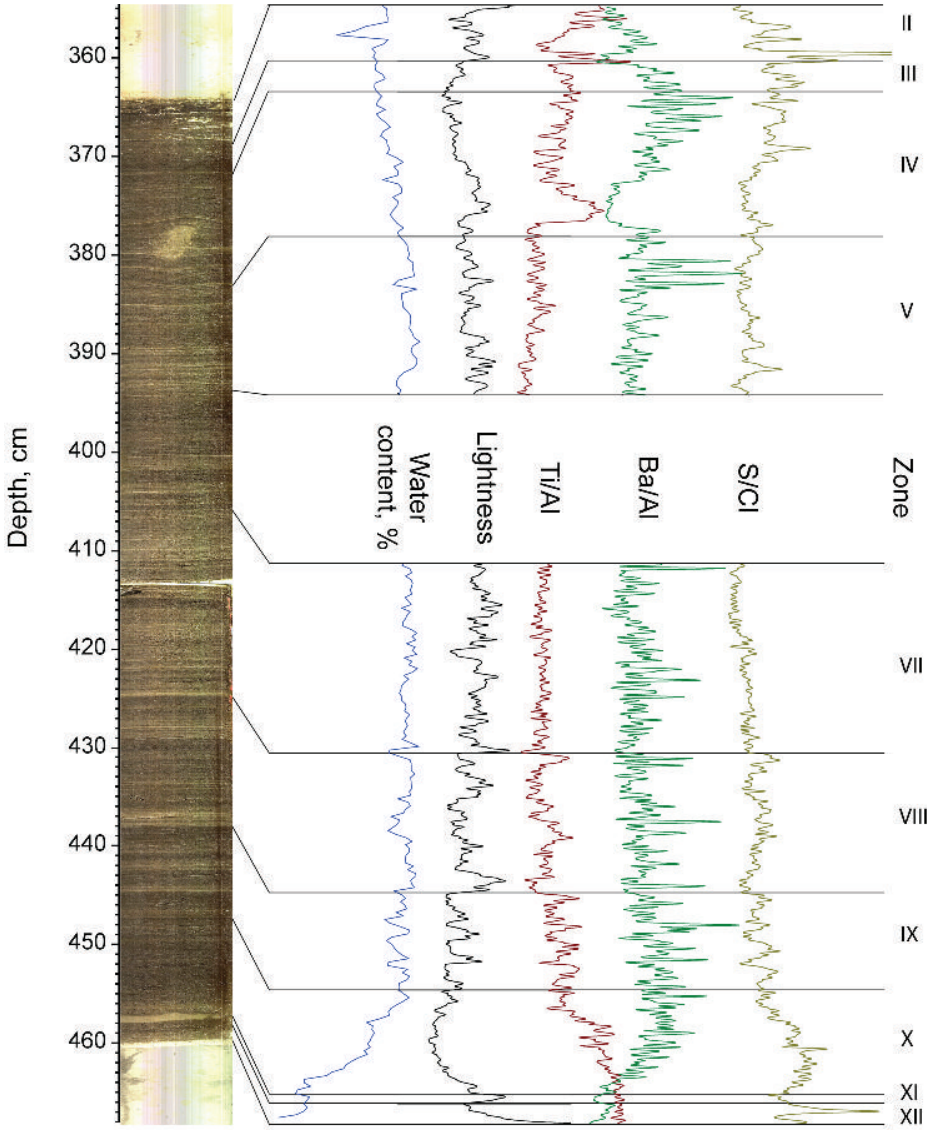

Figure 30: Exemplarily outcrops of water-content, sediment-lightness, Ti/Al, Ba/Al and S/Cl from zone II-V and VIII-XII from M51-3 SL103 illustrating the correlation of geochemical and geophysical measurements to the visible pattern of lamination. Water content results from discrete measurements with 3 mm spacing. Spacing of lightness and chemical elements is 0.6 mm (3 pt running mean of original spatial resolution). (Modified after Moller et al., 2011a)

The graph clearly documents a link between the pattern of layers, represented by sediment colour, water content and elemental ratios (such as Ti/Al, Ba/Al and S/Cl). This negative correlation between physical properties (lightness and water content) and elemental ratios (Ti/Al, Ba/Al, S/Cl) develops within Zone X and persists until Zone V or IV. In order to determine quantitatively, which elements and in what way they are related to the visible cm-scaled

layering (sediment colour), correlation analyses between sediment colour and all 8 elemental ratios of M51-3 SL103 and M51-3 SL104 were carried out separately for each zone (Figure 31).

This analysis reveals that the correlation between elemental abundances and sediment colour is not stationary throughout the sapropel. As expected, the transition zones and the bioturbated Zones showed a distinct pattern of correlation, reflecting the gradient across the transition and masking the higher-frequency variation. Even when the more homogenous core sapropel Zones IX to IV are considered, a clear shift in the correlation structure appears, separating Zones IX–VIII and VII–IV. The pattern is similar between the two cores, indicating a common control on the correlation. The difference between the two cores for Zone IV is caused by a single bioturbation structure in core M51-3 SL103 (Figure 30), which apparently introduced sediment with a chemical composition typical of Zone III deeper into the core.

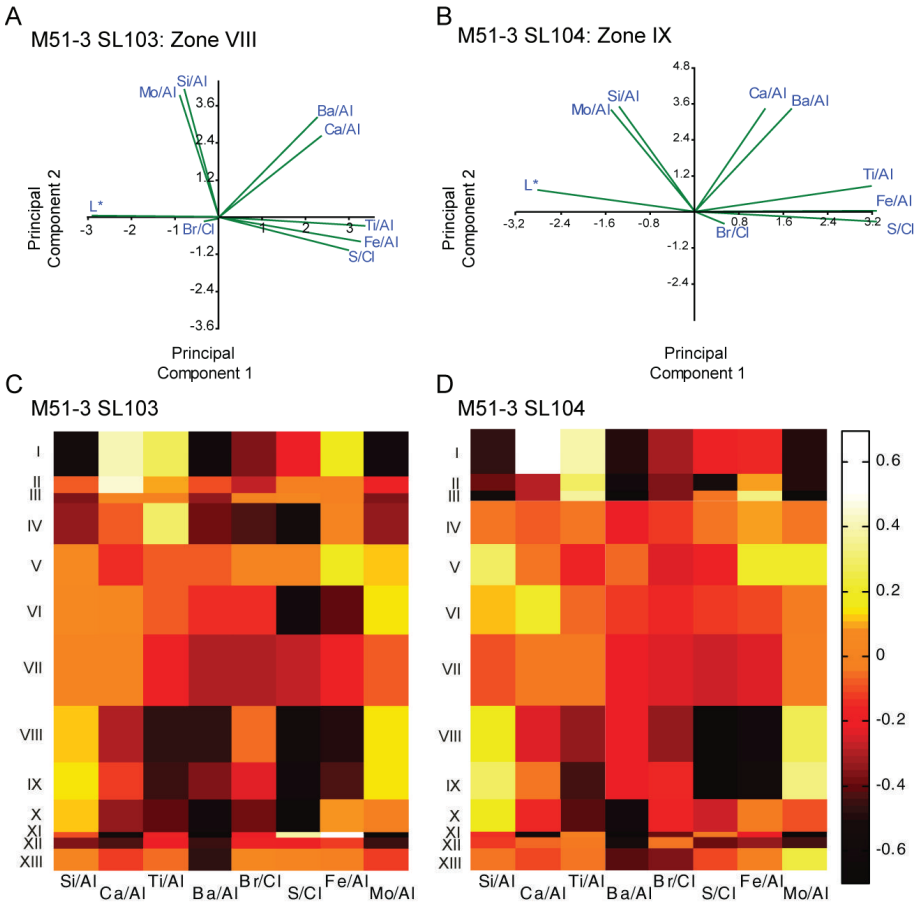

Figure 31: Planeplots of variables of principal component analyses of Zone VIII and IX from M51-3 SL103 and M51-3 SL104, illustrating the correlation of elements and lightness (L*) to each other by the direction and length of their vectors. Zone VIII and IX (A, B) reveal a grouping, whereby one group is located in the same direction than lightness (L*), indicating a positive correlation and the other group of elements away from lightness, indicating a negative correlation. (C, D) Pseudo colour visualization of Pearson correlation coefficient of elemental ratios to the lightness for each zone in the sediment cores M51-3 SL103 (C) and M51-3 SL104 (D). Bright colour indicates good positive correlation, darker colours indicate good negative correlation. (Thickness of individual zones is considered). (Modified after Moller et al., 2011a).

4.5 Faunal analysis

4.5.1. Pelagic microfossils

Planktonic foraminifera from U-channel samples

The absolute numbers of individuals of planktonic foraminifera in the here presented S_5 sapropel are highly variable and by average higher within the sapropel and can reach over 10000 individuals per gram sediment, while pre and post sapropel levels are as high as about 3000 individuals (Figure 32A). The onset of the sapropel is marked by a small increase in the absolute number of individuals and a subsequent dramatic drop to almost zero for a short period, corresponding to subunit XI, which is constituted by a single bright clayey layer. After this event the number of individuals increases erratically, whereby four pronounced clusters can be identified (~440 cm, ~422 cm, ~405 cm, ~370 cm) (Figure 32A). Before returning to the normal marine conditions, very low abundances are observed within the bioturbated top 2 cm (Figure 32A).

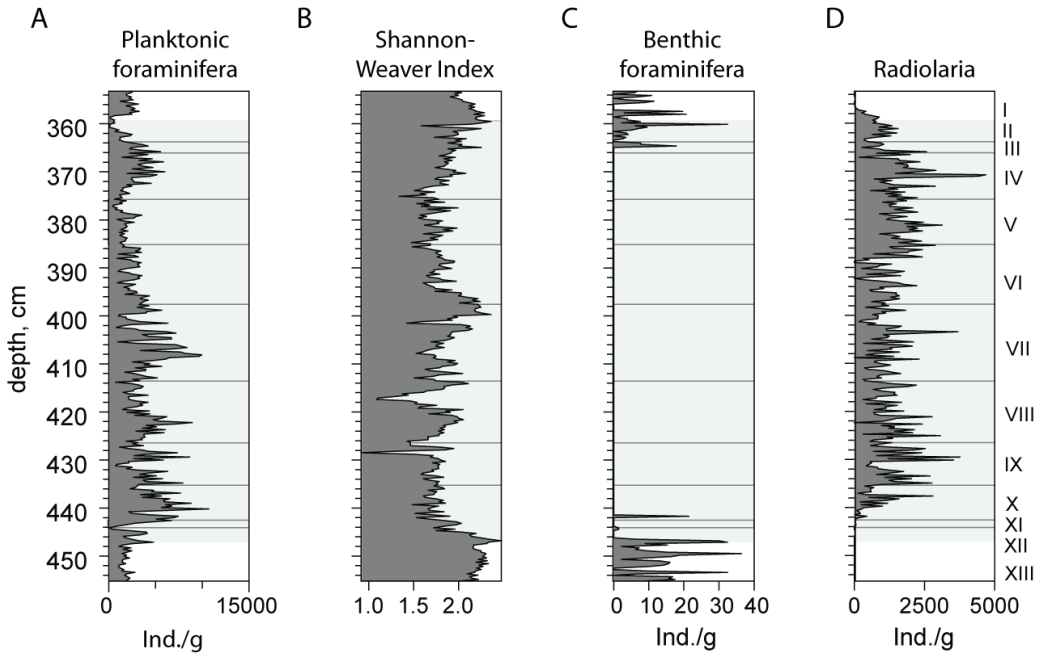

Figure 32: Faunal data from discrete samples (3 mm spacing) from a U-channel from M51-3 SL104. **A**: Total number of individuals of planktonic foraminifera per gram sediment **B**: Shannon Weaver Diversity Index calculated from proportional abundances of species of planktonic foraminifera (Shannon, 1948) **C**: Total number of benthic foraminifera per gram sediment. **D**: Total number of individuals of radiolaria per gram sediment. The visible part of the sapropel is shaded in gray, whereas the individual subunits are individually framed.

The varying proportions in the census counts of planktonic foraminifera, as shown in Figure 34 and Figure 35, are also mirrored in the in the diversity index of Shannon (1948) (Figure 32B). A drop in the diversity can be seen at the onset and the termination of the sapropel and low values are observed in zones X, IX and V. Nevertheless, the unusual hydrographic regime during sapropel formation does not automatically lead to a general lower diversity throughout the

complete sapropel interval, as the local maxima at about 398 cm and 421 cm show, where diversity is similar to the enclosing marls. Beside these trends, also events with extremely low diversities are found (401.5 cm, 417.4 cm and 428.5 cm). The exceptional low diversities in these samples are not a byproduct of a low number of individuals, since each sample contains 2000 individuals or more. Instead, these samples are mostly dominated by *G. bulloides* (73.6% in 428.5 cm, 61.8% in 401.5 cm) or *G. ruber* (85% in 417.4 cm).

Planktonic foraminifera in thin-sections

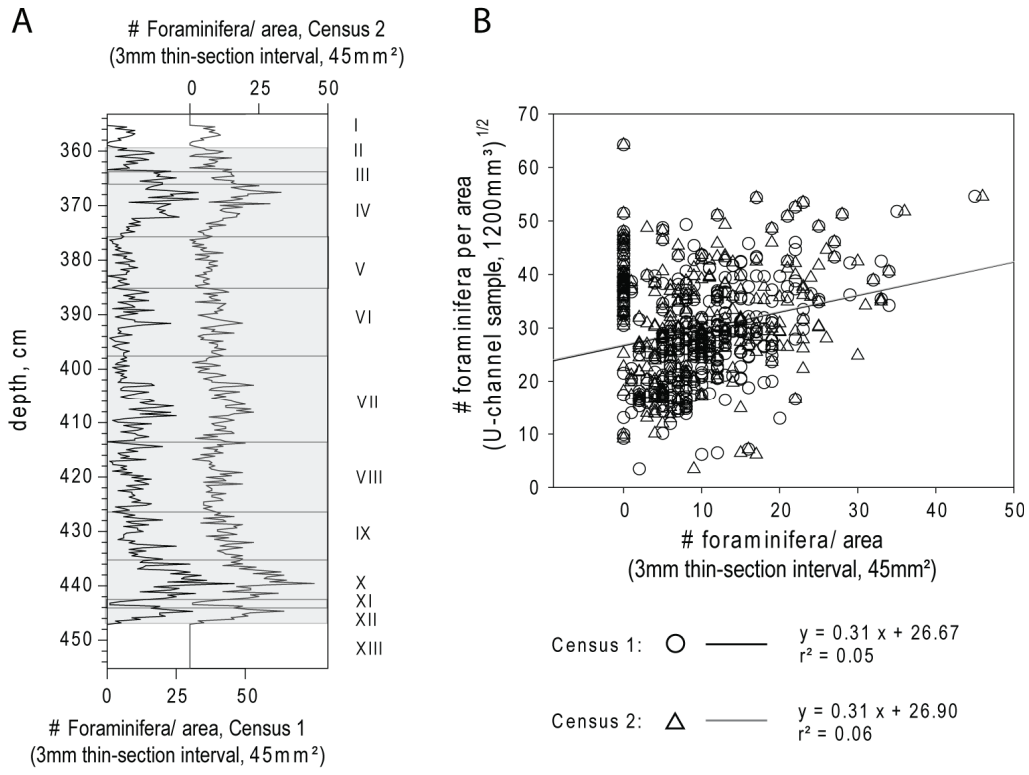

Figure 33: A) Census 1 and 2 of planktonic foraminifera. The census was performed in 3 mm intervals of photographic pictures from the resin impregnated thin sections. These 3 mm wide intervals are the same, being used for the census of varves, and also coincide with the U-channel samples (Chapters 3.3) and represent an area of 3 mm * 15 mm=45 mm². B) Cross plot of the numbers of specimen counted in the thin sections and the numbers of planktonic foraminifera per gram sediment (Size fraction >150 µm) as calculated from the washed samples.

As visible in Figure 18 and Figure 38, the resin impregnated thin sections did not only bring the sub-mm lamination to our attendance but also fairly embedded planktonic foraminifera, which were conserved during the resin impregnation as well. Along with the census of laminae, the number of planktonic foraminifera was determined in the same 3 mm intervals as well (Figure 17C), thus also corresponding with the data from the discrete U-channel samples. Here, the number of planktonic foraminifera ranges from 0 to 46 per 3 mm interval (corresponding to an area of 45 mm^2), whereby the planktonic foraminifera are generally more abundant within the sapropel, compared to the enclosing marls (Figure 33A). Also within the sapropel a high

variability in the number of planktonic foraminifera can be seen. Highest numbers occur near the base, whereby a pronounced gap with low abundances is represented by subunit XI. High numbers are also visible in zone IV and to a minor degree in the centre of zone VII (Figure 33A), which coincides with the observations in Figure 32A.

Since the numbers of planktonic foraminifera were determined in the washed samples, as well as in the two-dimensional thin sections, both methods can be compared in terms of redundancy. As visible in Figure 33B the sum of counted planktonic foraminifera from both approaches were cross-plotted, whereby the suggested linear correlation remains on a rather low level of significance (r^2 values of ~0.05 and ~0.06). The discrepancy between both methods is most likely owed to two different sources of error. While the numbers of specimens in the washed samples reach values of several thousand individuals, the thin sections bear a substantial lower number, which increases the probability of identical results and thus naturally lowers the sensitivity of this method. Another important aspect is that the washed samples represent only a selected size fraction of individuals above 150 µm, while the thin-sections represent the complete sample, without any preliminary constriction of investigated size fraction.

Benthic foraminifera and radiolaria

Compared to the large amounts of planktonic foraminifera, benthic foraminifera are rather rare, with highest abundances of 30 to 40 individuals per gram sediment. Furthermore, the typical distribution pattern for sapropels in general and S_5 in particular becomes apparent in Figure 32C, whereby the benthic foraminifera are present in the oxygenated sediments below and above the sapropel, but disappear within the first centimetres after the onset of the sapropel and reappear within the bioturbated top centimetres of the sapropel.

Figure 32D visualizes the numbers of tests of radiolaria (>150 µm) per gram in each sample. While the clayey marls below and above are almost free of radiolaria, they start to occur at the base of zone X, in a depth of about 442 cm. From here, abundances increase by trend but remain highly variable.

4.5.2. Planktonic foraminifera species abundances

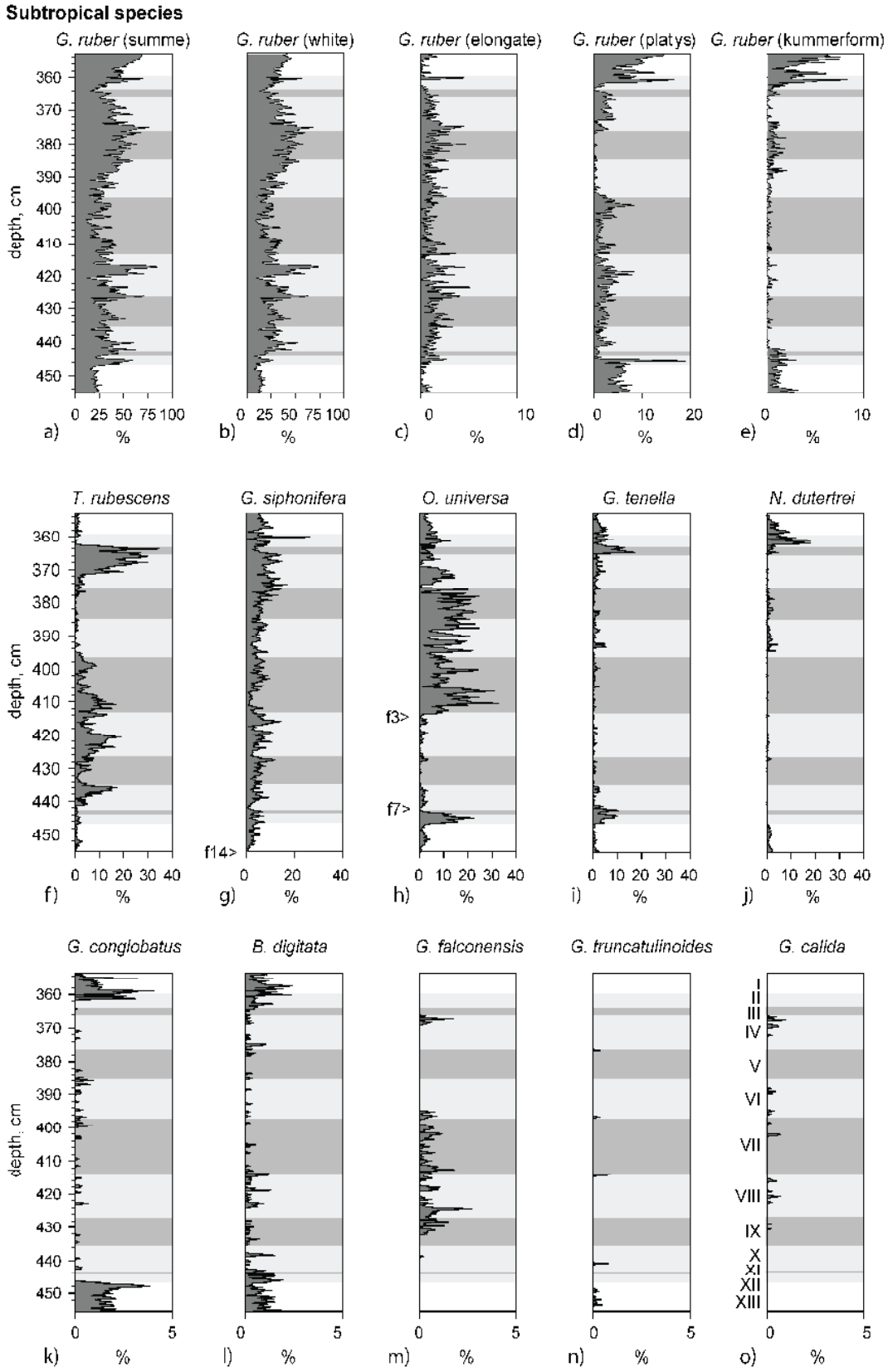

Figure 34: Census counts of subtropical species of planktonic foraminifera throughout the sapropel S_5 and the enclosing marls in M51-3 SL104 with original depth scale. Faunal events, following Cane et al. (2002) (Table 8), are added. The sapropel and the previously, optically defined subunits are highlighted as gray and light-gray zones.

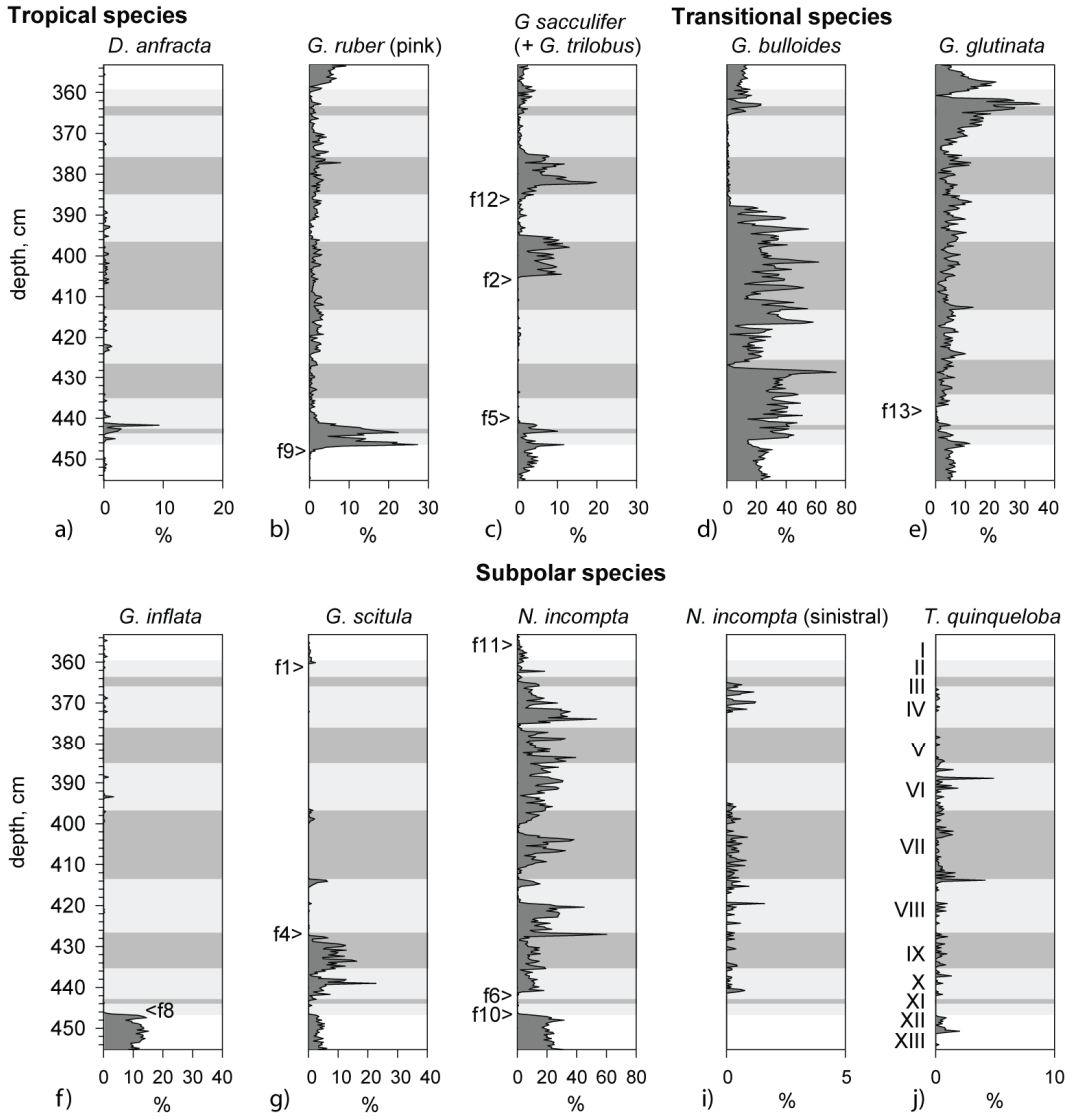

Figure 35: Census counts of tropical, transitional and sub polar species of planktonic foraminifera throughout the sapropel S_5 in M51-3 SL104 and the enclosing marls with original depth scale. Faunal events, following Cane et al. (2002) (Table 8), are added. The sapropel and the previously, optically defined subunits therein are highlighted as gray and light-gray zones.

Subtropical species

G. ruber is by far the most abundant species in the sapropel and the enclosing marls and has an average abundance of 29.6 %, which includes *G. ruber* (white) and the morphotypes *G. ruber* (elongate), *G ruber* (platys) and *G. ruber* (kummerform). Generally, *G. ruber* is dominated by its most common variety *G. ruber* (white). Here, abundances increase with the onset of the sapropel and pronounced clusters are visible in the lower part of the sapropel, with four sub-peaks and another cluster in the upper half of the sapropel with its centre at 375 cm. Above the sapropel, the frequencies of *G. ruber* remain on a higher level than below the sapropel. A similar pattern is visible in *G. ruber* (elongate), yet on a generally smoothed level. Deviating thereof, *G. ruber* (platys) and *G. ruber* (kummerform) are generally more abundant prior and after the sapropel

and about two-fold more rare within the sapropel. Remarkable here is a pronounced gap in *G. ruber* (platys) from 390 – 375 cm, which coincides with elevated frequencies in the other three morphotypes. *G. rubescens* does not show a defined trend, but is almost absent in the enclosing marls. Within the sapropel, the occurrence of *G. rubescens* is mostly concentrated to two intervals. The lower interval ranges from 440 – 395 cm, featuring four subordinated peaks. Yet, highest abundances instead are reached in the upper interval from 375 – 362 cm and drop to zero abundance after the tephra layer. *G. siphonifera* is fairly abundant throughout the sapropel and the enclosing marls, whereby a clear trend is not visible. Elevated abundances are apparent at a depth of 375 cm and a peak with a frequency of 25% at the top end of the sapropel. Peculiar low abundances occur at a depth of 454 cm, which we identify as faunal event f14 (Cane et al., 2002). *O. universa* is highly variable and generally more abundant within the sapropel, compared to the enclosing marls and unveils a pronounced gap from 414 – 443 cm, which define the faunal events f3 and f7. *G. tenella* always remains below 20% and highest abundances occur shortly after the onset of the sapropel and again in a short interval below the tephra layer at about 364 cm. Overall abundances of *N. dutertrei* are similar to *G. tenella* but the elevated frequencies are only reached once, in a short interval above the tephra layer. *G. conglobatus*, *B. digitata*, *G. falconensis*. *G. truncatulinoides* and *G. calida* are generally rare throughout the investigated interval with abundances below 5%. *G. conglobatus* and *B. digitata* are generally more common in the enclosing marls and almost disappear within the sapropel. In contrast, *G. falconensis* is only found within the sapropel. *G. truncatulinoides* and *G. calida* only occurs as single specimens in individual samples.

Tropical species

The abundances of the tropical species *G. ruber* (pink), *G. trilobus*, *G. sacculifer* and *D. anfracta* are mostly below 10% during most of the investigated interval or completely absent, but do show coherent peaks after the onset of the sapropel, where *G. ruber* (pink) reaches up to 27% (Faunal event f9). *G. sacculifer* (*G. trilobus*) further shows increased abundances in two intervals from 405 – 395 cm and from 385 – 375 cm (faunal events f2 and f12), where both species together reach values between 10% and 20% of the whole sample. *G. ruber* (pink) is almost absent below the sapropel, but seems to be more common again after the termination of the sapropel. In contrast thereof, *G. sacculifer* (*G. trilobus*) remains on a relative low level.

Transitional species

The comparability of species, which inhabit transitional waters is limited (Figure 35); While all species show a drop in their frequencies shortly after the onset, *G. bulloides* subsequently prospers and can dominate the lower third of the sapropel with frequencies of nearly 80%. *G. inflata* is abundant with ~10% in the marl below the sapropel. By the visible onset of the

sapropel, *G. inflata* disappears (Faunal event f8) and, despite single findings, remains absent throughout and also after the sapropel. *G. glutinata* remains below 10% until a depth of 370 cm where abundances increase and reach well above 20%. Apart from an interval from 443 cm to 436 cm (Faunal event f4), with frequencies of about 10%, *G. scitula* remains almost absent along the sapropel and reappears with low abundances at the termination of the sapropel (Faunal event f1).

Subpolar species

Subpolar species are represented by *N. incompta* (both, the regular dextral specimens and the more rare sinistral individuals) and *T. quinqueloba*. *N. incompta* has abundances of 20% below the sapropel but lower abundances after the termination of the sapropel. Within the sapropel, a clear trend is not visible, yet *N. incompta* is quite common throughout the sapropel with frequencies of 10 – 20%. Anyhow, the abundances in single samples can be above 40% as well as nearly absent in narrow intervals (faunal events f6 and f10). *T. quinqueloba* is generally rare and mostly below 2%. Beside two peaks with slightly elevated abundances within the sapropel and a defined disappearance with the onset of the sapropel, an articulated trend cannot be seen.

4.6 Stable $\delta^{13}C$ and $\delta^{18}O$ isotopes of planktonic foraminifera

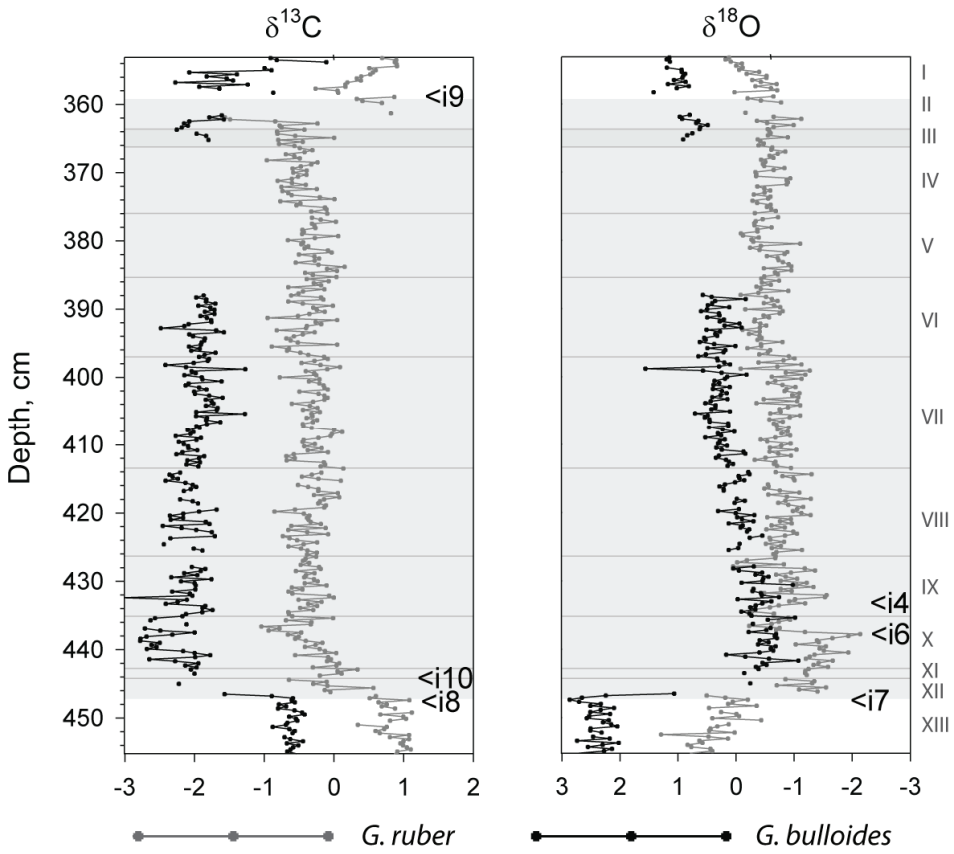

Figure 36: Carbon and oxygen isotopic measurements from *G. ruber* and *G. bulloides* in the size fraction 250 – 315 µm in M51-3 SL104 over the length of the S_5 sapropel and the enclosing marls with a spacing of 3 mm. Gaps represent samples without foraminifera in the regarded size fraction. Isotopic events at certain enrichments and depletions, according to Cane et al. (2002) are marked. Sapropel S_5 is shaded in gray and position of subunits are shown.

Generally, the oxygen isotopic curve shows a strong trend to negative values within the sapropel (Figure 36). Here, *G. ruber* and *G. bulloides* reach their most negative values directly after the onset of the sapropel with values of about -0.5 (*G. bulloides*) to -2 (*G. ruber*), which prevail into zone X to a depth of about 437.5 cm. Thereafter, oxygen isotopic values become more positive until the termination of the sapropel. In the case of *G. ruber*, this trend is not gradually but seems to happen in a step-wise manner at defined depths of 396.7 cm and 381.1 cm. Potentially due to a deeper habitat, the oxygen isotopic signal of *G. bulloides* is more damped and thus shows a more gradual trend.

Comparing the situation before and after the sapropel, the $\delta^{18}O$ ratio after the sapropel seems to remain on a decently more negative level than below the sapropel. Yet a clear proposition cannot be made, due to the limited number of samples. The contrast between both species is greatest in the enclosing marl below the sapropel with a difference of about 2, but becomes smaller within the sapropel and also remains so after the sapropel.

Overall, the pattern of the carbon isotopic values is comparable to the oxygen isotopy with generally more negative values within the sapropel compared to the enclosing marls. Yet, values remain on a stable level within the sapropel and do not feature a defined trend. Also the difference between *G. ruber* and *G. bulloides* remains constant throughout the investigated interval. According to other Eastern Mediterranean S_5 sapropels, the isotopic events, as defined in Cane et al. (2002) (Table 8) and also seen for example in Emeis et al. (2003), could be identified throughout the sapropel.

4.7 Sea surface temperature reconstruction

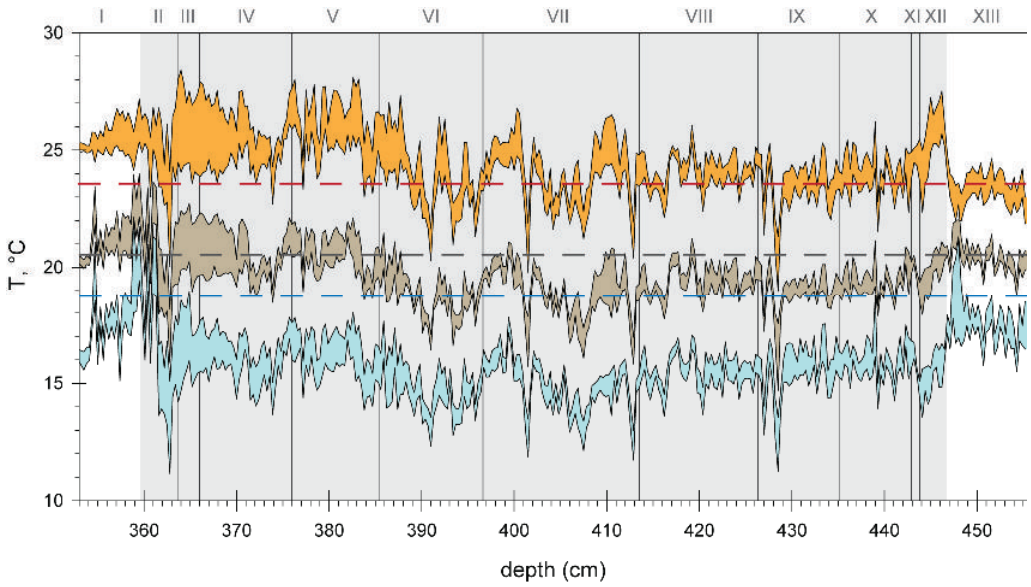

Figure 37: Curves of SST during summer (orange), winter (blue) and the annual average (brown), calculated from the ANN on the base of planktonic foraminifera. The temperatures are shown as hatched areas, indicating the upper and lower limit of the ANN-temperatures, and are calculated by addition or subtraction of the standard deviation from the calculated average of a ten-fold run of the ANN. The visible part of the sapropel is shaded gray and the boundaries of individual subunits are highlighted. Recent temperatures of summer (red), winter (blue) and the annual average (grey) at the Pliny Trench area (Conkright et al., 2002) are added as dashed horizontal line.

Below the onset of the sapropel, the paleotemperatures, reconstructed with the ANN-method, (Hayes et al., 2005) yield similar temperatures than today for summer as well as the annual average but lower temperatures during winter (~1°C). In contrast, after the sapropel, temperatures are above the present day temperatures during summer and also in the annual average and still slightly cooler during winter. Furthermore, temperature reconstructions before and after the sapropel tend to be more constant (Figure 37).

There is an enhanced seasonality within the sapropel, featuring temperature differences of about 9°C between summer and winter, while the seasonality of 5°C in the enclosing marls is significantly smaller. Also the variability of temperatures of a certain season or the annual average varies strongly throughout the sapropel. Zone X to VIII feature relatively constant temperatures, whereby the summer season and the annual average are comparable to the actual day and winter temperatures are about 3°C lower than the actual winter temperatures. Zone VII until the upper end of zone IV features higher variability and periods of pronounced high temperatures alternate with cool intervals. From zone IV on, generally warmer temperatures prevail until the end of the sapropel. Yet, here also the upper and lower boundaries of the assessed SSTs diverge and point at a situation that is more difficult to interpret for the ANN. Above the described progression of temperatures, very short scale trends with extreme low

temperatures are visible at certain depths (401.5 cm, 417.4 cm, 428.5 cm). In most cases, most likely, these rather extreme values are caused by samples that suffer from a low diversity and are instead dominated by only a few species (Figure 32), such as *G. bulloides*.

4.8 Sediment lamination

Although a faint layering can be macroscopically observed in the basal part of the sapropel (zone X, thin-sections 1.2-2.1, Figure 38), the thin sections of this interval reveal, that especially the bright laminae here are mostly non-existent or strongly underdeveloped, wavy and laterally inconsistent (Figure 38).

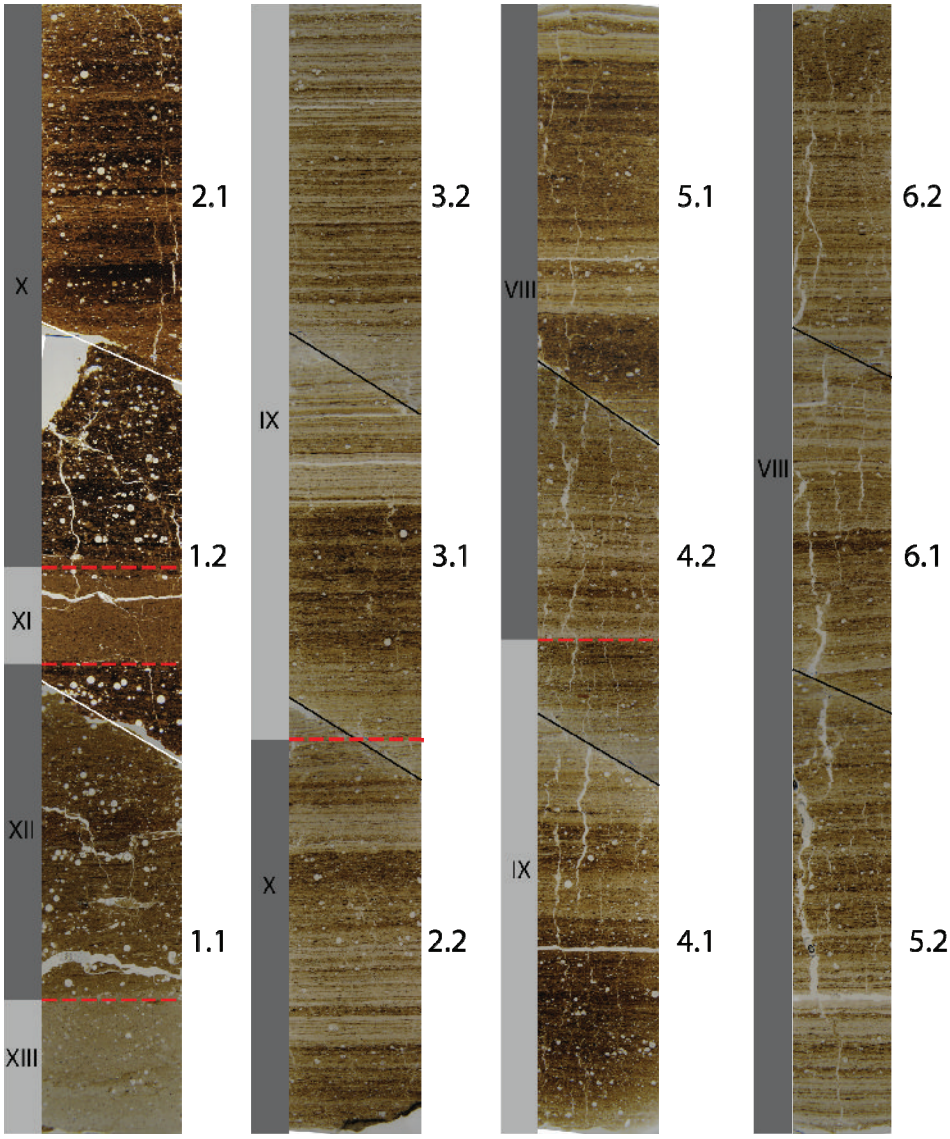

Figure 38: Photographic images of the resin impregnated thin-sections. The images were merged, according to the sampling-scheme in Figure 17. The widths of the individual thin-sections, which originally comprise 1.5 cm were aligned by cropping, since each thin-section experienced a certain and individual degree of erosion of material during the impregnation procedure. Fractures, mostly perpendicular or parallel orientated to the lamination, occurred during preparation and became fixated with resin and thus appear bright in the thin-sections. Planktonic foraminifera, also being impregnated, are visible as globular bright entities of various sizes throughout the sapropel. Diagonal lines indicate the original dimensions of the thin sections and are labelled on the right side with their number, according to the sampling scheme in Figure 17. Red dashed horizontal lines and gray and dark gray bars on the left sides of the images indicate the optically determined subunits, as declared in Figure 21.

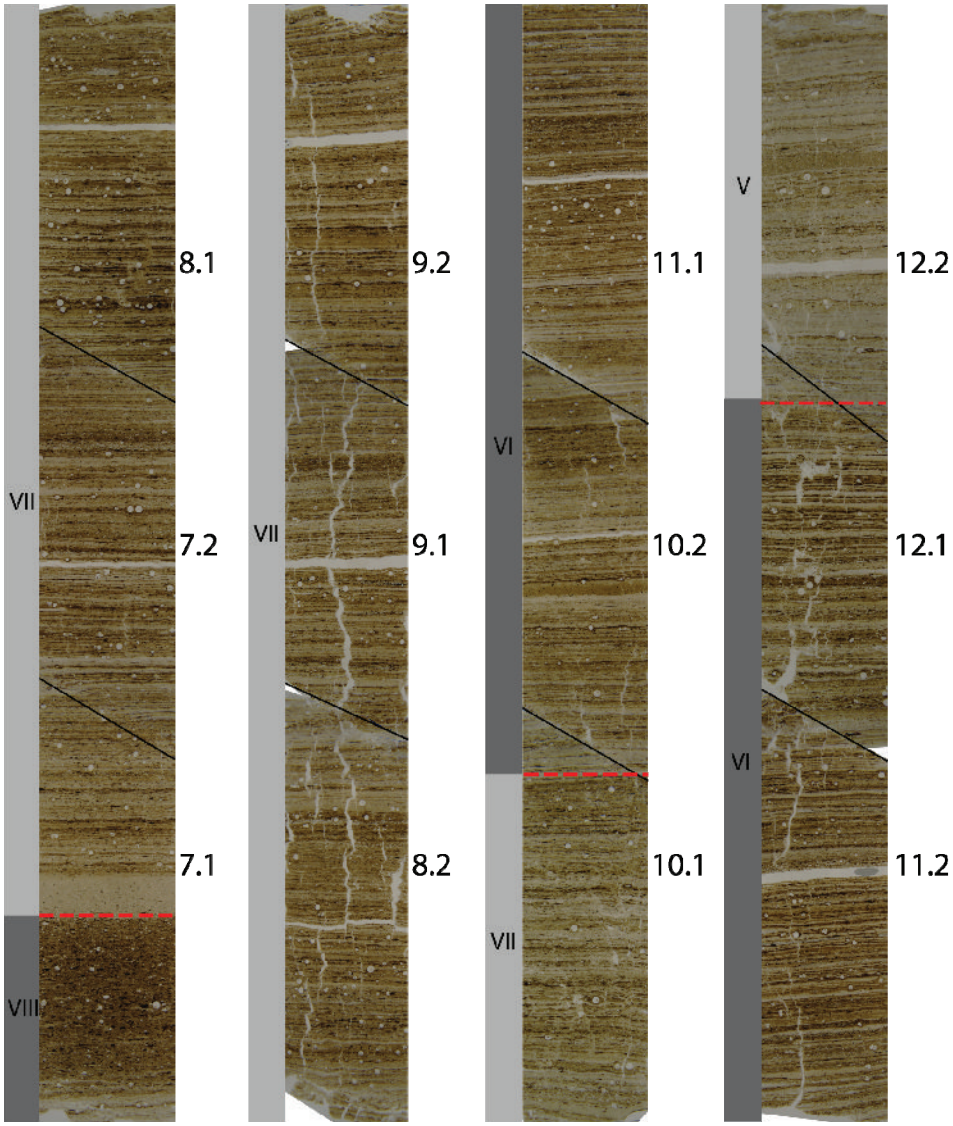

Figure 38 continued.

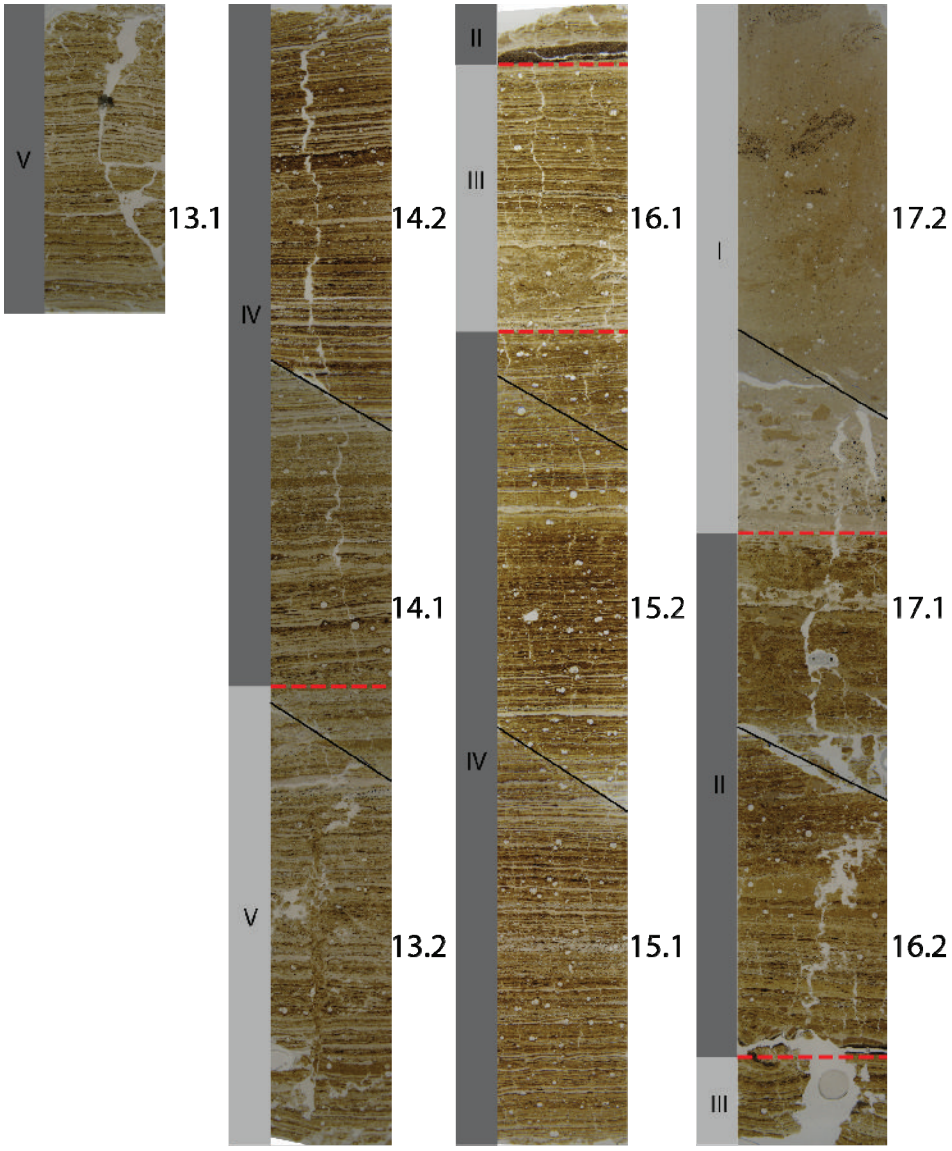

Figure 38 continued.

Based on analyses of smear slide samples (Wolff, 2011), the siliceous microfossils in zone X show severe signs of dissolution (Figure 39), which might be responsible for a collapse of the porous framework of diatom mats and a deformed optical impression of the residual in the thin-sections. Thus, the first laminae to be counted occur at a depth of 437.3 cm (uppermost part of zone X), 9 cm above the onset of the sapropel. From here, the lamination can be followed until the termination of the sapropel with little changes in opal dissolution, as is corroborated in the study of Wolff (2011) and a preliminary SEM for this study, conducted by Dr. Schulz (Figure 39).

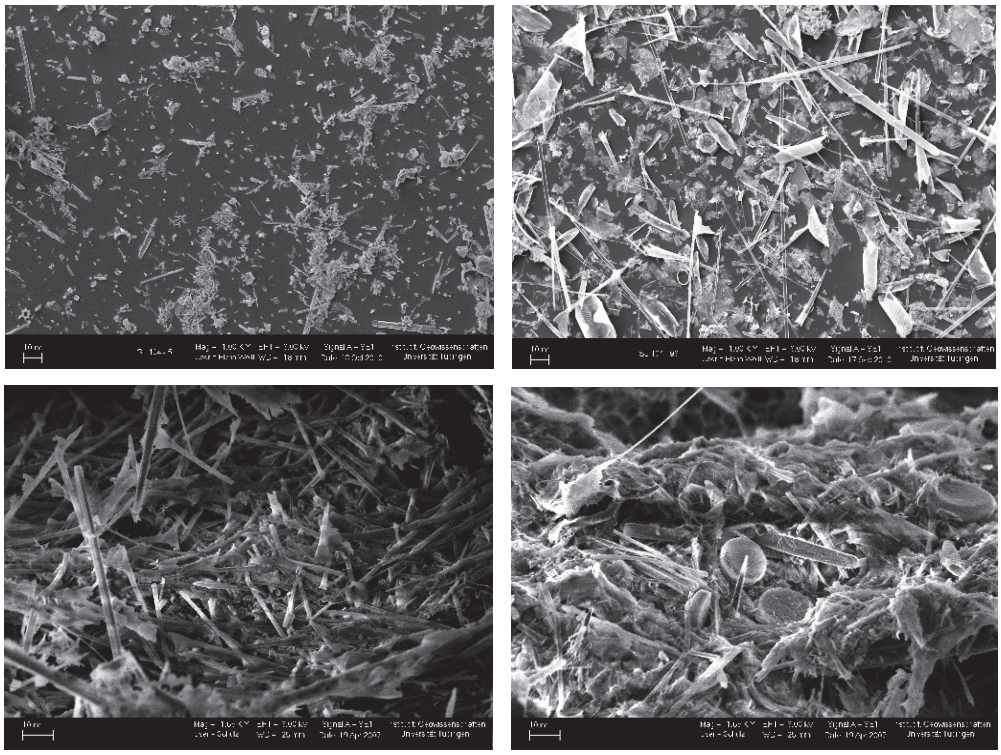

Figure 39: SEM pictures (1000x magnification) from the basal part (depth 440.2 cm, zone X) (**Top-left**) and the central part (depth 426.1 cm, zone VIII) (**Top-right**) of sapropel S_5 in core M51-3 SL104 (Wolff, 2011). The microfossils in the basal part of the sapropel (top-left) show signs of fragmentation and point at dissolution. The assemblage in the central part of the sapropel (top-right) shows a largely intact and diverse community of elongated diatoms. **Bottom:** SEM secondary electron images (taken by Dr. Hartmut Schulz) of fixed, dried and Pt-coated bits of sediment showing intact lamination. **Bottom-left**: Mat-like framework *Thalassionema* together with *Thalasiotrix*, calyptrae of *Rhizosolenia* and setae of *Chaetocerus* (Core GEOTÜ- SL103). **Bottom-right**: Dense and mixed assemblage of *Thalassionema*, calyptrae of *Rhizosolenia* and centric diatoms. Note the difference in the fabric and the overall absence of non-siliceous particles. Pictures were taken with a magnification of 1.65 k. Scale bar at the lower left of each image is 10 µm. (Bottom pictures from Moller et al., 2011a).

In one case, an extremely thick bright lamina can be observed in thin section 7.1 at a depth of 413 cm in SL104, together with a dark bed directly underneath (Figure 40, Figure 38 Thin-section 7.1), which also features an unusual thickness, compared to the majority of observed laminae couplets. While a bright lamina with extraordinary thickness has been observed only once, homogenous dark interceptions with thicknesses between 3 and 5 mm were observed twice at depths of 414 cm (Thin-section 7.1) and 433 cm (Thin-section 3.2). With contribution to the normally sub-mm thin laminae, these relative thick homogenous beds might depict periods, where potentially no typical diatom bed was formed, due to certain conditions in the environment. As it was not possible to define and count any subordinated lamination within these layers, we counted

Figure 40: Detail from thin section 7.1 with unusual thick bright above a dark laminae at the base, and regular developed laminae couplets in the upper third of the picture.

them as one lamina. Despite a potential error, we abandon a possible interpolation, since we cannot rule out the possibility of the formation of such an extremely thick laminae during one year, which has been reported for example from Antarctica, where seasonal export flux of diatoms produce varves with a thickness of about several centimetres (Pike et al., 2004).

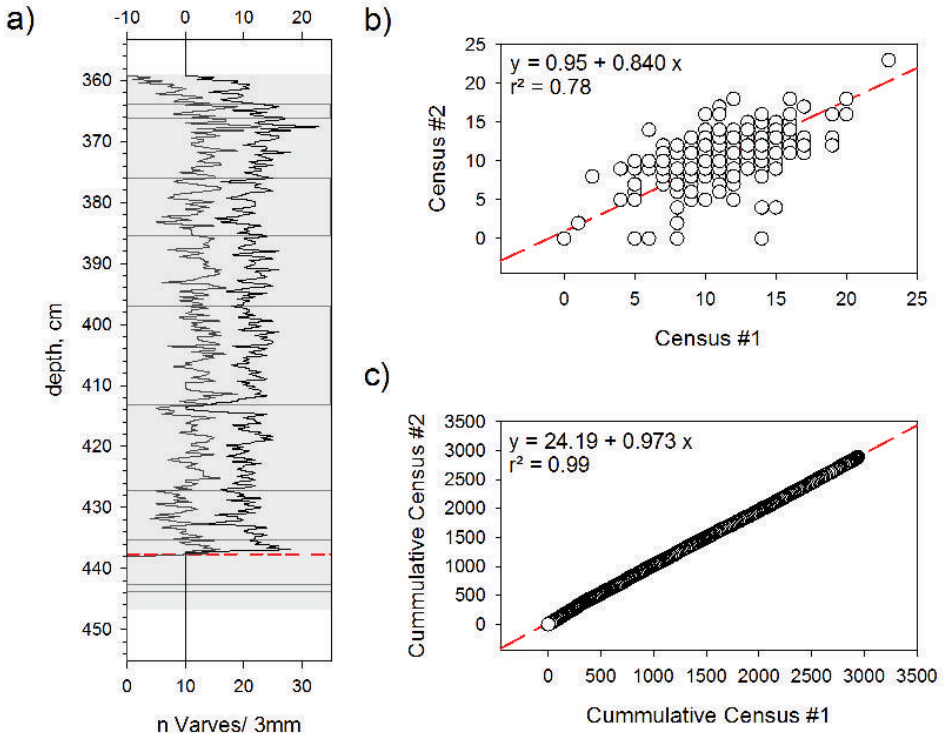

Figure 41: **a)** Census of varves per 3 mm interval in sapropel S_5 in core M51-3 SL104 from thin sections. The gray and black curve represent census 1 and 2, which were plotted with an arbitrary offset for enhanced readability and range from a minimum of 1 to a maximum of 23 varves per investigated 3 mm interval with an average of 11 varves. **b)** Cross-plot of census 1 and 2 with regression and r^2. The symmetric arrangement on both sides of the regression line indicates that deviations in both counts are not systematic and underline their comparability. **c)** Cross-plot of cumulative numbers of varves from census 1 and 2 with regression line, equation and r^2. Both counts are highly correlated and feature minimal differences. The slope, which is close to 1 highlights the redundancy of both counts.

Ultimately, we result in an overall number of 2889 varves in the first census and 2938 varves in the second census (Average 2913 varves (years) ± 1.2% standard deviation). As explained in chapter 3.6.2, the varves were counted in intervals of 3 mm, which coincide with the intervals from the discrete samples from the U-channels of M51-3 SL104. The number of varves within these intervals ranges from 1 to 23, with an average of 11 varves per 3 mm interval, whereas a trend cannot be identified (Figure 41a). Although both censuses occasionally show deviations between each other, this deviation is not systematic as is indicated by the symmetric arrangement around the regression-line (Figure 41b). The slope of the cross-plot of the cumulative counts (Figure 41c), which is close to one, indicates highly similar results in both counts, and also the high r^2 value proclaims only minor deviations between both census campaigns.

5 Discussion

5.1 Event based floating chronology of S_5

The sequence of disappearances and reappearances of planktonic foraminifera, as well as concentrations of stable isotope values throughout the investigated interval are shown in Figure 34, Figure 35 and Figure 36. This sequence is not unique for the S_5 sapropels from the Pliny Trench region, but instead is characteristic for S_5 sapropels from the Eastern Mediterranean and can be followed in at least 4 cores (Cane et al., 2002). Cane et al. (2002) made use of this phenomenon and established a regional S_5 chronology, which is based on defined events of disappearance and reappearance of different species of planktonic foraminifera as well as high and low points in the stable isotope record (Table 8).

Table 8: Overview of the correlation markers, assigned by Cane et al. (2002) and their depths below sediment surface (cm) in 971A, which holds the master stratigraphy for S_5 sapropels, and the here investigated S_5 interval from SL104 (modified after Cane et al.,2002).

Correlation point	Species/ Stable isotope	Definition	971A depth	SL104 depth
i1	*N. pachyderma* $\delta^{13}C$	Prominent isotopic depletion peak at sapropel cessation.	39.25	/
f1	*G. scitula* faunal	Last sample before species reappears in detectable quantities.	40.75	360.4
i2	*N. pachyderma* $\delta^{13}C$	Second prominent isotopic enrichment peak.	45.75	/
f2	*G. sacculifer* faunal	Last sample before species reappears in detectable quantities.	48.75	405.4
i3	*N. pachyderma* $\delta^{13}C$	Prominent isotopic depletion peak between i1 and i11.	49.75	/
f3	*O. universa* faunal	Last sample before species reappears in detectable quantities after short absence.	51.25	413.8
i4	*G. ruber* $\delta^{18}O$	Prominent shoulder of isotopic depletion after maximum enrichment within sapropel.	52.75	432.1
f4	*G. scitula* faunal	Species no longer present in detectable quantities.	53.25	427.3
i5	*N. pachyderma* $\delta^{13}C$	First prominent isotopic enrichment peak.	53.75	/
i6	*G. ruber* $\delta^{18}O$	Prominent shoulder before sharp enrichment trend.	56.25	437.8
f5	*G. sacculifer* faunal	Species no longer present in detectable quantities.	57.75	440.2
f7	*O. universa* faunal	Species no longer present detectable quantities after large abundance at sapropel base.	59.75	442.9
f6	*N. pachyderma* faunal	Last sample before species reappears in detectable quantities after short absence.	60.25	441.4
f8	*G. inflata* faunal	Species no longer present in detectable quantities.	61.75	445.9
i7	*G. ruber* $\delta^{18}O$	Mid-point of isotopic depletion at sapropel onset.	62.25	446.4
i8	*G. ruber* $\delta^{13}C$	Peak before isotopic depletion.	63.25	447.4
f9	*G. ruber* pink faunal	Last sample before species appears in detectable quantities.	63.75	448.3
f10	*N. pachyderma* faunal	Prominent peak below sapropel preceding sharp drop in abundance.	65.25	448
f11	*N. pachyderma* faunal	Lowest abundance of species after sapropel formation.	31.25	356.8
i9	*G. ruber* $\delta^{13}C$	Prominent peak in isotopic enrichment after sapropel.	31.25	353.5
f12	*G. sacculifer* faunal	Last sample before species reappears in detectable quantities.	43.75	387.1
i12	*N. pachyderma* $\delta^{18}O$	First major depletion.	55.75	/
f13	*G. glutinata* faunal	Species no longer present in detectable quantities within sapropel.	57.25	437.2
i10	*G. ruber* $\delta^{13}C$	Shoulder during isotopic depletion in basal third of the sapropel.	59.25	442.6
i11	*N. pachyderma* $\delta^{13}C$	Prominent isotopic depletion peak after sapropel onset.	59.25	/
f14	*G. siphonifera* faunal	Last sample before species appears in detectable quantities.	71.25	454.3

With exception of the oxygen isotopes of *N. pachyderma*, which have not been measured, all of these biostratigraphic events (Cane et al., 2002) were found in the here investigated S_5 sapropel. This circumstance marks an important result and underlines, that the here presented sapropel S_5 in M51-3 SL104 is well comparable to site 971A. It did not experience post depositional oxidation or bioturbation and is, despite its unusual thickness and the lamination, comparable to other Mediterranean S_5 sapropels. Due to the high degree of correlation, this should also account for the sapropel S_5 in M51-3 SL103 and M40-4 SL67, which further confirms a uniform picture of

planktonic foraminiferal event stratigraphy in the Eastern Mediterranean. Vice versa, the highly divergent thickness of S_5 sapropels (Figure 19, Figure 20) argue for a wide range of S_5 depositional and preservational conditions, obviously not primarily related to water depth.

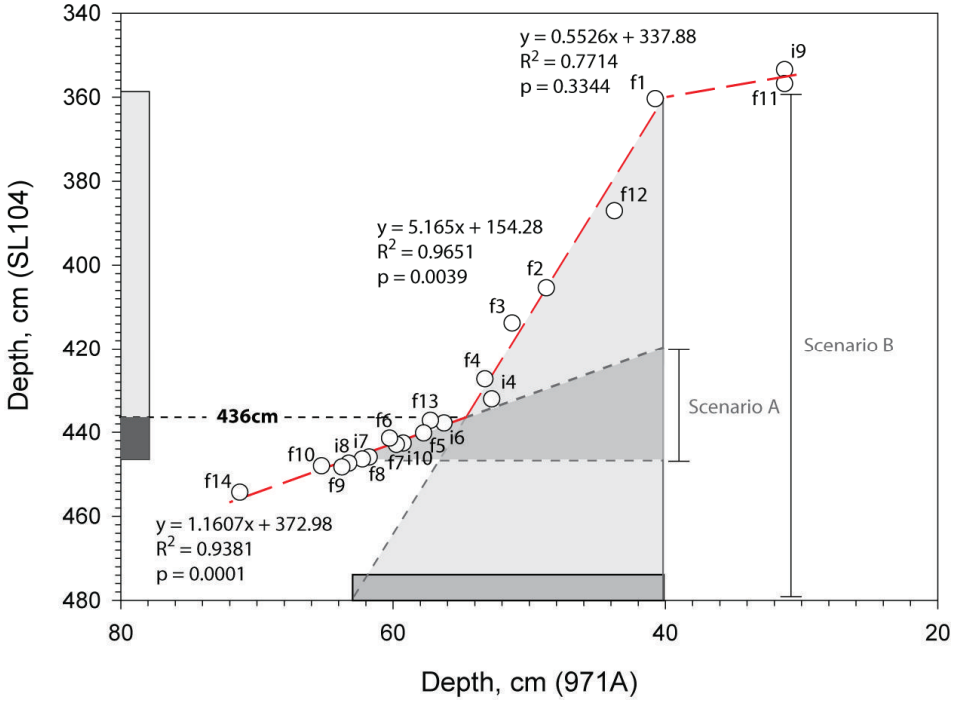

Figure 42: Depth-depth plot of faunal (f) and isotopic (i) events (Table 8) in and around sapropel S_5, as defined by Cane et al. (2002) between the here presented core M51-3 SL104 and 971A, which holds the master stratigraphy of S_5 sapropels from the Eastern Mediterranean. Sapropel S_5 in SL104 experienced a strong increase in sedimentation rate between i6 and i4 (Top of subunit X) at a depth of about 436 cm, according to the solution of the equations of both regression lines. Another shift to a lower sedimentation rate occurs at the termination of the sapropel (359.5 cm) close to f1. Scenario A simulates a permanent low rate of sedimentation according to the lower regression line and results in a theoretical thickness of 23 cm. Scenario B simulates a permanently high sedimentation rate and results in a theoretical thickness of about 120 cm.

As apparent from the depth-depth plot (Figure 42) of the faunal and isotopic events in SL104 and 971A, with the latter holding the master stratigraphy for S_5 sapropels (Cane et al., 2002), S_5 in SL104 experienced changes in the sedimentation rate between the isotopic events i6 and i4, as well as after faunal event f1, which marks the termination of the sapropel. Optimized for maximum fit, the linear regression lines, which describe the consecutive sequence of events (Table 8), intersect at a depth of ~436 cm, about 10.3 cm after the onset of the sapropel. The slope of the regression from event f14 to event f6 is 1.2 and is within the range of slopes, published by Cane et al. (2002). The interval from 436 cm until the termination (359.5 cm) is instead characterized by a slope of 4.7, which suggests more than 3.9 fold of sediment thickness in SL104 compared to 971A in the same time. After the termination of the sapropel (359.5 cm), the slope of the regression is lower and more comparable to the lower part of the sapropel and the underlying marl.

The reason for this massive increase in the sedimentation rate can be seen in the enhanced preservation of different species of elongated and mat forming diatoms. Whereas signs of dissolution were observed in the lower part of the sapropel (Figure 39) (Wolff, 2011), intact laminae were firstly observed at a depth of the basal part 437.3 cm (Figure 41). The calculated depth from the intersecting regression lines deviates slightly from this observation, but nevertheless represents a mathematical approximation, which supports the direct and actually used sediment observation (437.3 cm). Next to the optically observed visible sub-mm thin lamination, the enhanced sedimentation rate is also expressed in the values of water content and XRF abundances of Si/Ca as a result of strongly elevated deposition of the porous meshes of diatoms. As shown in Figure 43A, the abundances of Si in SL103 and SL104 do not increase immediately after the onset of the sapropel but start to rise coeval at a depth of ~445 cm on the common depth scale (~450.5 cm in SL103 and ~436.2 cm SL104). This pattern mimics the observations from the thin sections and supports the calculated depth of cross plots and ultimately suggests that the sapropel S_5 in the here investigated set of sediment cores experienced a shift into a more diatomitic regime ~9 cm after its onset. Also the water content accommodates for this issue, although the pattern here is slightly different: a first increase can be observed directly at the base of the sapropel, but, according to the Si/Ca abundances, a stable plateau is reached at a master scale depth of ~444 cm (~449.5 cm in SL103 and ~435.2 cm SL104). Throughout the sapropel, water content ranges between 70 – 80 %, which documents the strongly enhanced porosity, caused by the loose fabric of diatom frustules. As Figure 43B further indicates, a linear positive correlation exists, between water content and the abundance of silica in the sediment as soon as water content is above 65%. The samples below 65% water content comprise samples from the enclosing marls and the non-diatomitic part of the sapropel and illustrate, that variations in the water content between 40 – 65%, and thus the porosity, are possible without the obvious influence of diatoms.

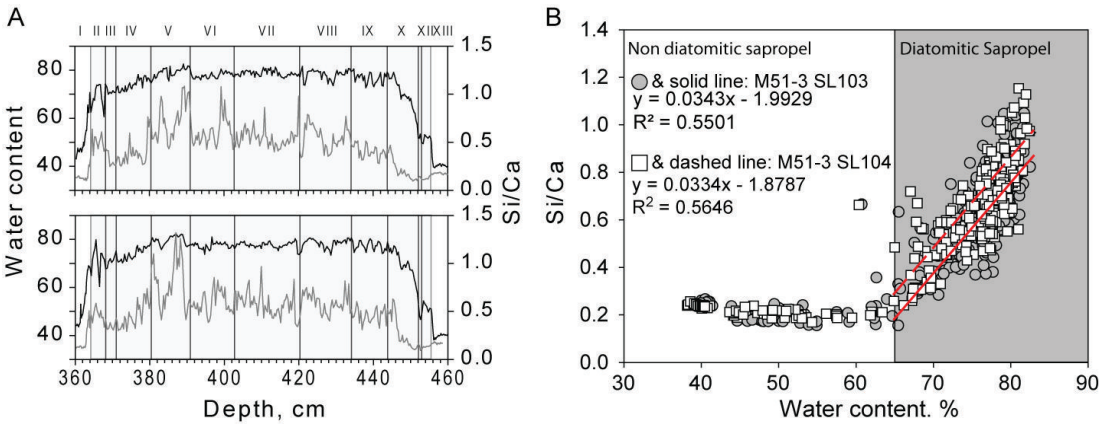

Figure 43: **A)** Water content (black curves) and Si/Ca abundances (grey curves) in SL103 and SL104. Silica values are firstly increasing at a depth of 437.3 cm, according to the occurrence of mat forming diatoms. Water content, and thus the sediment porosity, is increasing with the onset of the sapropel formation, but reaches highest values during the diatomitic facies. **B)** Cross plot between water content (Porosity) and abundances of Si/Ca. Water contents beyond 65 % can only be realized under the presence of the porous, silica tests of diatoms, where both parameters form a linear relationship. Water contents below 65%, go down to values of 38 % and reflect the natural variability of the enclosing marls and the non diatomitic sapropel in SL104. (From Moller et al. (2011a)).

With the two different modes of sedimentation, apparent in one sapropel interval, it is possible to create two theoretical end-member scenarios, which include either no diatomitic influence at all (Scenario A) or a development of the sapropel under a permanent diatomitic regime (Scenario B). In the simple graphical solution, shown in Figure 42, the lower regression line was extended until the upper limit of 971A for scenario A and result in a theoretical thickness of about 25 cm. This result is remarkable close to the supposed average S_5 sapropel thickness of 23 cm (Chapter 4.1, Figure 20) and also the results, proposed by Moller et al. (2011a) and Cramp and O'Sullivan (1999). In opposite, for scenario B, the regression line for the diatomitic interval was extended until the onset of the sapropel to simulate the presence of diatoms also in the actual non diatomitic basic 9 cm. Here we result in a theoretical thickness of 121 cm, which is very close to the 120 cm of S_5 in LC21 from the Aegean Sea (Marino et al., 2007), which marks the most intensely developed S_5 sapropel so far, although LC21 seems not to be diatomitic (personal communication with Eelco Rohling).

5.2 Varve and absolute chronology of S_5 in SL104

As shown in chapter 5.1, sapropel S_5 in the here presented material, experiences a severe increase in the sedimentation rate at 437.3 cm depth, 9 cm above the base of the sapropel, which was committed by the erratic occurrence of mat forming diatoms and is visible as sub-mm fine lamination, representing the annual late-spring to late summer blooms of mesh building diatoms species, such as *Rhizosolenia* and *Thalassionema*.

As shown in the depth-depth plot in Figure 42, the slope of the regression in the lower core interval from 446.5 cm to 436 cm is specified with 1.16x, which is well in the range of slopes of the other sediment cores, emerging from the depth-depth plot of KS205 (1.067x) and 967C (1.595x) against the master core 971A as shown in Cane et al. (2002). With respect to the rather loose result from the intersection given by the regression lines (Figure 42) and the first observed occurrence of mat forming diatoms in SL104 at a depth of 437.3 cm, we thus suggest, that this lower sapropelic interval from 446.5 cm to 437.3 cm developed under a similar environmental regime and similar sedimentation rates than other regular S_5 sapropels such as in 971A and KS205. Figure 19 and Figure 20 show, that the majority of S_5 sapropels in the Eastern Mediterranean range from 20 cm to 30 cm (Cramp and O'Sullivan, 1999; Moller et al., 2011a), whereby the averaged thickness adds up to ~23 cm (Moller et al., 2011a). With an assumed comparability of sedimentation rates, we thus suggest that the non-diatomitic basal interval in SL104 with a thickness of 9 cm already envelopes 39 % of an averaged, yet hypothetic, sapropel with 23 cm and thus also 39 % of its total record. Consequently, the diatomitic interval in SL104, with 2889 to 2938 counted varves, depict the remaining 61 % of the total duration. With these boundary conditions at hand, an overall age of 4753 and 4834 years is evaluated for the age of sapropel S_5 in SL104 and the other S_5 sapropels from the Pliny Trench sapropel and thus the peak warmth of the last interglacial period. Hereby, 1864 – 1896 years are delotted to the basal interval and 2889 – 2938 years to the clearly laminated facies, if we adopt our double-counted varve model as reliable (see discussion chapter 4.8). This is an interpolation, but it seems to be justified from the relative stability of the reconstructed environmental conditions, e.g. the paleo SSTs, stable isotopes, which show largest changes rather with the onset of the sapropel deposition, and relatively minor changes within the lower 9 cm of the sapropel.

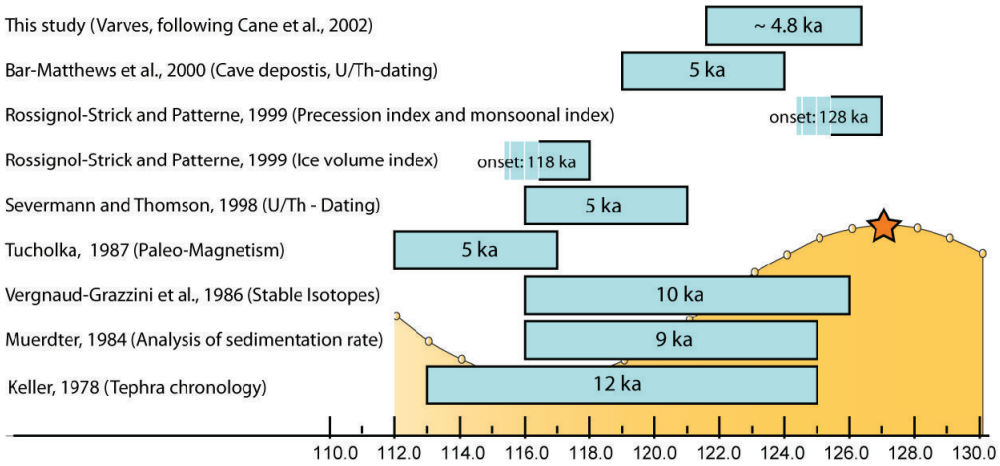

Figure 44: Duration and time frame of sapropel S_5 according to various methods from different studies. Qualitatively, the insolation curve is added in the background, with the insolation maximum at 127 ka further indexed with a ★.

So far, the here presented varve age with a duration of about 4.8 ka represents the most direct approach for the dating of the S_5 sapropel and is for example comparable to the youngest sapropel S_1, which could be dated directly with the C^{14} method. Compared to other studies, the result of this study is well in the range of yet known S_5 durations, as illustrated in Figure 44 (Tucholka et al., 1987; Severmann and Thomson, 1998; Rossignol-Strick and Paterne, 1999; Bar-Matthews et al., 2000), but is comparably short, especially, when compared to older studies (Keller et al., 1978; Muerdter et al., 1984; Vergnaud-Grazzini et al., 1986). However, a duration of only about 5 ka agrees well with the U/Th dated record from cave deposits, suggesting a wet phase in the Eastern Mediterranean. According to the lag of 3 ka, which is based on the difference of the midpoint of youngest S_1 sapropel (8.5 ka) and the correlated maximum in insolation (11.5 ka) and minimum in precession, respectively (Hilgen et al., 1995; Lourens et al., 1996; Langereis et al., 1997; Ziegler et al., 2010), the onset of the sapropel is here located at ~126.4 ka. To this end, our study provides a rather straight forward model for the duration of S_5, but not for the onset, where other studies allocate a 3 ka lag between insolation maxima and the onset of the sapropel formation instead of the midpoint.

5.3 Genetic model for S_5 sapropel formation

As shown in the results chapter, the anoxic conditions in the water column during the deposition of the sapropel as well as the enhanced thickness, both provide a high resolution window to the peak warmth of the last interglacial period. Similar to the multitude of studies (Cheddadi et al., 1998; Kühl and Litt, 2003; Sirocko et al., 2005), which gave proof to the assumption that sapropel S_5 has not been deposited under a stable climatic regime, this is further corroborated by variations of the here collected data, such as XRF elemental abundances, stable isotopes and planktonic foraminifera census counts. Here, our environmental proxies are discussed in terms of their environmental meaning for the aim of a genetic model of the Pliny Trench sapropels with their complex, yet highly structured pattern of layers (Figure 21). Special emphasis is laid on the onset of the diatomic facies about 1.9 ka after the onset of the sapropel formation, leading to a drastic increase in sedimentation rate. The various environmental parameters are discussed in a temporal context, according to the here developed age model.

5.3.1. Hydrographic changes

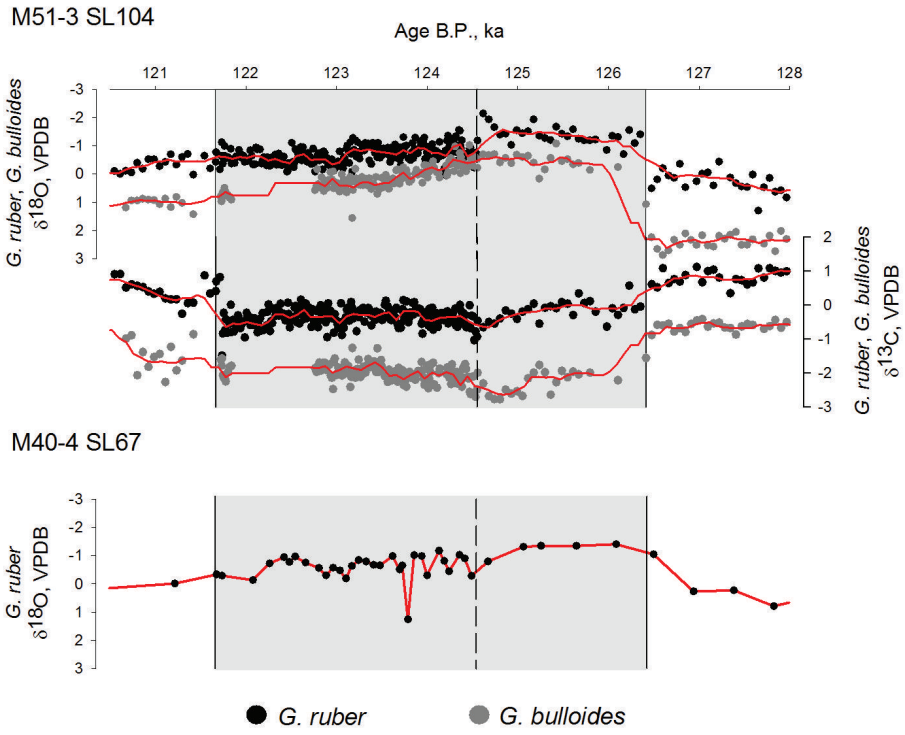

Figure 45: $\delta^{18}O$ and $\delta^{13}C$ anomaly of *G. ruber* and *G. bulloides* in M51-3 SL104 and M40-4 SL67 (Data of M40-4 SL67, taken from Schmiedl et al., 2003b). The visible sapropel interval is shaded in gray and the dashed vertical line indicates the onset of the laminated diatomitic facies. The time axis follows the here established age model (chapters 5.1 and 5.2).

The freshwater balance poses a fundamental parameter in the hydrographic framework of the Eastern Mediterranean basin. In the modern Mediterranean Sea, the input of freshwater remains low and results in a generally negative water balance, ultimately leading to an exchange of water masses with the open ocean and a defined thermohaline circulation pattern (Robinson et al.,

1992). In contrast, during sapropel formation, enhanced river discharge and precipitation (Rohling, 1994; Emeis et al., 2000) can be seen as major agents for inducing anoxic bottom water conditions due to the formation of a low salinity cap of water, which diminishes the overturning circulation.

Consequently, the oxygen isotopic record of S_5 in the sediment cores SL104 and SL67 (Schmiedl et al., 2003b) (Figure 45) show a characteristic pattern, which is comparable to the results of numerous other S_5 sapropels from the Eastern Mediterranean (Figure 46). With the onset of the visible part of the sapropel in SL104, a steep trend to light isotopic values is realized within one sample in *G. ruber* as well as *G. bulloides*. Based on the here presented age model, this suggests a duration of about ~60 years, during which the intensive vertical mixing in the water column collapsed. This duration is comparable to the results from Marino et al. (2007) (40 ± 20 years) for sediment core LC21. The slightly longer duration in our material might be due to differences in the temporal resolution at the base of the sapropel and potentially was significantly faster. This is affirmed, for example, at the termination of the sapropel, where the re-oxygenation is realized within 2 – 4 samples, suggesting a period of about 20 – 40 years. Similarly, also the $\delta^{13}C$ values do react to the sapropel formation and become lighter in both species, which can be interpreted as an increasing portion of recycled nutrients from the chemocline (Marino et al., 2007).

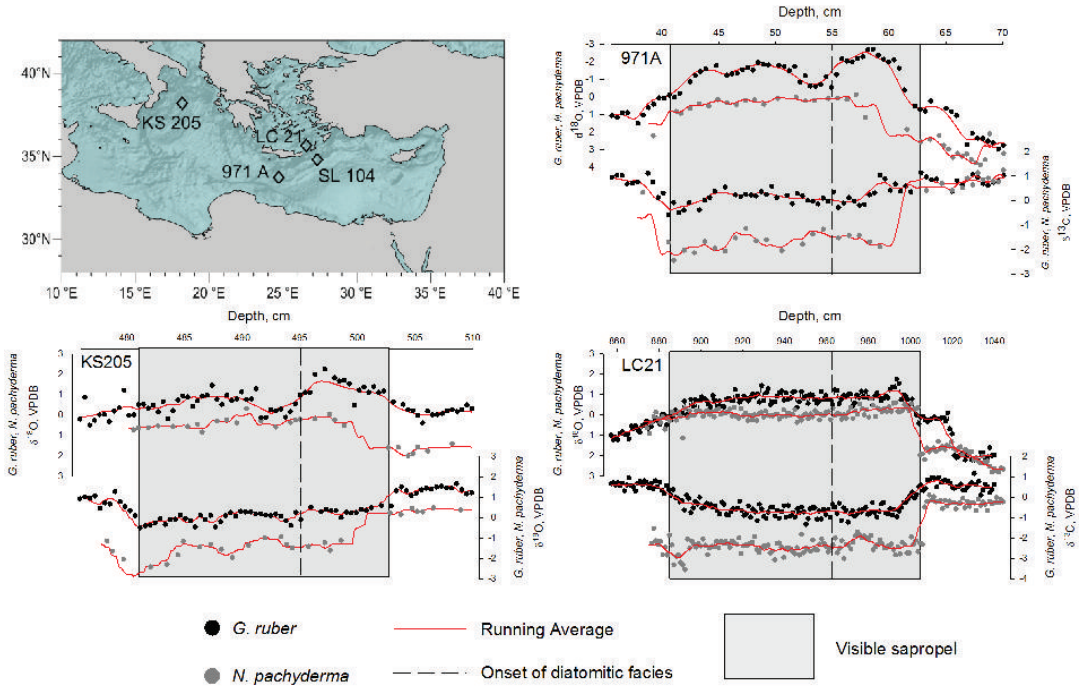

Figure 46: Sediment cores 971A, KS205 (Cane et al., 2002) and LC21 (Marino et al., 2007) (Raw data from Eelco Rohling) from the Eastern Mediterranean, containing sapropel S_5, together with their $\delta^{18}O$ and $\delta^{13}C$ concentrations in *G. ruber* and *N. pachyderma*. The depth of the onset of the lamination as observed in our cores is indicated by the dashed vertical line, and these depths in 971A, KS205 and LC21 were calculated by with the depths of faunal and isotopic events (Cane et al., 2002; Marino et al., 2007) of each core and M51-3 SL104.

As apparent from Figure 45, *G. bulloides* features heavier $\delta^{18}O$ values than *G. ruber*, which points at cooler and more saline waters of the intermediate water layer, of which *G. bulloides* is a typical inhabitant (Hemleben et al., 1989). We can also see that *G. bulloides* is affected more intensely by the $\delta^{18}O$ anomaly during sapropel formation than *G. ruber* and also approximates towards the values of *G. ruber*. A similar effect can also be observed in the S_5 interval of other localities between *G. ruber* and *N. pachyderma*, which also prefers intermediate waters (Sangiorgi et al., 2006)(Figure 46). This approximation in the oxygen isotopes, as observed for example in LC21 (Marino et al., 2007) and also KS205 is here ascribed to the habitat of *N. pachyderma*, becoming more similar to that of *G. ruber*. Although this pattern could be also interpreted as a shift of *N. pachyderma* into shallower habitat due to rising anoxia, as done by Sangiorgi et al. (2006), this is unlikely, since a similar approximation of $\delta^{13}C$ values in both species cannot be observed. With regard to the onset of the laminated diatomic facies at a depth of 437.3 cm in SL104 (dashed line in Figure 45), the strongest freshwater dilution is supposed to occur prior the diatomitic facies, as well as the heaviest values in $\delta^{13}C$. Interestingly, the occurrence of these diatoms exactly coincides with a strongest fallback to heavier $\delta^{18}O$ values. Since this large shift in the stable isotope record can be observed in most other S_5 sapropels in the Mediterranean (Figure 46), this suggests a major shift in the hydrographic pattern of the Eastern Mediterranean. Despite the broad similarities of S_5 in SL104 and SL67 (Figure 45) and other localities (Figure 46), also differences can be identified, which can be possibly assigned to the distance to the North African coast and the outflow of the Nile River as well as wadi river systems. Here for example, 971A shows a defined and instant increase to light oxygen isotopes as well as a varying evolution of $\delta^{18}O$ values. KS205 is situated in the Ionian Basin and shows the same pattern although with lower amplitude and a distinct temporary lag of events. In comparison with KS205 and 971A, $\delta^{18}O$ values of LC21 and SL104 are less variable in amplitude and become constantly heavier after the onset of the diatomitic lamination.

5.3.2. Terrestrial input

Amongst others, Mercone et al. (2001) showed a decrease in Ti contents during the warm period, when sapropel S_1 formed. Accordingly, Ti/Al ratios in the here investigated interval also show a clear decrease within the S_5 sapropel (Figure 47), suggesting a deposition during a period with an enhanced vegetation cover in North Africa, which decreases the deflation potential of the surface. This is consistent with multiple proxy data from Africa and the Middle East, indicating a major wet phase during this time (Bar-Matthews et al., 1999; Osborne et al., 2008). Interestingly, the depletion of Ti/Al does not start instantly with the onset of the visible part of S_5. Instead, Ti/Al remains on a high level, similar to that of the previous ice age in MIS6. A first gentle drop is visible at the base of Zone X, about 700 years after the start of the sapropel deposition. From here Ti/Al ratios steadily decrease and sharply drop in the upper part of zone

X at about 124.55 ka, which coincides with first observation of diatomitic laminae, as well as the severe drop in $\delta^{18}O$ values (Figure 45). Lowest values in Ti/Al are present in zones VII to V (Figure 47), from where they increase steadily until they reach a stable level after sapropel, which is as high as before the sapropel in SL103 and slightly lower in SL104. Given the bioturbation within the zone II and III, it is entirely possible that the onset of Ti deposition was sharper in reality, than it appears in the sapropel record.

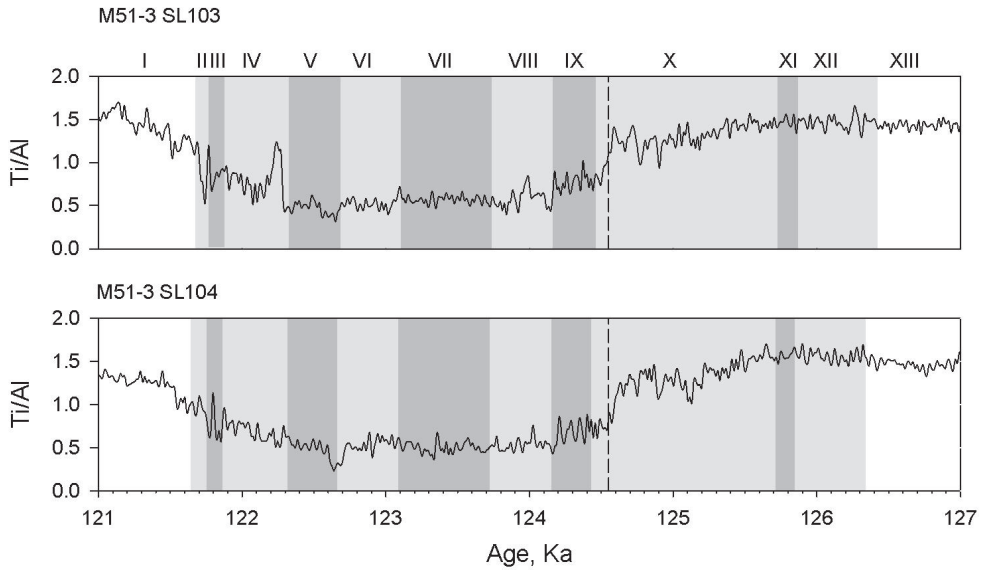

Figure 47: Elemental abundances of Ti/Al in M51-3 SL103 and M51-3 SL104, representing the terrestrial input. The time axis was raised with the information of major changes in the sedimentation rate given by faunal and isotopic events by Cane et al. (2002) as well as the minor changes in the sedimentation rate, given by the varve counts. The visible sapropel and the optically defined subunits are hatched in light-grey and grey and the onset of the diatomitic facies is marked by the dashed line at about 124.55 ka.

This abrupt change in the Ti/Al XRF abundances (Figure 47) might be compared to the African Humid Period (AHP) in the early phase of the Holocene from about 15 ka to 5.5 ka. Here, the study from deMenocal et al. (2000) states an immediate drop in the terrigenous input and Timm et al. (2010) mentions the positive vegetation-albedo-precipitation feedback for a further strengthening of the monsoon and accelerated establishment of humid conditions. Yet, we here see a temporal discrepancy, since the AHP and the drop in the terrigenous input is supposed to be triggered by a threshold in the insolation with values of 4.2% above the present day (deMenocal et al., 2000). Instead, the drop in Ti/Al in the here investigated sapropel follows the insolation maxima by about 2.5 ka. Both studies also mention the importance of non-linear feedback systems (deMenocal et al., 2000) as well the combined effects of orbital forcing and remote forcing from retreating ice-sheets (Timm et al., 2010) as necessary preconditions. Potentially these preconditions might not be fulfilled sufficiently during the moment of highest insolation at 127 ka but potentially in the mid and late periods of S_5 deposition.

Another explanation denotes a more important role of the $\delta^{18}O$, which points at a strongly diminished input of freshwater into the Mediterranean at the same time as abundances of Ti/Al drop. MIS 5e was characterized by an extreme northward shift of the North African Monsoonal System, potentially even beyond the Saharan Watershed (Larrasoaña et al., 2003). Potentially, this extreme northward penetration of the monsoonal precipitation did not prevail right from the beginning of the sapropel but firstly unfolded its full potential after a certain lag of about 1.9 ka. Subsequently the enhanced precipitation allows the development of a savannah-like plant coverage, which can store larger amounts of water and consequently diminishes the potential of deflation. Yet, beside the transport in wind-blown dust, Ti/Al is also transported by the Nile River and wadi river systems along the North African coast (Krom et al., 1999; Sangiorgi et al., 2006) and the highest freshwater input at the base of the sapropel, here might be responsible for a substantial portion in the Ti/Al input.

Focussing on the cm-scaled layering (Figure 30, Figure 31), Ti/Al is mostly enriched in the darker layers of the sapropel, whereas the brighter intervals feature lower values. Generally, dust, especially from the Sahara, penetrates the Mediterranean Sea throughout the year. Yet, the majority arrives during the wet season, where precipitation scavenges the dust-laden air (Bergametti et al., 1989; Molinaroli et al., 1993; Guerzoni et al., 1999; Gao et al., 2003). Since the Northern Hemisphere winter brings the majority of precipitation to the Mediterranean Sea (Figure 3), dark layers with enhanced Ti/Al abundances might thus be interpreted as more humid periods, lasting two to four decades. This is also in accordance to the generally enhanced precipitation over the Mediterranean during sapropel formation (Rohling, 1994).

5.3.3. Productivity

In the investigated cores, Ba/Al increases in zone X and sharply drops at the termination of the sapropel S_5 (Figure 48). The strongest enrichments of Ba are located near the base (Zone X) and also near the top of the sapropel (Zone IV), whereas the central part features the lower Ba/Al ratios. A similar two lobed pattern of biogenic barium and TOC (Figure 48) has previously been described by Weldeab et al. (2003a) for S_5 in core SL67 and also by Mercone et al. (2001) and Thomson et al. (2006) for the most recent sapropel S_1. A 'barite-front' (Torres et al., 1996), with high Ba values above and below the visible sapropel, caused by Ba remobilization, is not visible (Figure 48) and we therefore follow the conclusion of Weldeab et al. (2003b), interpreting Ba/Al ratios as a signal of productivity. This is significant, because this element shows a strong relationship to sediment properties on the level of the cm-scaled layering. Specifically, Ba is enriched in the darker layers, which is illustrated in Figure 30 and also in the results of the correlation analyses and PCA analyses (Figure 31).

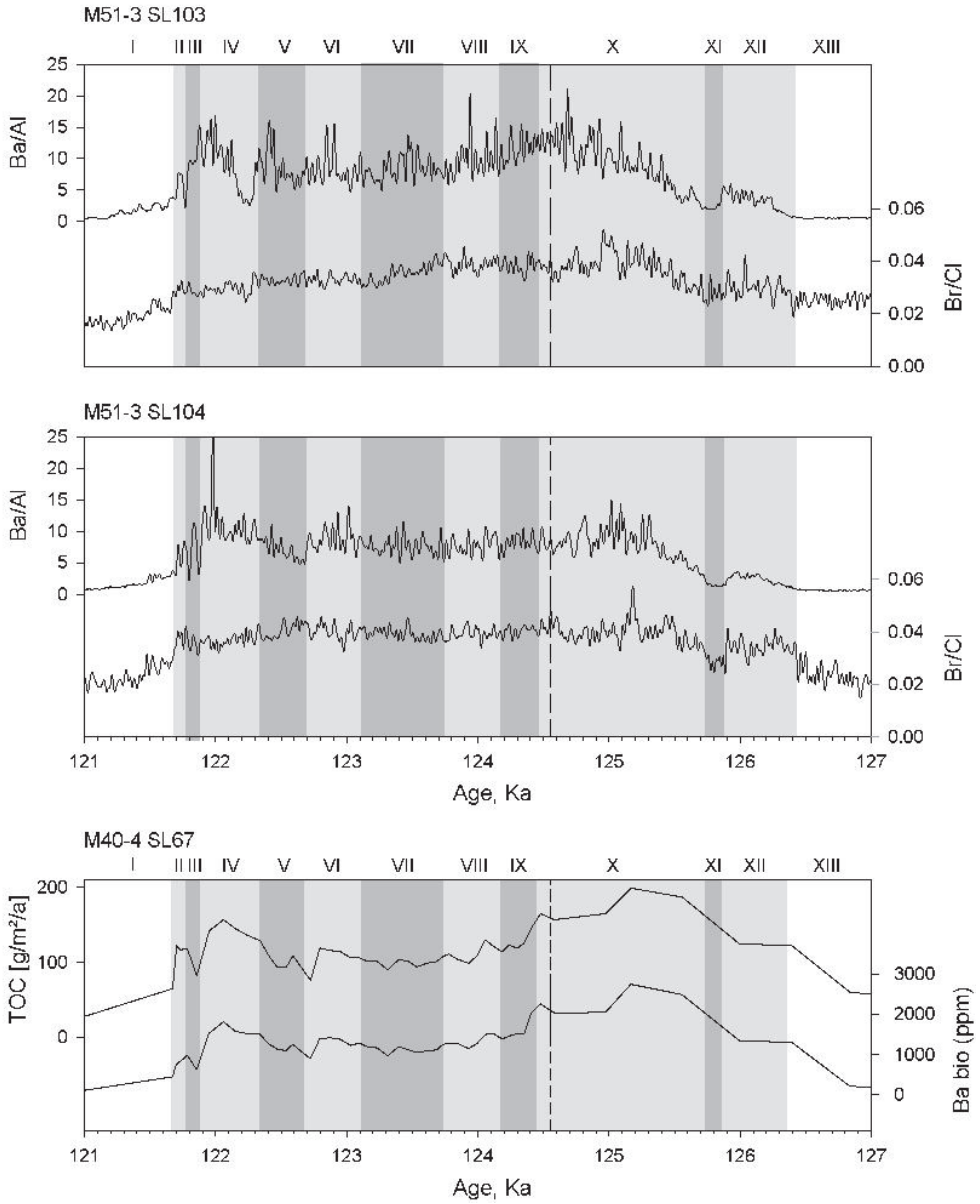

Figure 48: Elemental ratios of Ba/Al, Br/Cl in M51-3 SL103 and M51-3 SL104 reflecting the amount of productivity and direct measurements of biogenic barium and TOC in M40-4 SL67, (Weldeab et al., 2003a), here plotted against time. The time axis follows the age-model, raised in this study (chapters 5.1 and 5.2) and also applied to the data from Weldeab et al. (2003). The visible sapropel and the individual subunits are hatched in light-grey and grey. The onset of the diatomitic facies is marked by the vertical dashed line at about 124.55 ka.

In order to further underline the link between sediment properties and primary productivity, as suggested by Ba, we consider Br as another element, being potentially linked to the productivity. The terrestrial organic matter is relatively poor in Br, compared to marine organic matter (Mayer et al., 2007). This circumstance has been applied by Ziegler et al. (2008) to two sediment cores from the Arabian Sea and the Mediterranean and their results indicate a positive relationship between Br and TOC. Subsequently, M51-3 SL103 and M51-3 SL104 (Figure 48) show strongly increased values of Br/Cl throughout the sapropel and also the tendency to be enriched in darker layers relative to brighter layers (Figure 31).

Although parts of the high productivity at the base of the sapropel are resembled by the numbers of planktonic foraminifera (Figure 32A), this cannot be the sole explanation, since large numbers of foraminifera were also found in the middle part of the sapropel (zone VII), where Ba/Al is comparably low. Radiolarians were first observed at the top of zone X with modest abundances (Figure 32D) and also the low Si/Al ratios (Figure 50) point at another organism, which is not present in the fossil record of this interval. Rohling et al. (2006) and Marino et al. (2007) present measurements of the biomarker isorenieratene for sapropel S_5 in cores 971A (Marino et al., 2007) and LC21 (Figure 49). Isorenieratene is produced by green sulphur bacteria (Chlorobiaceae), which are able to perform photosynthesis under extreme low light conditions (0.0005% of the surface irradiance) and are thus able to exploit the nutrients at the chemocline as deep as 150 – 300 m (Overmann et al., 1992). Concentrations of isorenieratene and C_{org}-values in 971A (Marino et al., 2007) and LC21 (Figure 49) are highest shortly after the onset of the sapropel, which corresponds to the lower, indistinctly laminated interval of our cores and might affirm the high productivity as indicated by Ba/Al in SL103 and SL104 (Figure 48).

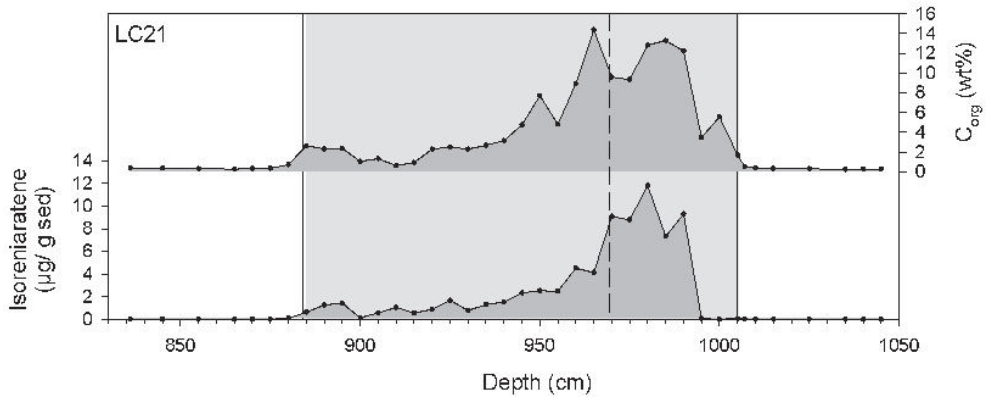

Figure 49: Concentration of C_{org} and Isoreniaratene in sapropel S_5 in sediment core LC21 from the Aegean Sea (Figure 46, Table 6). The visible sapropel is shaded in gray, and the depth of the onset of the laminated facies (dashed vertical line) in the here investigated core SL104 was calculated by the comparison of faunal and isotopic events (Marino et al., 2007) (Raw data of core LC21, by personal communication with Eelco Rohling).

While Marino et al. (2007) suggest a duration of 650 ± 250 years until the anoxia penetrates the photic zone, which would provide enhanced level of nutrients, we here result in a slightly longer duration of ~1.0 ka from the onset of sapropel formation until productivity (Ba/Al) starts to increase (Figure 48). This difference might be owed to the greater water depth and the more open marine conditions compared to LC21 in the Aegean Sea.

During the initial ~1.0 ka long episode of sapropel formation, the chemocline and the associated nutricline might have been too deep, to be exploited by deep dwelling diatoms, which were observed in depth as deep as ~150 m (Kemp et al., 2000). Instead, high productivity here might have been maintained by deeper dwelling green sulphur bacteria (Chlorobiaceae).

Summarized, the Ba/Al and Br/Cl ratios confirm the formation of the here investigated sapropel under an regime of enhanced productivity (Schrader and Matherne, 1981; Wehausen and Brumsack, 1999), being especially enriched within the darker layers of the sapropel. Since diatoms are most abundant in the brighter layers, it seems like an antagonism in the first point that the productivity is generally higher in the darker layers. Yet, this issue can be resolved, when following the previously (chapter 5.3.2) suggested idea of more intense or more prolonged winter conditions, being possibly indicated by the darker cm-scale layers and the underlying stronger developed dark winter-mixed laminae. Typically, productivity in the Mediterranean today is mostly restricted to the late winter (Figure 4), where enhanced mixing of the upper water column provides larger amounts of nutrients for the primary producers (Azov, 1986; Psarra et al., 2000). Consequently, darker layers would depict periods, where enhanced winter mixing of the upper water column provides more suitable conditions for shallow dwelling primary producers. Additionally, nutrients, such as iron, might also play an important role. Although Fe is interpreted as a proxy for redox conditions, it also is delivered to the Mediterranean Sea by aeolian transport, and similarly to Ti/Al, also enriched in the darker layers (See Fe/Al in Figure 31). Here, a vital agent might be the solubility of iron, which seems to be a complex function of the pH value of the water, in which the dust particles are transported. Also the photochemical reduction of Fe(III) to Fe(II) during long range transport ultimately improves the bioavailability of the iron (Colin et al., 1990; Zhuang et al., 1992; Gao et al., 2003) and might fuel productivity in the upper water column after the dust has been washed out from the air by precipitation. During such periods, specialized organisms, like the deep dwelling, mat forming diatoms, which exploit nutrients at the chemocline in a stratified water column (Villareal et al., 1993; Villareal et al., 1996; Kemp et al., 1999) would suffer from the enhanced mixing. Vice versa, within visually brighter intervals, diatom species, such as *Rhizosolenia* and *Thalassionema*, would benefit, since stratification is more pronounced, due to more intense summer conditions, while other, less specialized organisms would suffer from the lack of available nutrients.

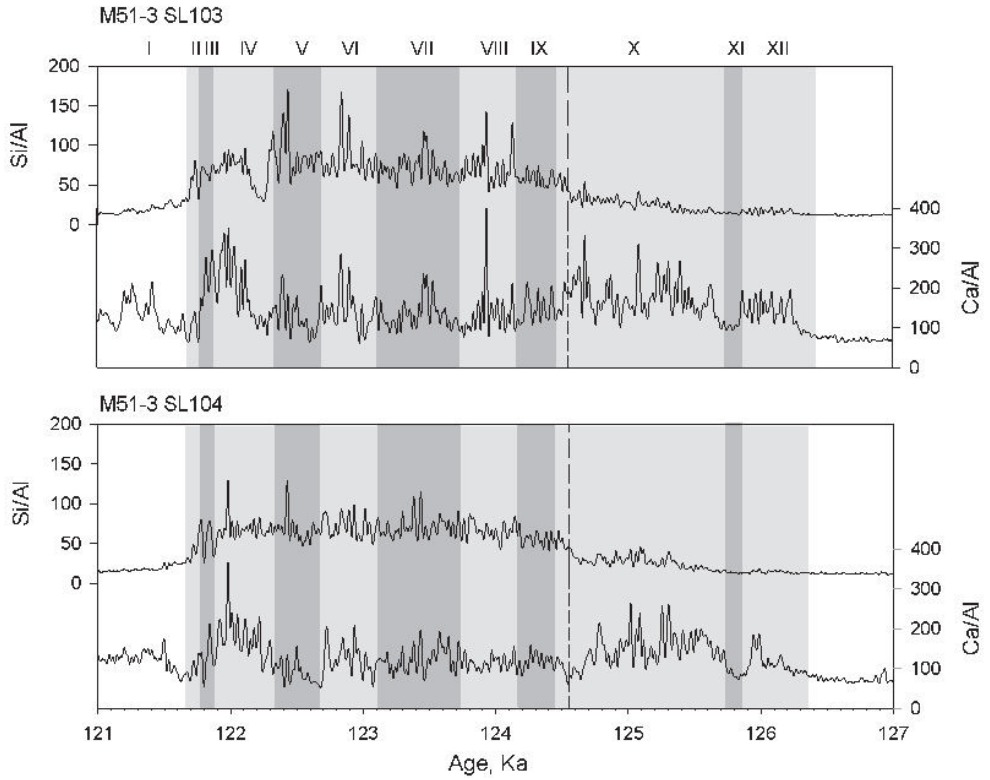

Figure 50: Elemental abundances of Si/Al and Ca/Al, reflecting the amount of productivity, here plotted against time. The time axis was built on the information of major changes in the sedimentation rate given by faunal and isotopic events by Cane et al., (2002), as well as on the minor changes in the sedimentation rate, given by the varve counts.

Normalized against Al, as terrestrial component, Si is here stressed to indicate productivity due the occurrence of diatoms as well as radiolarians and other silicoflagelates. Here Si/Al remains on a low level until the onset of zone X, where a small increase can be denoted and might be caused by radiolarians, which were firstly counted in zone X in the census counts (Figure 32D) but also by diatoms. In the latter case, the study of Wolff (2011) could prove the influence of dissolution (Figure 39), which diminishes the amount of detectable silicon. Si/Al further erratically increases at the top of zone X and coincides with the onset of the diatomitic lamination (dashed line in Figure 50). Generally, this enhanced level of Si/Al is held until the end of the sapropel, although the bioturbated top zones show strong variations. A defined correlation to the visible cm-thick beds is not as pronounced as for example in Ba. This might be explained by the different causative organisms (diatoms and radiolarians), which might favour different environmental niches and thus result in a more mixed signal. While the pattern of Ba and Br have been resembled in other studies (Brumsack and Wehausen, 1999; Mercone et al., 2001; Thomson et al., 2006), the here presented enrichment of Si due to the preserved diatomitic lamination is exceptional.

Focusing on the calcareous productivity, Ca/Al values increase within the sapropel, but remain variable throughout and can also be as low as below the sapropel (Figure 50). Highest values occur below the onset of the diatomitic lamination (Zone X) and here might in parts account for the higher Ba/Al values. Accordingly, Ca/Al and Ba/Al feature a common enrichment within zone IV. Similarly, planktonic foraminifera are also most common near the top (Zones IV, III) and the base (Zone X) of the sapropel in absolute numbers (Figure 32). A linear correlation between the absolute numbers of planktonic foraminifera and XRF abundances of Ca/Al is existent but remains weak (Figure 51). This issue can be expected, since the concentrations of other calcareous microfossils, like pteropods and calcareous nanoplankton have not been determined. Another reason is that for the planktonic foraminifera only the size fraction >150 µm was used, ignoring smaller species or juvenile specimens.

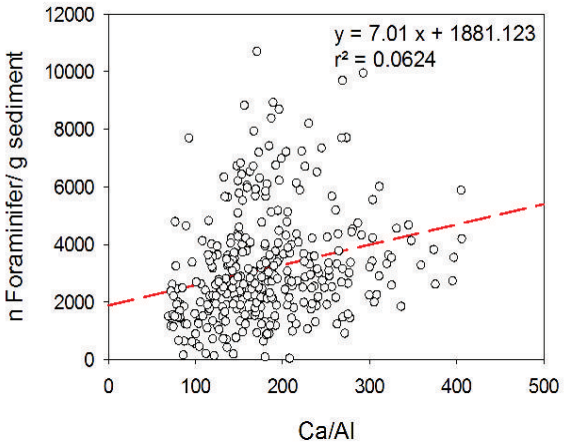

Figure 51: Sum of individuals of planktonic foraminifera in M51-3 SL104 (>150 µm), compared to the XRF Ca/Al ratios in M51-3 SL104. Linear regression is highlighted by the red, dashed line.

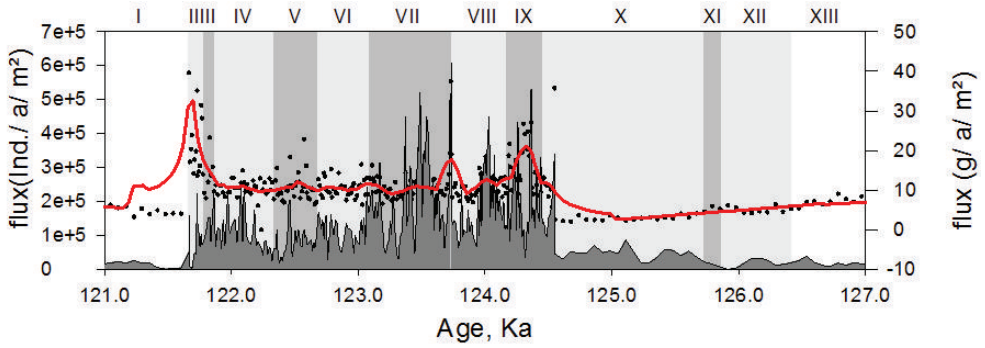

Figure 52: Accumulation rate of planktonic foraminifera in Individuals per year per m^2 (left axis, grey shaded area) and bulk accumulation rate from u-channel samples, given in grams of dry sediment per year per m^2 (black dots and running average as red line).

Due to the strongly increased sedimentation rate above 437.3 cm, resulting from the deposition of diatom mats, also the accumulation rates of planktonic foraminifera and bulk sediment increase (Figure 52). Since the U-channel from core SL104 was sampled with 3 mm spacing, the time within each sample can strongly vary, depending on the presence and the amount of annual varves. The strongest shift can be observed at the onset of the laminated part of the sapropel and the return to normal marine conditions at the end of the sapropel. While one sample in the laminated section catches ~11.3 years by average, the same interval from the enclosing marls and the poorly laminated lower sapropel section represents ~60 years.

Bulk sediment accumulation rate and planktonic foraminifera remain on a constant level of about 7 - 9 g/a/m² and ~10 - 20 thousand (k) individuals of planktonic foraminifera/a/m² respectively in the intervals below and above the sapropel, as well as the lower diatomitic interval of the sapropel. Within the laminated section of the sapropel, bulk accumulation rate increases up to ~40g/a/m², as well the numbers of foraminifera (30 - 50 k). This is an interesting result, since also some kind of dilution might be expected, due to the higher sedimentation rate. Instead, the planktonic foraminifera seem to keep pace with the sedimentation rate and become more common. Potentially, floating diatom mats pose an ideal source of nutrients for herbivorous planktonic foraminifera (Sangiorgi et al., 2006).

5.3.4. Redox conditions

In the S_5 sapropel in SL103 and SL104 (Figure 53), S/Cl is generally enriched, compared to the bright marls above and below the sapropel. Highest ratios of S/Cl are observed at the base of the sapropel, prior to the laminated interval, and also at the top of the sapropel, which roughly resembles a two-stage pattern and is not dissimilar to sapropel S_1 (Mercone et al., 2001) and also the patterns, seen in the productivity proxies of this study (Figure 48). Significant peaks outside the sapropelic interval (Figure 53) might be the result of exceptionally low Cl values, due to the lower porosity of the marls. A pronounced peak in S/Cl is visible in SL103 (Figure 53), between zone II and III and is supposed to be generated by the tephra layer (Figure 23). Yet, in SL104 (Figure 53) and also SL67 (Figure 25), a peak of similar strength is not observable.

An enrichment of sulphides, such as FeS_2 (pyrite), should also appear when normalizing Fe against Al, to compensate for dilution effects. The pattern of Fe/Al in (Figure 53, Figure 27) affirms the observations of S/Cl, as its levels are generally enhanced during sapropel. Like S/Cl, Fe/Al is especially enriched at the base and the top of the sapropel, but remains on this higher level until zone IX, whereas S/Cl already drops within zone X. A possible explanation for this phenomenon might be a shift in the ratio of FeS to FeS_2 precipitation. This is also supported by the decreasing ratio of Fe/S from zone X to IX, calculated from the ICP-OES measurements (Figure 54).

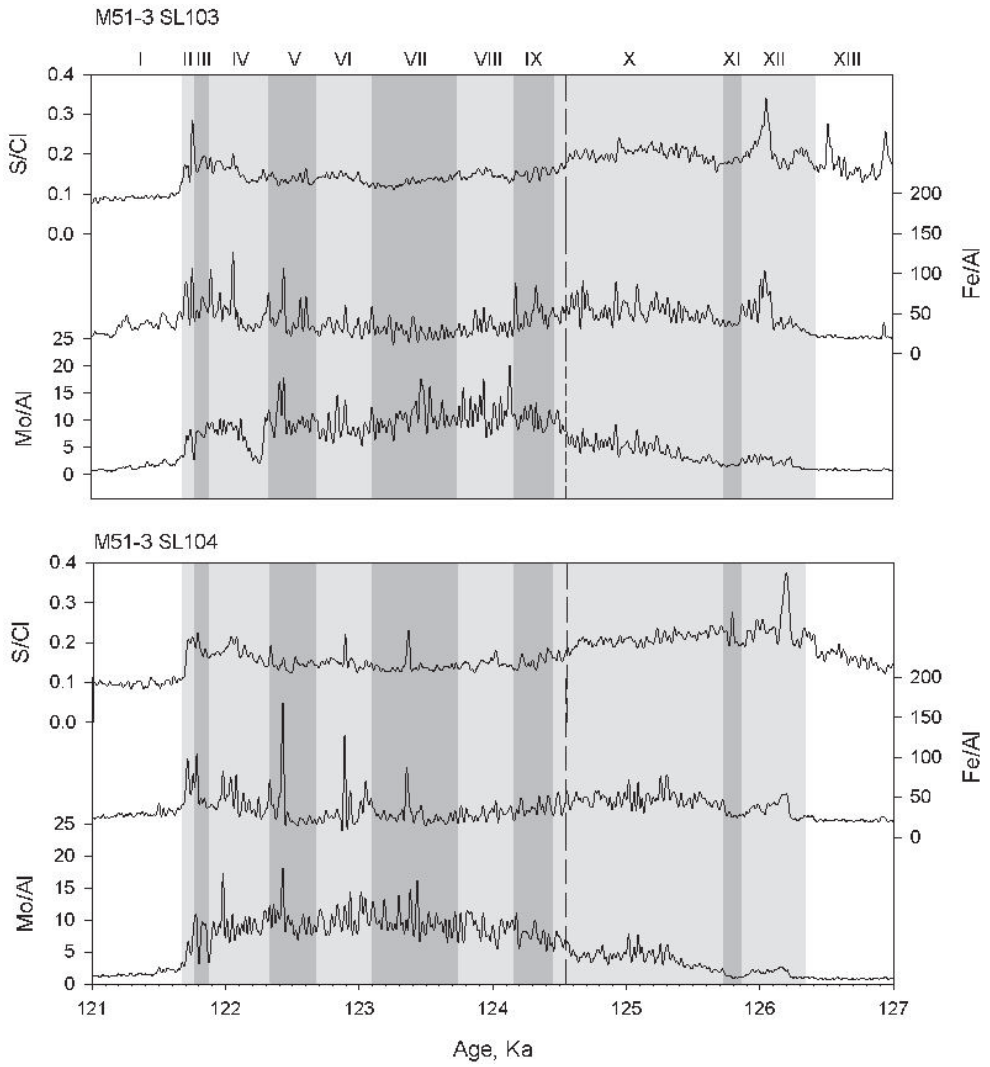

Figure 53: Elemental abundances of S/Cl, Fe/Al and Mo/Al of M51-3 SL103 and M51-3 SL104, reflecting the degree of water column anoxia, here plotted against time. The time axis follows the age-model, raised in this study (chapters 5.1 and 5.2). The visible sapropel and the individual subunits are hatched in light-grey and grey. The onset of the diatomitic facies is marked by the vertical dashed line at about 124.55 ka.

Beside the congruence between redox sensitive elemental ratios (Figure 53) and productivity proxies (Figure 48), we also observe a coincidence between high Sl/Cl and high Fe/Al and low oxygen isotopic ratios (Figure 45), which suggests the strongest fresh-water dilution of the upper water column during the first third of sapropel formation. Here, the strongest enrichment of sulphides might be seen as a consequence, due to the most intense reduction of deep water formation. Yet, productivity here is on a high level, too, favouring enrichment of sulphites. The relative low enrichments of sulphites in the centre of the sapropel might instead reflect a potential and temporally constrained stimulation of the water column, which is also in accordance with our interpretation of the freshwater balance from the oxygen isotope signal (Figure 45, Figure 46). Sancetta (1994) even describes a model, in which sapropel formation is possible without the imperative of anoxic bottom water conditions. On the cm-sale, both elemental ratios seem to be enriched in the dark layers (Figure 30, Figure 31). Since this pattern

coincides with the signals of terrestrial input (Ti/Al) and productivity (Ba/Al, Br/Cl), we suggest a causative link between enhanced productivity (Ba/Al) and elevated indicators for the lack of oxygen (S/Cl, Fe/Al).

Another element, which is enriched above its crustal abundance under anoxic conditions is Mo (Crusius et al., 1996; Calvert and Pedersen, 2007). Studies on the youngest Mediterranean sapropel S_1 indicate, that, for example, changes in the hydrography and the bottom water ventilation can have a strong impact on the enrichment of redox-sensitive trace metals (Calvert and Pedersen, 2007; Jilbert et al., 2010). Similarly to the mentioned redox sensitive elements, also Mo/Al becomes enriched within the sapropel, relative to the surrounding marls (Figure 53). A post-depositional remobilization of Mo, as documented by Thomson et al. (1995) in an S_1 sapropel with Mo-peaks above and below the sapropel, cannot be observed in here investigated material. Yet, in contrast to S/Cl and Fe/Al, Mo/Al is most intensely enriched during the laminated section of the sapropel with highest values in zone VII (Figure 53).

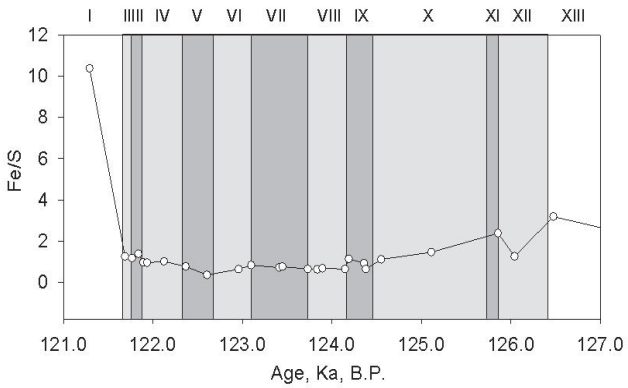

Figure 54: Fe/S ratio from ICP-OES Measurements in discrete samples in SL104 (Table 3). Sapropel S_5 and individual zones are shaded grey. Fe/S ratio drops from the base of the sapropel until zone VIII, which might depict a shift from FeS to FeS_2.

The PCA and also the correlation coefficients (Figure 31) suggest an enrichment of Mo/Al in the brighter layers of the sapropel in several zones, which further contrasts the ratios of S/Cl and Fe/Al as well as other elements, indicative for terrestrial input and productivity. This inverse relationship might be an artefact, due to the low concentration of Mo, as indicated by the weak correspondence between XRF-scanning data and the ICP-OES measurements (Figure 28). Yet, also a decoupling of the redox sensitive element Mo from export productivity (Ba) due to changes in deep water ventilation should be considered as a possible explanation (Jilbert et al., 2010). We further mention the overall congruence of curves of Mo/Al and Si/Al (Figure 50), which show the same gentle increase within Zone X and the major enrichment with the onset of diatomitic lamination. Based on a high resolution study on scallop shells in North West France (Barats et al., 2010), enrichments in molybdenum are proposed as a trace signal for spring blooms of diatoms, which suggests, that Mo/Al might also contain a portion of a productivity signal.

5.4 Environmental impact on the plankton during MIS 5e

5.4.1. Origin of the diatomaceous facies

The census of the varves (Figure 41) and the abundances of Si/Al from the XRF measurements (Figure 47) have shown that not the complete S_5 sapropel is represented by a distinctly laminated diatomitic facies. Instead, the initial 9 cm of the here investigated sapropel feature lower Si/Al ratios and show a less defined lamination. More clearly, signs of dissolution can be observed (Wolff, 2011) in this interval. Following the here established age model, a strict lamination firstly occurs about 1.9 ka after the onset of the sapropel. In order to explain this drastic shift in the fabric and preservation, generally two possible theories can be taken into account.

One possibility explains the strict lamination in a sapropel to be the result of enhanced diatom preservation. This theory implies that extended areas of high diatom production might have existed during the last interglacial in the Eastern Mediterranean, but preservation of this annual diatomic flux within sapropel horizons was limited to areas with exceptional bottom water conditions. An example for enhanced preservation is stated from the sapropel S_5 in cores 971A and 971C near the Napoli Mud Volcano. Here, S_5 in 971C is conspicuously thick (80 cm) and intermittently laminated, which, after Pearce et al. (1998) is due to the beneficial and isolated position in a moat, next to the Napoli Mud Volcano. In contrast, S_5 in 971A at the crest of this moat does not show signs of lamination and only has a thickness of 23 cm. In opposite to the silicon-poor waters of the Mediterranean, the waters, that fill this moat, are supposed to be saturated in Si from brines, which diminishes its otherwise corrosive character and benefits the preservation of silica shelled microfossils (Pearce et al., 1998). Another example comes from core GeoB 5836-2 from the hyper saline Shaban Deep in the Red Sea. Here, Seeberg-Elverfieldt et al. (2004; 2005) recovered laminated diatom oozes, which depict strong annual flux signals. Again, enhanced preservation is supposed to be favoured by the protective character of the brine-filled depression with silicon-saturated waters.

Alternatively, several studies report the existence of laminated sediments in generally Si-depleted bottom waters, as a result of certain configurations of oceanic fronts and enhanced productivity. For example, Gingele and Schmieder (2001) report gravity cores from the subtropical South Atlantic with enhanced preservation of an almost monospecific, diatomitic lamination. The formation of this lamination is supposed to last for about 10 ka, from 544 ka and 534 ka at the Mid Pleistocene Transient (MPT), and might be a result of enhanced productivity due to enhanced water column stratification. Other studies of similar phenomena come from Bodén and Backman (1996) and Yoder et al. (1994), which suggest oceanic frontal systems and

high productivity as a major factor for the formation of laminated, diatomitic sediments. According to these models, the massive amount of diatom frustules, which often form larger aggregates and also feature rapid rates of sinking, would further enhance their preservation potential, even under well ventilated conditions (Sancetta, 1994; Grigorov et al., 2002; Kemp et al., 2006).

Taking a closer look at the position of the here investigated cores from the Pliny Trench area, SL67, SL103 and SL104 are located in an almost identical water depth of about 2155 metres, on a rather flat shoulder between the Pliny Trench and the Strabo Trench. From the available bathymetric data (Figure 11), a depression structure, which could provide a certain degree of isolation, is not evident. We might suggest the presence of a brine-filled and buffered isolated deep, which remains invisible due to its small size and the rather coarse resolution of the bathymetric dataset. Anyhow, in that case, the very good preservation of siliceous microfossils is to be expected right from the start of sapropel S_5 and potentially also in the enclosing marls, which is not the case (Figure 32B, Figure 50). This also accounts for 971C, where no diatoms are preserved, neither in the clayey marls above and below S_5 nor in the well preserved sapropel S_1 (Danelian and Frydas, 1998).

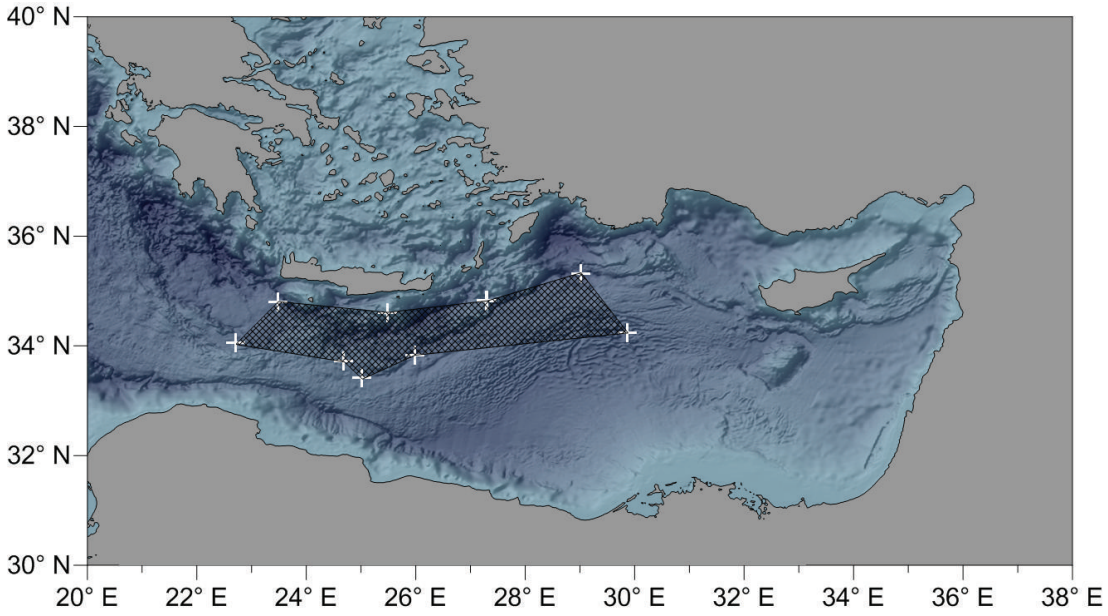

Figure 55: Compilation of sediment cores, containing sapropel S_5 with a reported opal preservation of diatoms or radiolarian in the Eastern Mediterranean (M51-3 SL103, M51-3 SL104, M40-4 SL67, DSPS site 128, ODP sites 969 and 971A). Cross hatchet area marks the proposed area of higher productivity. (Modified after Schrader and Matherne (1981) and Danelian and Frydas (1998)).

Upon this, the presence of the diatomitic lamination in our cores, most likely cannot be ascribed to beneficial topographic conditions at the positions of the cores. Instead we propose the lamination to be a primary signal of enhanced productivity of diatoms, upon environmental changes of the Eastern Mediterranean or at least a substantial part of it, which ultimately

enhances the preservation in the sediment due to the strongly increased flux of organic matter to the seafloor. Schrader and Matherne (1981), who investigated numerous S_5 sapropels from the Hellenic Trench System (Figure 55) also interpret the occurrence of diatoms and radiolaria as a signal of enhanced productivity due to enhanced nutrient levels. Particularly, frontal mixing in an area, which might span an area from the south of Crete to the southern coast of Turkey, is here supposed to play an important role. Similarly, also Danelian and Frydas (1998) propose an enhanced eutrophication of the water column, whereas the source of required nutrients is supposed to derive from the Nile River. Despite the sophisticated models of these studies and the unifying idea of elevated nutrient levels as a causative origin of deep dwelling diatom colonies, a sufficient trigger for the here presented sapropel, where the diatomitic lamination is firstly preserved about 1.9 ka after the sapropel onset, has not been figured out so far.

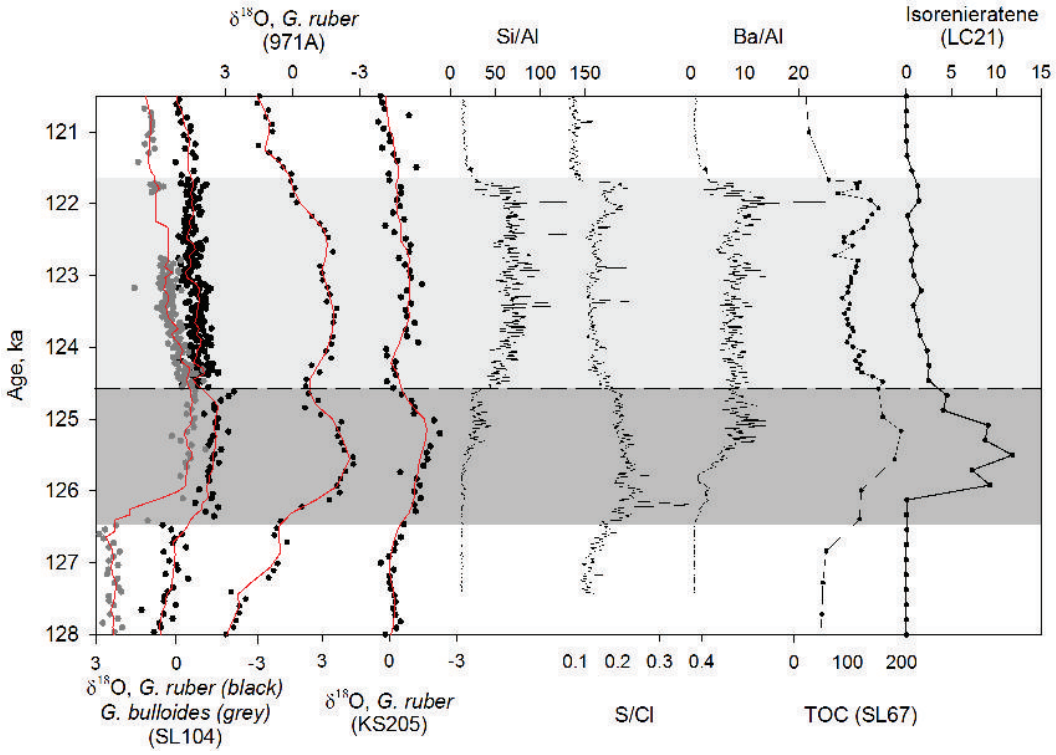

Figure 56: Oxygen isotopes of *G. ruber* and *G. bulloides* from SL104 and *G. ruber* from 971A. Juvenile index of *G, ruber* and XRF–ratios of Si/Al, S/Cl and Ba/Al from SL104. TOC values of SL67 (Schmiedl et al., 2003b) and the biomarker isorenieratene from LC21 from the Aegean Sea (Marino et al., 2007). All data follow the here established age model. Based on the observations in the here investigated sapropels, the onset of the diatomitic lamination is highlighted by the dashed line, separating the non-diatomitic basal 1.9 ka (grey) and the diatomitic upper 2.8 ka (light grey). All proxies, monitoring important environmental parameters, are characterized by a pronounced shift, to higher or lower values, which coincides with the first observation of mat-forming diatoms.

With regard to the data, being gathered and complemented in this study, a coherent and pronounced shift in a wide range of proxies occurs at the same time, when the annual lamination of diatoms mats has been distinctly observed for the first time (Figure 56). Along with the onset of the lamination (see dashed line and increasing Si/Al-ratios in Figure 56), also the $\delta^{18}O$ values instantly increase (Figure 56), which suggests a less intensive fresh water dilution. This maybe

diminishes the positive water balance of the Eastern Mediterranean and might thus strengthen the influence of inflowing surface waters from the Atlantic Ocean through the Strait of Gibraltar. This hypothesis is supported by S/Cl ratios (Figure 53), which drop at the same time and thus might point to an enhanced ventilation of the bottom waters. Beside the proxies, which more monitor hydrographic characteristics, also the pelagic ecosystem (productivity indices of Ba/Al, TOC and isorenieratene in Figure 56) shows a strong reaction with the entrance of the sapropel into the diatomitic facies. Although there is not necessarily a causative link between the mat-forming diatoms and the different productivity indices, these proxies might more likely reflect the collateral adaptation of organisms to the changing hydrographic conditions in the Eastern Mediterranean Sea.

Along with the proposed enhanced exchange of water with the open ocean, also oceanic gyres might subsequently become stimulated. Oceanic gyres and eddies are highly variable in shape and strength and occur in different scales in the Mediterranean. On the sub-basin scale, entities such as the Rhodes and Cyprus Gyre are the most energetic ones and might have been intensified with the break-up of the most intense stratification during the lower part of the sapropel as well as with increasing salinities (Robinson and Golnaraghi, 1993). Two strong whirls cover an area south east of Crete up to the southern coast of Turkey south of Rhodes (Figure 5) and today form an important locus of the formation of intermediate waters (Figure 6) (Tsimplis et al., 2006). Generally, gyres strongly depend on the underlying bathymetry (Robinson and Golnaraghi, 1993). We may thus assume a similar allocation of gyres during the peak of the last interglacial period than today, albeit their size, strength and shape might deviate from the modern situation, due to the altered oceanographic conditions.

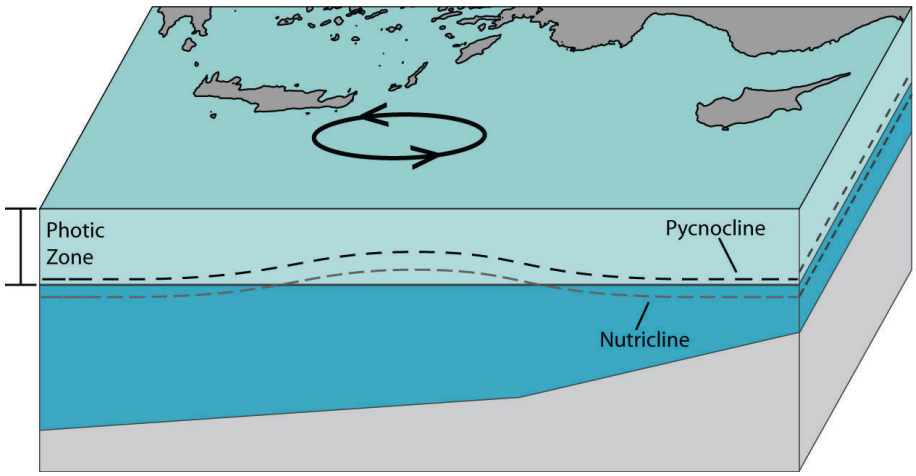

Figure 57: Graphic illustration of a cyclonic gyre in the Eastern Mediterranean and a proposed mechanism for enhanced, yet spatially restricted productivity in the photic zone. (Modified after Weldeab et al. (2003b)).

The area south east of Crete is also regarded as an oasis in the nutrient desert of the Eastern Mediterranean Sea (Siokou-Fragou, 1999), and today features the highest rates of primary productivity (Figure 4, page 8) as a result of a stronger vertical upward transport of nutrients (Salihoğlu et al., 1990). Here, a stimulation might provoke a local shoaling of the pycno- and nutricline, which potentially would reach into the photic zone and provide nutrients (Weldeab et al., 2003b) to the deep dwelling diatom colonies. The vertical transport of nutrients, at or within gyres, as well as a general shoaling of the nutricline has been affirmed by observational evidence and the subsequent computational modelling for example in the Pacific Ocean (Martin and Richards, 2001) and the Sargasso Sea (McGillicuddy Jr and Robinson, 1997; McGillicuddy Jr et al., 1999). Also in the modern Mediterranean Sea, the Rhodes Gyre forms a cyclonic dome, where the nutricline can be as shallow as 75 m and penetrates the euphotic zone (Malanotte-Rizzoli and Eremeev, 1999). Suggesting a weaker doming during sapropel formation, due to a less strong developed gyre, the less intensive upwelling might be outbalanced by a generally shallower nutricline at that time (Rohling and Gieskes, 1989; Rohling, 1994).

Further, this hypothesis also holds enough degrees of freedom to explain the differential thicknesses of S_5 sapropels in the Mediterranean, for example in 971A and 971C. 971C indeed might profit from the isolated position in a depression, allowing the accumulation of mats of diatoms, which otherwise would be prone to dissolution, as apparent in 971A and the basal interval of SL104 (SL103, SL67). With the more stimulated gyre after a certain period of time, productivity becomes strongly enhanced in SL103, SL104 and SL67 and allows the preservation of diatoms even without an isolated depression structure. 971A and 971C instead are not affected by the higher productivities and remain in the same mode of sedimentation, whereas 971C can profit from the isolated position (Pearce et al., 1998).

Beside the enhanced productivity, also a more efficient mechanism for the downward transport of diatom mats might play a role and further enhance their preservation potential. A sophisticated model by Adloff et al. (2011) highlights the potential of northerly winds from the Aegean Sea, the so-called Etesian Winds, to explain the temperature dipole in the Levantine Basin. Particularly, the Etesian Winds provoke westward directed Ekman transport of surface water, which is compensated by upwelling in the Eastern Levantin Basin and a downwelling south of Crete, located west of the centre oft the Etesian winds. Here, this sinking might potentially enhance the drawdown of the deep dwelling diatoms at the end of the summer.

5.4.2. Response of the micro fauna upon environmental changes

The Shannon-Weaver Diversity Index (Figure 32B) indicates that the onset and the termination of the sapropel are marked by lower diversities, where several species disappear, either for the duration of sapropel formation or a shorter interval and point at strong environmental changes. Anyhow, diversities within the sapropel can be as high as in sediments prior or after the sapropel or only slightly lower. Despite the implied different hydrographic conditions during sapropel formation, the Eastern Mediterranean cannot be regarded as a markedly extreme environment, being usually characterized by a very low faunal diversity (Kucera, 2007). Most changes in the planktonic foraminiferal abundances here occur within a few or even in between two samples (Figure 34, Figure 35). The pace of these changes in the abundances suggests more the behaviour towards certain thresholds instead of an adaptation to a gradual changing environmental parameter.

Yet, a common pattern among the different species is hard to identify and even species, which favour the same ranges in temperature show a highly individual behaviour throughout the deposition of the sapropel (Figure 34, Figure 35). This fact is also acknowledged by the detrended correspondence analysis (DCA) (Figure 58A), which illustrates the lack of a severe clustering of species. Generally the individual species are arranged in a regular manner around the samples, which suggests a rather low amount of similarities between each other. From the viewpoint of the individual samples, the DCA (Figure 58A) visualizes the shift of a more high productivity ocean with several deep dwelling species prior to sapropel formation (Zone XIII) to more oligotrophic conditions during and after the sapropel (Zone XII to I). This major oceanic shift at the onset of the sapropel formation can in parts also be read from Figure 58A and the allocation of individual species. Being located in upper-right corner, the pre-sapropel samples seem to be especially influenced by *G. inflata*, *G. conglobatus*, *T. quinqueloba*, *N. incompta*, *G. scitula* and also *N. dutertrei*, which feature a significant drop in their abundances at the beginning of the sapropel (Figure 34, Figure 35). This fact also allows for the interpretation of the disappearance of these species in terms of their different ecological demands, such as availability of nutrients, degree of anoxia and SST.

Living in water depths as deep as 400 m (Hemleben et al., 1989), the disappearance of *G. inflata* with the onset of the sapropel can thus be interpreted by the diminished overturning circulation due to the enhanced fresh water input and the subsequent lack of oxygen, especially, when assuming the shallowest anoxia to occur during the onset of sapropel formation (Thunell et al., 1982; Koch, 2010).

As the Mediterranean already provides suitable sub-tropical SSTs, and *G. conglobatus* also inhabits the photic zone of the water column, we here tend to the stronger seasonal contrast during sapropel formation as a potential reason for the disappearance of *G. conglobatus*, with winters, being too cold for this species (Koch, 2010).

As a sub-polar species, which also inhabits the cooler Atlantic waters (Hemleben et al., 1989), the decease of *T. quinqueloba* might be the result of higher temperatures during the onset of the investigated sapropel. Anyhow, low winter temperatures during sapropel formation might allow *T. quinqueloba* to survive and maintain a residual population from the previous glacial period (Hayes et al., 2005; Koch, 2010).

Since *N. incompta* disappears at the beginning of the sapropel and reappears after a short absence (Figure 35), it is difficult to point out a definite controlling factor, which might either be intense stratification or high summer temperatures, especially since *N. incompta* normally prefers temperate waters (Hemleben et al., 1989).

Similarly, also *G. scitula* prefers temperate waters and, after a short gap at the onset of the sapropel, reappears after a short period of absence. Inhabiting the water column even below the thermocline for most of the year (Hemleben et al., 1989; Pujol and Grazzini, 1995), anoxic conditions in the water column might pose a problem for *G. scitula*.

N. dutertrei is found in the tropics and is known for its preference of freshwater lenses (Bé and Tolderlund, 1971; Thunell et al., 1984). It is generally associated with Pleistocene sapropels, whereas the here investigated S_5 interval seems to be an exception as *N. dutertrei* remains below 5% and also disappears with the freshwater pulse at the very beginning of the sapropel. *N. dutertrei* prefers a rather shallow thermo and nutricline and is feeding of phytoplankton (Fairbanks and Wiebe, 1980). Potentially, the majority of diatoms which forms the Deep Chlorophyll Maximum reside out of the reach of *N. dutertrei*.

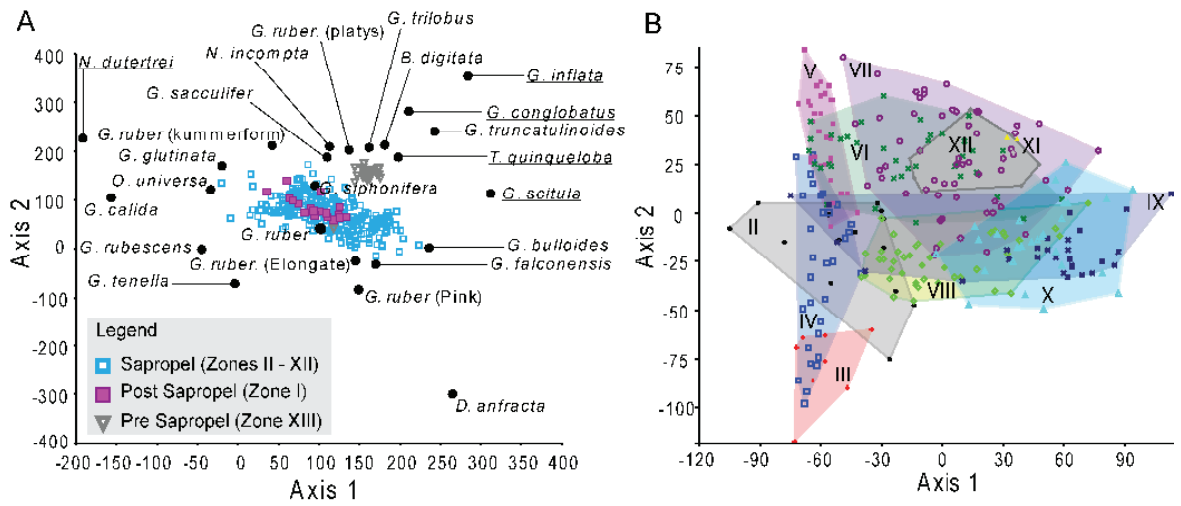

Figure 58: DCA of planktonic foraminiferal abundances of sapropel S_5 in SL104 (absolute numbers of individuals per gram sediment). Panel **A** visualizes the relationship between samples from the sapropel (Zones II – XII) and the enclosing marls below (Zone XIII) and above (Zone I), and also the controlling species of planktonic foraminifera. Panel **B** visualizes the relationship of sapropelic samples, subdivided into their actual individual subunits (II – XII).

Also within the sapropel, a pattern can be seen (Figure 58B), which slightly resembles the XRF abundance data (Figure 29). Here, the community of planktonic foraminifera holds sufficient differences throughout the formation of the sapropel, which similarly allows for the separation into the lithostratigraphic zones, as defined in chapter 4.2. The upper part of the sapropel (zone II – V) strongly differs from the basal zones X – XII and zone VII, whereas the subunits VI, VIII and IX take in a more intermediate position. In parts, the massive occurrence of diatoms might pose a factor by providing a source of nutrients, as well as potential hydrographic changes that occur at the same time.

Juvenile Index

Next to the interpretation of their individual abundances, also the morphological variability of planktonic foraminifera is used to track ambient changes. In samples from the Eastern Mediterranean, *G. scitula* for example showed variations in the pore density upon changing salinities of the surrounding water (Baumfalk et al., 1987). These authors investigated, samples from the sapropels S_5 and S_6 as well as non-sapropelic samples, where *G. scitula* formed more pores during sapropel formation than under regular conditions. Since sapropel S_6 formed under a cooler climate than S_5 (Emeis et al., 2003), it is assumed that the pore density more reflects salinity than temperature (Baumfalk et al., 1987). Such very time-consuming morphological investigations of the tests of planktonic foraminifera were not conducted for this study. Yet, abundances of planktonic foraminifera were counted in two different size fractions, which allows for the visualization and interpretation of the proportion of large individuals (>250 µm) towards the whole fraction (>150 µm) as an indicator for good health (Kucera, 2007). Concerning the test size of planktonic foraminifera, the temperature of the surrounding water

seems to be the most important factor (Kucera, 2007), whereas the size of the test increases toward the individual optimum of a species, and vice versa decreases, when the species is pushed out of its optimum, which has been shown for example for *N. pachyderma* (Malmgren and Kennett, 1972; Moller et al., 2011b). Since warmer waters have a lower capacity for holding dissolved CO_2, a higher saturation of $CaCO_3$ is reached from the polar to the tropic waters, allowing for a more effective calcification and a general increase of shell sizes of planktonic foraminifera towards the equator. This effect is further multiplied by the enhanced enzymatic activity and faster metabolism in the foraminifera in a warmer environment, which further enhances the rates of growth and calcification (Schmidt et al., 2004; Koch, 2010).

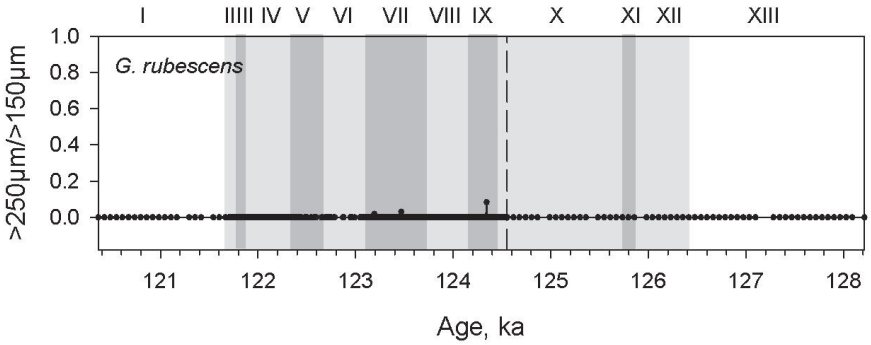

Figure 59: Proportion of the large fraction (>250 µm) towards the whole sample (>150 µm) of *G. rubescens* in M51-3 SL104. Being considered as a small species, *G. rubescens* is almost absent in the size fraction >250 µm.

Although 24 different species were recognized in our material, this kind of analysis is not meaningful for most species, since the chosen boundary of 250 µm only works for those species with an optimum near 250 µm. For example, the analysis of *G. rubescens* is not meaningful, since it occurs almost exclusively in the small size fraction, which strongly confines the sensitivity of this analysis (Figure 59). Also species, which do not occur permanently (I. e. *N. dutertrei*, *G. inflata*, *G. scitula*) in the investigated interval, can lead to misinterpretations.

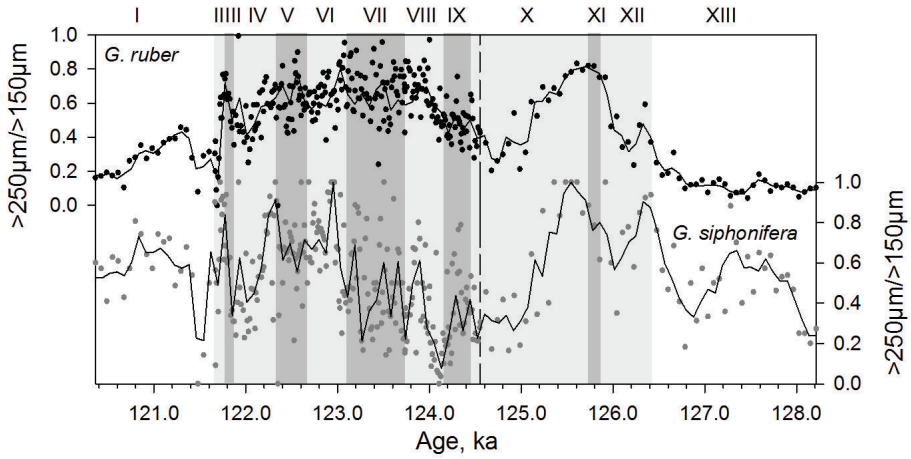

Figure 60: Development of the test size of individuals of planktonic foraminifera in M51-3 SL104 for *G. ruber* (white) (top graph) and *G. siphonifera* (bottom graph). Here, the size/ health is assessed by the proportion of the >250 µm size fraction of a sample against the total number of individuals in the sample, which comprises the size fraction >150 µm. Y-values toward 1 thus indicate a general increasing proportion of large specimen in their population.

Figure 60 summarizes the juvenile indices of *G. ruber* (white) and *G. siphonifera*, which are frequent enough and have test size spectra sensitive to the ><-250 µm criterion. Both species occur permanently in all samples and allow an uninterrupted monitoring throughout the sapropel and the adjacent marls. *G. ruber* and *G. siphonifera* largely resemble the same pattern, with larger individuals within the sapropel and smaller ones in the enclosing marls. Since both species today thrive the subtropical waters (Hemleben et al., 1989; Kucera, 2007), larger species within the sapropel generally suggest warmer SSTs, whereas the smaller test sizes in the marls reflect the cooler climates of the previous glacial period of MIS 6 and the following cooler period of MIS 5d. The transition from a population with almost exclusively small individuals to one with an almost exclusively large population takes place over a time span of about 1000 – 1200 years for *G. ruber*. Here, the transition for *G. siphonifera* takes place faster, which might be deduced to the general lower abundances and higher intersample variability, relative to *G. ruber*. Next to the strong contrast between sapropel and enclosing marls, also within the sapropel, the average individual size strongly varies. Here, the most articulated drop in the shell size occurs within zone X, for a period of 600 – 800 years, directly below the shift into the diatomitic facies. With the SST as the most important factor, for controlling the test size of planktonic foraminifera (Kucera, 2007), the here observed shift might indeed be the result of a cool period during the peak warmth of the last interglacial period, which is in accordance with a proposed mid Eemian cooling (Maslin et al., 1998; Sánchez-Goñi et al., 1999; Bauch et al., 2011). During this episode, a relaxation of the penetration of the Inter Tropical Convergence Zone, which is supposed to reach beyond the Saharan Watershed, is proposed and consequently diminishes the enhanced freshwater input along the North African coast. On the other hand, the retreat of the ITCZ would allow for a stronger influence of the northern climate system of the mid to high latitudes (Rohling et al., 2002).

Contrary to the findings in the juvenile index, a defined cooling in the ANN temperature record cannot be identified (Figure 37). Instead, there, the highest seasonal contrast occurs at zone XII of the sapropel, whereas temperatures in zones X – VIII are rather stable. Since the abundances of planktonic foraminifera might not be driven exclusively by the temperature alone, but also by changes in salinity, level of anoxia, stratification and availability of nutrients, the explanatory power of artificial neural networks might be limited during sapropel formation, due to the unusual hydrographic situation in the Mediterranean.

Benthic foraminifera

The presence of benthic foraminifera is largely controlled by the flux of nutrients to the sea floor and the availability of oxygen, whereas the latter one becomes increasingly important under low oxygen conditions. In contrast to planktonic foraminifera, salinity and temperature, here play a minor role (Jorissen et al., 2007). While S/Cl already increases several centimetres prior to the onset of the sapropel (Figure 53), the benthic foraminifera disappear with the onset of the visible part of the sapropel, when deep water formation collapsed. Reappearance occurs with the re-oxygenation of the bottom water, although, probably by bioturbation, tests of benthic foraminifera are found in the upper centimetres of the sapropel (Zone II and III) (Figure 32C). Contrary for example to Schmiedl et al. (1998), Schmiedl et al. (2003a) and Sangiorgi et al. (2006), who found low abundances of benthic foraminifera also in the centre of sapropel S_5 in cores KL51, BAN89-GC09 and SL67 and suggest a modest stimulated deep water formation, benthic foraminifera are permanently absent in SL104. The single findings of benthic foraminifera in SL67 (Schmiedl et al., 2003a) are in contrast to the nearby SL104 (Figure 32D). Here the difference might emerge from the different size fractions, being investigated, but also by sample-splitting, which was conducted prior to counting. Repeated events of re-oxygenation have been proposed during the formation of sapropel S_5 (Sancetta, 1994; Sangiorgi et al., 2006) and also for sapropels S_1 and S_6 (Casford et al., 2003), and might even be justified by slightly lower S/Cl and Fe/Al ratios in the centre of the here investigated cores (Figure 53). Anyhow, a repopulation by benthic foraminifera might have been suppressed effectively by the massive flux of diatoms to the seafloor (Kemp, 1996; Grigorov et al., 2002).

5.4.3. Seasonality and thickness of varves

As highlighted in chapter 4.4 and interpreted in chapter 5.3, a correlation exists between the macroscopic layering and the abundance of environmental elements. We also illustrated the origin of this cm-scaled layering to lay in the differential character of the subordinated sub-mm thin laminae couplets. Based on the elaborated model, which explains the lamination as a product of seasonal blooming events of mat forming diatoms and also upon the fact that the species therein are sensitive to changes in surrounding water body (Pearce et al., 1998), it thus

seems feasible, trying to link the differential character of this laminae couplets in terms of their thickness and contrast to the environmental conditions. Stressing an analogue from the terrestrial realm, it can be referred to trees, whereas also the thickness of annual rings allows assumptions about the duration of the phases of growth and resting.

Unlike shallow living diatoms, which are typical for the spring bloom, species of the genus of *Rhizosolenia* for example are known to persist throughout the summer. Here, special adaptations, like the active buoyancy control, allow the exploitation of nitrogen from deep nutrient pools in stratified water bodies (Villareal et al., 1993). Thickness of single summer laminae and the amount of diatoms therein, might therefore be indicative for beneficial environmental conditions. Especially, the duration of the growth period, the stability of the stratification and the availability of nutrients should be taken into account. A first hint has been suggested by the terrestrial input, visualized by Ti/Al (Figure 47). Here, the positive association of Ti/Al with darker layers was explained by enhanced precipitation, scavenging the dust-laden air, especially during the wet winter season. The enhanced precipitation might here be the escort of a more prolonged winter season or a generally cooler summer, where, in both cases, the temperature and wind induced mixing of the upper water column might be more intensive and less suitable for species of deep dwelling diatoms. Instead, less specialized planktonic organisms near the surface might benefit from enhanced nutrient input, as reflected by higher values of Ba/Al and Br/Cl (Figure 48). Although there is no information, how Etesian winds and the subsequently induced downwelling at the end of the summer (Adloff et al., 2011) influences the sinking of diatom mats or their preservation potential in the sediment, this issue might be regarded as a further factor, which could alter the quality of lamination in the sediment. The Etesian winds are associated with the Azores anticyclone and the Asian Low (Harding et al., 2009) and it could be speculated that the cm-scaled layering here reflects decadal lasting variations in the influence of the Azores High.

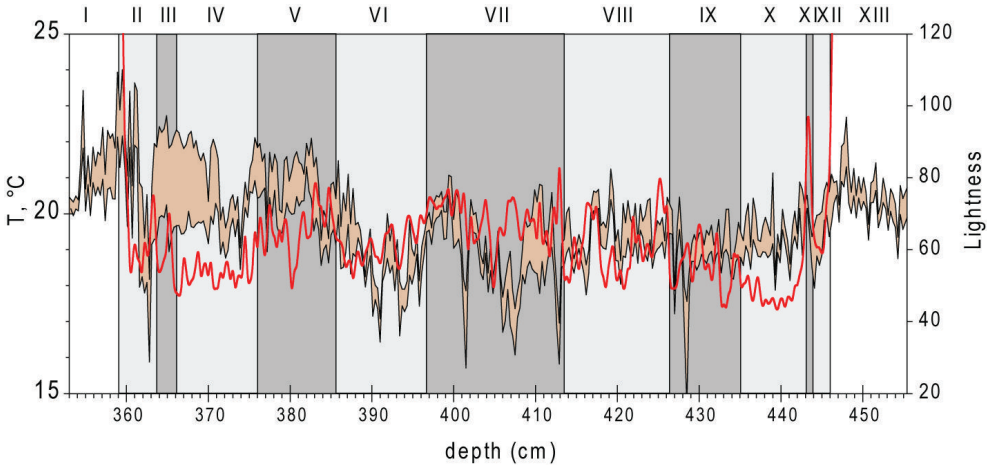

Figure 61: Combination of the assessed SSTs from the ANNs for the annual average (fawn coloured area) and the sediment lightness (red line). The sapropel and the individual subunits are highlighted in grey and light-grey.

To underline our suggestions, Figure 61 combines the annual average in SST from the ANNs and the measurements from sediment lightness, which represents the layering and thus the underlying differential shape of the annual lamination. Since both sets of data represent strongly deduced proxies, we do not wish to establish a strict linear relation between them. Yet, from Figure 61, especially in the central part of the sapropel, a certain degree of linkage becomes apparent and seems to affirm our assumptions.

As already mentioned, the calculated values from the ANNs most likely do not only represent the SST but more likely depict a combination of several environmental factors, such as stratification, fresh water dilution, primary productivity, temperature and possibly further unknown factors. Thus, Figure 61 might more suggest the dependency of the deep dwelling diatoms to these environmental parameters instead of temperature alone.

5.5 Cyclicities

As shown in the previous chapters, the formation of sapropel S_5 in the here observed material did not take place under constant environmental conditions. Instead, measurements of elemental abundances (Figure 47, Figure 48, Figure 50, Figure 53), isotopic ratios (Figure 45, Figure 46) and faunal abundances (Figure 34, Figure 35) in the here presented material as well as from the literature show coinciding trends. Due to the above-average thickness and the subsequent high resolution sampling, the here presented S_5 sapropel further resolves a short scale variability in the XRF scan data and the faunal data, which might feature a rhythmic component.

As described in chapter 3.5, the wavelet analysis was conducted over an interval, comprising zones IV to X. This excludes the enclosing marls (subunits I and XIII), the bioturbated top centimetres (zones II and III) as well as the very onset of the sapropel (zones XI and XII), which is characterized by its chemical signature, to be more similar to the enclosing marl below, than the rest of the sapropel. Due to the major and minor changes in the sedimentation rate, not the original data were introduced to the wavelet analyses. Instead, a time linear interpolated dataset is used, wherein the data points have an equal distance of 2 years (As for the XRF elemental abundances in Figure 47, Figure 48, Figure 50 and Figure 53) or 20 years (For data from discrete sampling as in Figure 45). Elements with the most pronounced periodicities in the S_5 Sapropel of M51-3 SL104 are shown in Figure 62, together with the original string of data (grey) and also the high pass filtered version of the interval (black), which contributes the data string that was actually introduced to the wavelet analysis and blinds out long term trends. Here Ti/Al, S/Cl, Br/Cl, $\delta^{18}O$ and the juvenile indices of *G. ruber* and *G. siphonifera* show consistent significant periodicities, especially in the frequency bands with about 180 – 240 years and 80 – 90 years. Further significances in Ti/Al, S/Cl and Br/Cl are also assigned to frequencies shorter than 30 years. Anyhow, significance to these frequencies firstly occurs in sub unit IX, where the resolution of the data increases, due to the higher sedimentation rate. Further, significance here might result from the red noise spectrum, whose amplitude naturally becomes lower with increasing frequency. Having said this, cyclicities, shorter than 30 years, are not further interpreted. Here the frequency space between 250 years and about 50 years seems more reliable and artefacts due to normalization of the raw counts of XRF-scan data can be excluded, since normalization was conducted either with Al or Cl or represent isotopic measurements and faunal data at all. While the longer of the two cycles is quite consistent in the here investigated interval, the occurrence of the shorter periodicity seems more patchy. This does not necessarily mean that this periodicity only occurs to a certain time, but instead can be the result of an

amplitude modulation of this signal by other signals within the dataset, which might drop the signals amplitude below the level of significance.

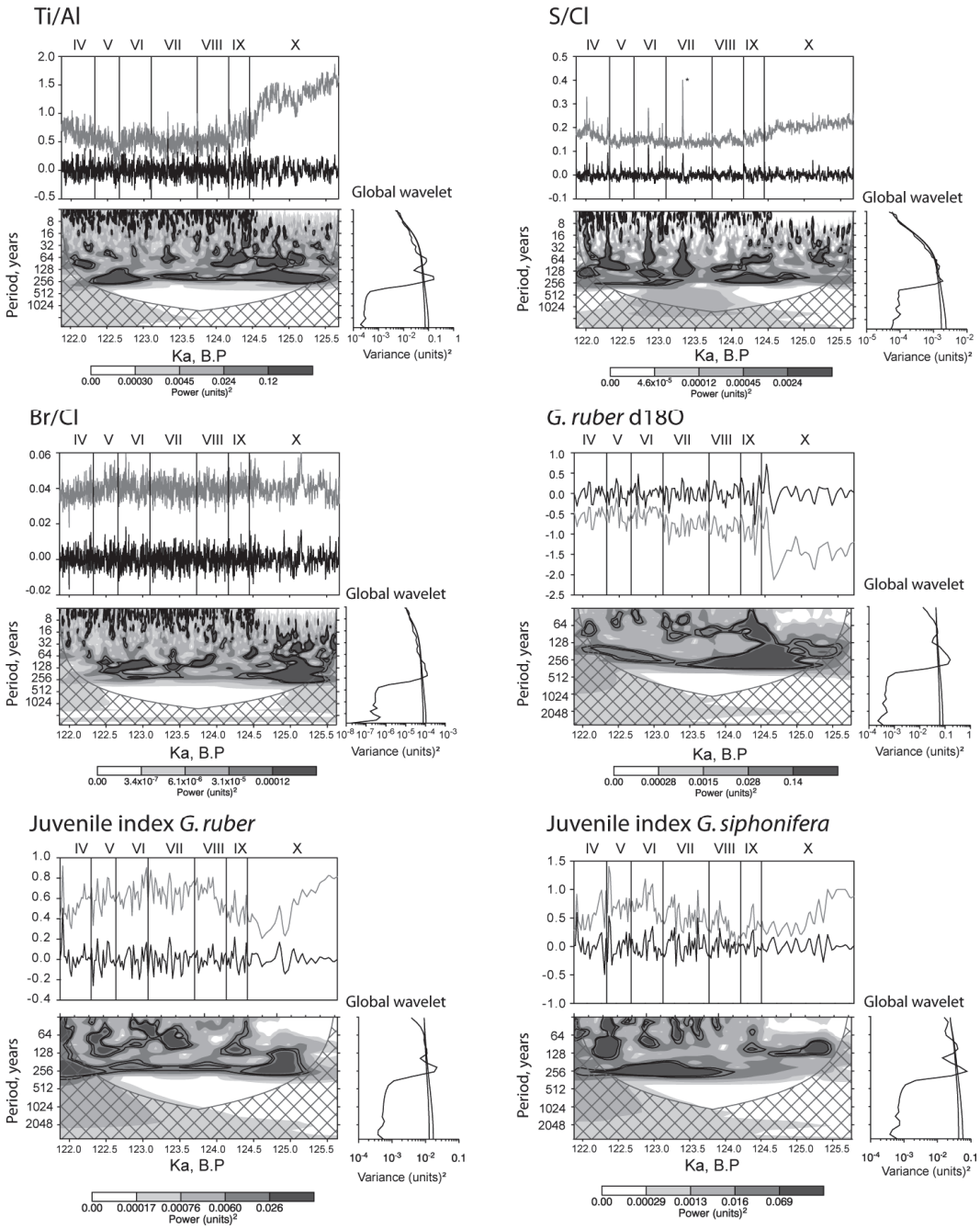

Figure 62: Wavelet power spectrum of Ti/Al, S/Cl, Br/Cl, $\delta^{18}O$ (*G. ruber*) and the juvenile indices for *G. ruber* (white) and *G. siphonifera* in M51-3 SL104 from zones IV to X. Additionally, the original elemental abundances (grey curve) as well as the high pass filtered data, which represent the actual input data for the wavelet analysis, are added above the wavelet power spectrum. The cut-off frequencies of the high pass filters were designed with frequencies of 0.006 for XRF abundances and 0.054 for the discrete samples, both corresponding to ~360 years. The global wavelet shows the overall significance of each signal. The asterisk in the elemental abundances of S/Cl marks an outlier, which has been deleted in the input dataset for a clearer signal.

Despite the significance of the signals, unveiled in this undisturbed sapropel interval, it is difficult to identify a direct causative link to a howsoever natured initiator. Apparently, the lengths of periodicities with about 180 – 240 years and 80 – 90 years coincide with the lengths

of certain cyclicities traced for example in sunspots, namely the Gleissberg cycle, given with a length of about 80 – 90 years (Friis-Christensen and Lassen, 1991; Rind, 2002) and the Suess cycle with a supposed length of 210 years (Rind, 2002) or a range between 180 – 208 years (Speranza et al., 2003). Indeed, the basic mechanisms for these solar cycles themselves are not clarified completely and are supposed to have their origin in the suns inertial motions (Wolff, 1976; Charvatova, 2000). Anyhow, their effects are traceable on Earth and variations in the suns activity can be reconstructed from trees (Bard et al., 1997). Particularly, trees incorporate, next to the regular ^{12}C, the cosmogenic isotope ^{14}C, which is produced in the upper atmosphere by cosmic rays, penetrating the atmosphere of the Earth. High numbers of sunspots, which indicate enhanced solar activity, effectively deflect the bombardment of cosmic rays and thus result in a lower production of ^{14}C. Vice versa, lower sunspot activity results in an enhanced production of ^{14}C by a diminished deflection of cosmic rays from the atmosphere of the Earth.

Yet, the variation of the insolation during an 11 year lasting Schwabe cycle only accounts for about 0.08% and also during the Maunder sunspot minima from 1645 – 1715 AD (Eddy, 1976; Ribes and Nesme-Ribes, 1993), the insolation was only 0.2 – 0.35% below the present day (Haigh, 1994; Bard et al., 2000; Crowley, 2000). Following Rind (2002), this reduction in solar energy was too small, to account for climatic changes on the Earth. Instead, natural cycles within the atmosphere-ocean system might play a role, although Rind concedes, that this cannot explain the isotopic variations. Irrespective of the responsible mechanisms and the amount of changes in the solar irradiance, the solar minimum of Maunder coincides with the coolest episode of a period, known as the little ice-age from 1400 – 1700 AD (Mann et al., 2009). Foregoing to this period, other solar minima such as the one of Spörer (1400 – 1550 AD), Wolf (1250 – 1350 AD) and Oort (950 – 1150 AD) (Agnihotri et al., 2002) are also characterized by a certain cooling and can be seen as a manifestation of the Suess cycle (Eddy, 1976; Haeberli and Holzhauser, 2003; Raspopov et al., 2008). Here, multiple studies repeatedly proofed the coincidence of these sun spot minima and for example the progression of alpine glaciers (Haeberli and Holzhauser, 2003) and pluvial phases in the East African highlands (Verschuren et al., 2000; Trauth et al., 2003). The Gleissberg-cycle with its length between 80 – 90 years is potentially the product of an amplitude modulation of the well known 11 year lasting Schwabe cycle (Braun et al., 2005). The environmental impact of this cycle is more difficult to point out, but a potential link to Daansgard-Oeschger events is mentioned in Braun et al. (2005).

As mentioned above, a causative link between solar cycles and the climatic variations on the Earth is not an imperative. Alternatively, also variations in the atmosphere-ocean system feature a periodic character and must be comprised as a potential origin of climatic patterns. Here, we mention the Atlantic Multi Decadal Oscillation (AMO), which, with a cyclicity of 60 – 70 years, is

close to the 80 – 90 years periodicity, found in our data. The AMO is characterized by episodes of warmer and cooler SSTs and influences large parts of the Northern Hemispheres climate. Here, Benson et al. (2007) for example could link draught periods in North America and the subsequent suffering of several native cultures to the AMO. Other studies such as Folland et al. (1986) and Zhang and Delworth (2006) directly link the AMO with rainfall in India and the Sahel.

Since a temporal coincidence exists between the here unravelled cycles and distinct environmental cycles, but the very instigator cannot identified clearly, we here want to focus more on potential effects in the environment. Taking a closer look to the imprint of the cyclicities to the lithological characteristics of the S_5 sapropel, we can see that especially the shorter cycle (80 – 90 years) seems to find its expression in the cm-scale layering, as illustrated in the lithological description (Chapter 4.2). The cm-scaled layering itself is the result of the differential balance between the diatomitic bright laminae (summer) and the darker mixed laminae of the winter. As we propose, the layering is not accidental, but correlated to abundances of certain environmental sensitive elements, monitoring the terrestrial input, oceanic productivity or anoxia. Furthermore, we suggest that short time climatic changes in the length of decades, which are monitored by these variations, themselves arrange the hydrographic changes, which benefit or disadvantage the blooming of deep dwelling diatoms. The cyclic character of these variations in the XRF abundances seems to underline this hypothesis and suggests the influence of an external agitator.

The longer, ~210 year lasting signal in the here presented data is more difficult interpret. Although the signal is more of a permanent character, an expression in the lithology remains elusive. A potential explanation might be that this periodicity results from some kind of clustering of the cm-thick visible layers, which creates a longer, superimposing signal.

Concluding, the significant periodicities are summarized in Figure 63. The occurrence of cyclicities of 80 – 90 years cycle as well as a longer 180 – 240 years cycle has been verified in several proxies. These results indicate that beside the well known effects of long lasting cycles, caused by Earths orbital parameters, the regional Eemian climate was also affected by short-scaled external forcing, leading to changes in the depositional system, which appear to have been closely linked with the pelagic ecosystem. Previously, van de Berg et al. (2011) and Ganopolski and Robinson (2011) have suggested that the climate of the previous interglacial was influenced to a larger amount by the insolation than the present day, which is more under the influence of greenhouse gases. Upon the rather small magnitude of insolation changes, inherent in the solar cycles, their influence today might be smaller than during the Eemian epoch

as well as their predictive power for the actual Holocene. Yet, we do not want to fully exclude the applicability of our results for the Holocene epoch, as several studies verified solar forcing in the low latitudes (Fleitmann et al., 2003) as well in the North Atlantic (Bond et al., 2001). With the results of this work, the previously mentioned studies (Bond et al., 2001; Fleitmann et al., 2003) are further strengthened, as solar cycles seem to be a persistent feature of the climatic system of the Earth. Anyhow, this influence is poorly constrained and potentially underestimated in actual general circulation models (Haigh, 1999), especially with regard to the anthropogenic bias. Should the shorter of the two cycles (80 – 90 years) instead more reflect the AMO, instead of a sole extraterrestrial forcing, the impact during the Eemian period might be more articulated, since higher greenhouse gas concentration today might overhaul and blur the unfolding effects today (Schlesinger and Ramankutty, 1994).

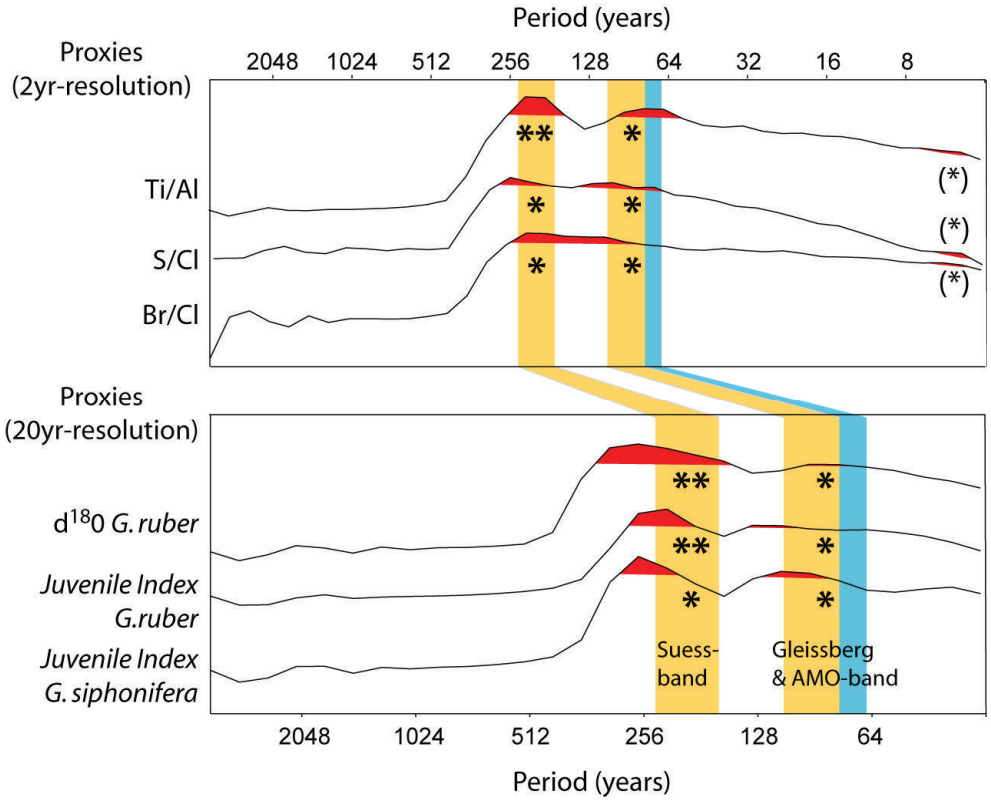

Figure 63: Global wavelets from the here investigated proxies. Following the global wavelets in Figure 62, significant periodicities are hatched in red. Discussed time bands, which comprise the solar cycles of Gleissberg and Suess, as well as the AMO are indicated as yellow and blue bars. The continuity of a signal as observed in Figure 62 is indicated, whereby ** indicates a more permanent presence throughout the observed section. * instead, indicates permanent but interrupted occurrence and (*) is regarded as noise.

6 Conclusions

The S_5 sapropels, investigated in three sediment cores from the Pliny Trench area, all feature a comparable, yet unusual thickness of about 90 cm and a striking pattern of cm-thick layers, which themselves are the product of the differential character of the sub-mm fine annual diatomitic lamination. The unusual thickness and the relative short duration of sapropel formation enables the collection and interpretation of various environmental sensitive data with highest temporal resolution, allowing the reconstruction of processes and shifts on the scale of decades. Summarizing the results from the here investigated expanded and laminated S_5 sapropels from the Eastern Mediterranean Sea, we can conclude that the issues, addressed in the introduction, could be solved. Following the declared aims of the study in chapter 1.4, the most important results can be summarized as follows:

1. The conspicuous, cm-scaled layering, and thus, also the underlying finer lamination is highly correlated in all three cores, suggesting, that this visual pattern of layers is not a random, singular phenomenon, but more likely reflects changes, acting on at least a regional scale. Defined by the optical impression and corroborated by multivariate statistics on XRF elemental ratios of environmental sensitive proxies, the expanded S_5 interval and the enclosing marls were subdivided into a total of 13 subunits. Differences between the individual zones became apparent by their chemical signature and suggest the development of the sapropel along a certain chemical gradient (Moller et al., 2011a). Along with the macroscopic, cm-scaled layering, a strong correlation exists to elemental ratios, covering the most important environmental parameters. In particular, the dark layers reflect periods of enhanced terrestrial input, productivity and anoxia, whereas the brighter layers, the corresponding elemental ratios feature lower abundances. Themselves being the result of the differential character of the annual sub-mm fine lamination, caused by deep dwelling diatoms, the cm-scaled layering is suggested to pose the visual observable expression of intra Eemian climate variability (Moller et al., 2011a).

2. Using event-based biostratigraphy on planktonic foraminifera (Cane et al., 2002), it could be shown, that the sapropel is comparable to other S_5 sapropels from the Eastern Mediterranean and did not experience post-depositional oxidation. It became also apparent, that the sapropel can be bisected into a laminated, diatomitic upper interval and a weakly laminated lower interval, where the intact laminae are affected by dilution. Based on faunal and isotopic events it could be shown that this lower interval (~9 cm) is comparable to other non-diatomitic S_5 sapropels and comprises 39% of the thickness and age of an average S_5 sapropel from the Mediterranean. Counting of the laminae in the upper, well preserved interval (~78 cm), which

captures the other 61% of the duration of S_5 formation, let us result in ~2900 varves (years), ultimately leading to a total age of about 4.8 ka, with about 1.9 ka in the lower and 2.9 ka in the upper interval. This total duration, is well comparable with actual results from the literature, albeit it marks the lower end of published S_5 durations. Still floating, the beginning of sapropel formation is allocated at about 126.4 ka, lagging the midpoint of sapropel formation 3 ka behind the insolation maximum at 127 ka.

3: Based on the here elaborated age model, the collapse of the bottom water ventilation at the onset of the sapropel, which allows the undisturbed accumulation of organic matter, was realized within ~50 years, but most likely even more rapidly. Since anoxic conditions started to evolve already before the sapropel formation, a threshold like behaviour is suggested. Also the termination of the sapropel occurred within a comparable short range of time. Within the sapropel, further short-time changes can be observed and find their optically expression in the cm-scaled layering, which comprise few (mostly 2 – 4) decades. Yet, the most striking event in our cores is the onset of the diatomitic facies itself, which must have been triggered by strong shifts the environmental boundary conditions. Amongst others, a shift to heavier $\delta^{18}O$ values points at a diminished freshwater input to the Eastern Mediterranean and thus, an enhanced exchange of surface water through the Strait of Gibraltar. The onset of the distinct lamination, which we date to ~124.5 ka may reflect stimulated gyres and eddies in the area of the Hellenic Trench and might result in a local shoaling of the nutricline, favouring the enhanced primary productivity of mat forming diatoms. Subsequently, this could favour the primary productivity and the downward flux of mat-forming diatoms to the sediment, being preserved even in the Si undersaturated waters of the Mediterranean.

4: Generally, S_5 developed under warmer conditions, relative to the periods before and after sapropel formation, as is indicated for example by increasing abundances of *G. ruber* as a typical ambassador of subtropical species and also their tendency to grow larger test sizes within the sapropel. Despite their shortcomings also the SSTs from ANNs suggest slightly warmer temperatures within the sapropel as well as stronger seasonal contrasts. Yet, a certain cooling is indicated, about 1.0 ka after the onset of the sapropel (125.4 ka), lasting for about 0.8 – 1.0 ka. The identification of an intra Eemian cooling is consistent with studies on terrestrial (Karabanov et al., 2000; Sánchez Goñi et al., 2000) and marine material (Maslin et al., 1998; Rohling et al., 2002) and a potential stronger influence of the high-latitude climate system could here provide an explanation. The already mentioned drop in $\delta^{18}O$ at the same time documents the diminished monsoonal influence and further strengthens this finding of an intra Eemian cooling and a temporal south-ward retreat of the ITCZ.

5. Additionally to these unique and larger climatic changes, there are also signs of cyclic variations in environmental sensitive proxies, being visually expressed in the cm-scaled layering. The length of these cycles corresponds to that of certain solar cycles (Suess-cycle 180 – 210 years, Gleissberg-cycle 80 – 90 years) as well as the AMO (60 – 70 years), potentially pointing to an external cyclic forcing. Anyhow, their influence during the Eemian epoch might be stronger, compared to the Holocene, especially since the amplitudes of solar cycles are rather small, and the influence of the insolation on the contemporary climate system is weaker than during MIS 5e (van de Berg et al., 2011).

To give an outlook for future investigations, the highest priority is the determination of the absolute age of the thin ash layer, found in the upper part of the sapropel, complementing the actual age datings of the sapropel with an absolute age for the onset and the termination, which is, so far, still floating. Another potential analysis would comprise a closer look to the terrestrial input by analysing the size fraction and composition of the clastic material in the sapropel, allowing for a more direct analysis of the terrestrial input. Clay mineralogy might depict another analysis to follow, and might provide details about the provenance of terrestrial input, further allowing to track potential changes therein throughout the formation of the sapropel. Furthermore, the measurement of various biomarkers will clarify the high productivity at the poorly laminated basal part of the sapropel. Despite the high resolution of the XRF scanning, instrumental, noise is a poorly constrained issue, which could be bypassed with elemental microprobe analysis on the resin impregnated thin sections.

7 Appendix

The appendix of this study strictly follows the figures, tables and plates therein. Each figure, table and plate is represented by a folder within the directory “Figures_tables_and_data”, containing the original image file as used in the study, as well as the necessary data to reproduce them.

- Fig01_mediterranean_tectonic
- Fig02_mediterranean_topography_and_basins
- Fig03_climate_data_athen_alexandria_valencia
- Fig04_chlorophyll_like_pigments
- Fig05_mediterranean_currents
- Fig06_intermediate_and_deep_water_formation
- Fig07_monsoon_index
- Fig08_potential_circulation
- Fig09_varve_scheme
- Fig10_MIS_stages_and_insolation
- Fig11_core_locations_of_SL67_SL103_SL104
- Fig12_M51-3 SL103_overview_photography
- Fig13_5_curves_of_lightness
- Fig14_illustration_of_a_PCA
- Fig15_wavelet_examples
- Fig16_double_L-channel_illustration
- Fig17_sampling_scheme_of_SL104
- Fig18_selected_outcrops_from_thin-sections
- Fig19_S5-sapropel_thicknesses
- Fig20_crossplots_thickness_vs_waterdepth_vs_depth
- Fig21_overview_SL67_SL103_SL104
- Fig22_thinsection_4.2
- Fig23_tephra_layer
- Fig24_water-content_and_magsus
- Fig25_XRF_abundances_SL67
- Fig26_XRF_abundances_SL103
- Fig27_XRF_abundances_SL104
- Fig28_ICP OES_XRF_crossplots
- Fig29_cluster_and_PCA
- Fig30_SL103_XRF_outcrops

- Fig31_PCA_and_pearson
- Fig32_faunal_data_overview
- Fig33_PF_in_thinsections
- Fig34 _Fig35_PF_abundances
- Fig36_isotopes_from_Gruber_and_Gbulloides
- Fig37_ANN_temperatures
- Fig38_stacked_thinsections
- Fig39_SEM-pictures
- Fig40_thick_laminae
- Fig41_census_of_laminae
- Fig42_crossplots_of_biostratigraphic_events
- Fig43_water_and_SiCa_content
- Fig44_various_S5-sapropel_ages
- Fig45_Fig46_isotopes_with_timeaxis
- Fig47_Fig48_Fig50_Fig53_chemical abundances
- Fig49_isoreniaratene_Corg_LC21
- Fig51_crossplot_PF_CaAl
- Fig52_accumulation_rate
- Fig54_ICP-OES_FeS-ratio
- Fig55_diatomitic_S5_sapropels_map
- Fig56_combined_proxies
- Fig57_nutricline_shoaling
- Fig58_DCA_of_PF
- Fig59-Fig60_juvenile_indices
- Fig61_ANN_and_sediment_colour
- Fig62_waveletanalysis
- Fig63_global_wavelet
- Plate01_planktonic_foraminifera
- Plate02_planktonic_foraminifera
- Table01_sapropel_ages
- Table02_data_on_SL67_SL103_SL104
- Table03_ICP_OES_sample_depths
- Table04_ANN_species
- Table05_resin_impregnation_batch_composition
- Table06_S5-sapropel_thicknesses
- Table07_ICP_OES_measurements

– Table08_biostratigraphic_events

Additionally the supplementary data contain the files *"XRF_data_stitched.xls" and "input_data_for_wavelet_analysis.xls",* where the most important data of faunal, geochemical and geophysical abundances and concentrations are presented in a more combined way. A CD with the above mentioned files containing all data pertaining to this dissertation can be obtained from the author upon request.

8 Acknowledgements

First of all, I want to express my greatest gratitude to my parents for giving me the possibility to attain my education, through their care and support.

I wish to thank my supervisor Hartmut Schulz, allowing for a very high degree of freedom and autonomy throughout the whole project. I owe further gratitude to Michal Kučera for his task as a second supervisor and often providing fresh ideas.

I am especially grateful to Yvonne Hamann, Olaf Dellwig and Nils Andersen, who provided the measurements on the material and without their support, this work would not have been possible. I want to thank Dr. Jennifer Pike and Thomas Gregory for introducing me into the secrets of fluid displacive soft sediment preparation. Further gratitude go to Eelco Rohling, supporting this work with several sets of raw data and. Wolfgang Kürner is to thank for the construction of tools, making the work more effective and accurate. I also thank Margret Bayer for helping with organizational issues in an uncomplicated and friendly way. I thank Peer Jeisicke, who prepared a multitude of thin sections by hand, and in this way contributes to this work. Libuše Rammerstorfer was always a straight forward help in the search for literature. I am also indepted to my office mate Peter Fittkau for assistance with the SEM and providing gallons of coffee and tea.

Fabian Bonitz is thanked for the processing of countless samples and also Mirjam Koch and Elena Wolff, who did their own research-work on the material and enriched the project with their results. Ralf Aurahs, Garbiele Trommer, Michael Siccha, Petra Heinz, Manuel Weinkauf, Anne-Katrin Enge, Agnes Weiner, Franziska Simmank, Kerstin Braun, Ute Treppke, Wolfram Schinko, Jan-Peter Friedrich, Janina Dynowski and Sofie Jehle are also thanked for providing their knowledge and encouragement when I needed it.

Lastly and by no means least I want to thank Anja Böhm for providing formal corrections and baering my lamentations.

9 References

Adloff, F., Mikolajewicz, U., Kucera, M., Grimm, R., Maier-Reimer, E., Schmiedl, G., and Emeis, K. C., 2011, Upper ocean climate of the Eastern Mediterranean Sea during the Holocene Insolation Maximum–a model study: Climate of the Past Discussions, v. 7, pp. 1457-1509.

Agnihotri, R., Dutta, K., Bhushan, R., and Somayajulu, B. L. K., 2002, Evidence for solar forcing on the Indian monsoon during the last millennium: Earth and Planetary Science Letters, v. 198, no. 3-4, pp. 521-527.

Albarède, F., 2009, Geochemistry: An Introduction, Cambridge, Cambridge University Press, 262pp.

Amante, C., Eakins, B. W., and Center, N. G. D., 2009, ETOPO1 1 arc-minute global relief model: procedures, data sources and analysis, US Dept. of Commerce, National Oceanic and Atmospheric Administration, National Environmental Satellite, Data, and Information Service, National Geophysical Data Center, Marine Geology and Geophysics Division.

Anderson, D. M., Prell, W. L., and Barratt, N. J., 1989, Estimates of Sea Surface Temperature in the Coral Sea at the Last Glacial Maximum: Paleoceanography, v. 4, no. 6, pp. 615-627.

Armstrong, H., and Brasier, M. D., 2005, Microfossils, Wiley-Blackwell, 304pp.

Azov, Y., 1986, Seasonal patterns of phytoplankton productivity and abundance in nearshore oligotrophic waters of the Levant Basin (Mediterranean): Journal of Plankton Research, v. 8, no. 1, pp. 41-43.

Bar-Matthews, M., Ayalon, A., and Kaufman, A., 2000, Timing and hydrological conditions of Sapropel events in the Eastern Mediterranean, as evident from speleothems, Soreq cave, Israel: Chemical Geology, v. 169, no. 1-2, pp. 145-156.

Bar-Matthews, M., Kaufman, A., and Wasserburg, G. J., 1999, The Eastern Mediterranean paleoclimate as a reflection of regional events: Soreq cave, Israel: Earth and Planetary Science Letters, v. 166, no. 1-2, pp. 85-95.

Barats, A., Amouroux, D., Pécheyran, C., Chauvaud, L., Thébault, J., and Donard, O. F. X., 2010, Spring molybdenum enrichment in scallop shells: a potential tracer of diatom productivity in temperate coastal environments (Brittany, NW France): Biogeosciences, v. 7, no. 1, pp. 233-245.

Bard, E., Jouannic, C., Hamelin, B., Pirazzoli, P., Arnold, M., Faure, G., Sumosusastro, P., and Syaefudin, 1996, Pleistocene sea levels and tectonic uplift based on dating of corals from Sumba Island, Indonesia: Geophys. Res. Lett., v. 23, no. 12, pp. 1473-1476.

Bard, E., Raisbeck, G., Yiou, F., and Jouzel, J., 2000, Solar irradiance during the last 1200 years based on cosmogenic nuclides: Tellus B, v. 52, no. 3, pp. 985-992.

Bard, E., Raisbeck, G. M., Yiou, F., and Jouzel, J., 1997, Solar modulation of cosmogenic nuclide production over the last millennium: comparison between 14C and 10Be records: Earth and Planetary Science Letters, v. 150, no. 3-4, pp. 453-462.

Barrier, E., Chamot-Rooke, N., Giordano, G., Morelli, A., and Brouillet, J., 2004, Geodynamic map of the Mediterranean: Commission for the Map of the World, CCGM.

Bauch, H. A., Kandiano, E. S., Helmke, J., Andersen, N., Rosell-Mele, A., and Erlenkeuser, H., 2011, Climatic bisection of the last interglacial warm period in the Polar North Atlantic: Quaternary Science Reviews, v. 30, no. 15-16, pp. 1813-1818.

Baumfalk, Y. A., Troelstra, S. R., Ganssen, G., and Van Zanen, M. J. L., 1987, Phenotypic variation of Globorotalia scitula (foraminiferida) as a response to Pleistocene climatic fluctuations: Marine Geology, v. 75, no. 1-4, pp. 231-240.

Bé, A. W. H., and Tolderlund, D. S., 1971, Distribution and ecology of living planktonic foraminifera in surface waters of the Atlantic and Indian Oceans, in: The micropalaeontology of Oceans (B. M. Funnel and W. R. Riedel, eds), Cambridge University Press, Cambridge, v. 20, pp. 105–149.

Benson, L. V., Berry, M. S., Jolie, E. A., Spangler, J. D., Stahle, D. W., and Hattori, E. M., 2007, Possible impacts of early-11th-, middle-12th-, and late-13th-century droughts on western Native Americans and the Mississippian Cahokians: Quaternary Science Reviews, v. 26, no. 3-4, pp. 336-350.

Bergametti, G., Dutot, A. L., Buat-Ménard, P., Losno, R., and Remoudaki, E., 1989, Seasonal variability of the elemental composition of atmospheric aerosol particles over the northwestern Mediterranean: Tellus B, v. 41, no. 3, pp. 353-361.

Berger, A., 1978, Long-term variations of caloric insolation resulting from the earth's orbital elements: Quaternary Research, v. 9, no. 2, pp. 139-167.

Berger, A., and Loutre, M. F., 1991, Insolation values for the climate of the last 10 million years: Quaternary Science Reviews, v. 10, no. 4, pp. 297-317.

Berner, R. A., and Berner, E. K., 1997, Silicate weathering and climate: Tectonic uplift and climate change, pp. 353-364.

Bethoux, J. P., Gentili, B., Morin, P., Nicolas, E., Pierre, C., and Ruiz-Pino, D., 1999, The Mediterranean Sea: a miniature ocean for climatic and environmental studies and a key for the climatic functioning of the North Atlantic: Progress In Oceanography, v. 44, no. 1-3, pp. 131-146.

Björklund, K. R., and De Ruiter, R., 1987, Radiolarian preservation in Eastern Mediterranean anoxic sediments: Marine Geology, v. 75, no. 1-4, pp. 271-281.

Blow, W. H., 1959, Age, correlation, and biostratigraphy of the upper Tocuyo (San Lorenzo) and Pozón formations, Ithaca, N.Y.,, Paleontological Research Insitution.

Bodén, P., and Backman, J., 1996, A laminated sediment sequence from the northern North Atlantic Ocean and its climatic record: Geology, v. 24, no. 6, pp. 507-510.

Bond, G., Kromer, B., Beer, J., Muscheler, R., Evans, M. N., Showers, W., Hoffmann, S., Lotti-Bond, R., Hajdas, I., and Bonani, G., 2001, Persistent Solar Influence on North Atlantic Climate During the Holocene: Science, v. 294, no. 5549, pp. 2130-2136.

Bosch, J. H. A., Cleveringa, P., and Meijer, T., 2000, The Eemian stage in the Netherlands; history, character and new research: Geologie en Mijnbouw/ Journal of Geosiences v. 79, pp. 135-145.

Boucher, K., 1975, Global climate, London, English Universities Press Ltd., 326pp.

Bradley, W. H., 1938, Mediterranean sediments and Pleistocene sea levels: Science, v. 88, no. 2286, pp. 376-379.

Brady, H. B., 1877, Supplementary Note on the Foraminifera of the Chalk (?) of the New Britain Group. Geological Magazine (Decade II), v. 4 , pp. 534-536.

Brady, H. B., 1879, Notes on some of the reticularian Rhizopoda of the Challenger Expedition II: additions to the knowledge of porcellaneous and hyaline types: Quarterly Journal of Microscopical Science, v. 19, pp. 20-63.

Brady, H. B., 1882, Report on the Foraminifera in Tizard & Murray, Exploration of the Faròe Channel during the summer of 1880 in HMS «Knight Errant», with subsidiary reports (1880-1882), no.111, pp. 708-717.

Braun, H., Christl, M., Rahmstorf, S., Ganopolski, A., Mangini, A., Kubatzki, C., Roth, K., and Kromer, B., 2005, Possible solar origin of the 1,470-year glacial climate cycle demonstrated in a coupled model: Nature, v. 438, no. 7065, pp. 208-211.

Brumsack, H.-J., and Wehausen, R., 1999, A geochemical record of precession-induced cyclic eastern Mediterranean sedimentation; implications for northern Sahara humidity during the Pliocene: Naturwissenschaften, v. 86, pp. 281-286.

Bryden, H. L., and Kinder, T. H., 1991, Steady two-layer exchange through the Strait of Gibraltar: Deep-sea research. Part A. Oceanographic research papers, v. 38, no. 1, pp. 445-463.

Calvert, S. E., 1983, Geochemistry of Pleistocene sapropels and associated sediments from the eastern Mediterranean: Oceanologica Acta, v. 6, pp. 255-267.

Calvert, S. E., and Fontugne, M. R., 2001, On the late Pleistocene-Holocene sapropel record of climatic and oceanographic variability in the eastern Mediterranean: Paleoceanography, v. 16, no. 1, pp. 78-94.

Calvert, S. E., Nielsen , B., and Fontugne, M. R., 1992, Evidence from nitrogen isotope ratios for enhanced productivity during formation of eastern Mediterranean sapropels: Nature, v. 359, pp. 223–225.

Calvert, S. E., and Pedersen, T. F., 2007, Elemental proxies for palaeoclimatic and palaeoceanographic variability in marine sediments: interpreatation and application, *in* C. Hillaire-Marcel, A. d. V., ed., Proxies in late Cenozoic Paleoceanography, Volume 1, Elsevier, pp. 567-644.

Cane, T., Rohling, E. J., Kemp, A. E. S., Cooke, S., and Pearce, R. B., 2002, High-resolution stratigraphic framework for Mediterranean sapropel S5: defining temporal relationships between records of Eemian climate variability: Palaeogeography, Palaeoclimatology, Palaeoecology, v. 183, no. 1-2, pp. 87-101.

Casford, J. S. L., Rohling, E. J., Abu-Zied, R. H., Fontanier, C., Jorissen, F. J., Leng, M. J., Schmiedl, G., and Thomson, J., 2003, A dynamic concept for eastern Mediterranean circulation and oxygenation during sapropel formation: Palaeogeography, Palaeoclimatology, Palaeoecology, v. 190, pp. 103-119.

Caspers, G., Merkt, J., Müller, H., and Freund, H., 2002, The Eemian Interglaciation in Northwestern Germany: Quaternary Research, v. 58, no. 1, pp. 49-52.

Charvatova, I., Can origin of the 2400-year cycle of solar activity be caused by solar inertial motion? 2000, Volume 18, Springer, pp. 399-405.

Cheddadi, R., Mamakowa, K., Guiot, J., de Beaulieu, J. L., Reille, M., Andrieu, V., Granoszewski, W., and Peyron, O., 1998, Was the climate of the Eemian stable? A quantitative climate reconstruction from seven European pollen records: Palaeogeography, Palaeoclimatology, Palaeoecology, v. 143, no. 1-3, pp. 73-85.

Cifelli, R., 1961, Globigerina incompta, a new species of pelagic foraminifera from the North Atlantic: Contributions from the Cushman Foundation for Foraminiferal Research, v. 12, pp. 83-86.

Cita, M. B., Vergnaud-Grazzini, C., Robert, C., Chamley, H., Ciaranfi, N., and d'Onofrio, S., 1977, Paleoclimatic record of a long deep sea core from the eastern Mediterranean: Quaternary Research, v. 8, no. 2, pp. 205-235.

Colin, J. L., Jaffrezo, J. L., and Gros, J. M., 1990, Solubility of major species in precipitation: factors of variation: Atmospheric Environment. Part A. General Topics, v. 24, no. 3, pp. 537-544.

Comas, M. C., Zahn, R., and Klaus, A., 1996, Proceedings in the Ocean Drilling Program, Initial Reports., 161, College Station, TX (Ocean Drilling Program)

Conkright, M. E., Locarnini, R. A., Garcia, H. E., O'Brien, T. D., Boyer, T. P., Stephens, C., and Antonov, J. I., 2002, World Ocean Atlas 2001: objective analyses, data statistics and figures CD-ROM documentation, 17 pp.

Coste, B., Corre, P. L., and Minas, H. J., 1988, Re-evaluation of the nutrient exchanges in the strait of gibraltar: Deep Sea Research Part A. Oceanographic Research Papers, v. 35, no. 5, pp. 767-775.

Cramp, A., and O'Sullivan, G., 1999, Neogene sapropels in the Mediterranean: a review: Marine Geology, v. 153, no. 1-4, pp. 11-28.

Crowley, T. J., 2000, Causes of climate change over the past 1000 years: Science, v. 289, no. 5477, pp. 270-277.

Crusius, J., Calvert, S., Pedersen, T., and Sage, D., 1996, Rhenium and molybdenum enrichments in sediments as indicators of oxic, suboxic and sulfidic conditions of deposition: Earth and Planetary Science Letters, v. 145, no. 1-4, pp. 65-78.

d'Orbigny, A. D., 1826, Tableau méthodique de la classe des Céphalopodes: Annales des Sciences Naturelles (Paris), v. 1(7), pp. 245-315.

d'Orbigny, A. D., 1839a, Foraminifères des Iles Canaries: In Barker-Webb, P., and Berthelot, S. (eds.), Histoire Naturelle des Iles Canaries 2, pt2, Zool., Paris, pp. 119-146.

d'Orbigny, A. D., 1839b, Foraminiferes; In: de la Sagra, R. (ed.): Histoire physique, politique et naturelle de l'Ile de Cuba 8, Paris, 224pp.

Danelian, T., and Frydas, D., Late Quaternary polycystine radiolarians and silicoflagellates of a diatomaceous sapropel from the Eastern Mediterranean, Sites 969 and 9711998, Volume 160, Ocean Drilling Program, pp. 137-154.

Darling, K. F., Kucera, M., Kroon, D., and Wade, C. M., 2006, A resolution for the coiling direction paradox in Neogloboquadrina pachyderma: Paleoceanography, v. 21, no. 2, PA2011, pp. 1-14.

de Lange, G. J., Boelrijk, N. A. I. M., Catalano, G., Corselli, C., Klinkhammer, G. P., Middelburg, J. J., Müller, D. W., Ullman, W. J., Van Gaans, P., and Woittiez, J. R. W., 1990, Sulphate-related

equilibria in the hypersaline brines of the Tyro and Bannock Basins, eastern Mediterranean: Marine Chemistry, v. 31, no. 1-3, pp. 89-112.

de Lange, G. J., and ten Haven, H. L., 1983, Recent sapropel formation in the eastern Mediterranean: Nature, v. 305, no. 5937, pp. 797-798.

de Rijk, S., Hayes, A., and Rohling, E. J., 1999, Eastern Mediterranean sapropel S1 interruption: an expression of the onset of climatic deterioration around 7 ka BP: Marine Geology, v. 153, no. 1-4, pp. 337-343.

de Vernal, A., Rosell-Melé, A., Kucera, M., Hillaire-Marcel, C., Eynaud, F., Weinelt, M., Dokken, T., and Kageyama, M., 2006, Comparing proxies for the reconstruction of LGM sea-surface conditions in the northern North Atlantic: Quaternary Science Reviews, v. 25, no. 21-22, pp. 2820-2834.

deMenocal, P., Ortiz, J., Guilderson, T., Adkins, J., Sarnthein, M., Baker, L., and Yarusinsky, M., 2000, Abrupt onset and termination of the African Humid Period: rapid climate responses to gradual insolation forcing: Quaternary Science Reviews, v. 19, no. 1-5, pp. 347-361.

Dymond, J., Suess, E., and Lyle, M., 1992, Barium in Deep-Sea Sediment: A Geochemical Proxy for Paleoproductivity: Paleoceanography, v. 7, no. 2, pp. 163-181.

Eddy, J. A., 1976, The Maunder Minimum: Science, v. 192, no. 4245, pp. 1189-1202.

Egger, J. G., 1893, Foraminiferen aus Meeresgrundproben, gelothet von 1874 bis 1876 von S.M.Sch. Gazelle: Königlich Bayerische Akademie der Wissenschaften, München, M.-Ph. C1., Abh., v. 2, pp. 193-458.,

Emeis, K.-C., Sakamoto, T., Wehausen, R., and Brumsack, H.-J., 2000, The sapropel record of the eastern Mediterranean Sea - results of Ocean Drilling Program Leg 160: Palaeogeography, Palaeoclimatology, Palaeoecology, v. 158, no. 3-4, pp. 371-395.

Emeis, K. C., Robertson, A. H., and Richter, C., 1996, Proceedings of the Ocean Drilling Program, Initial Report 160, 971 pp.

Emeis, K. C., Schulz, H., Struck, U., Rossignol-Strick, M., Erlenkeuser, H., Howell, M. W., Kroon, D., Mackensen, A., Ishizuka, S., Oba, T., Sakamoto, T., and Koizumi, I., 2003, Eastern Mediterranean surface water temperatures and $\delta^{18}O$ composition during deposition of sapropels in the late Quaternary: AGU, 0883-8305, 18 pp.

Fairbanks, R. G., and Wiebe, P. H., 1980, Foraminifera and chlorophyll maximum: vertical distribution, seasonal succession, and paleoceanographic significance: Science, v. 209, no. 4464, pp. 1524-1526.

Field, M. H., Huntley, B., and Muller, H., 1994, Eemian climate fluctuations observed in a European pollen record: Nature, v. 371, no. 6500, pp. 779-783.

Fleitmann, D., Burns, S. J., Mudelsee, M., Neff, U., Kramers, J., Mangini, A., and Matter, A., 2003, Holocene forcing of the Indian Monsoon recorded in a stalagmite from Southern Oman: Science, v. 300, no. 5626, pp. 1737-1739.

Folland, C., Palmer, T., and Parker, D., 1986, Sahel rainfall and worldwide sea temperatures, 1901–85: Nature, v. 320, no. 6063, pp. 602-607.

Fontugne, M. R., and Calvert, S. E., 1992, Late Pleistocene Variability of the Carbon Isotopic Composition of Organic Matter in the Eastern Mediterranean: Monitor of Changes in Carbon Sources and Atmospheric CO_2 Concentrations: Paleoceanography, v. 7, no. 1, pp. 1-20.

Friedrich, O., Schmiedl, G., and Erlenkeuser, H., 2006, Stable isotope composition of Late Cretaceous benthic foraminifera from the southern South Atlantic: Biological and environmental effects: Marine Micropaleontology, v. 58, no. 2, pp. 135-157.

Friis-Christensen, E., and Lassen, K., 1991, Length of the Solar Cycle: An indicator of solar activity closely associated with climate: Science, v. 254, no. 5032, pp. 698-700.

Frisch, W., and Meschede, M., 2007, Plattentektonik: Kontinentverschiebung und Gebirgsbildung, Darmstadt, Primus Verlag, 192 pp,

Frydas, D., and Hemleben, C., 2007, Opal phytoplankton assemblages of the late Quaternary sapropel layers S_5 and S_7 from the southeastern Mediterranean Sea ("Meteor"-Cruise 40/4, Site 67): Revue de Micropaléontologie, v. 50, pp. 169-183.

Gacic, M., Kovacevic, V., Manca, B., Papageorgiou, E., Poulain, P., Scarazzato, P., and Vetrano, A., 1996, Thermohaline properties and circulation in the Strait of Otranto: Dynamics of Mediterranean Straits and Channel, Bulletin de l'Institut Oceanographique, Monaco, n. special, v. 17, pp. 117-145.

Ganopolski, A., and Robinson, A., 2011, Palaeoclimate: The past is not the future: Nature Geosci, v. 4, no. 10, pp. 661-663.

Gao, Y., Fan, S. M., and Sarmiento, J. L., 2003, Aeolian iron input to the ocean through precipitation scavenging: A modeling perspective and its implication for natural iron fertilization in the ocean: J. Geophys. Res, v. 108, pp. 4221.

Gardner, M. W., and Dorling, S. R., 1998, Artificial neural networks (the multilayer perceptron)-a review of applications in the atmospheric sciences: Atmospheric Environment, v. 32, no. 14-15, pp. 2627-2636.

Gascard, J., and Richez, C., 1985, Water masses and circulation in the Western Alboran Sea and in the Straits of Gibraltar: Progress In Oceanography, v. 15, no. 3, pp. 157-216.

Gilman, C., and Garrett, C., 1994, Heat flux parameterizations for the Mediterranean Sea: The role of atmospheric aerosols and constraints from the water budget: Journal of Geophysical Research, v. 99, no. C3, pp. 5119-5134.

Gingele, F. X., and Schmieder, F., 2001, Anomalous South Atlantic lithologies confirm global scale of unusual mid-Pleistocene climate excursion: Earth and Planetary Science Letters, v. 186, no. 1, pp. 93-101.

Giunta, S., Negri, A., Maffioli, P., Sangiorgi, F., Capotondi, L., Morigi, C., Principato, M. S., and Corselli, C., 2006, Phytoplankton dynamics in the eastern Mediterranean Sea during Marine Isotopic Stage 5e: Palaeogeography, Palaeoclimatology, Palaeoecology, v. 235, no. 1-3, pp. 28-47.

Goes, S., Giardini, D., Jenny, S., Hollenstein, C., Kahle, H. G., and Geiger, A., 2004, A recent tectonic reorganization in the south-central Mediterranean: Earth and Planetary Science Letters, v. 226, no. 3-4, pp. 335-345.

Gornitz, V., 2009, Encyclopedia of paleoclimatology and ancient environments, Springer Verlag, 1049 pp.

Gough, D. O., 1981, Solar interior structure and luminosity variations: Solar Physics, v. 74, no. 1, pp. 21-34.

Gourgiotis, A., 2004, Etude géochimique du Sapropèle S5 de Méditerranée orientale: une approche radiochimique. Serait-il possible que les sapropèles soient des indicateurs des grands évènements sismiques?: DEA Océanologie Météorologie et Environnement, Laboratoire des Sciences du Climat et de l'Environnement, CNRS-CEA, Université P. et M. Curie Paris IV.

Grigorov, I., Pearce, R. B., and Kemp, A. E. S., 2002, Southern Ocean laminated diatom ooze: mat deposits and potential for palaeo-flux studies, ODP leg 177, Site 1093: Deep Sea Research Part II: Topical Studies in Oceanography, v. 49, no. 16, pp. 3391-3407.

Guerzoni, S., Molinaroli, E., Rossini, P., Rampazz0, G., Quarantotto, G., De Falco, G., and Cristini, S., 1999, Role of desert aerosol in metal fluxes in the Mediterranean area: Chemosphere, v. 39, no. 2, pp. 229-246.

Guiot, J., Pons, A., de Beaulieu, J. L., and Reille, M., 1989, A 140,000-year continental climate reconstruction from two European pollen records: Nature, v. 338, pp. 309-313.

Haeberli, W., and Holzhauser, H., 2003, Alpine glacier mass changes during the past two millennia: Pages News, v. 11, no. 1, pp. 13–15.

Haigh, J. D., 1994, The role of stratospheric ozone in modulating the solar radiative forcing of climate: Nature, v. 370, no. 6490, pp. 544-546.

Haigh, J. D., 1999, A GCM study of climate change in response to the 11-year solar cycle: Quarterly Journal of the Royal Meteorological Society, v. 125, no. 555, pp. 871-892.

Hammer, Ø., and Harper, D. A. T., 2006, Paleontological data analysis, Wiley-Blackwell, 351 pp.

Harding, A. E., Palutikof, J., and Holt, T., 2009, The climate system: The Physical Geography of the Mediterranean. Oxford University Press, Oxford, pp. 69-88.

Hasselmann, K., 1976, Stochastic climate models Part I. Theory: Tellus, v. 28, no. 6, pp. 473-485.

Hayes, A., Kucera, M., Kallel, N., Sbaffi, L., and Rohling, E. J., 2005, Glacial Mediterranean sea surface temperatures based on planktonic foraminiferal assemblages: Quaternary Science Reviews, v. 24, no. 7-9, pp. 999-1016.

Heinrichs, H., Brumsack, H. J., and Loftfield, N., 1986, Verbessertes Druckaufschlusssystem für biologische und anorganische Materialien, Weinheim, VCH, v. 3.

Hemleben, C., Becker, T., Bellas, S., Benningsen, G., Casford, J., Cagatay, N., Emeis, K. C., Engelen, B., Ertan, T., Fontanier, C., Friedrich, O., Frydas, D., Giunta, S., Hoffelner, H., Jorissen, F. J., Kahl, K., Kaszemeik, K., Lykousis, V., Meier, S., Nickel, G., Overman, J., Pross, J., Reichel, T., Robert, C., Rohling, E., Ruschmeier, W., Sakinc, M., Schiebel, R., Schmiedl, G., Schubert, K., Schulz, H., Tischnak, J., and Truscheit, T., 2003, Ostatlantik-Mittelmeer-Schwarzes Meer Part 3 Cruise No. 51, Leg 3 14 November – 10 December 2001, Valetta – Istanbul: METEOR-Berichte 03-1, Institut für Meereskunde der Universität Hamburg.

Hemleben, C., Spindler, M., and Anderson, O. R., 1989, Modern Planktonic Foraminifera, New York, Springer-Verlag, 363 pp.

Hieke, W., Hemleben, C., Linke, P., Türkay, M., and Weikert, H., 1999, Mittelmeer 1997/98, Cruise No 40: 28. October 1997 - 10. February 1998.: Meteor-Berichte 99-2, Institut für Meereskunde der Universität Hamburg.

Hieke, W., Sigl, W., and Fabricius, F., 1973, Morphological and structural aspects of the Mediterranean Ridge SW of Peloponnesus (Ionian Sea): Bulletin of the Geological Society, Greece, v. 10, pp. 109–126.

Hilgen, F. J., 1991, Astronomical calibration of Gauss to Matuyama sapropels in the Mediterranean and implication for the Geomagnetic Polarity Time Scale: Earth and Planetary Science Letters, v. 104, no. 2-4, pp. 226-244.

Hilgen, F. J., Krijgsman, W., Langereis, C. G., Lourens, L. J., Santarelli, A., and Zachariasse, W. J., 1995, Extending the astronomical (polarity) time scale into the Miocene: Earth and Planetary Science Letters, v. 136, no. 3-4, pp. 495-510.

Hofker, J., 1956, Foraminifera Dentata foraminifera of Sata Cruz and Thatch Island, Virgin Archipelago, West Indies: spolia zoological museum kobenhavn, v. 15, pp. 1-237.

Howell, M. W., and Thunell, R. C., 1992, Organic carbon accumulation in Bannock Basin: evaluating the role of productivity in the formation of eastern Mediterranean sapropels: Marine Geology, v. 103, no. 1-3, pp. 461-471.

Hsü, K., Ryan, W., and Cita, M., 1973, Late Miocene desiccation of the Mediterranean: Nature, v. 242, no. 5395, pp. 240-244.

Jenkins, R., de Vries, J. L., and De Vries, J., 1967, Practical X-ray spectrometry, Springer-Verlag, 182 pp.

Jilbert, T., Reichart, G. J., Mason, P., de Lange, G. J., Menviel, L., Timmermann, A., Timm, O., Mouchet, A., Xu, J., and Kuhnt, W., 2010, Short-time-scale variability in ventilation and export productivity during the formation of Mediterranean sapropel S1: Paleoceanography, v. 25, no. 4, pp. PA4232.

Jolliffe, I., 2005, Principal Component Analysis, John Wiley & Sons, Ltd, Encyclopedia of Statistics in Behavioral Science, 2352pp.

Jorissen, F. J., Fontanier, C., and Thomas, E., 2007, Chapter Seven Paleoceanographical Proxies Based on Deep-Sea Benthic Foraminiferal Assemblage Characteristics, *in* Claude, H. M., and Anne De, V., eds., Developments in Marine Geology, Volume Volume 1, Elsevier, pp. 263-325.

Jouzel, J., Barkov, N., Barnola, J., Bender, M., Chappellaz, J., Genthon, C., Kotlyakov, V., Lipenkov, V., Lorius, C., and Petit, J., 1993, Extending the Vostok ice-core record of palaeoclimate to the penultimate glacial period: Nature, v. 364, no. 6436, pp. 407-412.

Karabanov, E. B., Propenko, A. A., Williams, D. F., and Khursevich, G. K., 2000, Evidence for mid-Eemian cooling in continental climatic record from Lake Baikal: Journal of Paleolimnology, v. 23, no. 4, pp. 365-371.

Keller, J., Ryan, W., Ninkovich, D., and Altherr, R., 1978, Explosive volcanic activity in the Mediterranean over the past 200,000 yr as recorded in deep-sea sediments: Bulletin of the Geological Society of America, v. 89, no. 4, pp. 591-604.

Kemp, A., Pearce, R., Grigorov, I., Rance, J., Lange, C., Quilty, P., and Salter, I., 2006, The production of giant marine diatoms and their export at oceanic frontal zones: implications for Si and C flux in stratified oceans: Global Biogeochemical Cycles, v. 20, no. GB4S04.

Kemp, A. E. S., 1996, Laminated sediments as palaeo-indicators: Geological Society, London, Special Publications, v. 116, no. 1, pp. vii-xii.

Kemp, A. E. S., and Baldauf, J. G., 1993, Vast Neogene laminated diatom mat deposits from the eastern equatorial Pacific Ocean: Nature, v. 362, pp. 141-143.

Kemp, A. E. S., Pearce, R. B., Koizumi, I., Pike, J., and Rance, S. J., 1999, The role of mat-forming diatoms in the formation of Mediterranean sapropels: Nature, v. 398, no. 6722, pp. 57-61.

Kemp, A. E. S., Pike, J., Pearce, R. B., and Lange, C. B., 2000, The "fall dump" -- a new perspective on the role of a "shade flora" in the annual cycle of diatom production and export flux: Deep Sea Research Part II: Topical Studies in Oceanography, v. 47, no. 9-11, pp. 2129-2154.

Kidd, R. B., Cita, M. B., and Ryan, W. B. F., 1978, Stratigraphy of eastern Mediterranean sapropel sequences recovered during DSDP Leg 42A and their paleoenvironmental significance: Initial Reports DSDP, v. 42, no. 421-443.

Koch, M., 2010, Die Reaktion planktischer Foraminiferen auf Umweltveränderungen während der Bildung von Sapropel S5 aus dem Eem Interglazial im östlichen Mittelmeer, Diplomarbeit: Fakultät für Biologie, Eberhard-Karls Universität, Tübingen, 138 pp.

Krijgsman, W., Hilgen, F. J., Raffi, I., Sierro, F. J., and Wilson, D. S., 1999, Chronology, causes and progression of the Messinian salinity crisis: Nature, v. 400, no. 6745, pp. 652-655.

Krom, M. D., Michard, A., Cliff, R. A., and Strohle, K., 1999, Sources of sediment to the Ionian Sea and western Levantine basin of the Eastern Mediterranean during S-1 sapropel times: Marine Geology, v. 160, no. 1-2, pp. 45-61.

Kucera, M., 2007, Planktonic Foraminifera as Tracers of Past Oceanic Enviroments, *in* C. Hillaire-Marcel, A. d. V., ed., Proxies in late Cenozoic Paleoceanography, Volume 1, Elsevier, pp. 213-262.

Kühl, N., and Litt, T., 2003, Quantitative time series reconstruction of Eemian temperature at three European sites using pollen data: Vegetation history and Archaeobotany, v. 12, no. 4, pp. 205-214.

Kukla, G., and Briskin, M., 1983, The age of the 4/5 isotopic stage boundary on land and in the oceans: Palaeogeography, Palaeoclimatology, Palaeoecology, v. 42, no. 1-2, pp. 35-45.

Kukla, G. J., Bender, M. L., de Beaulieu, J.-L., Bond, G., Broecker, W. S., Cleveringa, P., Gavin, J. E., Herbert, T. D., Imbrie, J., Jouzel, J., Keigwin, L. D., Knudsen, K.-L., McManus, J. F., Merkt, J., Muhs, D. R., Mueller, H., Poore, R. Z., Porter, S. C., Seret, G., Shackleton, N. J., Turner, C., Tzedakis, P. C., and Winograd, I. J., 2002, Last interglacial climates: Quarternary Research, v. 58, no. 1, pp. 2-13.

Kullenberg, B., 1952, On the salinity of the water contained in marine sediments: Goteborgs K. Vetenskaps. Vitt-Sambal. Handl.,, v. 6, pp. 3-37.

Langereis, C. G., Dekkers, M. J., Lange, G. J. d., Paterne, M., and vanSantvoort, P. J. M., 1997, Magnetostratigraphy and astronomical calibration of the last 1.1 Myr from an eastern

Mediterranean piston core and dating of short events in the Brunhes: Geophysical Journal international, v. 129, pp. 75-94.

Larrasoaña, J., Roberts, A., Rohling, E., Winklhofer, M., and Wehausen, R., 2003, Three million years of monsoon variability over the northern Sahara: Climate Dynamics, v. 21, no. 7, pp. 689-698.

Larrasoaña, J. C., Roberts, A. P., and Rohling, E. J., 2008, Magnetic susceptibility of eastern Mediterranean marine sediments as a proxy for Saharan dust supply?: Marine Geology, v. 254, no. 3-4, pp. 224-229.

Lascaratos, A., Roether, W., Nittis, K., and Klein, B., 1999, Recent changes in deep water formation and spreading in the eastern Mediterranean Sea: a review: Progress In Oceanography, v. 44, no. 1-3, pp. 5-36.

Leyer, I., and Wesche, K., 2007, Multivariate Statistik in der Ökologie, Springer, 221pp,

Limonov, A. F., Woodside, J. M., Cita, M. B., and Ivanov, M. K., 1996, The Mediterranean Ridge and related mud diapirism: a background: Marine Geology, v. 132, no. 1-4, pp. 7-19.

Linsley, B. K., 1996, Oxygen-isotope record of sea level and climate variations in the Sulu Sea over the past 150,000 years.

Lisiecki, L. E., and Raymo, M. E., 2005, A Plio-Pleistocene stack of 57 globally distributed benthic 18O records: Paleoceanography, v. 20, pp. 522–533.

Litt, T., Junge, F. W., and Böttger, T., 1996, Climate during the Eemian in north-central Europe—a critical review of the palaeobotanical and stable isotope data from central Germany: Vegetation history and Archaeobotany, v. 5, no. 3, pp. 247-256.

Lohmann, G. P., and Schweitzer, P. N., 1990, Globorotalia truncatulinoides' growth and chemistry as probes of the past thermocline: 1. shell size: Paleoceanography, v. 5, no. 1, pp. 55-75.

Lourens, L. J., 2004, Revised tuning of Ocean Drilling Program Site 964 and KC01B (Mediterranean) and implications for the delta 0-18, tephra, calcareous nannofossil, and geomagnetic reversal chronologies of the past 1.1 Myr: Paleoceanography, v. 19, no. 3, pp. PA3010.

Lourens, L. J., Antonarakou, A., Hilgen, F. J., Van Hoof, A. A. M., Vergnaud-Grazzini, C., and Zachariasse, W. J., 1996, Evaluation of the Plio-Pleistocene Astronomical Timescale: Paleoceanography, v. 11, no. 4, pp. 391-413.

Malanotte-Rizzoli, P., and Eremeev, V. N., 1999, The Eastern Mediterranean as a laboratory basin for the assessment of contrasting ecosystems, Kluwer Academic Publishers, 540pp.

Malanotte-Rizzoli, P., Manca, B. B., D'Alcalà, M. R., Theocharis, A., Bergamasco, A., Bregant, D., Budillon, G., Civitarese, G., Georgopoulos, D., Michelato, A., Sansone, E., Scarazzato, P., and Souvermezoglou, E., 1997, A synthesis of the Ionian Sea hydrography, circulation and water mass pathways during POEM-Phase I: Progress In Oceanography, v. 39, no. 3, pp. 153-204.

Maldonado, A., Kelling, G., and Anastasakis, G., 1981, Late Quaternary sedimentation in a zone of continental plate convergence -- The central Hellenic Trench system: Marine Geology, v. 43, no. 1-2, pp. 83-110.

Malmgren, B., and Kennett, P., 1972, Biometric analysis of phenotypic variation; globigerina pachyderma (Ehrenberg) in the South Pacific Ocean: Micropaleontology v. 18, pp. 241-248.

Malmgren, B. A., and Nordlund, U., 1997, Application of artificial neural networks to paleoceanographic data: Palaeogeography, Palaeoclimatology, Palaeoecology, v. 136, no. 1-4, pp. 359-373.

Mangini, A., and Schlosser, P., 1986, The formation of Eastern Mediterranean sapropels: Marine Geology, v. 72, no. 1-2, pp. 115-124.

Mann, M. E., Zhang, Z., Rutherford, S., Bradley, R. S., Hughes, M. K., Shindell, D., Ammann, C., Faluvegi, G., and Ni, F., 2009, Global signatures and dynamical origins of the Little Ice Age and Medieval Climate Anomaly: Science, v. 326, no. 5957, pp. 1256-1260.

Marino, G., Rohling, E. J., Rijpstra, W. I. C., Sangiorgi, F., Schouten, S., and Damsté, J. S. S., 2007, Aegean Sea as driver of hydrographic and ecological changes in the eastern Mediterranean: Geology, v. 35, no. 8, pp. 675-678.

Martin, A. P., and Richards, K. J., 2001, Mechanisms for vertical nutrient transport within a North Atlantic mesoscale eddy: Deep Sea Research Part II: Topical Studies in Oceanography, v. 48, no. 4-5, pp. 757-773.

Martinez-Ruiz, F., Kastner, M., Paytan, A., Ortega-Huertas, M., and Bernasconi, S. M., 2000, Geochemical evidence for enhanced productivity during S1 sapropel deposition in the eastern Mediterranean: Paleoceanography, v. 15, no. 2, pp. 200–209.

Maslin, M., Sarnthein, M., Knaack, J.-J., Grootes, P., and Tzedakis, C., 1998, Intra-interglacial cold events: an Eemian-Holocene comparison: Geological Society, London, Special Publications, v. 131, no. 1, pp. 91-99.

Mather, A., 2009, Tectonic Setting and Landscape Development, The physical geography of the Mediterranean, Oxford University Press, pp. 5-33.

Mayer, L. M., Schick, L. L., Allison, M. A., Ruttenberg, K. C., and Bentley, S. J., 2007, Marine vs. terrigenous organic matter in Louisiana coastal sediments: The uses of bromine:organic carbon ratios: Marine Chemistry, v. 107, no. 2, pp. 244-254.

McCoy, F. W., 1974, Late Quaternary sedimentation in the Eastern Mediterranean Sea: Harvard.

McGillicuddy Jr, D. J., Johnson, R., Siegel, D. A., Michaels, A. F., Bates, N. R., and Knap, A. H., 1999, Mesoscale variations of biogeochemical properties in the Sargasso Sea: Journal of Geophysical Research, v. 104, no. C6, pp. 13381-13394.

McGillicuddy Jr, D. J., and Robinson, A. R., 1997, Eddy-induced nutrient supply and new production in the Sargasso Sea: Deep Sea Research Part I: Oceanographic Research Papers, v. 44, no. 8, pp. 1427-1450.

Menzel, D., van Bergen, P. F., Schouten, S., and Sinninghe Damsté, J. S., 2003, Reconstruction of changes in export productivity during Pliocene sapropel deposition: a biomarker approach: Palaeogeography, Palaeoclimatology, Palaeoecology, v. 190, pp. 273-287.

Mercone, D., Thomson, J., Abu-Zied, R. H., Croudace, I. W., and Rohling, E. J., 2001, High-resolution geochemical and micropalaeontological profiling of the most recent eastern Mediterranean sapropel: Marine Geology, v. 177, no. 1-2, pp. 25-44.

Mercone, D., Thomson, J., Croudace, I. W., Siani, G., Paterne, M., and Troelstra, S., 2000, Duration of S1, the Most Recent Sapropel in the Eastern Mediterranean Sea, as Indicated by Accelerator Mass Spectrometry Radiocarbon and Geochemical Evidence: Paleoceanography, v. 15, no. 3, pp. 336-347.

Milder, J. C., Montoya, J. P., and Altabet, M. A., 1999, Carbon and nitrogen stable isotope ratios at sites 969 and 974; interpreting spatial gradients in sapropel properties: In Proc. ODP, Scientific Res., 161 (ed. R. Zahn, M. C. Comas, and A. Klaus) Vol. 161, pp. 401–411. Ocean Drilling Project.

Molinaroli, E., Guerzoni, S., and Rampazzo, G., 1993, Contribution of Saharan dust to the central Mediterranean basin: SPECIAL PAPERS-GEOLOGICAL SOCIETY OF AMERICA, pp. 303-303.

Moller, T., Schulz, H., Hamann, Y., Dellwig, O., and Kucera, M., 2011a, Sedimentology and geochemistry of an exceptionally preserved last interglacial sapropel S_5 in the Levantine Basin (Mediterranean Sea): Marine Geology.

Moller, T., Schulz, H., and Kucera, M., 2011b, The effect of sea surface properties on shell morphology and size of the planktonic foraminifer Neogloboquadrina pachyderma in the North Atlantic: Palaeogeography, Palaeoclimatology, Palaeoecology.

Morigi, C., 2009, Benthic environmental changes in the Eastern Mediterranean Sea during sapropel S5 deposition: Palaeogeography, Palaeoclimatology, Palaeoecology, v. 273, no. 3-4, pp. 258-271.

Muerdter, D. R., 1984, Low-salinity surface water incursions across the Strait of Sicily during late Quaternary sapropel intervals: Marine Geology, v. 58, no. 3-4, pp. 401-414.

Muerdter, D. R., Kennett, J. P., and Thunell, R. C., 1984, Late Quaternary sapropel sediments in the eastern Mediterranean Sea: Faunal variations and chronology: Quaternary Research, v. 21, no. 3, pp. 385-403.

Müller, U. C., Pross, J., and Bibus, E., 2003, Vegetation response to rapid climate change in Central Europe during the past 140,000 yr based on evidence from the Füramoos pollen record: Quaternary Research, v. 59, pp. 235-245.

Munsell, Soil Color Charts, 1995, 617 Little Britain Road, New Windsor, NY 12553, The Geological Society of America, GretagMacbeth.

Myers, P. G., Haines, K., and Rohling, E. J., 1998, Modeling the Paleocirculation of the Mediterranean: The Last Glacial Maximum and the Holocene with Emphasis on the Formation of Sapropel S1: Paleoceanography, v. 13, no. 6, pp. 586-606.

Natland, M. L., 1938, New species of foraminifera from off the west coast of North America and from the later Tertiary of the Los Angeles Basin :Scripps Inst. Oceanogr. Bull., v. 4, pp. 137-164.,

Nijenhuis, I. A., Brumsack, H. J., and De-Lange, G. J., 1998, 16. The trace element budget of the Eastern Mediterranean during sapropel formation: Proceedings of the Ocean Drilling Program, Scientific Results, Vol. 160; Chapter 50.

Nolet, G. J., and Corliss, B. H., 1990, Benthic foraminiferal evidence for reduced deep-water circulation during sapropel deposition in the eastern Mediterranean: Marine Geology, v. 94, no. 1-2, pp. 109-130.

Numberger, L., Hemleben, C., Hoffmann, R., Mackensen, A., Schulz, H., Wunderlich, J.-M., and Kucera, M., 2009, Habitats, abundance patterns and isotopic signals of morphotypes of the planktonic foraminifer Globigerinoides ruber (d'Orbigny) in the eastern Mediterranean Sea since the Marine Isotopic Stage 12: Marine Micropaleontology, v. 73, no. 1-2, pp. 90-104.

Ocean Project (Comission of the European Communities European Space Agency), 1980, Chlorophyll-Like Pigment Concentration In The Mediterranean (CZCS-DERIVED) MG/M3.

Olausson, E., 1960, Description of sediment cores from the Mediterranean and the Red Sea: Report of the Swedish Deep Sea Expedition 1947-1948

Olausson, E., 1961, Studies of deep-sea cores: Report of the Swedish Deep Sea Expedition 1947-1948, v. Goeteborg Sweden, pp. 337–391.

Osborne, A. H., Vance, D., Rohling, E. J., Barton, N., Rogerson, M., and Fello, N., 2008, A humid corridor across the Sahara for the migration of early modern humans out of Africa 120,000 years ago: Proceedings of the National Academy of Sciences, v. 105, no. 43, pp. 16444-16447.

Parker, F. L., 1958, Eastern Mediterranean Foraminifera: Report of the Swedish Deep Sea Expedition 1947-1948, v. 8, pp. 217-283.

Parker, F. L., 1962, Planktonic foraminiferal species in Pacific sediments: Micropaleontology, v. 8, pp. 219-254.

Parker, F. L., 1967, Late Tertiary biostratigraphy (planktonic foraminifera) of tropical Indo-Pacific deep-sea cores: Bulletins of American Paleontology, v. 52, no. 235, pp. 116-208.

Passier, H. F., Bosch, H. J., Nijenhuis, I. A., Lourens, L. J., Böttcher, M. E., Leenders, A., Sinninghe Damsté, J., de Lange, G. J., and De Leeuw, J., 1999a, Sulphidic Mediterranean surface waters during Pliocene sapropel formation: Nature, v. 397, no. 6715, pp. 146-149.

Passier, H. F., Middelburg, J. J., de Lange, G. J., and Böttcher, M. E., 1999b, Modes of sapropel formation in the eastern Mediterranean: some constraints based on pyrite properties: Marine Geology, v. 153, no. 1-4, pp. 199-219.

Pearce, R., Kemp, A., Koizumi, I., Pike, J., Cramp, A., and Rowland, S., A lamina-scale, SEM-based study of a late Quaternary diatom-ooze sapropel from the Mediterranean Ridge, Site 9711998, Volume 160, Ocean Drilling Program, pp. 349-363.

Phedorin, M. A., and Goldberg, E. L., 2005, Prediction of absolute concentrations of elements from SR XRF scan measurements of natural wet sediments: Nuclear Instruments and Methods in Physics Research Section A: Accelerators, Spectrometers, Detectors and Associated Equipment, v. 543, no. 1, pp. 274-279.

Pike, J., and Kemp, A. E. S., 1996, Preparation and analysis techniques for studies of laminated sediments, Geological Society of London, Geological Society, London, Special Publications, v. 1, 37 pp.

Pike, J., Stickley, C., Maddison, E., Leventer, A., Brachfeld, S., Domack, E., Dunbar, R., Manley, P., and McClennen, C., Late Quaternary biosiliceous laminated marine sediments from Antarctica: Seasonality during a period of rapid climate change2004, Volume 1, pp. 02.

Pinardi, N., and Masetti, E., 2000, Variability of the large scale general circulation of the Mediterranean Sea from observations and modelling: a review: Palaeogeography, Palaeoclimatology, Palaeoecology, v. 158, no. 3-4, pp. 153-173.

Postuma, J., 1971, Manual of planktonic foraminifera.

Potonié, H., 1904, Über Faulschlamm-(Sapropel)-Gesteine: Sitzungsberichte der Gesellschaft Naturforschender Freunde zu Berlin, pp. 243-245.

Psarra, S., Tselepides, A., and Ignatiades, L., 2000, Primary productivity in the oligotrophic Cretan Sea (NE Mediterranean): seasonal and interannual variability: Progress In Oceanography, v. 46, no. 2-4, pp. 187-204.

Pujol, C., and Grazzini, C. V., 1995, Distribution patterns of live planktic foraminifers as related to regional hydrography and productive systems of the Mediterranean Sea: Marine Micropaleontology, v. 25, no. 2-3, pp. 187-217.

Raspopov, O., Dergachev, V., Esper, J., Kozyreva, O., Frank, D., Ogurtsov, M., Kolström, T., and Shao, X., 2008, The influence of the de Vries (200-year) solar cycle on climate variations: Results from the Central Asian Mountains and their global link: Palaeogeography, Palaeoclimatology, Palaeoecology, v. 259, no. 1, pp. 6-16.

Ravelo, A. C., and Hillaire-Marcel, C., 2007, The Use of Oxygen and Carbon Isotopes of Foraminifera in Paleoceanography, *in* Claude, H.-M., and Anne De, V., eds., Developments in Marine Geology, Volume Volume 1, Elsevier, pp. 735-764.

Reuss, A. E., 1850, Neue Foraminiferen aus den Schichten des österreichischen Tertiärbeckens, KK Hof-und Staatsdruckerei,

Revel, M., Ducassou, E., Grousset, F. E., Bernasconi, S. M., Migeon, S., Revillon, S., Mascle, J., Murat, A., Zaragosi, S., and Bosch, D., 2010, 100,000 Years of African monsoon variability recorded in sediments of the Nile margin: Quaternary Science Reviews, v. 29, no. 11-12, pp. 1342-1362.

Ribes, J., and Nesme-Ribes, E., 1993, The solar sunspot cycle in the Maunder minimum AD1645 to AD1715: Astronomy and Astrophysics, v. 276, pp. 549-563.

Richards, A. F., 1967, Marine geotechnique: proceedings, University of Illinois Press, pp. 327,

Rind, D., 2002, The sun's role in climate variations: Science, v. 296, no. 5568, pp. 673-677.

Robertson, A., 1996, Mud volcanism on the Mediterranean Ridge: Initial results of Ocean Drilling Program Leg 160: Geology, v. 24, no. 3, pp. 239.

Robertson, A. H. F., and Kopf, A., 1998, Tectonic setting and processes of mud volcanism on the Mediterranean Ridge accretionary complex: evidence from Leg 160: Proceedings of the Ocean Drilling Program, Scientific Results, Vol. 160; Chapter 50.

Robinson, A. R., and Golnaraghi, M., 1993, Circulation and dynamics of the Eastern Mediterranean Sea; quasi-synoptic data-driven simulations: Deep Sea Research Part II: Topical Studies in Oceanography, v. 40, no. 6, pp. 1207-1246.

Robinson, A. R., Leslie, W. G., Theocharis, A., and Lascaratos, A., 2009, Mediterranean Sea circulation: Ocean Currents: A Derivative of the Encyclopedia of Ocean Sciences, pp. 283.

Robinson, A. R., Malanotte-Rizzoli, P., Hecht, A., Michelato, A., Roether, W., Theocharis, A., Ünlüata, Ü., Pinardi, N., Artegiani, A., Bergamasco, A., Bishop, J., Brenner, S., Christianidis, S., Gacic, M., Georgopoulos, D., Golnaraghi, M., Hausmann, M., Junghaus, H. G., Lascaratos, A., Latif, M. A., Leslie, W. G., Lozano, C. J., Oguz, T., Özsoy, E., Papageorgiou, E., Paschini, E., Rozentroub, Z., Sansone, E., Scarazzato, P., Schlitzer, R., Spezie, G. C., Tziperman, E., Zodiatis, G., Athanassiadou, L., Gerges, M., and Osman, M., 1992, General circulation of the Eastern Mediterranean: Earth-Science Reviews, v. 32, no. 4, pp. 285-309.

Rohling, E., Abu-Zied, R., Casford, J., Hayes, A., and Hoogakker, B., 2009, The marine environment: present and past, The physical geography of the Mediterranean, Oxford University Press, pp. 33-69.

Rohling, E. J., 1994, Review and new aspects concerning the formation of eastern Mediterranean sapropels: Marine Geology, v. 122, no. 1-2, pp. 1-28.

Rohling, E. J., Cane, T. R., Cooke, S., Sprovieri, M., Bouloubassi, I., Emeis, K. C., Schiebel, R., Kroon, D., Jorissen, F. J., Lorre, A., and Kemp, A. E. S., 2002, African monsoon variability during the previous interglacial maximum: Earth and Planetary Science Letters, v. 202, no. 1, pp. 61-75.

Rohling, E. J., and Gieskes, W. W. C., 1989, Late Quaternary changes in Mediterranean intermediate water density and formation rate: Paleoceanography, v. 4, no. 5, pp. 531-545.

Rohling, E. J., Grant, K., Hemleben, C. H., Siddall, M., Hoogakker, B. A. A., Bolshaw, M., and Kucera, M., 2007, High rates of sea-level rise during the last interglacial period: Nature Geoscience, v. 1, no. 1, pp. 38-42.

Rohling, E. J., and Hilgen, F. J., 1991, The eastern Mediterranean climate at times of sapropel formation: a review: Journal of Geosciences, Institute of Applied Geoscience T. N. O. Royal Geological Mining, Society of the Netherlands Utrecht Netherlands, v. 70, pp. 253-264.

Rohling, E. J., Jorissen, F. J., and Stigter, H. C. d., 1997, 200 year interruption of Holocene sapropel formation in the Adriatic Sea: Journal of Micropalaeontology, v. 16, pp. 97-108.

Rohling, E. J., Sprovieri, M., Cane, T., Casford, J. S. L., Cooke, S., Bouloubassi, I., Emeis, K. C., Schiebel, R., Rogerson, M., Hayes, A., Jorissen, F. J., and Kroon, D., 2004, Reconstructing past planktic foraminiferal habitats using stable isotope data: a case history for Mediterranean sapropel S5: Marine Micropaleontology, v. 50, no. 1-2, pp. 89-123.

Rossignol-Strick, M., 1983, African monsoons, an immediate climate response to orbital insolation: Nature, v. 304, no. 46-49.

Rossignol-Strick, M., 1985, Mediterranean Quaternary sapropels, an immediate response of the African monsoon to variation of insolation: Palaeogeography, Palaeoclimatology, Palaeoecology, v. 49, no. 3-4, pp. 237-263.

Rossignol-Strick, M., Nesteroff, W., Olive, P., and Vergnaud-Grazzini, C., 1982, After the deluge: Mediterranean stagnation and sapropel formation: Nature, v. 295, no. 5845, pp. 105-110.

Rossignol-Strick, M., and Paterne, M., 1999, A synthetic pollen record of the eastern Mediterranean sapropels of the last 1 Ma: implications for the time-scale and formation of sapropels: Marine Geology, v. 153, no. 1-4, pp. 221-237.

Rothwell, R. G., 2006, New techniques in sediment core analysis, Geological Society Publishing House.

Ruggieri, G., 1967, The Miocene and later evolution of the Mediterranean Sea: Aspects of Tethyan biogeography, London, Systematic Studies Association, Publication, v. 7, pp. 283-290.

Rutten, A., de Lange, G. J., Hayes, A., Rohling, E. J., de Jong, A. F. M., and van der Borg, K., 1999, Deposition of sapropel S1 sediments in oxic pelagic and anoxic brine environments in the eastern Mediterranean: differences in diagenesis and preservation: Marine Geology, v. 153, no. 1-4, pp. 319-335.

Ryan, W., 1972, Stratigraphy of Late Quaternary sediments in the eastern Mediterranean: The Mediterranean Sea: a natural sedimentation laboratory, pp. 149–169.

Ryan, W. B. F., and Cita, M. B., 1977, Ignorance concerning episodes of ocean-wide stagnation: Marine Geology, v. 23, no. 1-2, pp. 197-215.

Saito, T., Thompson, P. R., and Breger, D., 1981, Systematic Index of Recent and Pleistocene Planktonic Foraminifera Univ, Tokyo Press, 190pp.

Salihoğlu, İ., Saydam, C., Baştürk, Ö., Yilmaz, K., Göçmen, D., Hatipoğlu, E., and Yilmaz, A., 1990, Transport and distribution of nutrients and chlorophyll-a by mesoscale eddies in the northeastern Mediterranean: Marine Chemistry, v. 29, no. 0, pp. 375-390.

Sancetta, C., 1994, Mediterranean Sapropels: Seasonal stratification yields high production and carbon flux: Paleoceanography, v. 9, no. 2, pp. 195-196.

Sánchez-Goñi, M., Eynaud, F., Turon, J. L., and Shackleton, N. J., 1999, High resolution palynological record off the Iberian margin: direct land-sea correlation for the Last Interglacial complex: Earth and Planetary Science Letters, v. 171, no. 1, pp. 123-137.

Sánchez-Goñi, M. F., 2007, 13. Introduction to climate and vegetation in Europe during MIS5, *in* Frank Sirocko, M. C. M. F. S. G., and Thomas, L., eds., Developments in Quaternary Sciences, Volume Volume 7, Elsevier, pp. 197-205.

Sánchez Goñi, M., Loutre, M. F., Crucifix, M., Peyron, O., Santos, L., Duprat, J., and Malaize, B., 2005, Increasing vegetation and climate gradient in Western Europe over the Last Glacial Inception (122-110 ka): data-model comparison: Earth and Planetary Science Letters, v. 231, no. 1-2, pp. 111-130.

Sánchez Goñi, M. F., Turon, J., Eynaud, F., Shackleton, N., and Cayre, O., 2000, Direct land/sea correlation of the Eemian, and its comparison with the Holocene: a high-resolution palynological record off the Iberian margin: Geologie en Mijnbouw, v. 79, no. 2/3, pp. 345-356.

Sangiorgi, F., Dinelli, E., Maffioli, P., Capotondi, L., Giunta, S., Morigi, C., Principato, M. S., Negri, A., Emeis, K.-C., and Corselli, C., 2006, Geochemical and micropaleontological characterisation of a Mediterranean sapropel S5: A case study from core BAN89GC09 (south of Crete): Palaeogeography, Palaeoclimatology, Palaeoecology, v. 235, no. 1-3, pp. 192-207.

Sarnthein, M., 1978, Sand deserts during glacial maximum and climatic optimum: Nature, v. 272, no. 5648, pp. 43-46.

Schiebel, R., Bijma, J., and Hemleben, C., 1997, Population dynamics of the planktic foraminifer Globigerina bulloides from the eastern North Atlantic: Deep Sea Research Part I: Oceanographic Research Papers, v. 44, no. 9-10, pp. 1701-1713.

Schlesinger, M. E., and Ramankutty, N., 1994, An oscillation in the global climate system of period 65-70 years: Nature, v. 367, no. 6465, pp. 723-726.

Schmidt, D. N., Renaud, S., Bollmann, J., Schiebel, R., and Thierstein, H. R., 2004, Size distribution of Holocene planktic foraminifer assemblages: biogeography, ecology and adaptation: Marine Micropaleontology, v. 50, no. 3-4, pp. 319-338.

Schmiedl, G., Hemleben, C., Keller, J., and Segl, M., 1998, Impact of climatic changes on the benthic foraminiferal fauna in the Ionian Sea during the last 330,000 years: Paleoceanography, v. 13, no. 5, pp. 447- 458.

Schmiedl, G., Mitschele, A., Beck, S., Emeis, K.-C., Hemleben, C., Schulz, H., Sperling, M., and Weldeab, S., 2003a, Benthic foraminiferal record of ecosystem variability in the eastern Mediterranean Sea during times of sapropel S5 and S6 deposition: Palaeogeography, Palaeoclimatology, Palaeoecology, v. 190, no. 0, pp. 139-164.

Schmiedl, G., Mitschele, A., Beck, S., Weldeab, S., Schulz, H., Hemleben, C., Sperling, M. R., and Emeis, K.-C., 2003b, Stable oxygen isotope signal of Globigerinoides ruber across sapropel S5 in core M40/4_67SL from the lower bathyal of the western Levantine Basin. doi:10.1594/PANGAEA.115078, In Supplement to: Schmiedl G., Mitschele A., Beck S.; Weldeab S., Schulz H., Hemleben C., Sperling M. R., Emeis K.-C. (2003): Benthic foraminiferal record of ecosystem variability in the eastern Mediterranean Sea during times of sapropel S5 and S6 formation. Palaeogeography, Palaeoclimatology, Palaeoecology, v. 190, no. 0, pp. 139-164.

Schrader, H., and Matherne, A., 1981, Sapropel formation in the eastern Mediterranean Sea: evidence from preserved opal assemblages: Micropaleontology, v. 27, no. 2, pp. 191-203.

Schultz, J., 2008, Die Ökozonen der Erde, Stuttgart, Ulmer, 368 pp.,

Seeberg-Elverfeldt, I., Lange, C., Pätzold, J., and Kuhn, G., 2005, Laminae type and possible mechanisms for the formation of laminated sediments in the Shaban Deep, northern Red Sea: Ocean Science, v. 1, no. 2, pp. 113-126.

Seeberg-Elverfeldt, I. A., Lange, C. B., Arz, H. W., Pätzold, J., and Pike, J., 2004, The significance of diatoms in the formation of laminated sediments of the Shaban Deep, Northern Red Sea: Marine Geology, v. 209, no. 1-4, pp. 279-301.

Seidenkrantz, M. S., Bornmalm, L., Johnsen, S. J., Knudsen, K. L., Kuijpers, A., Lauritzen, S. E., Leroy, S. A. G., Mergeal, I., and Schweger, C., 1996, Two-step deglaciation at the oxygen isotope stage 6/5e transition: the Zeifen-Kattegat climate oscillation: Quaternary Science Reviews, v. 15, no. 1, pp. 63-75.

Severmann, S., and Thomson, J., 1998, Investigation of the ingrowth of radioactive daughters of 238U in Mediterranean sapropels as a potential dating tool: Chemical Geology, v. 150, no. 3, pp. 317-330.

Shackleton, N. J., Chapman, M., Sanchez-Goni, M. F., Pailler, D., and Lancelot, Y., 2002, The classic marine isotope Substage 5e: Quarternary Research, v. 58, no. 1, pp. 14-16.

Shackleton, N. J., and Opdyke, N. D., 1973, Oxygen isotope and palaeomagnetic stratigraphy of Equatorial Pacific core V28-238: Oxygen isotope temperatures and ice volumes on a 105 year and 106 year scale: Quaternary Research, v. 3, no. 1, pp. 39-55.

Shannon, C., 1948, A mathematical theory of communication: The Bell System Technical Journal, v. 27, no. 7, pp. 379-423.

Siokou-Fragou, I., 1999, Plankton characteristics in the Aegean, Ionian and NW Levantine Seas: The Eastern Mediterranean as a Laboratory Basin for the Assessment of Contrasting Ecosystems, v. 51, pp. 465-473.

Sirocko, F., Seelos, K., Schaber, K., Rein, B., Dreher, F., Diehl, M., Lehne, R., Jager, K., Krbetschek, M., and Degering, D., 2005, A late Eemian aridity pulse in central Europe during the last glacial inception: Nature, v. 436, no. 7052, pp. 833-836.

Speranza, A., Van Geel, B., and Van der Plicht, J., 2003, Evidence for solar forcing of climate change at ca. 850 cal BC from a Czech peat sequence: Global and Planetary Change, v. 35, no. 1-2, pp. 51-65.

Spindler, M., Hemleben, C., Salomons, J. B., and Smit, L. P., 1984, Feeding behavior of some planktonic foraminifers in laboratory cultures: The Journal of Foraminiferal Research, v. 14, no. 4, pp. 237-249.

St-Onge, G., Mulder, T., Francus, P., and Long, B., 2007, Continuous Physical Properties of Cored Marine Sediments *in* C. Hillaire-Marcel, A. d. V., ed., Proxies in late Cenozoic Paleoceanography, Volume 1, Elsevier, pp. 63-98.

Stoner, J. S., and St-Onge, G., 2007, Magnetic Stratigraphy in Paleoceanography: Reversals, Excursions, Paleointensity, and Secular Variation, *in* C. Hillaire-Marcel, A. d. V., ed., Proxies in late Cenozoic Paleoceanography, Volume 1, Elsevier, pp. 63-98.

Stratford, K., Williams, R. G., and Myers, P. G., 2000, Impact of the circulation on Sapropel Formation in the eastern Mediterranean: Global Biogeochemical Cycles, v. 14, no. 2, pp. 683-695.

Struck, U., Emeis, K.-C., Voß, M., Krom, M. D., and Rau, G. H., 2001, Biological productivity during sapropel S5 formation in the Eastern Mediterranean Sea: evidence from stable isotopes of nitrogen and carbon: Geochimica et Cosmochimica Acta, v. 65, no. 19, pp. 3249-3266.

Szabo, B. J., Ludwig, K. R., Muhs, D. R., and Simmons, K. R., 1994, Thorium-230 ages of corals and duration of the last interglacial sea-level high stand on Oahu, Hawaii: Science, v. 266, no. 5182, pp. 93-96.

tenHaven, H. L., Baas, M., Kroot, M., Leeuw, J. W. d., Schenck, P. A., and Ebbing, J., 1987, Late Quaternary Mediterranean sapropels. III: Assessment of source of input and palaeotemperature as derived from biological markers: Geochimica et Cosmochimica Acta, v. 51, no. 4, pp. 803-810.

Thomson, J., Croudace, I. W., and Rothwell, R., 2006, A geochemical application of the ITRAX scanner to a sediment core containing eastern Mediterranean sapropel units: New Techniques in Sediment Core Analysis. Geological Society, London.

Thomson, J., Higgs, N. C., Wilson, T. R. S., Croudace, I. W., Lange, G. J. D., and Santvoort, P. J. M. V., 1995, Redistribution and geochemical behaviour of redox-sensitive elements around S1, the most recent eastern Mediterranean sapropel: Geochimica et Cosmochimica Acta, v. 59, no. 17, pp. 3487-3501.

Thunell, R. C., 1978, Distribution of recent planktonic foraminifera in surface sediments of the Mediterranean Sea: Marine Micropaleontology, v. 3, no. 2, pp. 147-173.

Thunell, R. C., and Williams, D. F., 1982, Paleoceanographic events associated with Termination II in the Eastern Mediterranean: Oceanologica Acta, v. 5, pp. 229-233.

Thunell, R. C., Williams, D. F., and Belyea, P. R., 1984, Anoxic events in the Mediterranean Sea in relation to the evolution of late Neogene climates: Marine Geology, v. 59, no. 1-4, pp. 105-134.

Thunell, R. C., Williams, D. F., and Kennett, J. P., 1977, Late Quaternary paleoclimatology, stratigraphy and sapropel history in eastern Mediterranean deep-sea sediments: Marine Micropaleontology, v. 2, pp. 371-388.

Timm, O., Kohler, P., Timmermann, A., and Menviel, L., 2010, Mechanisms for the onset of the African Humid Period and Sahara: Journal of Climate, v. 23, no. 10, pp. 2612–2633.

Tjallingii, R., Röhl, U., Kölling, M., and Bickert, T., 2007, Influence of the water content on X-ray fluorescence core-scanning measurements in soft marine sediments: Geochemistry Geophysics Geosystems, v. 8, no. 2, pp. 1-12.

Torrence, C., and Compo, G., 1998, A practical guide to wavelet analysis: Bulletin of the American Meteorological Society, v. 79, pp. 61-78.

Torres, M. E., Brumsack, H. J., Bohrmann, G., and Emeis, K. C., 1996, Barite fronts in continental margin sediments: a new look at barium remobilization in the zone of sulfate reduction and formation of heavy barites in diagenetic fronts: Chemical Geology, v. 127, no. 1-3, pp. 125-139.

Trauth, M. H., 2007, MATLAB® Recipes for Earth Sciences 2nd edition, Springer, 298pp,

Trauth, M. H., Deino, A. L., Bergner, A. G. N., and Strecker, M. R., 2003, East African climate change and orbital forcing during the last 175 kyr BP: Earth and Planetary Science Letters, v. 206, no. 3-4, pp. 297-313.

Triantaphyllou, M., Antonarakou, A., Kouli, K., Dimiza, M., Kontakiotis, K., Papanikolaou, M., Ziveri, P., Mortyn, P., Lianou, V., Lykousis, V., and Dermitzakis, M., 2009, Late Glacial–Holocene ecostratigraphy of the south-eastern Aegean Sea, based on plankton and pollen assemblages: Geo-Marine Letters, v. 29, no. 4, pp. 249-267.

Tsimplis, M. N., Zervakis, V., Josey, S. A., Peneva, E. L., Struglia, M. V., Stanev, E. V., Theocharis, A., Lionello, P., Malanotte-Rizzoli, P., Artale, V., Tragou, E., and Oguz, T., 2006, Chapter 4 Changes in the oceanography of the Mediterranean Sea and their link to climate variability, *in* P. Lionello, P. M.-R., and Boscolo, R., eds., Developments in Earth and Environmental Sciences, Volume Volume 4, Elsevier, pp. 227-282.

Tucholka, P., Fontugne, M., Guichard, F., and Paterne, M., 1987, The Blake magnetic polarity episode in cores from the Mediterranean Sea: Earth and Planetary Science Letters, v. 86, no. 2-4, pp. 320-326.

Tzedakis, P., 1993, Long-term tree populations in northwest Greece through multiple Quaternary climatic cycles: Nature, v. 364, no. 6436, pp. 437-440.

van de Berg, W. J., van den Broeke, M., Ettema, J., van Meijgaard, E., and Kaspar, F., 2011, Significant contribution of insolation to Eemian melting of the Greenland ice sheet: Nature Geosci, v. 4, no. 10, pp. 679-683.

Van Straaten, L., 1966, Micro-malacological investigation of cores from the southeastern Adriatic Sea: Proc. Koninol-Nederl. Akad. Van Wetenshappen, v. 69, pp. 429-445.

van Straaten, L. M. J. U., 1970, Holocene and late-Pleistocene sedimentation in the Adriatic Sea: Geologische Rundschau, v. 60, no. 1, pp. 106-131.

Vannucci, G., 2004, An atlas of Mediterranean seismicity, Istituto Nazionale di Geofisica e Vulcanologia, Editrice Compositori,

vanSantvoort, P. J. M., deLange, G. J., Langereis, C. G., Dekkers, M. J., and Paterne, M., 1997, Geochemical and paleomagnetic evidence for the occurrence of ''missing'' sapropels in eastern Mediterranean sediments: Paleoceanography, v. 12, no. 6, pp. 773-786.

Vergnaud-Grazzini, C., Devaux, M., and Znaidi, J., 1986, Stable isotope “anomalies” in Mediterranean Pleistocene records: Mar. Micropaleontol, v. 10, pp. 35-69.

Vergnaud-Grazzini, C., Ryan, W. B. F., and Bianca Cita, M., 1977, Stable isotopic fractionation, climate change and episodic stagnation in the eastern Mediterranean during the late Quaternary: Marine Micropaleontology, v. 2, pp. 353-370.

Verschuren, D., Laird, K. R., and Cumming, B. F., 2000, Rainfall and drought in equatorial east Africa during the past 1,100 years: Nature, v. 403, no. 6768, pp. 410-414.

Villareal, T. A., Altabet, M. A., and Culver-Rymsza, K., 1993, Nitrogen transport by vertically migrating diatom mats in the North Pacific Ocean: Nature, v. 363, no. 6431, pp. 709-712.

Villareal, T. A., Woods, S., Moore, J. K., and CulverRymsza, K., 1996, Vertical migration of Rhizosolenia mats and their significance to NO3− fluxes in the central North Pacific gyre: Journal of Plankton Research, v. 18, no. 7, pp. 1103-1121.

Walker, J. C. G., Hays, P., and Kasting, J., 1981, A negative feedback mechanism for the long-term stabilization of the Earth's surface temperature: Journal of Geophysical Research, v. 86, no. C10, pp. 9776-9782.

Watkins, J. M., Mix, A. C., and Wilson, J., 1996, Living planktic foraminifera: tracers of circulation and productivity regimes in the central equatorial Pacific: Deep Sea Research Part II: Topical Studies in Oceanography, v. 43, no. 4–6, pp. 1257-1282.

Wehausen, R., and Brumsack, H. J., 1999, Cyclic variations in the chemical composition of eastern Mediterranean Pliocene sediments: a key for understanding sapropel formation: Marine Geology, v. 153, no. 1-4, pp. 161-176.

Weldeab, S., Emeis, K.-C., Hemleben, C., Schmiedl, G., and Schulz, H., 2003a, Biogenic barium concentrations and productivity reconstruction of sediment core M40/4_SL671 in the eastern Mediterranean Sea.doi:10.1594/PANGAEA.69830, In Supplement to: Weldeab S., Emeis K.-C. Hemleben C., Schmiedl G., Schulz H. (2003): Spatial productivity variations during formation of sapropels S5 and S6 in the Mediterranean Sea: Evidence from Ba contents. Palaeogeography, Palaeoclimatology, Palaeoecology, 191(2), 169-190.

Weldeab, S., Emeis, K.-C., Hemleben, C., Schmiedl, G., and Schulz, H., 2003b, Spatial productivity variations during formation of sapropels S5 and S6 in the Mediterranean Sea: evidence from Ba contents: Palaeogeography, Palaeoclimatology, Palaeoecology, v. 191, no. 2, pp. 169-190.

Weltje, G. J., and Tjallingii, R., 2008, Calibration of XRF core scanners for quantitative geochemical logging of sediment cores: Theory and application: Earth and Planetary Science Letters, v. 274, no. 3-4, pp. 423-438.

Wengert, M., 2002, Wavelet Toolbox in Java, Diplomarbeit: Universtiät Stuttgart, Geodätisches Institut.

Williams, D. F., and Thunell, R. C., 1979, Faunal and oxygen isotopic evidence for surface water salinity changes during sapropel formation in the eastern Mediterranean: Sedimentary Geology, v. 23, no. 1-4, pp. 81-93.

Woillard, G. M., 1978, Grande Pile peat bog: A continuous pollen record for the last 140,000 years: Quaternary Research, v. 9, no. 1, pp. 1-21.

Wold, S., Esbensen, K., and Geladi, P., 1987, Principal component analysis: Chemometrics and Intelligent Laboratory Systems, v. 2, no. 1-3, pp. 37-52.

Wolff, C. L., 1976, Timing of solar cycles by rigid internal rotations: The Astrophysical Journal, v. 205, pp. 612-621.

Wolff, E., 2011, Aufbereitung und Auszählverfahren zur Quantifizierung von silicatischem Plankton im laminierten Sapropel S5 des östlichen Mittelmeeres: Studienarbeit: Eberhard-Karls Universität, Tübingen, 49 pp.

World-Meteorological-Organization, 2010, World Weather Information Service.

Wüst, G., 1960, Die Tiefenzirkulation des Mittelländischen Meeres in den Kernschichten des Zwischen- und des Tiefenwassers: Deutsche Hydrographische Zeitschrift, v. 13, no. 3, pp. 105-131.

Wüst, G., 1961, On the vertical circulation of the Mediterranean Sea: J. Geophys. Res., v. 66, no. 10, pp. 3261-3271.

Yoder, J. A., Ackleson, S. G., Barber, R. T., Flament, P., and Balch, W. M., 1994, A line in the sea: Nature, v. 371, no. 6499, pp. 689-692.

Zhang, R., and Delworth, T. L., 2006, Impact of Atlantic multidecadal oscillations on India/Sahel rainfall and Atlantic hurricanes: Geophys. Res. Lett, v. 33, pp. L17712.

Zhuang, G., Yi, Z., Duce, R. A., and Brown, P. R., 1992, Link between iron and sulphur cycles suggested by detection of Fe (ll) in remote marine aerosols: Nature, v. 355, no. 6360, pp. 537-539.

Ziegler, M., Jilbert, T., de Lange, G. J., Lourens, L. J., and Reichart, G.-J., 2008, Bromine counts from XRF scanning as an estimate of the marine organic carbon content of sediment cores: Geochem. Geophys. Geosyst., v. 9, no. 5, pp. Q05009.

Ziegler, M., Tuenter, E., and Lourens, L. J., 2010, The precession phase of the boreal summer monsoon as viewed from the eastern Mediterranean (ODP Site 968): Quaternary Science Reviews, v. 29, no. 11–12, pp. 1481-1490.